

**SCATTERING FROM A CHIRAL CYLINDER  
OF ARBITRARY CROSS-SECTION ABOVE  
A DIELECTRIC HALF-SPACE**

A DISSERTATION SUBMITTED TO  
THE GRADUATE SCHOOL OF  
ENGINEERING AND NATURAL SCIENCES  
OF ISTANBUL MEDIPOL UNIVERSITY

IN PARTIAL FULFILLMENT OF THE REQUIREMENTS FOR  
THE DEGREE OF  
DOCTOR OF PHILOSOPHY

IN

ELECTRICAL, ELECTRONICS ENGINEERING AND CYBER SYSTEMS

By

Hassan Sajjad

January, 2021

SCATTERING FROM A CHIRAL CYLINDER OF ARBITRARY  
CROSS-SECTION ABOVE A DIELECTRIC HALF-SPACE

By Hassan Sajjad

January, 2021

We certify that we have read this dissertation and that in our opinion it is fully adequate, in scope and in quality, as a dissertation for the degree of Doctor of Philosophy.

---

Prof. Dr. Ercümen ARVAS (Advisor)

---

Prof. Dr. Cengiz ÖZZAİM (Co-Advisor)

---

Prof. Dr. Fatih Erdoğan SEVİLGEN

---

Prof. Dr. Şehabeddin Taha İMECİ

---

Assoc. Prof. Dr. Mehmet Kemal ÖZDEMİR

---

Assoc. Prof. Dr. Hamid TORPİ

Approved by the Graduate School of Engineering and Natural Sciences:

---

Assoc. Prof. Dr. Yasemin Yüksel Durmaz  
Director of the Graduate School of Engineering and Natural Sciences

## Foreword

This dissertation is submitted as a fulfillment of the requirements for the degree of Doctor of Philosophy to Electrical, Electronics Engineering and Cyber Systems at Istanbul Medipol University. The work presented herein was conducted under the supervision of Prof. Dr. Ercüment Arvas and Prof. Dr. Cengiz Özzaim between November 2017 and December 2020.

The thesis begins with an abstract written in both English and Turkish. This is followed by Chapter 1, which summarizes the aim and purpose of this dissertation. Chapter 2 presents a brief history of chiral materials and solutions to some simple scattering problems using the moments method. Chapter 3 explains our simple proposed solution to the problem of electromagnetic scattering from two dimensional chiral cylinders of arbitrary cross-section above a dielectric half-space using the perturbation method and the Method of Moments.

This problem does not have an exact solution so formulating a simple approximate solution was a tedious task. However, my advisors were always available and willing to answer my queries. We have validated the proposed method by comparing our results with some special cases available in the literature.

This thesis is addressed to readers with a good understanding of the electromagnetic theory, surface equivalence principle, and the Method of Moments. It should be of particular interest to researchers working with chiral materials. A detailed parametric analysis of various chiral scatterers with different cross-sections is presented.

It has been a long journey but a fruitful one. I would like to take this opportunity to thank my advisors, the faculty members, staff, my friends, and colleagues for their help and making my stay at Medipol a memorable one.

**Hassan Sajjad**

Istanbul, January, 2021



I hereby declare that all information in this document has been obtained and presented in accordance with academic rules and ethical conduct. I also declare that, as required by these rules and conduct, I have fully cited and referenced all material and results that are not original to this work.

Name, Last Name: HASSAN SAJJAD

Signature :

## Acknowledgement

After thanking Allah (SWT) the most merciful and the most benevolent, I would like to express my sincere gratitude, most profound appreciation, and indebtedness to my advisor, Prof. Dr. Ercümend Arvas, for his compassion, unparalleled expert guidance, constant encouragement, and support throughout my stay at Medipol. He has always been very accommodating and approachable. I consider myself fortunate to have him as my supervisor.

I am also thankful to my co-advisor, Prof. Dr. Cengiz Özzaim, for his critical suggestions and stimulating discussions. Without his suggestions, guidance, and motivation this work would have taken much longer to complete.

I am grateful to Prof. Dr. Fatih Erdoğan Sevilgen, Prof. Dr. Şehabeddin Taha İmeci, Dr. Mehmet Kemal Özdemir, Dr. Hamid Torpi, Dr. Seyit Ahmet Sis, and Dr. Hüseyin Şerif Savcı for serving on my dissertation committee.

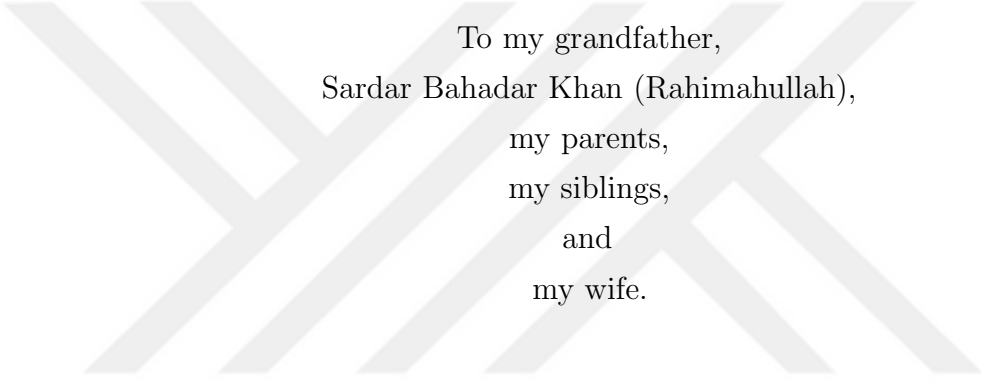
I am thankful to Prof. Dr. Hüseyin Arslan for making me and my wife feel welcomed in the university. I would also like to thank Prof. Dr. Talip Alp for his meaningful discussions on various exciting topics, which provided a much-needed escape from the daily grind. I am also thankful to the staff, faculty members, my colleagues, and friends at Medipol.

I would especially like to thank Dr. Serhend Arvas for his invaluable help in various projects. He has always been open to discussions, be it academic or non-academic.

I am thankful to all my family members, including my in-laws, for their constant prayers and support. A special thanks to my cousin, Mahrukh, and my father for proofreading parts of this dissertation.

I am indebted to my beloved parents and siblings for their immense love, understanding, unconditional support, and consistent prayers. I am thankful to my brother for taking care of the family in my absence.

Finally, I would like to thank my dear wife, Sana Khan, for her continuous support and endless love without which this work would have not been completed.



To my grandfather,  
Sardar Bahadar Khan (Rahimahullah),  
my parents,  
my siblings,  
and  
my wife.

# Contents

<b>1</b>	<b>Introduction</b>	<b>1</b>
1.1	The Main Problem . . . . .	2
1.2	Motivation . . . . .	4
1.3	Contribution of This Dissertation . . . . .	5
1.4	Structure of The Dissertation . . . . .	6
<b>2</b>	<b>Background of Chiral Materials and Solution to Some Simple Problems</b>	<b>8</b>
2.1	Background . . . . .	9
2.2	The Constitutive Relations . . . . .	12
2.3	Plane Waves in Chiral Media . . . . .	13
2.3.1	General Plane Waves . . . . .	13
2.4	The Method of Moments in Brief . . . . .	16
2.5	Solutions to Some Simple Problems . . . . .	17
2.5.1	Scattering From a Thin PEC Strip . . . . .	18
2.5.2	Scattering From Multiple Conducting Cylinders . . . . .	18
2.5.3	Scattering From Dielectric Cylinders in Free-Space . . . . .	20
2.5.4	Scattering From PEC and Dielectric Cylinders in Free-Space . . . . .	21
2.5.5	Scattering From a PEC Cylinder Above a Ground Plane . . . . .	23
2.5.6	Scattering From a Dielectric Cylinder Above a Ground Plane . . . . .	25
2.5.7	Scattering From a Chiral Cylinder in Free-Space . . . . .	28
2.5.8	Scattering From Multiple Chiral Cylinders . . . . .	30
<b>3</b>	<b>EM Scattering From a Chiral Cylinder Above a Dielectric Half-Space</b>	<b>36</b>

3.1	Introduction . . . . .	37
3.2	Integral Equations . . . . .	39
3.3	Application of The Perturbation Method . . . . .	46
3.4	Application of Moments Method . . . . .	52
3.5	Numerical Results: Validation . . . . .	60
3.5.1	Convergence Study for Strip Width . . . . .	62
3.5.2	Limiting Cases: Comparison with Literature . . . . .	68
3.5.3	Effect of Chirality on Scattering width . . . . .	74
3.5.4	Parametric Analysis: A Circular Dielectric Cylinder Above a Dielectric Half-Space . . . . .	76
3.6	Scattering from Circular Chiral Cylinders . . . . .	88
3.6.1	Lossless Scatterers . . . . .	88
3.6.2	Lossy Scatterers . . . . .	94
3.7	Scattering from Rectangular Chiral Cylinder . . . . .	101
3.7.1	Effect of Chirality . . . . .	103
3.7.2	Effect of Incident Angle . . . . .	105
3.8	Scattering from Square Chiral Cylinder . . . . .	108
3.9	Scattering From Elliptical Cylinders . . . . .	112
3.9.1	Different Eccentric Elliptical Cylinders . . . . .	118
3.10	Scattering From Triangular Cylinders . . . . .	120
3.11	Advantages and Disadvantages of Surface Formulation . . . . .	123
<b>4</b>	<b>Conclusion</b>	<b>126</b>
<b>A</b>	<b>Scattering By A Circular Chiral Cylinder: An Exact Solution</b>	<b>136</b>
A.1	TM Incidence . . . . .	137
A.2	TE Incidence . . . . .	140
A.3	Scattered Fields . . . . .	141
<b>B</b>	<b>The Moment Matrix and Computation of Some Moment Matrix Elements</b>	<b>144</b>
<b>C</b>	<b>Plane Waves in Chiral Media</b>	<b>156</b>
C.1	Plane Waves Produced by an Electric Current Sheet in a Chiral Medium . . . . .	157



C.2 Another Way of Writing The Fields . . . . . 158



# List of Figures

1.1	Flow chart of different computational electromagnetics techniques.	2
1.2	The original problem . . . . .	3
2.1	Examples: Chiral objects . . . . .	9
2.2	Current density: Thin PEC strip . . . . .	19
2.3	Scattered field from a thin PEC strip . . . . .	19
2.4	Scattered far-field: Square and triangular PEC cylinders . . . . .	20
2.5	Scattered far-field: Dielectric scatterers . . . . .	21
2.6	Scattered far-field: PEC Square & dielectric triangular scatterers .	22
2.7	Semi-circular PEC cylinder above ground plane . . . . .	24
2.9	Equivalent currents on the surface of a lossless dielectric cylinder with a square cross-section placed above a ground plane . . . . .	27
2.10	Bistatic scattering from a square chiral cylinder . . . . .	29
2.11	Bistatic scattering width from two circular chiral cylinders . . . . .	31
2.12	Bistatic scattering width of a PEC and a chiral cylinder placed next to each other. The cylinders are surrounded by free-space ( $\epsilon_0, \mu_0$ ). Radius of cylinders is $0.1\lambda_0$ , $d = 0.5\lambda_0$ , and the chiral cylinder is characterized by $\epsilon_2 = 2\epsilon_0$ , $\mu_2 = 2\mu_0$ , $\xi_2 = 0.003$ . . . . .	32
2.13	Bistatic scattering width for the setup shown in Fig. 2.12, with the chiral cylinder properties changed to those of free-space. . . . .	33
2.14	Bistatic scattering of circular chiral cylinder above a PEC strip . .	35
3.1	Bistatic scattering width of a circular PEC cylinder in free-space and when it is placed above a DHS. . . . .	40
3.2	Bistatic scattering width of a circular dielectric cylinder in free- space and when it is placed above a (DHS). . . . .	41

3.3	Bistatic scattering width of a circular chiral cylinder in free-space and when it is placed above a (DHS). . . . .	41
3.4	Chiral object of arbitrary cross-section above half-space . . . . .	42
3.5	External equivalence for the the original problem of Fig. 3.4 . . . . .	43
3.6	Internal equivalence for the dielectric half-space of the original problem in Fig. 3.4. . . . .	44
3.7	Internal equivalence for the chiral cylinder of the original problem in Fig. 3.4. . . . .	46
3.8	An auxiliary problem for the original problem of Fig. 3.4. . . . .	47
3.9	External equivalence for the auxiliary problem of Fig. 3.8. . . . .	47
3.10	Internal equivalence for the auxiliary problem of Fig. 3.8. . . . .	48
3.11	A different way of representing the original problem. The surface of the dielectric half-space is divided into near ( $S_{dn}$ ) and far ( $S_{df}$ ) regions. . . . .	50
3.12	External equivalent problem, showing the excitation and the impressed currents. . . . .	51
3.13	Discretization of the $S_c$ and $S_{dn}$ into $N_1$ and $N_2$ segments, respectively. . . . .	53
3.14	Problems under consideration . . . . .	61
3.15	Equivalent perturbed electric surface current on a $w = 10\lambda_0$ dielectric strip. PEC cylinder radius = $0.5\lambda_0$ . . . . .	63
3.16	Equivalent perturbed electric surface current on a $30\lambda_0$ dielectric strip for the setup in Fig. 3.15. . . . .	63
3.17	Equivalent perturbed electric surface current on a $60\lambda_0$ dielectric strip for the setup in Fig. 3.15. . . . .	64
3.18	Equivalent perturbed magnetic surface current on a $10\lambda_0$ dielectric strip for the setup in Fig. 3.15. . . . .	64
3.19	Equivalent perturbed magnetic surface current on a $30\lambda_0$ dielectric strip for the setup in Fig. 3.15. . . . .	65
3.20	Equivalent perturbed magnetic surface current on a $60\lambda_0$ dielectric strip for the setup in Fig. 3.15. . . . .	65
3.21	Equivalent surface electric current on the PEC cylinder for various strip widths for the setup shown in Fig. 3.15. TM excitation, $\phi^i = 90^\circ$ , $r = 0.5\lambda_0$ , $d = 0.5\lambda_0$ , $\epsilon_b = \epsilon_c = 4\epsilon_0$ , $\mu_b = \mu_c = \mu_0$ . . . . .	66

3.22	Bistatic scattering width for various dielectric strip widths for the setup shown in Fig. 3.15. TM excitation, $\phi^i = 90^\circ$ , $r = 0.5\lambda_0$ , $d = 0.5\lambda_0$ , $\epsilon_b = \epsilon_c = 4\epsilon_0$ , $\mu_b = \mu_c = \mu_0$ . . . . .	67
3.23	Verification I: Far-field of circular chiral cylinder above a dielectric half-space . . . . .	69
3.24	Verification II: Comparison of the bistatic scattering width (BSW) for different dielectric constants of the cylinder. . . . .	70
3.25	Circular PEC cylinder above half-space: $\phi^i = 90^\circ$ . . . . .	72
3.26	Circular PEC cylinder above half-space: $\phi^i = 120^\circ$ . . . . .	73
3.27	BSW variation Vs chirality admittance . . . . .	75
3.28	Effect of cylinder radius on perturbed currents: $J_Z$ . . . . .	77
3.29	Effect of cylinder radius on perturbed currents: $M_L$ . . . . .	78
3.30	Effect of cylinder radius on perturbed currents: $J_L$ . . . . .	79
3.31	Effect of cylinder radius on perturbed currents: $M_Z$ . . . . .	80
3.32	Effect of cylinder height on perturbed currents: $J_Z$ . . . . .	81
3.33	Effect of cylinder height on perturbed currents: $M_L$ . . . . .	82
3.34	Effect of chiral cylinder's height on perturbed currents . . . . .	83
3.35	Effect of incidence angle on perturbed currents: $J_Z, M_L$ . . . . .	85
3.36	Effect of incidence angle on perturbed currents: $J_L, M_Z$ . . . . .	86
3.37	Circular chiral cylinder: Perturbed currents & far-fields . . . . .	89
3.38	BSRCS comparison: Chiral, dielectric, & PEC circular cylinders . . . . .	91
3.39	Co-pol BSRCS: Circular chiral cylinder . . . . .	92
3.40	X-pol BSRCS: Circular chiral cylinder . . . . .	93
3.41	Co-pol BSRCS: Lossy circular chiral cylinder . . . . .	95
3.42	X-pol BSRCS: Lossy circular chiral cylinder . . . . .	96
3.43	Co-pol far-field amplitude: Lossy circular chiral cylinder . . . . .	97
3.44	Co-pol BSRCS: Effect of $\xi$ on lossy circular chiral scatterer . . . . .	98
3.45	X-pol BSRCS: Effect of $\xi$ on lossy circular chiral scatterer . . . . .	99
3.46	Co-pol far-field amplitude: different $\xi$ . . . . .	99
3.47	X-pol far-field amplitude: different $\xi$ . . . . .	100
3.48	Perturbed currents due to a rectangular chiral cylinder placed above a dielectric half-space . . . . .	102

3.49	Scattered far-fields due to a rectangular chiral cylinder placed above a dielectric half-space. The setup is shown in inset of Fig. 3.48. . .	102
3.50	TM Case, co-pol BSRCS: Rectangular cylinder, different $\xi$ . . . .	103
3.51	TM Case, x-pol BSRCS: Rectangular cylinder, different $\xi$ . . . .	104
3.52	TM Case, Perturbed currents: Rectangular cylinder, different $\xi$ .	105
3.53	TM Case, co-pol far-field: Rectangular cylinder, different $\phi^i$ . . .	106
3.54	TM Case, x-pol BSRCS: Rectangular cylinder, different $\xi$ . . . .	107
3.55	Perturbed currents due to a square chiral cylinder placed above a dielectric half-space . . . . .	108
3.56	Scattered far-fields due to a square chiral cylinder placed above a dielectric half-space. The setup is shown in inset of Fig. 3.55. . . .	109
3.57	Effect of $\xi$ on the co-polar component of the scattering width of a square chiral cylinder placed above a dielectric half-space . . . . .	110
3.58	Effect of $\xi$ on the cross-polar component of the scattering width of a square chiral cylinder placed above a dielectric half-space. Setup shown in Fig. 3.55 . . . . .	110
3.59	BSRCS Comparison: Square chiral, dielectric, & PEC cylinders .	111
3.60	BSRCS: Elliptical chiral cylinder above half-space . . . . .	113
3.61	Far-field amplitude, elliptical chiral cylinder above half-space . . .	114
3.62	BSRCS elliptical cylinder: Effect of $\xi$ . . . . .	116
3.63	Scattered far-field amplitude of elliptical cylinder: Effect of $\xi$ . . .	117
3.64	Circular and elliptical cylinders of different sizes . . . . .	119
3.65	Perturbed currents and far-fields: chiral wedge above half-space .	121
3.66	BSRCS: chiral wedge above half-space . . . . .	122
3.67	Condition number variation of the moment matrix with $k_0 X_L$ for a rectangular chiral cylinder placed above a dielectric half-space. . .	124
A.1	A circular chiral cylinder illuminated by TM/TE plane wave. . . .	137
A.2	TM case: Bistatic scattering width of a circular chiral cylinder excited from $\phi^i = 180^\circ$ . . . . .	143
A.3	TE case: Bistatic scattering width of a circular chiral cylinder excited from $\phi^i = 180^\circ$ . . . . .	143

B.1 Discretization of the cylinder ( $S_b$ ) and the  $S_{cn}$  region of the dielectric interface. . . . . 145

B.2 The lateral current on the  $m^{th}$  segment of surface  $S_c$  and the charge associated with it. . . . . 149

C.1 An infinite current sheet in an unbounded chiral medium. . . . . 157

C.2 Equivalent problem for Fig. C.1. (a) Setup for the *plus* medium and (b) Setup for the *minus* medium. . . . . 161



# List of Symbols

$\nabla \cdot$	Divergence Operator
$\nabla \times$	Curl Operator
$\rho'$	Position vector to source segment
$\rho_m$	Position vector to field segment
$\eta$	Wave impedance in regular dielectric medium
$\eta_c$	Wave impedance in chiral medium
$\hat{x}, \hat{y}, \hat{z}$	Unit vectors of the cartesian coordinate system
$\langle \cdot \rangle$	Inner product
$\mathbf{B}$	Magnetic flux density [Wb/m <sup>2</sup> ]
$\mathbf{D}$	Electric flux density [C/m <sup>2</sup> ]
$\mathbf{E}$	Electric field intensity [V/m]
$\mathbf{E}^{inc}$	Incident electric field
$\mathbf{H}$	Magnetic field intensity [A/m]
$\mathbf{H}^{inc}$	Incident magnetic field
$\mathbf{J}$	Surface electric current [A/m]
$\mathbf{J}_{PO}$	Electric physical optic current
$\mathbf{M}$	Surface magnetic current [V/m]

$\mathbf{M}_{PO}$	Magnetic physical optic current
$\mathbf{n}, \hat{n}$	Unit normal vector pointing outwards from the surface
$E_z^i$	Z-component of the incident electric field (TM Incidence)
$H_z^i$	Z-component of the incident magnetic field (TE Incidence)
$\omega$	Angular frequency
$\sigma_z$	Co-polarized bistatic scattering width
$\sigma_\phi$	Cross-polarized bistatic scattering width
$\sigma_{BSW}$	Bistatic scattering width
$H_0^{(2)}(\cdot)$	Hankel function of the second kind and order zero
$h_1, k^+$	Wavenumber for right hand circular polarized wave
$h_2, k^-$	Wavenumber for left hand circular polarized wave
$\epsilon_a, \epsilon_0$	Permittivity of free-space ( $8.85 \times 10^{-12}$ F/m)
$\epsilon_c$	Permittivity of chiral media
$\epsilon_d$	Permittivity of dielectric half-space
$\lambda_0$	Free-space wavelength
$\mu_a, \mu_0$	Permeability of free-space ( $4\pi \times 10^{-7}$ H/m)
$\mu_c$	Permeability of chiral media
$\mu_d$	Permeability of dielectric half-space
$\phi^i$	Incident angle in degrees
$\phi$	Observation angle for the scattered fields in degrees
$\xi$	Chirality admittance of the chiral medium



# Abbreviations

<b>2-D</b>	Two Dimensional
<b>BSRCS</b>	Bistatic Radar Cross-Section
<b>BSW</b>	Bistatic Scattering Width
<b>CFIE</b>	Combined Field Integral Equations
<b>Co-Pol</b>	Co-Polarized
<b>DBF</b>	Drude-Born-Fedorov
<b>EFIE</b>	Electric Field Integral Equations
<b>FDTD</b>	Finite Difference Time Domain
<b>FEM</b>	Finite Element Method
<b>FVTD</b>	Finite Value Time Domain
<b>GO</b>	Geometric Optics
<b>HFIE</b>	Magnetic Field Integral Equations
<b>LHCP</b>	Left Hand Circularly Polarized
<b>MoM</b>	Method of Moments
<b>NDIV</b>	Number of Division
<b>PEC</b>	Perfect Electric Conductor
<b>PO</b>	Physical Optics
<b>PTD</b>	Physical Theory of Diffraction
<b>RAMs</b>	Radar Absorbing Materials
<b>RCS</b>	Radar Cross-Section
<b>RHCP</b>	Right Hand Circularly Polarized
<b>TE</b>	Transverse Electric Field
<b>TM</b>	Transverse Magnetic Field
<b>UTD</b>	Uniform Theory of Diffraction
<b>X-Pol</b>	Cross-Polarized

## ÖZET

# DİELEKTRİK YARI-UZAY ÜZERİNDE KİRAL BİR SİLİNDİRDEN ELEKTROMANYETİK SAÇILMA

Hassan Sajjad

Elektrik-Elektronik Mühendisliği ve Siber Sistemler, Doktora

Tez Danışmanı: Prof. Dr. Ercümen ARVAS

Tez Eş Danışmanı: Prof. Dr. Cengiz ÖZZAİM

Ocak, 2021

Dielektrik yarı uzay üzerinde bulunan rastgele kesitli iki boyutlu (2-D) homojen bir kiral silindirden elektromanyetik saçılma problemi için basit bir sayısal çözüm sunulmuştur. Yüzey eşdeğerlik ilkesi ve Moment Yöntemi (MoM) kullanılarak, silindir ve dielektrik yarı uzay bilinmeyen eşdeğer elektrik ve manyetik yüzey akımlarıyla değiştirilir. Yüzeylerdeki elektrik alanın teğet bileşenlerinin sürekliliği sağlanarak, bir dizi elektrik alan integral denklemi (EFIE) elde edilir. İki dielektrik yarı uzayın kesiştiği düzlem sonsuz olduğu için konvansiyonel MoM direkt tatbik edilemez. Bu nedenle, pertürbasyon yöntemi kullanılarak sonsuz arayüzey sonlu genişlikte bir düzlem ile değiştirilir. Bu yaklaşık problem geleneksel MoM ile çözülür. Temel fonksiyonlar olarak darbe fonksiyonu, test için Galerkin Metodu kullanılır. Uyarma vektörü, gelen alana ek olarak cismin olmadığı durumdaki dielektrik yarı uzaydan yansıyan alanı da içermektedir. Her iki TM ve TE düzlem dalga uyarımları kullanılmaktadır.

Hesaplanan sayısal sonuçlar, kiral silindirdeki eşdeğer akımları, arayüzdeki pertürbasyon akımları ve çeşitli geometriler için saçılan alanları içerir. Cismin kiralite parametresinin incelenmesi sonucunda, kiralitenin, saçıcının radar kesitini (RCS) kontrol etmede etkili bir şekilde kullanılabileceği ortaya çıkmıştır. Saçılan alanlar basit bir teori ile hesaplanamayacağı için böyle bir çalışmaya gerek duyulmuştur. Geliştirilen algoritmanın geçerliliğini kontrol etmek için bazı basit problemlerin sonuçları da sunulmaktadır. Önerilen metodun avantajları ve dezavantajları tartışılmıştır.

*Anahtar sözcükler:* Bistatik saçılma kesiti, kiral malzemeler, dielektrik yarı uzay, Momentler Yöntemi, pertürbasyon yöntemi, yüzey eşdeğerlik ilkesi.

## ABSTRACT

# SCATTERING FROM A CHIRAL CYLINDER OF ARBITRARY CROSS-SECTION ABOVE A DIELECTRIC HALF-SPACE

Hassan Sajjad

Ph.D. in Electrical, Electronics Engineering and Cyber Systems

Advisor: Prof. Dr. Ercümen ARVAS

Co-Advisor: Prof. Dr. Cengiz ÖZZAİM

January, 2021

A simple numerical solution for electromagnetic scattering from a two dimensional (2-D) homogeneous chiral cylinder of arbitrary cross-section placed above a dielectric half-space is presented. The surface equivalence principle and the Method of Moments (MoM) are used to replace the cylinder and the dielectric half-space by unknown equivalent electric and magnetic surface currents. By satisfying the continuity of the electric field's tangential components at the surfaces, a set of electric field integral equations (EFIE) is obtained. Since the dielectric surface is of infinite extent, the conventional MoM cannot be applied directly. Therefore, a perturbation method is used where a strip of finite width approximates the surface of the half-space. Then, this approximate problem is solved numerically with the conventional MoM. Pulses are used as basis functions and Galerkin's method is used for testing. The excitation vector now contains the reflected field from the dielectric half-space in addition to the incident field. Both TM and TE excitations are treated.

Computed numerical results include equivalent currents on the chiral cylinder, perturbed currents on the interface, and the scattered fields for various geometries. Studying various parameters for the chiral material revealed that the extra degree of freedom, chirality admittance, can be used effectively in controlling the radar cross-section (RCS) of the scatterer. However, the scattered fields cannot be predicted by simple theory, hence the need for such a study. Results for some simple problems are presented as well to check the validity of the developed algorithm. Advantages and disadvantages of the proposed method are discussed towards the end.

*Keywords:* Bistatic scattering width, chiral materials, dielectric half-space, Method of Moments, perturbation method, surface equivalence principle.

# Chapter 1

## Introduction

In the recent years, numerical methods have been used extensively to solve electromagnetic (EM) problems. These problems are mostly related to antenna computations and scattering. Many commercial softwares are available to solve these problems but they might not be the best choice for researchers due to their high costs and complex nature. Another factor is the simulation time required to solve complex geometry problems. These simulations can last for days and weeks even on a high-end workstation. Therefore, developing a source code to find approximate solution for a complex problem using FORTRAN or MATLAB is a more viable solution in terms of cost and time.

There are countless problems in electromagnetics but very few have exact solutions. These problems must be solved approximately by numerical techniques. This led to the development of various numerical methods over the years. Figure 1.1 shows a flow chart of the various techniques that are used by researchers. All these techniques are very well developed and the details can be easily found in the literature. These methods are divided into two groups, low frequency and high frequency. They are further divided into time and frequency domain methods. In this work, the Method of Moments (MoM) is used.

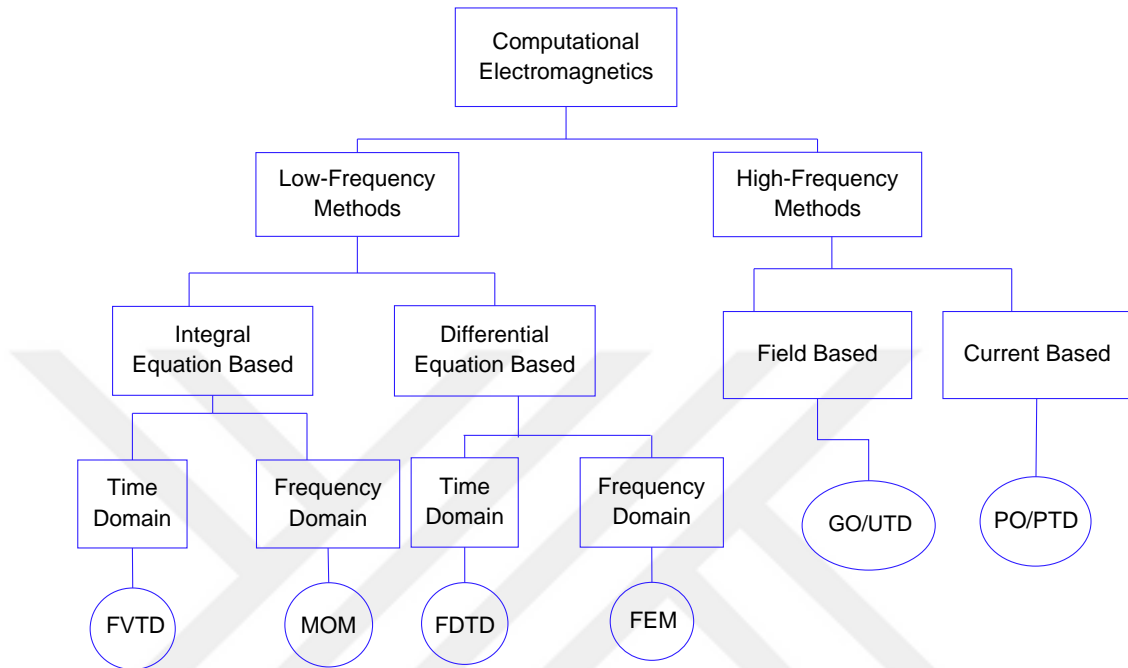


Figure 1.1: Flow chart of different computational electromagnetics techniques.

## 1.1 The Main Problem

In this work, the aim is to formulate and solve the problem of electromagnetic scattering from a two dimensional (2-D) homogeneous chiral cylinder of arbitrary cross-section above a dielectric half-space. The original problem under consideration is shown in Fig. 1.2. The arbitrary shaped homogeneous chiral cylinder is placed in free space ( $\epsilon_a = \epsilon_0$ ,  $\mu_a = \mu_0$ ). The surface of the chiral body is denoted by  $S_c$ . The relative permittivity of the cylinder is given by  $\epsilon_c$ , the permeability is denoted by  $\mu_c$ , and the chirality admittance is represented by  $\xi$ . The dielectric half-space is characterized by  $(\epsilon_d, \mu_d)$ . Its surface is denoted by  $S_d$ . The setup is illuminated by an incident TM or TE plane wave with an incident angle  $\phi^i$ .  $\mathbf{E}^{inc}$  and  $\mathbf{H}^{inc}$  are the incident electric and magnetic fields, respectively.

The problem under consideration is solved using MoM and the perturbation method. In this method, the infinite surface of the dielectric interface is approximated by a strip of finite width. This use of the perturbation method makes the

implementation of conventional MoM feasible. Computed results include equivalent surface currents on the chiral cylinder and the interface and the scattered fields in both regions. It is observed that, depending on the cylinder's height above the interface, these results converge as the finite width of the strip is increased. The computed results are validated by assuming some special cases and comparing them with the results in the literature.

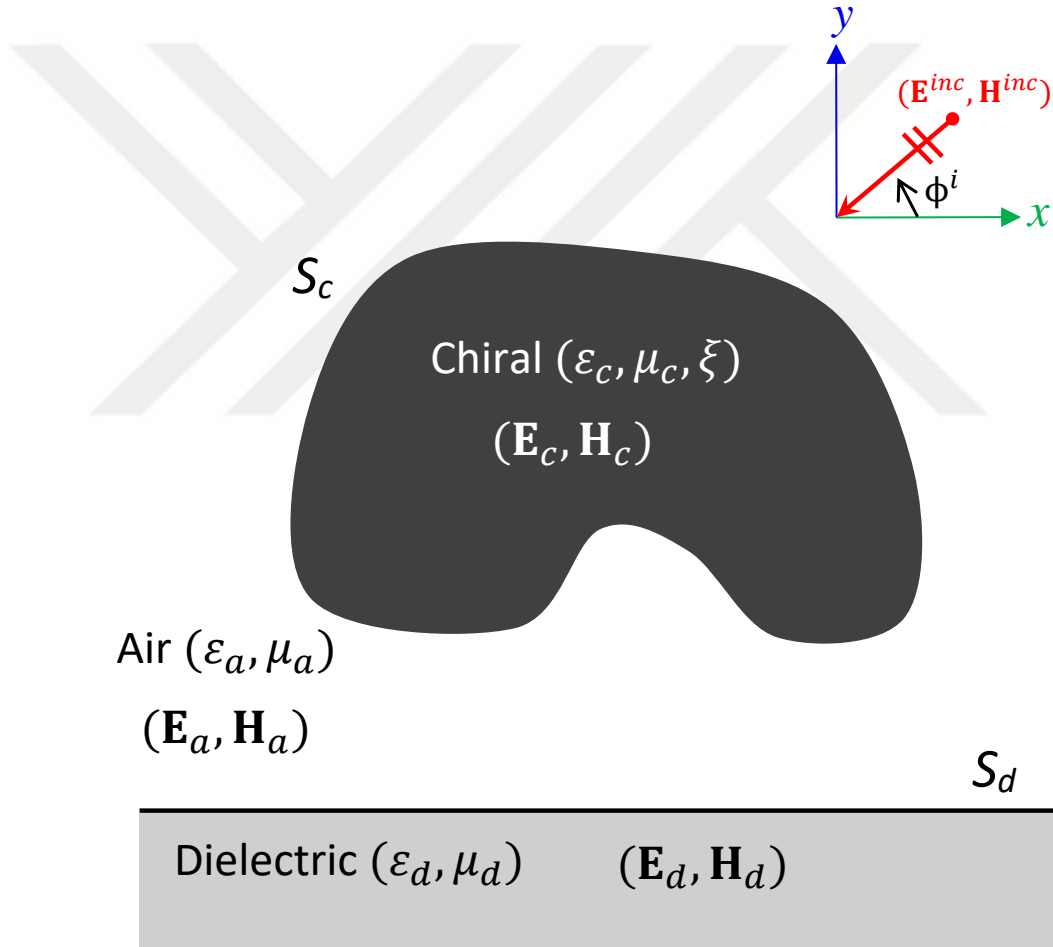


Figure 1.2: A chiral Cylinder of arbitrary cross-section placed above a dielectric half-space illuminated by a TM or TE plane wave.

## 1.2 Motivation

Computation of radar cross-section (RCS), its prediction and reduction, has been studied and discussed by many researchers over the years. This is achieved by various techniques, for instance, body shaping and using electromagnetic (EM) absorbing materials as coating. One of the main application of such a study is in defense industry, to enhance the stealth technology for fighter jets.

For applications where the transmitter (Tx) and the receiver (Rx) are at the same location, RCS reduction refers to reduction of monostatic radar cross-section (MSRCS). Whereas, if the Tx and Rx are at different locations, it's called bistatic radar cross-section (BSRCS). For two-dimensional (2-D) problems, these terms are called monostatic/bistatic scattering width or echo width.

Generally, for reducing RCS, body shaping and coating of radar absorbing materials (RAMs) are used. In the former case, the body of the scatterer is designed so that the EM waves are steered in a direction other than the incident wave's direction. This can be an effective technique for MSRCS reduction, where the aim is to reduce the back-scattered fields [1]. RAMs on the other hand are used to reduce both, MSRCS and BSRCS. Here, the EM waves are absorbed by the material as heat due to its electric and magnetic losses. Previous study [2, 3], shows that chiral materials can be used to effectively control the scattered fields. This has led to an in depth investigation of the material, since its inception in 1971 [4].

This work is an extension of the problem solved in [5] which deals with the problem of scattering from a 2-D chiral cylinder of arbitrary cross-section in free-space. It is of vital importance to analyze the scattering behaviour of the chiral scatterer in the vicinity of other objects, specifically a half-space. This study can be applied in remote sensing applications and geophysical explorations. Therefore, in this work, scattering properties of a 2-D chiral cylinder of arbitrary cross-section are studied in the presence of a dielectric half-space. It has been well established by earlier researchers that the scattering properties of chiral materials

cannot be predicted by simple theory, even in free-space. Introducing a half-space into the problem makes it more complicated. The scattering behavior of a chiral cylinder above a dielectric half-space can be much different than the scattering behavior of the same cylinder in free-space. Finding a solution to this problem is the motivation behind this work.

The aim is to come up with a simple numerical solution and to develop a computer algorithm that can help in finding solutions to these problems accurately and efficiently. The proposed method should not be computationally intensive and it must be capable and robust enough to identify, in case of any spurious results, the incorrect solutions. This can be done by analyzing the condition number of the matrix. Based on these findings, chiral material can be better characterized and used more effectively to control its scattering. Such a study can find wide use in designing EM absorbing materials for cloaking and reducing RCS of arbitrary shaped objects.

### **1.3 Contribution of This Dissertation**

A simple solution for the problem of EM scattering from a homogeneous 2-D chiral cylinder of arbitrary cross-section placed above a dielectric half-space is presented here. Surface equivalence principle [6] is used to replace the chiral cylinder and the half-space interface with unknown equivalent electric and magnetic surface currents. By satisfying the boundary conditions for the tangential electric field component, a set of electric field integral equations (EFIEs) are obtained. These equations are solved numerically, using the Method of Moments [7]. However, due to the distribution of the unknowns on the infinite interface, moments solution cannot be used to solve these equations in the current form. Therefore, perturbation method is used to approximate the original problem. An auxiliary problem is used with a known solution i.e., scattering from a dielectric interface with the body removed. Combination of the two problems lead to a set of new coupled vector field integral equations. The unknowns representing the half-space interface become negligible in the far away region from the body. In other words, the infinite region problem



is reduced to a finite region which makes the discretization feasible for applying MoM.

## 1.4 Structure of The Dissertation

A gradual approach has been applied instead of directly solving the main problem. The dissertation structure is discussed below.

Chapter 2 presents a brief literature review on chiral materials. Then, the constitutive relations that govern the chiral media are presented. This is followed by a basic introduction of plane waves in chiral materials. Finally, towards the end of the chapter some simple problems are discussed. These problems are solved by using the surface equivalence principle and the conventional method of moments. Computed results include the magnitude of the scattered fields and bistatic scattering width for various problems. The problems discussed are: scattering from 2-D PEC and dielectrics cylinders of arbitrary cross-sections, scattering from multiple PEC and dielectric cylinders, scattering from PEC and/or dielectric cylinders above a PEC plane, and scattering from a chiral cylinder of arbitrary cross-section in free-space. Finally, this chapter also discusses the electromagnetic scattering from multiple chiral cylinders of arbitrary cross-section surrounded by free-space. Numerical results included are the co-polarized and cross-polarized bistatic scattering width for (i) Multiple chiral cylinders in free-space and (ii) PEC cylinder placed in the vicinity of a chiral cylinder.

Chapter 3 presents the main problem of scattering from a 2-D chiral cylinder of arbitrary cross-section placed above a dielectric half-space. The perturbation method is used to approximate the dielectric half-space by a dielectric strip of finite width. The integral equations formulation is presented along with the application of the moments method. Numerical results are validated by comparing with published results and some limiting cases. Computed results include the equivalent surface currents on the cylinder, the perturbed currents on the dielectric interface, and the scattered fields. Various parametric studies are also presented

to understand the effect of chirality and the presence of the half-space on the scattered fields in the upper and lower half-spaces.

Finally, Chapter 4 contains the summary of this work.



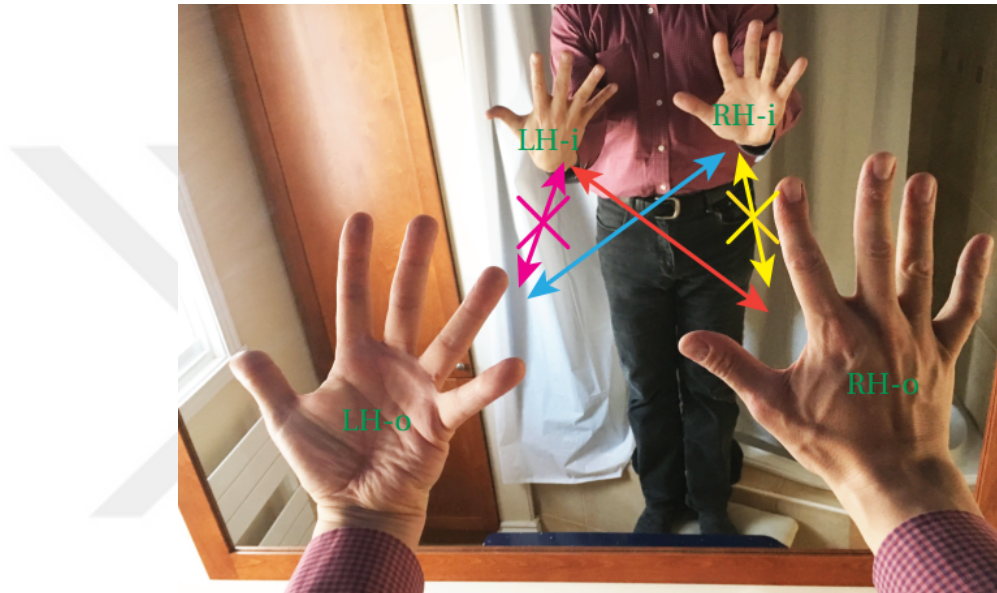
## Chapter 2

# Background of Chiral Materials and Solution to Some Simple Problems

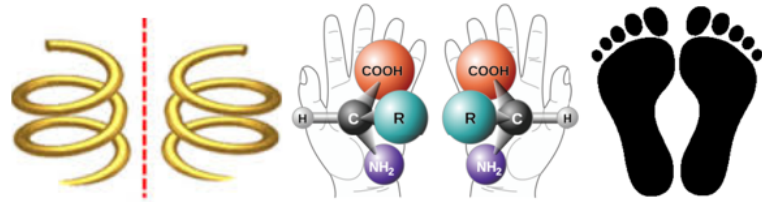
In simple and plain words, chirality refers to the property of objects according to which they cannot superimpose their mirror image without translation or rotation. Objects which are not chiral are called achiral. A very comprehensive example of chirality is given in [8], shown in Fig. 2.1a, for understanding the phenomenon easily. The original left- and right-hands are represented by LH-o and RH-o, respectively, and their images, in the reflection are denoted by LH-i and RH-i. It is clear from the image that RH-o corresponds to LH-i and LH-o corresponds to RH-i. To understand the non-superimposable nature of the chiral objects, consider the right hand and its image in the mirror. RH-i and RH-o are finger-to-finger aligned, but RH-o shows its back and the RH-i shows its palm. If RH-i is flipped, it will align back-to-back but the finger-to-finger alignment will be lost.

Chiral objects can be man-made and also found naturally, for example, DNA in biochemistry, gloves and golf clubs in sports, helical antennas and screws in engineering. Some common examples of chiral objects are shown Fig. 2.1b. A material made of chiral molecules or other chiral particles is called a chiral medium.

These materials have a special property due to which the polarization plane of the EM waves, traveling through it, is rotated. This phenomenon is called *optical activity*. This behaviour was observed in 1811 by Arago [9] and later on studied by other researchers [10–12].



(a)



\*google images

\*Wikimedia commons

\*google images

(b)

Figure 2.1: Examples of chiral objects. (a) Human hands and their reflection in a mirror. Image taken from [8], (*Photograph: Raphaël Caloz*). (b) Other examples of chiral objects.

## 2.1 Background

Besides the study in the optical domain, wave interaction with chiral objects was studied for the first time by Lindman in 1920-22 and Pickering in 1945. However, the modern history of electromagnetic chirality dates back to 1979, when

Jaggard *et al.* presented a macroscopic model of the interaction of electromagnetic waves with chiral structures in [13]. The next study on chirality appeared in 1982 by Engheta and Mickelson [14], where they considered transition radiation from a chiral plate. In 1986, Silverman studied scattering from chiral/achiral interfaces [15]. From 1986 to 1990 Lakhtakia *et al.*, worked on scattering from chiral and achiral interfaces in [16–18]. These authors also studied scattering by mirror-conjugated chiral interface and scattering by a periodic chiral/achiral interface in [19,20]. Similarly, scattering from chiral slabs and infinitely backed chiral materials have also been presented in [21–23]. These studies helped in demonstrating scattering from flat surfaces but the practical problems were more complex which demanded further investigations.

Objects of cylindrical and spherical shapes are encountered frequently in EM problems, which led to Bohren’s research on problems involving scattering from homogeneous spheres [24], spherical shells [25], and cylinders [26]. He solved these problems using eigenfunction solutions. Latktakia *et al.*, investigated the eigenmodes of a chiral coated conducting sphere in order to explore the practical aspects of chiral media [27]. They studied a perfectly conducting sphere filled with a homogeneous and isotropic chiral medium which forms the base for a microwave resonator, an important circuit element. Klusken and Newman used the volume equivalence principle to find scattering from a cylinder of arbitrary cross-section [28]. In another study, Engheta and Jaggard [29] linked the models of chiral media to their constitutive relations. They investigated the waves in unbounded chiral medium and studied different interface problems. For example, chiral-achiral interface where they studied the reflection and refraction. Along with this, they worked on the radiation problems from different sources in chiral media. These and other studies such as, antennas radiating in infinite chiral media [30], point dipole radiating inside a chiral sphere [31], and scattering by perfectly conducting bodies in an infinite medium [32] have been studied extensively. Scattering from 2-D homogeneous chiral cylinder of arbitrary cross-section is studied by Alkanhal and Arvas in [5]. The above mentioned studies gave an insight into the scattering behavior of frequently encountered geometries. The reason behind studying each case separately is that the scattering behavior

of chiral objects cannot be predicted by the application of simple theory.

After a thorough research on the chiral materials, researchers investigated the effect of chiral coatings applied to dielectric and perfectly conducting bodies to analyze the scattering behavior. A numerical solution has been provided for the EM scattering problem from a chiral coated metal cylinder (two-dimensional) of arbitrary cross-section in [33]. The authors observed that the results obtained from the chiral coated cylinder were different from the results of a dielectric coated cylinder. These results could not be predicted without the application of a numerical method. The results were compared with exact eigenfunction solution given in [28]. Allam mentioned in a military technical college report [34], that chiral materials can be used for absorbing EM waves. Chiral coatings have also been applied to dielectric cylinders with various thicknesses and material properties in [35], to observe depolarization properties of chiral materials. The coatings helped in reducing the radar cross-section. A study on the coupled surface integral equation solution of EM scattering by chiral coated conducting bodies with arbitrary shape is presented in [36]. The authors concluded that the bistatics cross-section is reduced due to the chiral coating. In a similar study, RCS for a chiral coated dielectric sphere has been studied in [37], with different chiral parameters and various thicknesses of chiral coating.

The effects of chiral materials have also been analyzed in real life complex problems where a strip may be buried in a chiral medium, or antenna placed inside a chiral radome, or EM waves interacting with twisted metal cylinders. For instance, the analysis of axisymmetric chiral radome [38] showed that adding chirality to the bodies, changed the direction of the scattered field such that it was different from the incident fields. Similarly, scattering of electromagnetic plane wave by a perfect electric conducting (PEC) strip in homogeneous isotropic chiral medium has been studied in [39]. Another interesting and recent study in 2016 on scattering due to twisted PEC cylinder coated with chiral/chiro-ferrite mediums in [40], showed larger scattering. These studies show that the chirality parameter has to be optimized in order to achieve the desired properties.

From all the study, undertaken on the chiral materials in the 20<sup>th</sup> and early

21<sup>st</sup> century, it has been established that the polarization rotation is a result of the electromagnetic coupling of chiral particles. The constitutive relations, which play an important role in the field analysis, for the chiral materials have been studied in great details and are presented in the next section.

From the literature survey it was observed that the chiral materials help in reducing RCS and acts as absorbing materials for EM waves unlike chiro-ferrites or simple dielectric coatings over PEC. Despite the immense amount of research on chiral materials the problem of a 2-D chiral body of arbitrary cross-section in the presence of a dielectric half-space has not been studied. The main aim of this work is to analyze the scattering behavior of chiral materials when they are placed above a dielectric half-space.

## 2.2 The Constitutive Relations

Over the years, different constitutive relations for chiral materials have been used by researchers. Three common sets are used in the literature. Initially proposed by Fedorov in 1959 [41], then inspired by Drude [42], Born modified the relations to [43],

$$\mathbf{D} = \epsilon_{\text{DBF}}(\mathbf{E} + \xi_{\text{DBF}} \nabla \times \mathbf{E}) \quad (2.1)$$

$$\mathbf{B} = \mu_{\text{DBF}}(\mathbf{H} + \xi_{\text{DBF}} \nabla \times \mathbf{H}) \quad (2.2)$$

In 1962, Post proposed another set of parameters [44],

$$\mathbf{D} = \epsilon \mathbf{E} - j\xi \mathbf{B} \quad (2.3)$$

$$\mathbf{H} = \frac{1}{\mu} \mathbf{B} - j\xi \mathbf{E} \quad (2.4)$$

and Lindell [45] gave the third set of relations,

$$\mathbf{D} = \epsilon_L \mathbf{E} - j\xi_L \mathbf{H} \quad (2.5)$$

$$\mathbf{B} = \mu_L \mathbf{H} + j\xi_L \mathbf{E} \quad (2.6)$$

Here,  $\mathbf{D}$  is the electric flux density or electric displacement ( $\text{C}/\text{m}^2$ ),  $\mathbf{E}$  is the electric field intensity ( $\text{V}/\text{m}$ ),  $\mathbf{H}$  is the magnetic field intensity ( $\text{A}/\text{m}$ ), and  $\mathbf{B}$  is the magnetic flux density ( $\text{Wb}/\text{m}^2$ ). The material is characterized by  $\epsilon$ ,  $\mu$ ,  $\xi$  which, respectively, represent the permittivity, permeability, and the chirality parameter for the three different sets of relations. The subscript DBF denotes the Drude-Born-Fedorov parameters, and the subscript L represents Lindell's parameters. In this dissertation, the constitutive relations given in (2.3) and (2.4) are used. The above given relations are equivalent and can be transformed from one form to another. The details can be found in [45].

## 2.3 Plane Waves in Chiral Media

Before proceeding further it is important to understand the propagation of plane waves in a chiral medium. Here, we briefly introduce this phenomenon.

### 2.3.1 General Plane Waves

The source-free Maxwell's equations can be written as:

$$\nabla \times \mathbf{E} = -j\omega\mathbf{B} \quad (2.7)$$

$$\nabla \times \mathbf{H} = j\omega\mathbf{D} \quad (2.8)$$

$e^{j\omega t}$  time dependence is assumed and suppressed. Replacing the constitutive relations (2.3) and (2.4) in (2.7) and (2.8), we get the following set of Maxwell's equations for chiral media.

$$\nabla \times \mathbf{E} = \omega(\xi\mu\mathbf{E} - j\mu\mathbf{H}) \quad (2.9)$$

$$\nabla \times \mathbf{H} = \omega[j(\epsilon + \mu\xi^2)\mathbf{E} + \xi\mu\mathbf{H}] \quad (2.10)$$



Here,  $\xi$  is known as the chiral admittance. It can be shown that the following  $\mathbf{E}_R^+$  and  $\mathbf{H}_R^+$  is a solution to (2.9) and (2.10).

$$\mathbf{E}_R^+ = A(\hat{x} - j\hat{y})e^{-jh_1z} \quad (2.11)$$

$$\mathbf{H}_R^+ = \frac{A}{\eta_c}(\hat{y} + j\hat{x})e^{-jh_1z} \quad (2.12)$$

Here,  $A$  is an arbitrary constant. The wavenumber ( $h_1$ ) and the wave impedance ( $\eta_c$ ) in the chiral medium are given by:

$$h_1 = \omega\mu\xi + \sqrt{k^2 + (\omega\mu\xi)^2} \quad (2.13)$$

$$\eta_c = \frac{\eta}{\sqrt{1 + (\eta\xi)^2}} \quad (2.14)$$

where,  $k = \omega\sqrt{\mu\epsilon}$  and  $\eta = \sqrt{\mu/\epsilon}$  are the wave number and the wave impedance in a regular dielectric medium.  $\mathbf{E}_R^+$  and  $\mathbf{H}_R^+$  in (2.11) and (2.12) represent a right-hand circularly polarized (RHCP) uniform ( $\frac{\partial}{\partial x} = 0 = \frac{\partial}{\partial y}$ ) plane wave travelling in  $+z$  direction with the wave number  $h_1$ .

Similarly, one can show that  $\mathbf{E}_L^+$  and  $\mathbf{H}_L^+$  is also a solution to (2.9) and (2.10).

$$\mathbf{E}_L^+ = C(\hat{x} + j\hat{y})e^{-jh_2z} \quad (2.15)$$

$$\mathbf{H}_L^+ = \frac{C}{\eta_c}(\hat{y} - j\hat{x})e^{-jh_2z} \quad (2.16)$$

where,  $C$  is an arbitrary constant, and the wavenumber ( $h_2$ ) is given by:

$$h_2 = -\omega\mu\xi + \sqrt{k^2 + (\omega\mu\xi)^2} \quad (2.17)$$

$\mathbf{E}_L^+$  and  $\mathbf{H}_L^+$  in (2.15) and (2.16) represent a left-hand circularly polarized (LHCP) uniform ( $\frac{\partial}{\partial x} = 0 = \frac{\partial}{\partial y}$ ) plane wave travelling in  $+z$  direction with the wavenumber  $h_2$ .

It is important to mention here that that, if  $h_1$  in (2.11) and (2.12) is replaced with  $h_2$ , the resulting fields will not satisfy (2.9) and (2.10). Similarly, if  $h_2$  is replaced with  $h_1$ , the resulting fields will not satisfy (2.9) and (2.10). This means that,  $h_1$  is the wavenumber associated with the RHCP wave and  $h_2$  is the

wavenumber associated with the LHCP wave. Note also that a uniform plane wave of the following form with arbitrary  $E_x$  and  $E_y$  and  $\beta = h_1$  or  $\beta = h_2$  will not satisfy (2.9) and (2.10).

$$\mathbf{E}(z) = [\hat{x}E_x + \hat{y}E_y]e^{-j\beta z} \quad (2.18)$$

$$\mathbf{H}(z) = [\hat{x}H_x + \hat{y}H_y]e^{-j\beta z} \quad (2.19)$$

In simple words, this means that a uniform plane wave, in a chiral medium, cannot be linearly or elliptically polarized. It must be circularly polarized.

Since (2.9) and (2.10) are homogeneous equations then the sum of  $(\mathbf{E}_R^+, \mathbf{H}_R^+)$  and  $(\mathbf{E}_L^+, \mathbf{H}_L^+)$  will be the general form of a uniform plane wave traveling in a chiral medium  $(\epsilon, \mu, \xi)$  in  $+z$  direction. Given below, is the most general form of such a wave.

$$\mathbf{E}^+ = A(\hat{x} - j\hat{y})e^{-jh_1z} + C(\hat{x} + j\hat{y})e^{-jh_2z} \quad (2.20)$$

$$\mathbf{H}^+ = \frac{A}{\eta_c}(\hat{y} + j\hat{x})e^{-jh_1z} + \frac{C}{\eta_c}(\hat{y} - j\hat{x})e^{-jh_2z} \quad (2.21)$$

Similarly, a plane wave traveling in  $-z$  direction in a chiral medium is given by,

$$\mathbf{E}^- = F(\hat{x} + j\hat{y})e^{jh_1z} + G(\hat{x} - j\hat{y})e^{jh_2z} \quad (2.22)$$

$$\mathbf{H}^- = \frac{F}{\eta_c}(-\hat{y} + j\hat{x})e^{jh_1z} + \frac{G}{\eta_c}(-\hat{y} - j\hat{x})e^{jh_2z} \quad (2.23)$$

The terms with wavenumber  $h_1$  represent a RHCP wave and those with wavenumber  $h_2$  represent a LHCP wave. The superscripts  $\pm$  with  $\mathbf{E}$  and  $\mathbf{H}$  represent the  $+z$  and  $-z$  propagation of the wave, respectively.

Since RHCP and LHCP waves in (2.20)-(2.23) travel with different phase velocities, the polarization of the total wave rotates. It has been shown in literature that, if a linearly polarized wave impinges on a air-chiral interface, part of the wave is reflected back to the air and another part is transmitted into the chiral medium. The reflected wave maintains its linear polarization but the part transmitted to the chiral medium is now circular polarized. For a much more detailed explanation, refer to [8]. As a simple example, plane waves due to an electric current sheet in a chiral medium is presented in Appendix C.

## 2.4 The Method of Moments in Brief

In this frequency domain method, the unknown function is expanded in terms of known functions with unknown coefficients. The method starts with an exact linear operator equation which is then solved approximately. The computed result is an approximation to the exact result. Given the operator equation,

$$L(f) = g \quad (2.24)$$

where  $L$  is a linear operator,  $g$  is a known function, and  $f$  is unknown. In case of electromagnetics  $L$  is an integro-differential operator,  $f$  is the unknown function (the equivalent surface currents in our case) and  $g$  is a known excitation (the incident plane wave in our case). The unknown function  $f$  is expanded into  $N$  weighted basis or expansion functions,

$$f = \sum_{n=1}^N \alpha_n h_n(x) \quad (2.25)$$

Where  $h_n(x)$  is the expansion function and  $\alpha_n$  is the expansion coefficient. After substituting (2.25) in (2.24), we have the following,

$$L\left(\sum_{n=1}^N \alpha_n h_n(x)\right) = g \quad (2.26)$$

Since  $L$  is a linear operator, (2.26) can be written as,

$$\sum_{n=1}^N \alpha_n L(h_n(x)) \quad (2.27)$$

When (2.27) is tested by a set of testing functions  $w_m(x)$ ,

$$\left\langle w_m, \sum_{n=1}^N \alpha_n L(h_n(x)) \right\rangle = \langle w_m, g \rangle, \quad m = 1, 2, \dots, N. \quad (2.28)$$

The brackets  $\langle \cdot \rangle$  stand for the defined inner product which is used in the testing process. Equation (2.28) can be written as  $N$  independent equations which takes the form of (2.29) in its matrix form,

$$\begin{bmatrix} Z_{11} & Z_{12} & \dots & Z_{1N} \\ Z_{21} & Z_{22} & \dots & Z_{2N} \\ \vdots & \vdots & \ddots & \vdots \\ Z_{N1} & Z_{N2} & \dots & Z_{NN} \end{bmatrix} \begin{bmatrix} \alpha_1 \\ \alpha_2 \\ \vdots \\ \alpha_N \end{bmatrix} = \begin{bmatrix} g_1 \\ g_2 \\ \vdots \\ g_N \end{bmatrix} \quad (2.29)$$

A typical element  $Z_{mn}$  and  $g_m$  are given by

$$Z_{mn} = \langle w_m, L(h_n(x)) \rangle \quad (2.30)$$

$$g_m = \langle w_m, g(x) \rangle \quad (2.31)$$

The unknown coefficients can be calculated readily by taking inverse of the  $Z$  matrix, called the moment matrix, as shown below:

$$[\alpha] = [Z]^{-1} [g] \quad (2.32)$$

Much more details can be found in [6].

## 2.5 Solutions to Some Simple Problems

The purpose of this dissertation is to compute scattering from a 2-D chiral cylinder of arbitrary cross-section above a dielectric half-space using the method of moments and the perturbation method. The main aim is to write a MATLAB program that can solve this problem. Starting with the main problem, directly, would make our code prone to errors. Therefore, instead of immediately solving the main problem, first, some simpler problems were solved to gain confidence in our developed algorithm. The results computed by our MATLAB program are in excellent agreement with those of the FORTRAN code given in [46] and those of other researchers. This gave us confidence in our developed algorithm. We started with the simplest problem of scattering from a thin PEC strip in free-space and gradually increased the complexity of the problems. The results were verified on each step. For the sake of completeness the following problems are presented in this section.

1. Scattering from a PEC cylinder of arbitrary cross-section.
2. Scattering from a dielectric cylinder of arbitrary cross-section.
3. Scattering from multiple PEC and/or dielectric cylinders of arbitrary cross-section.

4. Scattering from a PEC cylinder of arbitrary cross-section above a PEC plane.
5. Scattering from a dielectric cylinder of arbitrary cross-section above a PEC plane.
6. Scattering from a chiral cylinder of arbitrary cross-section in free-space.
7. Scattering from multiple chiral cylinders in free-space.

### **2.5.1 Scattering From a Thin PEC Strip**

First, a very simple problem of scattering from a thin PEC strip in free-space is solved. The strip is excited by a plane TM wave with an incident angle  $\phi^i = 90^\circ$ . The conventional MoM is used to solve this problem. Pulses are used as expansion functions and Galerkin's method is used for testing. For a detailed application of the moments method refer to [46]. Figure 2.2 shows the surface current density on the thin highly conducting strip. Our results are in excellent agreement with [46], Fig. 12-15 of [47], and Fig. 2 of [48]. Figure 2.3 shows the bistatic scattering width (BSW) for the PEC strip in free-space.

### **2.5.2 Scattering From Multiple Conducting Cylinders**

Next, we compute scattering from multiple conducting cylinders in free-space. As an example, cylinders of square and triangular cross-sections are considered. The setup and the bistatic scattering width for this problem are shown in Fig. 2.4. The system is excited by a plane TM wave from  $\phi^i = 90^\circ$  direction. The MATLAB and FORTRAN results are in excellent agreement.

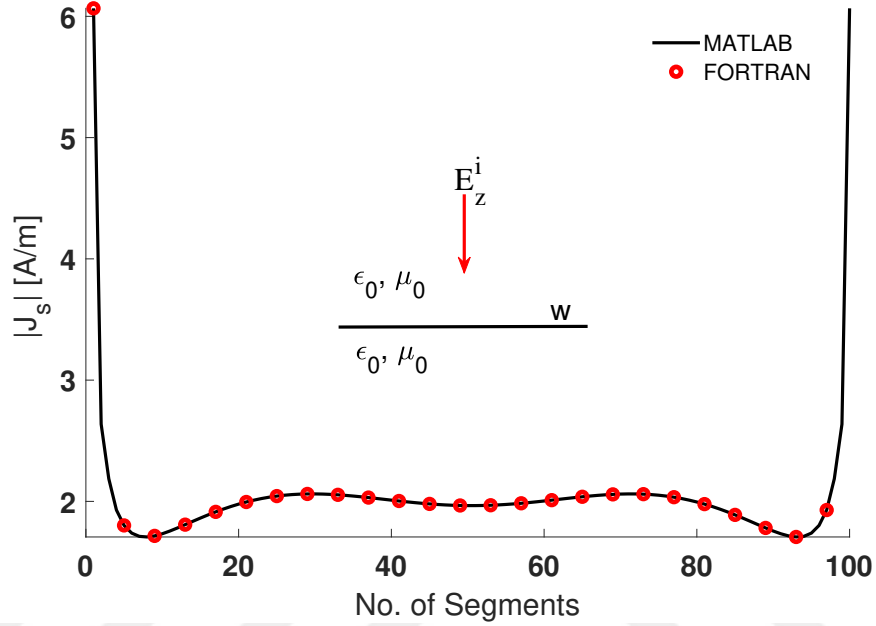


Figure 2.2: Current density induced on a thin PEC strip of width  $w = 2\lambda_0$  when excited by a plane TM wave with  $\phi^i = 90^\circ$ .

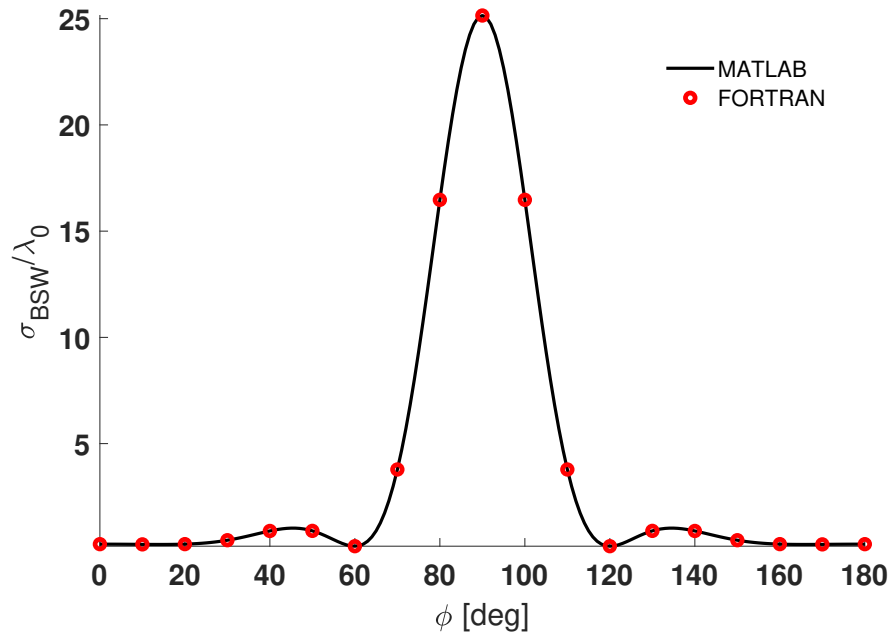


Figure 2.3: Bistatic scattered field for a thin PEC strip of width  $2\lambda_0$ .

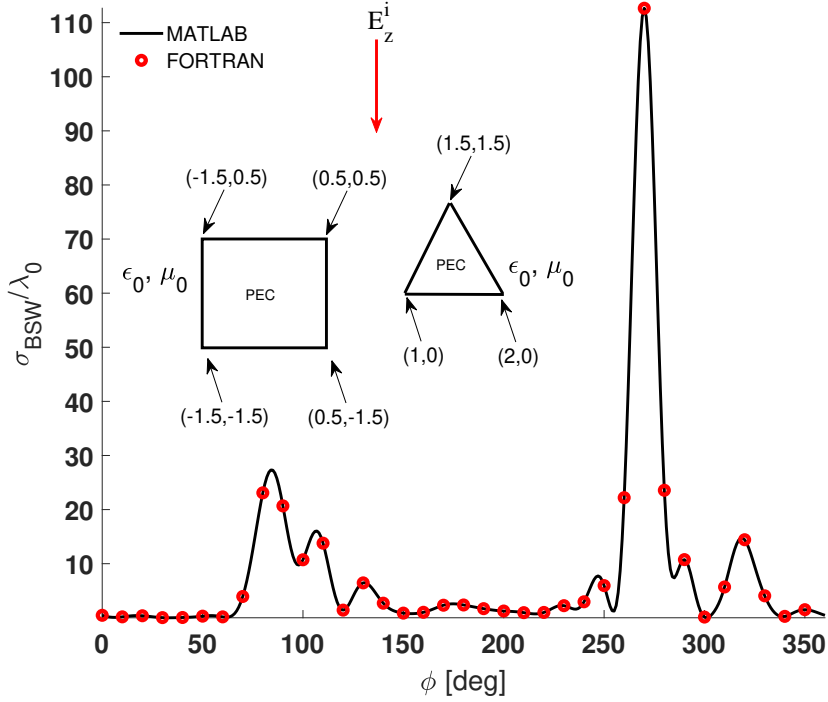


Figure 2.4: Bistatic scattered far-field from two PEC cylinders illuminated by a TM plane wave from  $\phi^i = 90^\circ$  direction.

### 2.5.3 Scattering From Dielectric Cylinders in Free-Space

Here, the algorithm is verified for scattering from multiple dielectric cylinders in free-space. As an example, the same square and triangular cylinders (now dielectric) immersed in free-space are considered. The cylinders are characterized by  $(\epsilon_1 = \epsilon_2 = 4\epsilon_0, \mu_1 = \mu_2 = \mu_0)$ . It can be seen in Fig. 2.5 that for the dielectric cylinders the back- and forward-scattered fields have reduced significantly and scattered field in other directions has increased.

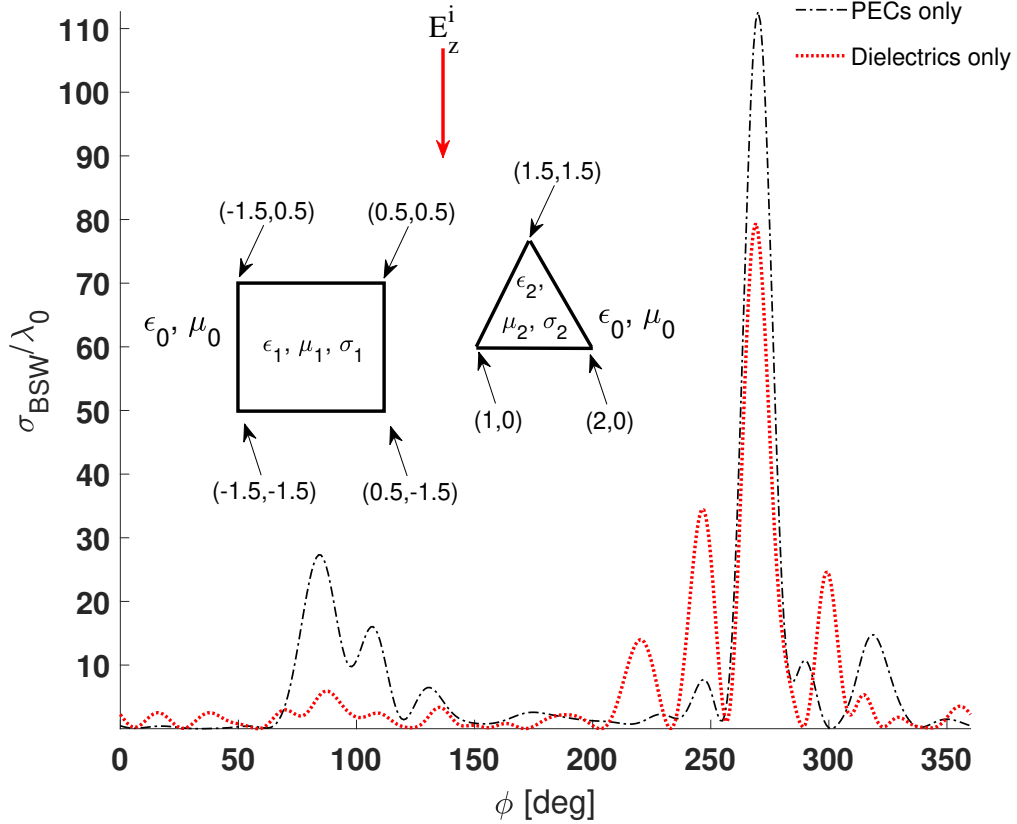


Figure 2.5: Bistatic scattered far-field for two dielectric cylinders, with square and triangular cross-sections, placed in the proximity of each other in free-space. The system is illuminated by a TM plane wave with the incident angle with  $\phi^i = 90^\circ$ .

### 2.5.4 Scattering From PEC and Dielectric Cylinders in Free-Space

In this section, we validate our MATLAB code for the problem of a square PEC cylinder and a triangular dielectric cylinder. The dielectric cylinder is characterized by  $\epsilon_1 = 4\epsilon_0$ ,  $\mu_1 = \mu_0$ . The problem setup and the scattered fields are shown in Fig. 2.6. The scattered field is also compared with that of a PEC and dielectric cylinders of the same dimensions.



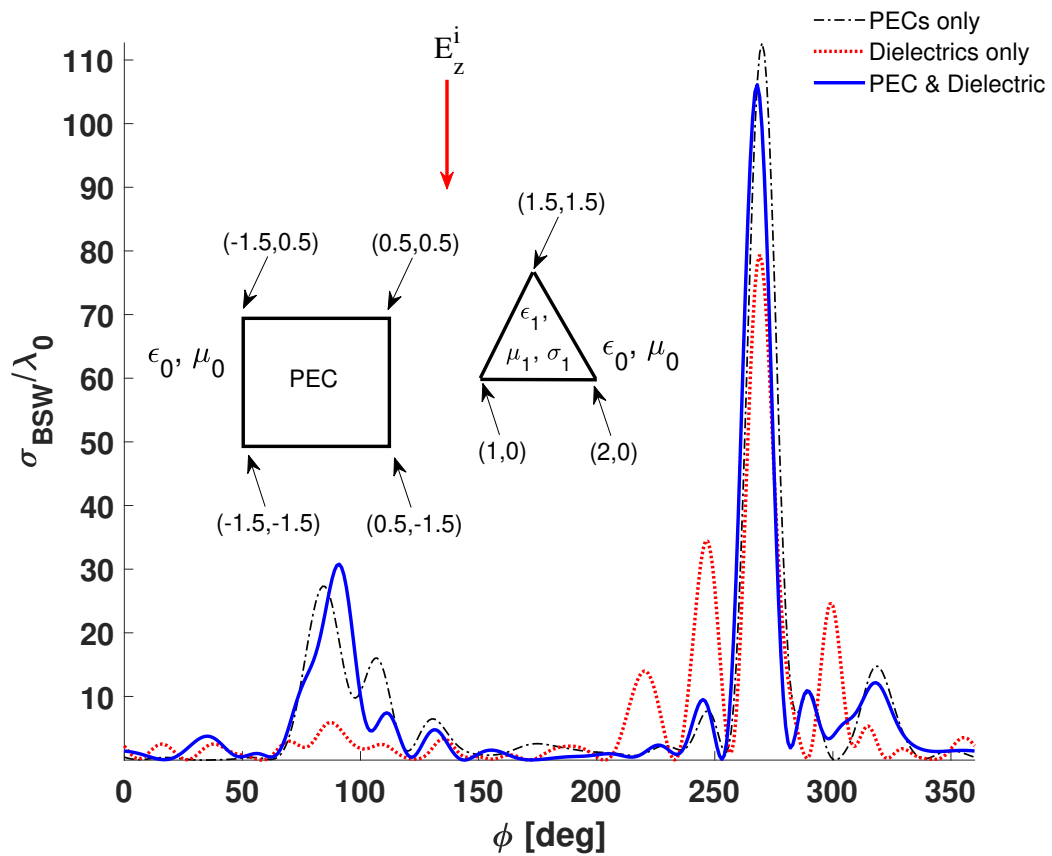


Figure 2.6: Bistatic scattered far-field due to a PEC square placed in the vicinity of a lossless dielectric ( $\epsilon_1 = 4\epsilon_0$ ,  $\mu_1 = \mu_0$ ) triangular cylinder. The setup is illuminated by a TM plane wave incident from  $\phi^i = 90^\circ$  direction.

## 2.5.5 Scattering From a PEC Cylinder Above a Ground Plane

After solving the free-space problems, we advanced to problems where the conducting scatterer is above a ground plane. As an example, a semi-circular conducting cylinder placed above an infinite ground plane is considered. The original problem is shown in Fig. 2.7a.  $B_1$  is the semi-circular PEC cylinder of radius  $\lambda_0$  and the red solid line represents the perfectly conducting ground plane. The method of images is used to obtain the equivalent model and MoM is used to solve the problem numerically.

In the equivalent problem shown in Fig. 2.7b, we have two bodies  $B_1$  and  $B_2$ , and two sources  $S_1$  and  $S'_1$ . Notice that the ground plane is removed and a semi-circular PEC cylinder ( $B_2$ ) which is the mirror image of  $B_1$  is introduced. A second source  $S'_1$  which is the image of  $S_1$  has also been added. In this problem, the incident wave is impinging the cylinder with an angle  $\phi^i = 90^\circ$  for  $S_1$  and  $\phi^i = -90^\circ$  for  $S'_1$ . As can be seen from the geometry, this problem is similar to solving a full circular cylinder with two excitations. There are two methods of solving this problem, the *brute force* method and the *smart way*. These methods are discussed next.

### The Brute Force Method and the Smart Solution

For a single body problem the equation that we need to satisfy is

$$\mathbf{E}_{tan}^s(\mathbf{J}_c) = -\mathbf{E}_{tan}^i \quad \text{on } S \quad (2.33)$$

where  $S$  is the surface of the cylinder and  $\mathbf{E}_{tan}^s$  is the scattered field produced due to  $\mathbf{J}_c$ . For our problem we need to satisfy the following two equations, since we have the original body ( $B_1$ ) and its image ( $B_2$ ),

$$\mathbf{E}_{tan}^s(\mathbf{J}_c + \mathbf{J}'_c) = -\mathbf{E}_{tan}^i + \mathbf{E}_{tan}^{i'} \quad \text{on } B_1 \quad (2.34)$$

$$\mathbf{E}_{tan}^s(\mathbf{J}_c + \mathbf{J}'_c) = -\mathbf{E}_{tan}^i + \mathbf{E}_{tan}^{i'} \quad \text{on } B_2 \quad (2.35)$$

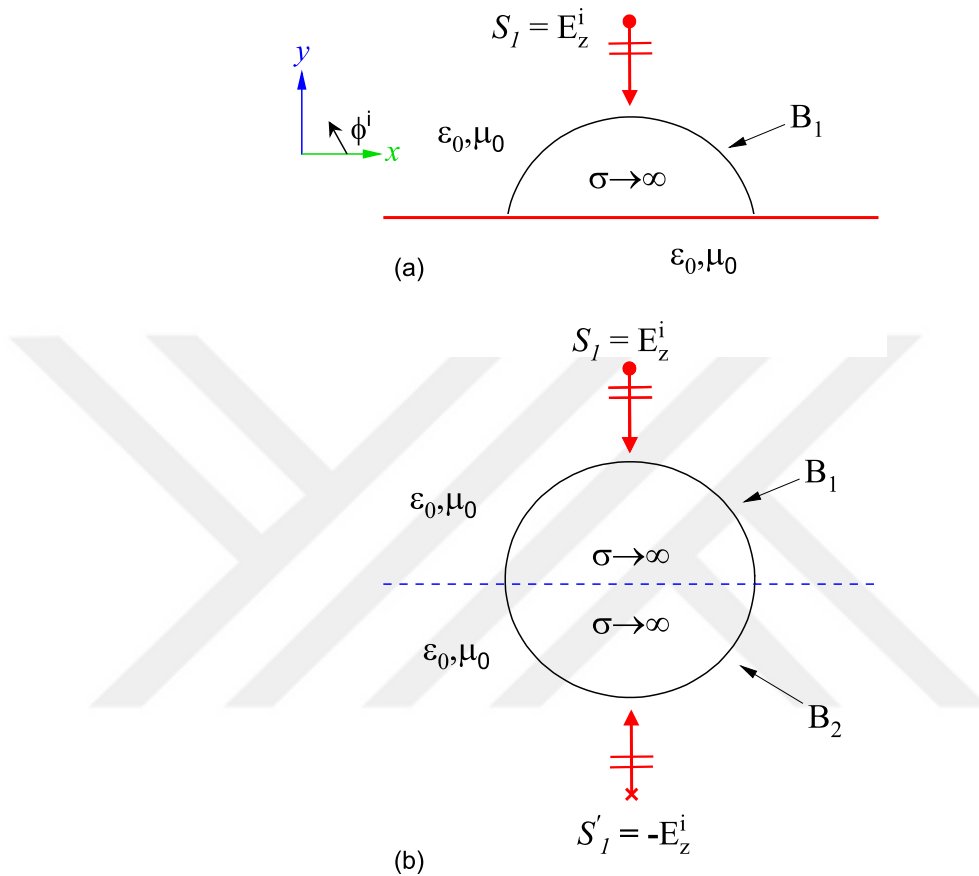


Figure 2.7: A semi-circular PEC cylinder (radius =  $\lambda_0$ ) placed above (touching) a conducting ground plane. The setup is excited with a TM plane wave. (a) Original problem, (b) Equivalent image problem.

The primed quantities remind us that they are related to the image cylinder. By applying MoM to the two body problem with two sources, the currents on both cylinders were computed.

The magnitude and phase of the induced surface currents on the cylinders are shown in Fig. 2.8.

Since the currents on the image cylinder ( $B_2$ ) are image of those on the original cylinder  $B_1$  so we do not need to solve for both the currents. In this case, we can model the problem in a smart way where the number of unknowns reduce to half. However, the moment matrix elements are more complex now. It takes the same

amount of time to fill the matrix but the matrix inversion time reduces due to its smaller size. The induced surface electric currents for both the methods are compared in Figs. 2.8a and 2.8b. It can be seen that, in the smart solution, the number of unknowns reduced to 180 instead of 360 in the brute force case. The results are in excellent agreement.

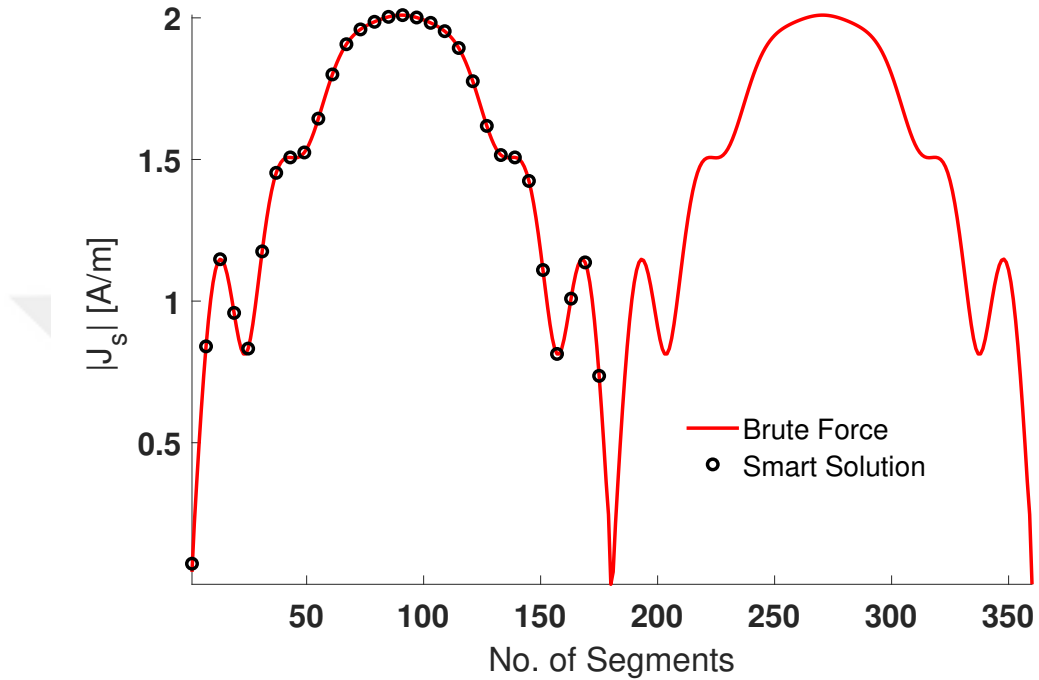
### 2.5.6 Scattering From a Dielectric Cylinder Above a Ground Plane

The developed algorithm is also capable of solving for a 2-D dielectric cylinder of arbitrary cross-section placed above a ground plane. The same brute force method and smart solution is used to solve the problem.

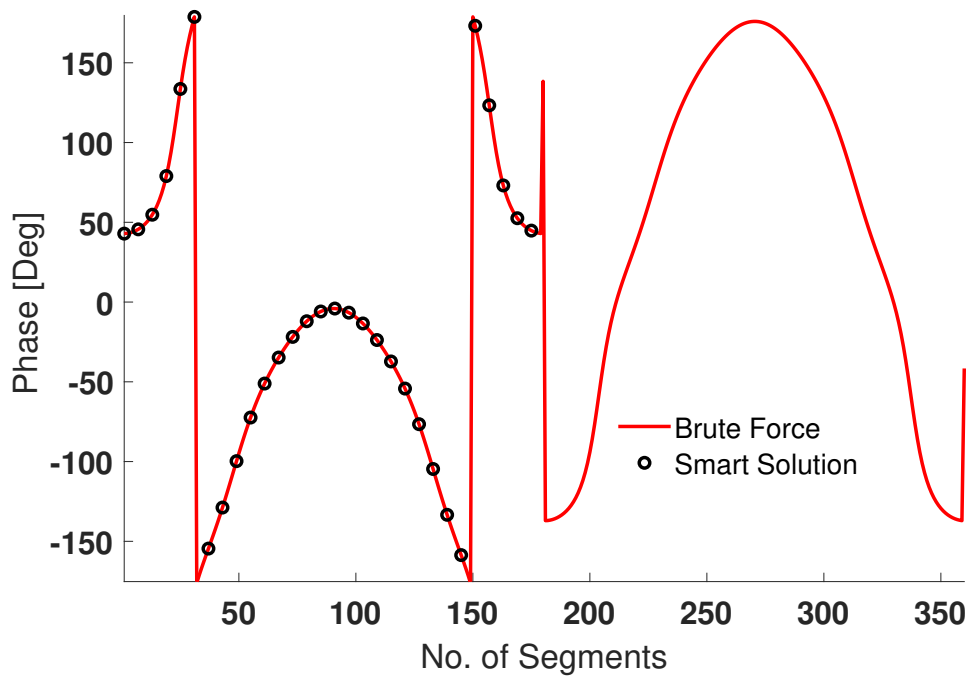
As an example, consider a dielectric cylinder with a square cross-section placed a distance  $d$  above a ground plane. The setup is excited by a TM incident field impinging with an angle  $\phi^i = 90^\circ$ . The problem setup and the equivalent surface electric and magnetic currents are shown in Fig. 2.9. Table 2.1 shows a comparison of the simulation time for the two methods. The superiority of the smart solution in terms of the reduced unknowns and the simulation time is clearly visible for the problems discussed here.

Table 2.1: Comparison of the simulation time for the brute force method and the smart solution for the two problems discussed above.

Cylinder	Solution Type	Segments/Unknowns	Sim. Time (sec)
Semi-Circular PEC	Brute Force	360/360	41
	Smart Solution	180/180	20
Dielectric Square	Brute Force	800/1600	204
	Smart Solution	400/800	101

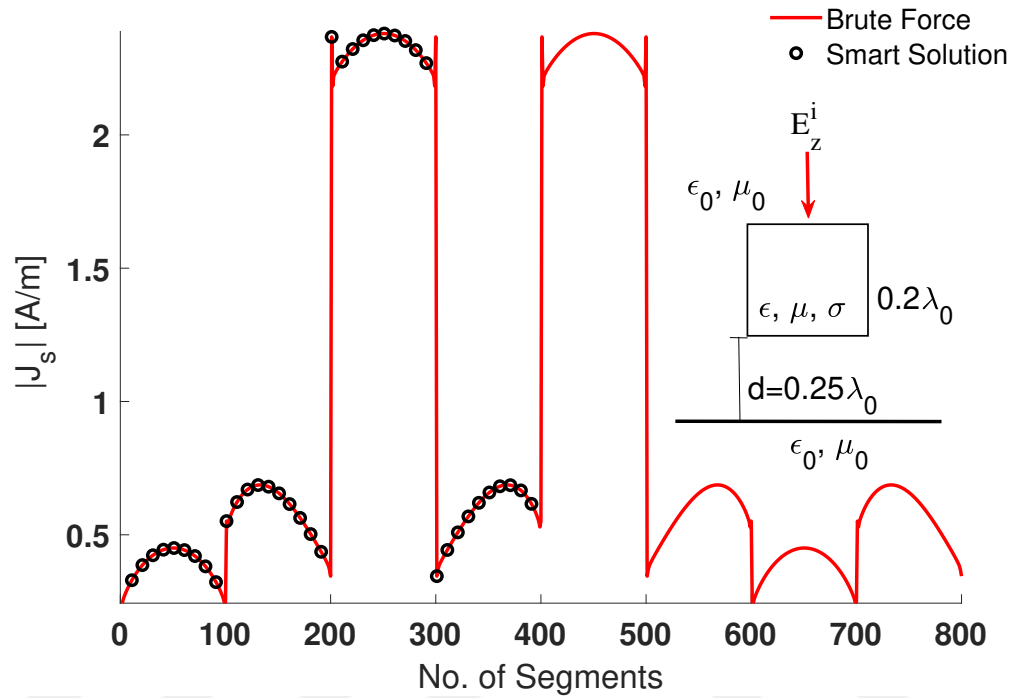


(a) Magnitude of the surface electric current.

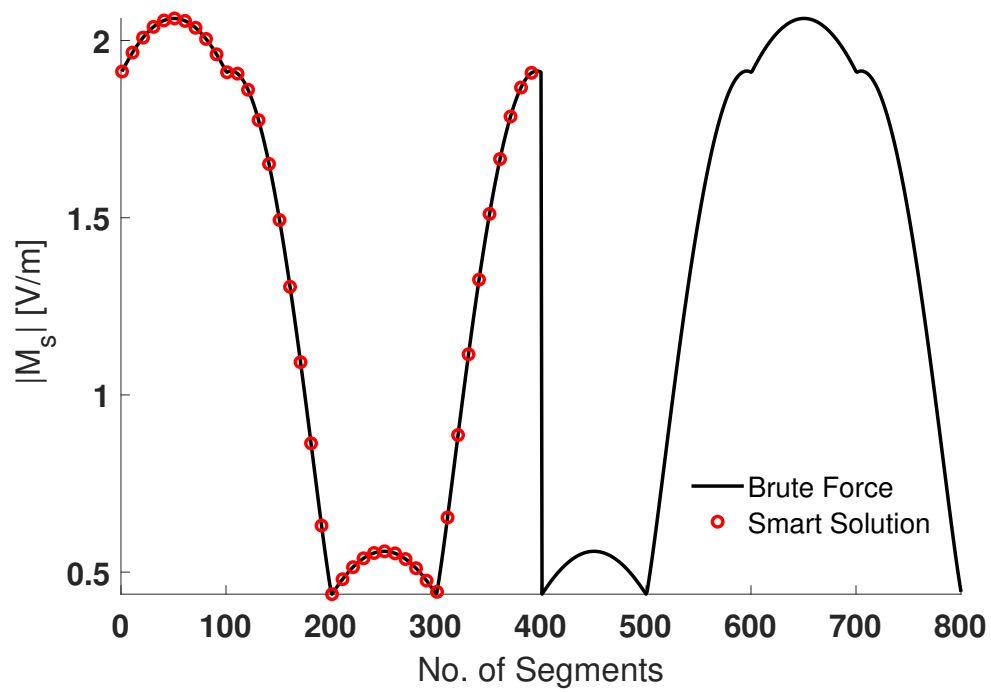


(b) Phase of the surface electric current.

Figure 2.8: Induced currents on a semi-circular PEC cylinder placed above a ground plane. The brute force and the smart solution methods are compared.



(a) Surface electric current.



(b) Surface magnetic current.

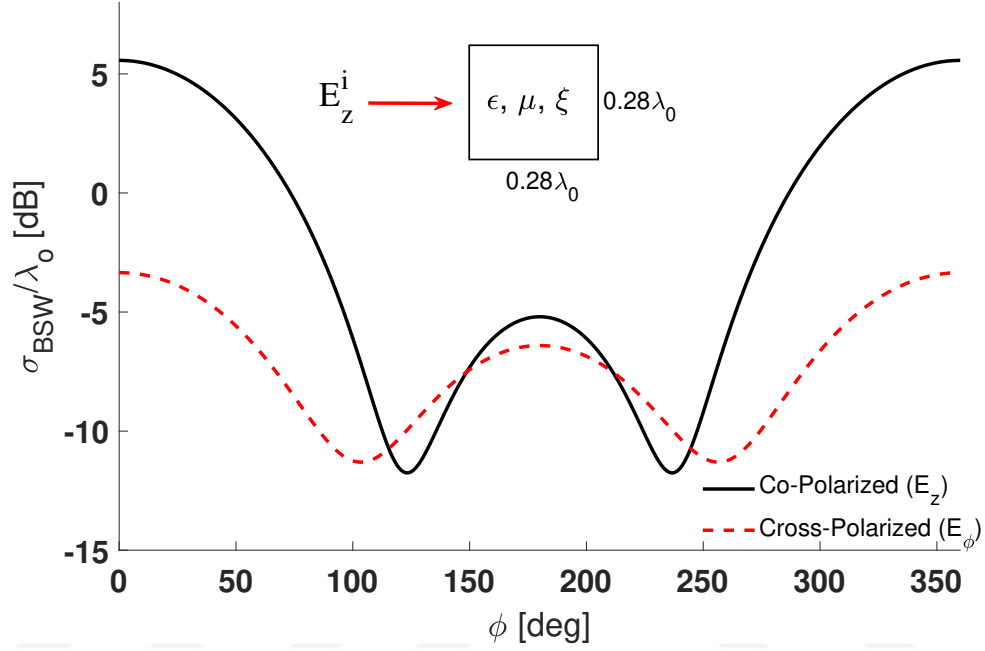
Figure 2.9: Equivalent currents on the surface of a lossless dielectric ( $\epsilon = 2\epsilon_0, \mu = \mu_0$ ) cylinder with a square cross-section placed  $0.25\lambda_0$  above a conducting ground plane, excited by a TM plane wave from  $\phi^i = 90^\circ$ .

## 2.5.7 Scattering From a Chiral Cylinder in Free-Space

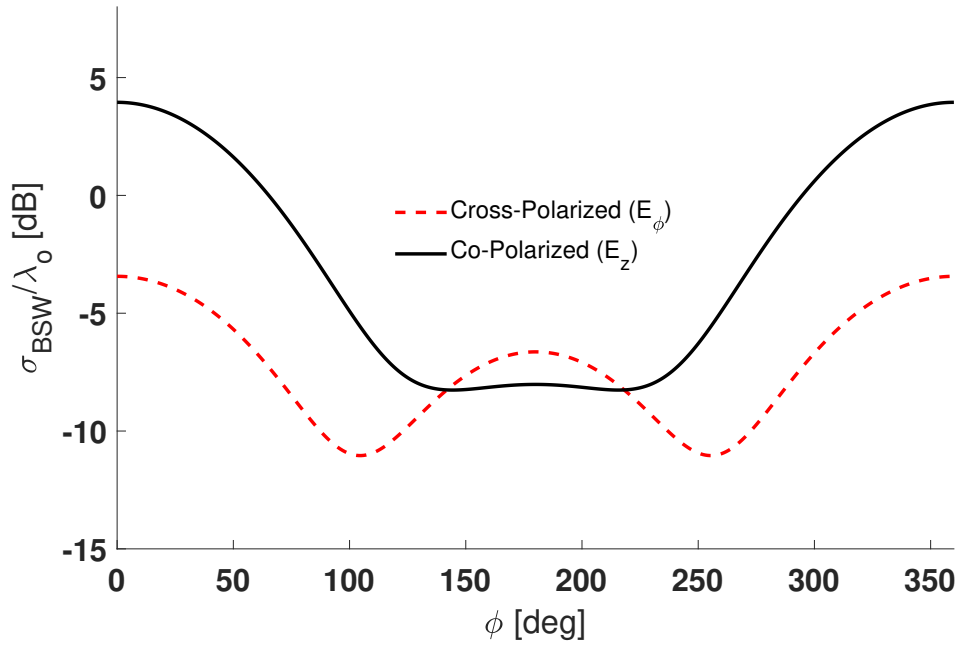
The MATLAB code was modified to solve for scattering from a chiral cylinder of arbitrary cross-section in free-space. Results from our code were in very good agreement with the exact eigenfunction solution for TM and TE plane wave incidence for a circular chiral cylinder. The results are discussed in Figs. A.2 and A.3 in Appendix A.

As another example, scattering from a lossless, isotropic, and homogeneous chiral cylinder with a square cross-section is computed for TM and TE plane wave incidence. The chiral cylinder is characterized by  $\epsilon_r = 3$ ,  $\mu_r = 2$ ,  $\xi = 0.0005$ . The co- and cross-polar components of the bistatic scattering width are shown in Fig. 2.10. The results are in good agreement with those presented in [49].

After having confidence in our results and the developed code, next, we compute scattering from multiple chiral cylinders of arbitrary cross-section in free-space.



(a) TM excitation



(b) TE excitation

Figure 2.10: Bistatic scattering width of a chiral cylinder with a square cross-section, excited by a plane wave from  $\phi^i = 180^\circ$ . The cylinder is characterized by  $\epsilon_r = 3$ ,  $\mu_r = 2$ ,  $\xi = 0.0005$ .



## 2.5.8 Scattering From Multiple Chiral Cylinders

Finally, the algorithm is extended to solve for multiple chiral cylinders in free-space. This is the last step before solving our main problem. The results in this section are validated by solving some special cases. This further strengthened our confidence in the developed code. The problems presented here are:

- Scattering from multiple chiral cylinders
- Scattering from a chiral cylinder in the presence of a PEC cylinder

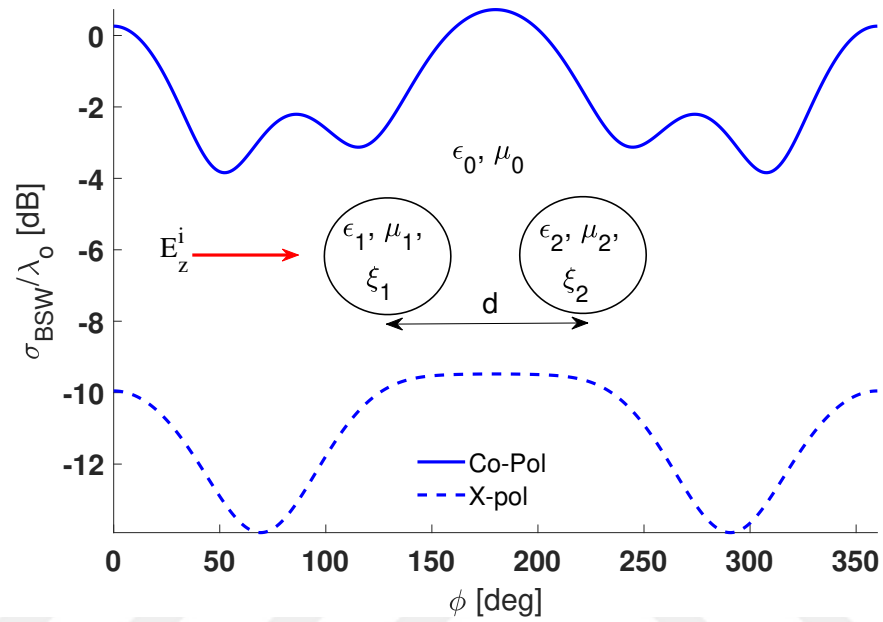
This is the most generalized form of our MATLAB algorithm for computing scattering from 2-D objects of arbitrary cross-section in free-space.

### 2.5.8.1 Scattering From Multiple Chiral Cylinders

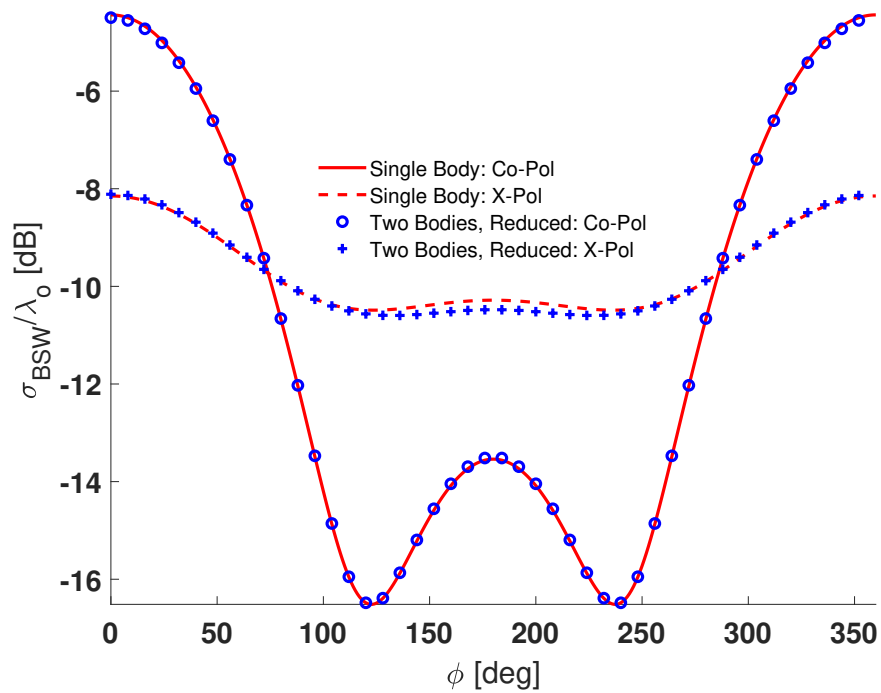
The first problem solved here is scattering from multiple chiral cylinders immersed in free-space. Cylinder 1 and cylinder 2, each of radius  $0.1\lambda_0$  are characterized by  $\epsilon_1 = 1.5\epsilon_0$ ,  $\mu_1 = 4\mu_0$ ,  $\xi_1 = 0.0005$  and  $\epsilon_2 = 2\epsilon_0$ ,  $\mu_2 = 3\mu_0$ ,  $\xi_2 = 0.07$ , respectively. Centers of the cylinders are  $0.5\lambda_0$  apart. The bistatic scattering width of the cylinders, when excited from  $\phi = 180^\circ$ , is shown in Fig. 2.11a.

### Verification

In order to verify the solution, the material properties of cylinder 2 are changed to  $\epsilon_2 = \epsilon_0$ ,  $\mu_2 = \mu_0$ ,  $\xi_2 = 0$ . In this case, our problem reduces to a single body problem which has been compared with the exact solution (Fig. A.2). Comparison of the single chiral and the reduced two body problem is shown in Fig. 2.11b, which are in good agreement.



(a)



(b)

Figure 2.11: (a) Bistatic scattering width of two circular chiral cylinders and (b) when the cylinder on the right (cylinder 2) is assigned free-space properties.

### 2.5.8.2 Scattering from a PEC and Chiral Cylinder

After having verified the code for multi-body chiral objects, a PEC circular cylinder is placed in the proximity of a circular chiral cylinder. The two cylinders are excited by TM plane wave incident from  $\phi = 90^\circ$ . The problem setup and the co-polarized and cross-polarized bistatic scattering widths are shown in Fig. 2.12.

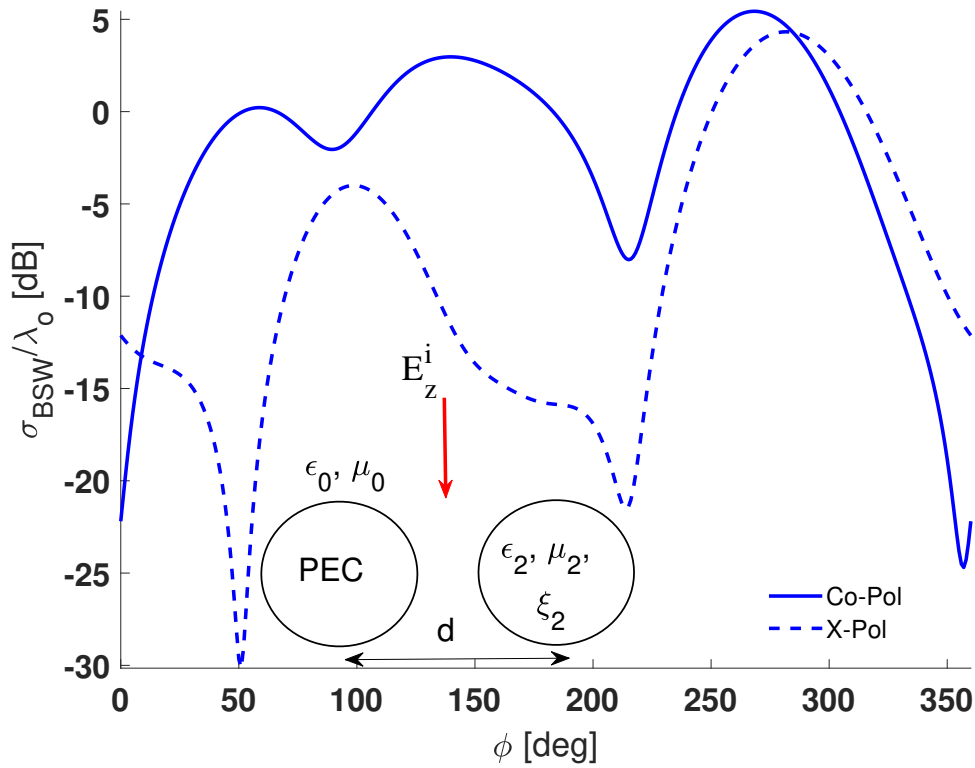


Figure 2.12: Bistatic scattering width of a PEC and a chiral cylinder placed next to each other. The cylinders are surrounded by free-space ( $\epsilon_0, \mu_0$ ). Radius of cylinders is  $0.1\lambda_0$ ,  $d = 0.5\lambda_0$ , and the chiral cylinder is characterized by  $\epsilon_2 = 2\epsilon_0$ ,  $\mu_2 = 2\mu_0$ ,  $\xi_2 = 0.003$ .

## Verification-I

The results are verified by a limiting case where the chiral cylinder is assigned free-space properties. This means that the chiral cylinder no longer exists. The bistatic scattering width of this reduced problem must match with that of a single PEC cylinder of the same dimensions. The results are compared in Fig. 2.13 which are in very good agreement.

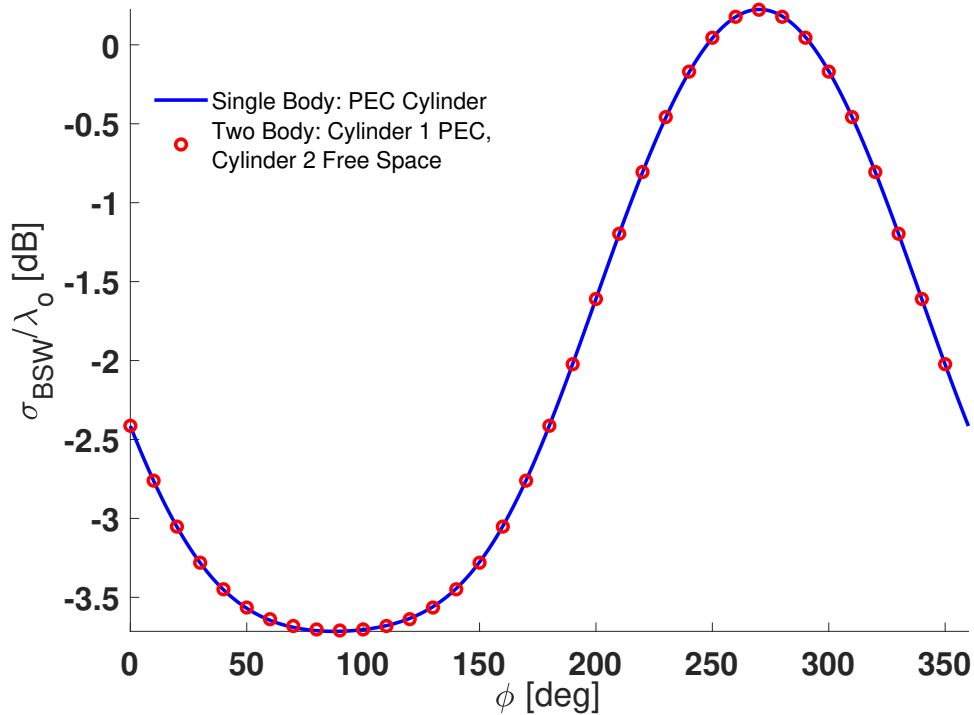


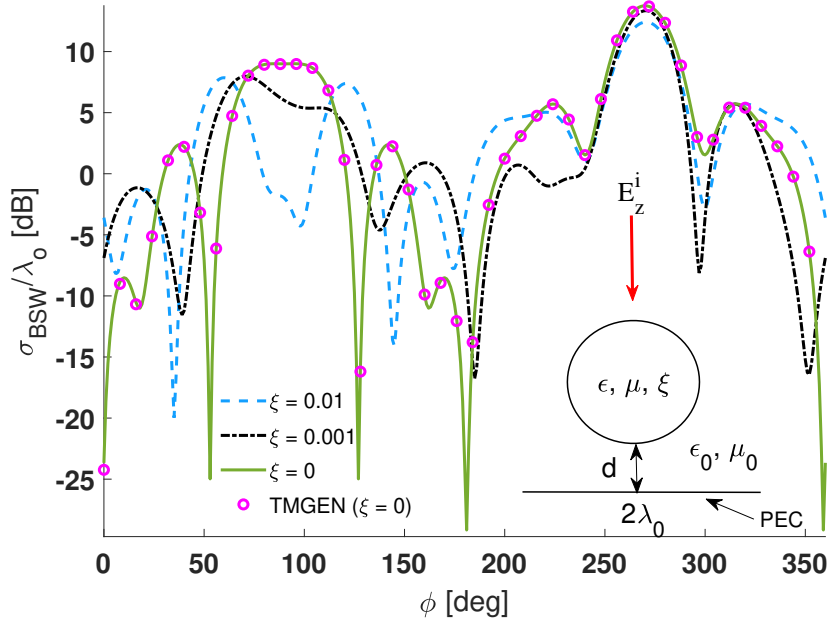
Figure 2.13: Bistatic scattering width for the setup shown in Fig. 2.12, with the chiral cylinder properties changed to those of free-space.

## Verification-II

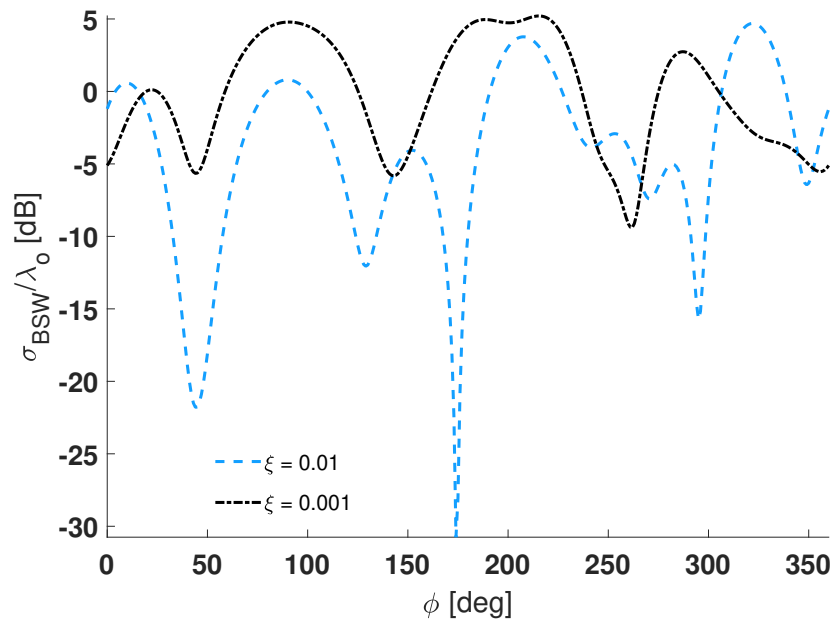
A simple study is presented here in which a circular chiral cylinder of radius  $0.5\lambda_0$  is placed symmetrically above a PEC strip of width  $2\lambda_0$ . Distance  $d$  between the strip and cylinder is  $0.3\lambda_0$ . The chiral cylinder is characterized by  $(\epsilon = 4\epsilon_0, \mu = \mu_0, \xi)$ . The structure is illuminated by a TM plane wave from  $\phi = 90^\circ$ . The chirality

admittance  $\xi$  of the chiral cylinder was varied and the effect on the scattering width was observed. Finally, when the chirality admittance was set to zero, the results agreed ‘exactly’ with the results from the FORTRAN code of [46]. This gave us further confidence in our MATLAB code. The results for the co-polarized and cross-polarized scattered fields are shown in Fig. 2.14. Note that the cross-polar component of the bistatic scattering width has disappeared when the chirality admittance is set to zero, as expected.

The study performed in the above sections proved that the developed algorithm is reliable. After solving these problems, we are now able to advance to the main problem, i.e., scattering for a 2D chiral cylinder of arbitrary cross-section above a dielectric half-space. This problem is discussed in the next chapter.



(a) Co-polarized



(b) Cross-polarized

Figure 2.14: Bistatic scattering width of a circular chiral cylinder (radius =  $0.5\lambda_0$ ) above a finite width PEC strip. Distance  $d = 0.3\lambda_0$ ,  $\epsilon = 4\epsilon_0$ ,  $\mu = \mu_0$ ,  $\xi$ . The chirality admittance value ( $\xi$ ) is varied.

## Chapter 3

# EM Scattering From a Chiral Cylinder Above a Dielectric Half-Space

In this chapter, a simple numerical solution for electromagnetic scattering from a two dimensional (2-D) homogeneous chiral cylinder of arbitrary cross-section placed above a dielectric half-space is presented. The surface equivalence principle and the Method of Moments (MoM) are used to replace the cylinder and the dielectric half-space by unknown equivalent electric and magnetic surface currents. By satisfying the continuity of the tangential components of the electric field at the surfaces, a set of electric field integral equations (EFIE) is obtained. The dielectric surface is of infinite extent, the conventional MoM cannot be applied directly. Therefore, a perturbation method is used where a strip of finite width approximates the surface of the half-space. Then, this approximate problem is used with conventional MoM. Pulses are used as basis functions and Galerkin's method is used for testing. The excitation vector now contains the reflected field from the dielectric half-space in addition to the incident field. Both TM and TE excitations are treated. Equivalent currents on the chiral cylinder, perturbed currents on the interface, and the scattered fields are presented for various geometries.

It is observed that, depending on the cylinder's height above the interface, these results converge as the finite width of the strip is increased. The computed results are validated by assuming some special cases and comparing them with the results in the literature.

### 3.1 Introduction

Since its conception, chiral materials have been a topic of keen interest for many researchers. Due to optical activity in these materials, the plane of a linearly polarized light ray is rotated [50]. A chiral medium can be artificially produced at low gigahertz frequencies [51]. The extra degree of freedom, the chirality parameter, provides an efficient way to control the scattering properties of chiral coated objects [52]. Various techniques such as T-matrix method [53], volume formulation [54], eigenfunction solutions [55], finite difference time domain (FDTD) [56], and method of moments (MoM) [5, 6, 57] along with others have been used to compute plane wave scattering from chiral objects. Analytical and numerical solutions for 2-D perfect electric conductors (PEC) and dielectric objects, above and below a half-space, have been studied extensively [58–64].

The scattering properties of 2-D chiral objects have not been investigated thoroughly in the presence of a dielectric half-space or a PEC plane. This study can find various applications such as in the field of antennas, radar cross-section alteration, remote sensing, geoscience, and bioscience applications. The proposed system can mimic some actual micro/nano-structures above substrates in photonic applications. This demands further investigation of chiral objects, especially in the presence of a half-space. For more details the readers are referred to an elegant review article on chiral metamaterials [65].

The problem of electromagnetic waves interaction with three dimensional (3-D) arbitrary shaped chiral targets above a lossy half-space is solved using surface integral equations [66–69]. The chiral medium is split into two different regular homogeneous dielectric media and by using the discrete complex image method



(DCIM) the spatial domain half-space Green's functions are obtained [66–68]. A hybrid method is also used to solve 3-D chiral body above half-space using hybrid finite elements methods [70]. On the other hand, the perturbation method combined with MoM (used in this work) solves a set of coupled vector electric field integral equations to formulate the problem, which is relatively simple to understand and implement in 2-D. The proposed formulation is very simple because homogeneous space operators are used instead of the numerical computations of the half-space Green's functions which involve Sommerfeld integrals. This method can be generalized to 3-D problems as well.

The scattering behaviour of a cylinder above a dielectric half-space can be very different than the behaviour of the same cylinder when it is in free-space. Figure 3.1 shows this difference in the bistatic scattering width in the backward region ( $0^\circ < \phi < 180^\circ$ ) for a PEC circular cylinder of radius  $0.25\lambda_0$ , where  $\lambda_0$  is the free-space wavelength. This cylinder is illuminated by a TM wave with angle of incidence  $\phi^i = 90^\circ$ . It is seen that when this cylinder is in free-space the scattered field in the backward direction is almost constant. On the other hand, when this cylinder is placed at a height  $d = 0.5\lambda_0$  above a dielectric half-space ( $\epsilon_d=4\epsilon_0$ ,  $\mu_d=\mu_0$ ) the back-scattered field ( $\phi = 90^\circ$ ) has been reduced by about 5 dB, and major lobes are introduced in other directions. In Fig. 3.2 results are given when the PEC of Fig. 3.1 is replaced by a dielectric cylinder ( $\epsilon_c=6\epsilon_0$ ,  $\mu_c=1.5\mu_0$ ). For the dielectric cylinder above the half-space in Fig. 3.2, an increase of 3 dB in the back-scattered field can be observed relative to the free-space case. Furthermore, a 4 dB increase can be seen at  $15^\circ$  and  $165^\circ$  relative to the field of the dielectric cylinder in the free-space.

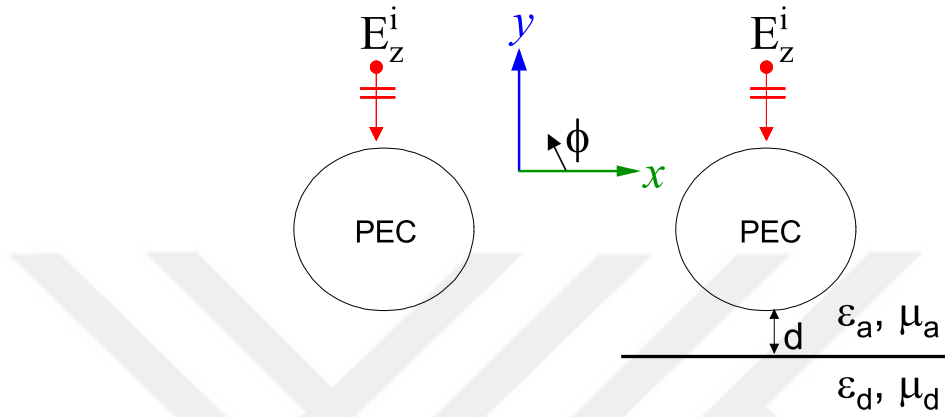
We are not aware of any results in the literature for the scattering behavior of a chiral cylinder of arbitrary cross-section above a dielectric half-space. That was the motivation behind this work. Figure 3.3 shows the result when the cylinder of Fig. 3.1 is replaced by a chiral cylinder ( $\epsilon_c=6\epsilon_0$ ,  $\mu_c=1.5\mu_0$ ,  $\xi=0.002$ ). The co-polar component of the scattered field at  $30^\circ$  and  $150^\circ$  has increased by 20 dB relative to the free-space case. Similarly, the cross-polar component of the scattered field at  $23^\circ$  and  $155^\circ$  has increased by about 15 dB in the presence of the half-space. The results in the presence of the half-space are computed for the first

time in this work. The procedure used to obtain these results is explained next.

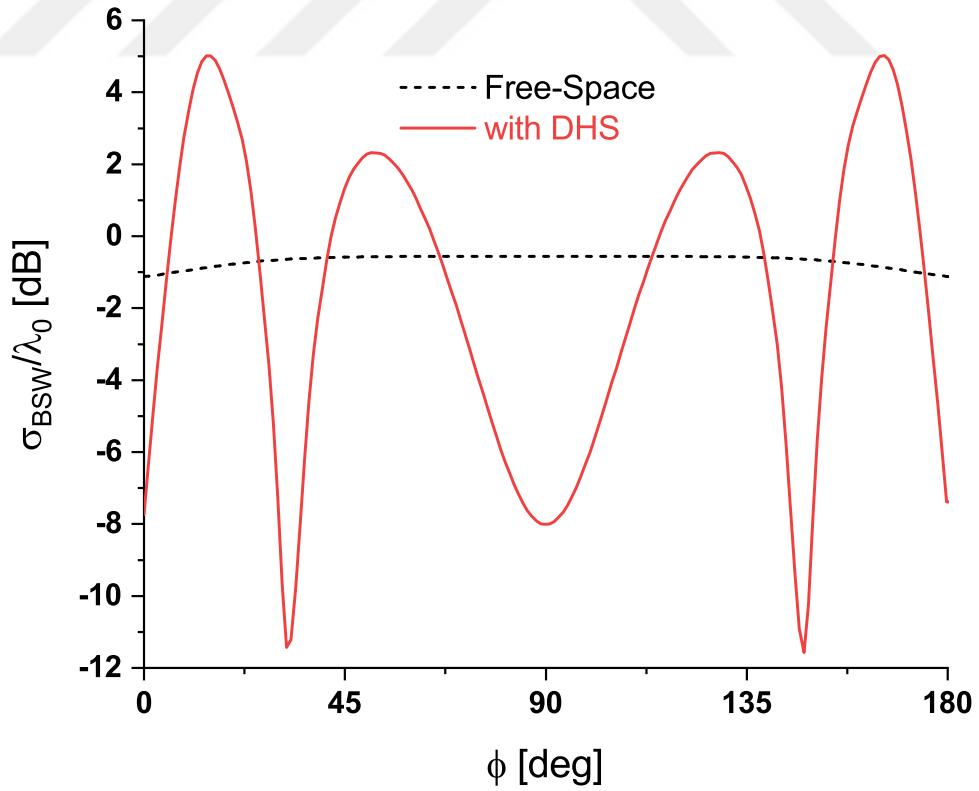
## 3.2 Integral Equations

Figure 3.4 shows the original problem under consideration. A 2-D homogeneous chiral cylinder of arbitrary cross-section is placed above a dielectric half-space. The surfaces of the chiral cylinder and the interface are represented by  $S_c$  and  $S_d$ , respectively. The cylinder is placed in free space ( $\epsilon_a = \epsilon_0$ ,  $\mu_a = \mu_0$ ) and is parallel to the  $z$ -axis. The dielectric half-space is characterized by  $(\epsilon_d, \mu_d)$ . The chiral cylinder is characterized by  $(\epsilon_c, \mu_c, \xi)$ . The parameter  $\xi$  denotes the chirality admittance of the chiral cylinder. The setup is excited by a TM or a TE plane wave with incident angle  $\phi^i$ . The excitation varies harmonically according to  $e^{j\omega t}$  (suppressed).  $\mathbf{E}^{inc}$  and  $\mathbf{H}^{inc}$  denote the incident electric and magnetic fields.  $\mathbf{E}_a$  and  $\mathbf{H}_a$  denote the total fields external to the cylinder above the half-space. The subscript ‘a’ is used to remind us that these fields are in the air region ( $\epsilon_a = \epsilon_0$ ,  $\mu_a = \mu_0$ ). Similarly, the fields in the dielectric half-space are represented by  $\mathbf{E}_d$  and  $\mathbf{H}_d$ , and the fields internal to the chiral cylinder are given by  $\mathbf{E}_c$  and  $\mathbf{H}_c$ . This problem does not have an exact solution, therefore an approximate problem is solved using the perturbation method and MoM.

Surface equivalence principle [7] is used to divide the original problem of Fig. 3.4 into three simpler equivalent problems, as shown in Figs. 3.5, 3.6, and 3.7. In the external equivalent problem of Fig. 3.5, the chiral cylinder and the dielectric half-space are removed. The whole space is characterized by  $(\epsilon_0, \mu_0)$ . The fields internal to the fictitious surface  $S_c$  and below the surface  $S_d$  are assumed to be zero. The field external to these surfaces is postulated to be  $\mathbf{E}_a$  and  $\mathbf{H}_a$ . To account for this discontinuity, equivalent surface currents  $\mathbf{J}_d$  and  $\mathbf{M}_d$  are placed on the surface  $S_d$  and equivalent surface currents  $\mathbf{J}_c$  and  $\mathbf{M}_c$  are placed on the



(a) (Left) PEC cylinder in free-space and (right) PEC cylinder above dielectric half-space (DHS).



(b)

Figure 3.1: Bistatic scattering width of a circular PEC cylinder in free-space and when it is placed above a DHS.

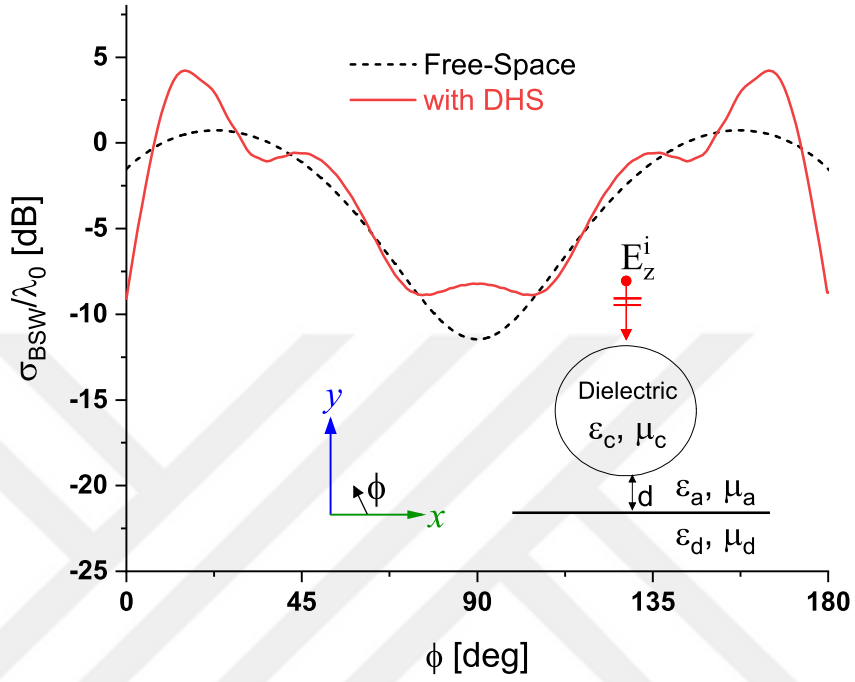


Figure 3.2: Bistatic scattering width of a circular dielectric cylinder in free-space and when it is placed above a (DHS).

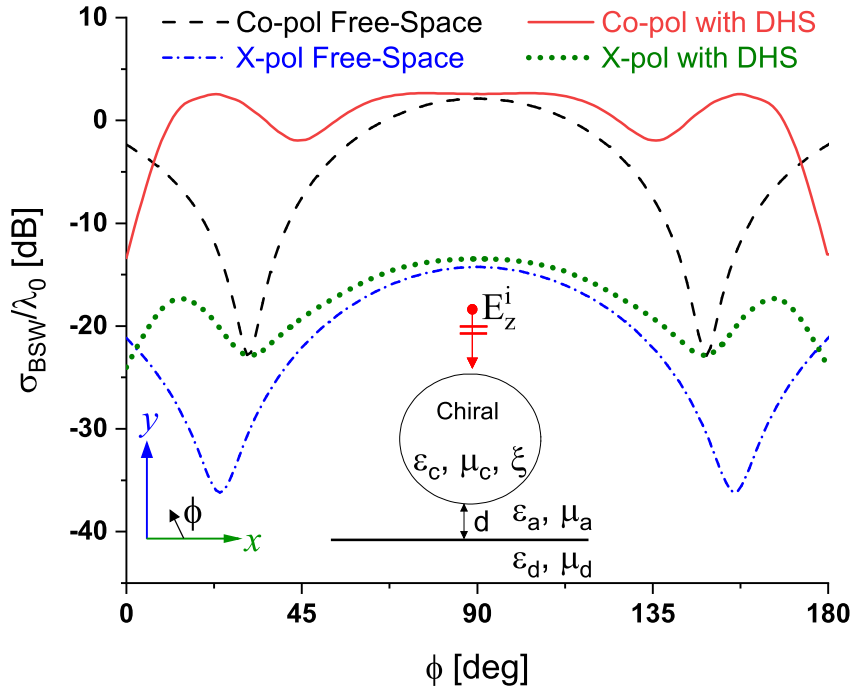


Figure 3.3: Bistatic scattering width of a circular chiral cylinder in free-space and when it is placed above a (DHS).

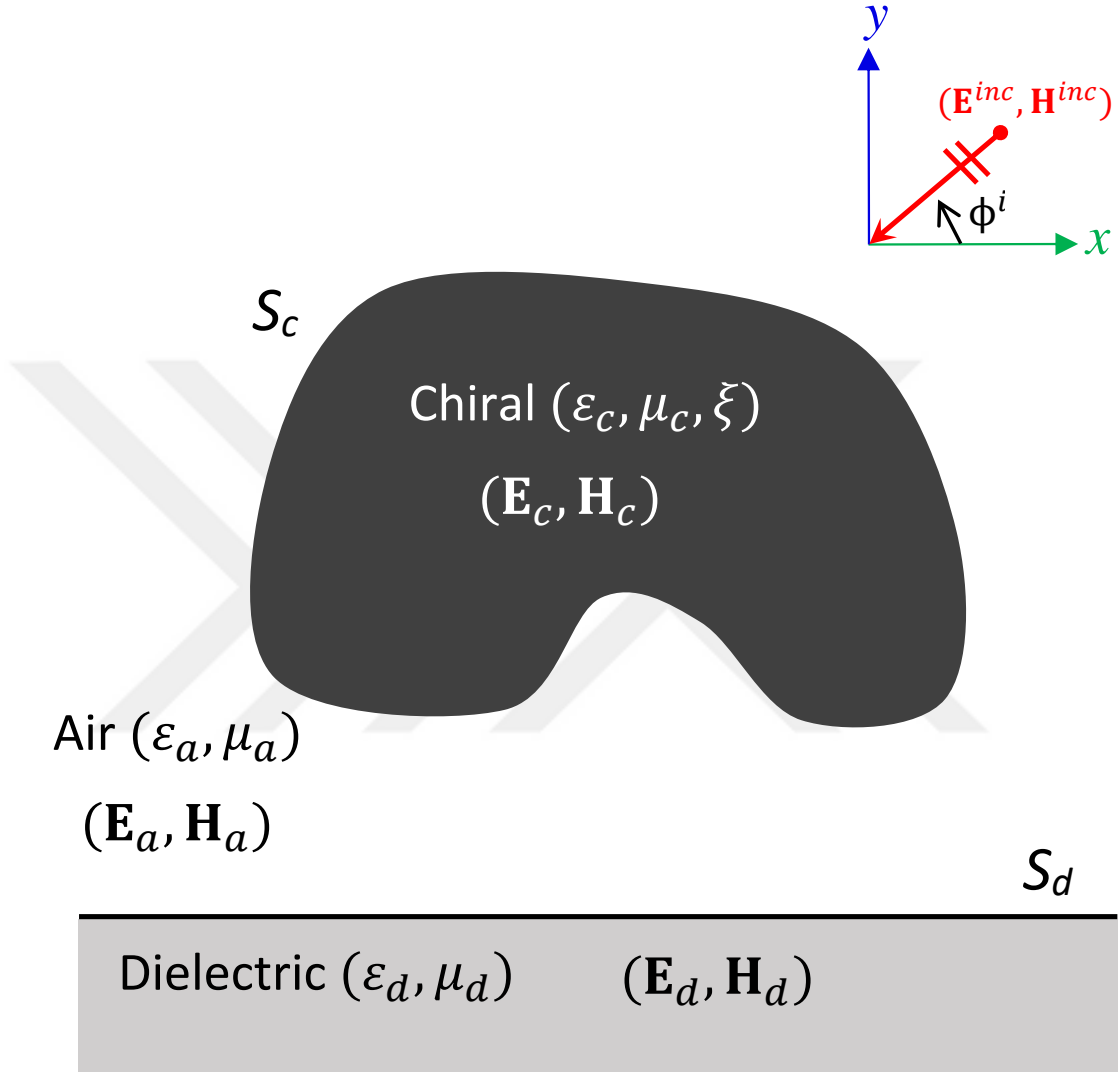


Figure 3.4: The original problem: A 2-D chiral cylinder of arbitrary cross-section above a dielectric half-space excited by a plane wave.

surface  $S_c$ . These currents are given by,

$$\mathbf{J}_c = \mathbf{n}_c \times \mathbf{H}_a^{c+} \quad (3.1)$$

$$\mathbf{J}_d = \mathbf{n}_d \times \mathbf{H}_a^{d+} \quad (3.2)$$

$$\mathbf{M}_c = -\mathbf{n}_c \times \mathbf{E}_a^{c+} \quad (3.3)$$

$$\mathbf{M}_d = -\mathbf{n}_d \times \mathbf{E}_a^{d+} \quad (3.4)$$

where  $\mathbf{n}_c$  and  $\mathbf{n}_d$ , respectively, are the unit normal vectors pointing outwards from

the surfaces  $S_c$  and  $S_d$  as shown in Fig. 3.5.  $(\mathbf{E}_a^{c+}, \mathbf{H}_a^{c+})$  show the total field just outside  $S_c$  in Fig. 3.5 and Fig. 3.4. Similarly,  $(\mathbf{E}_a^{d+}, \mathbf{H}_a^{d+})$  represent the field just outside  $S_d$  in Fig. 3.5 and Fig. 3.4.

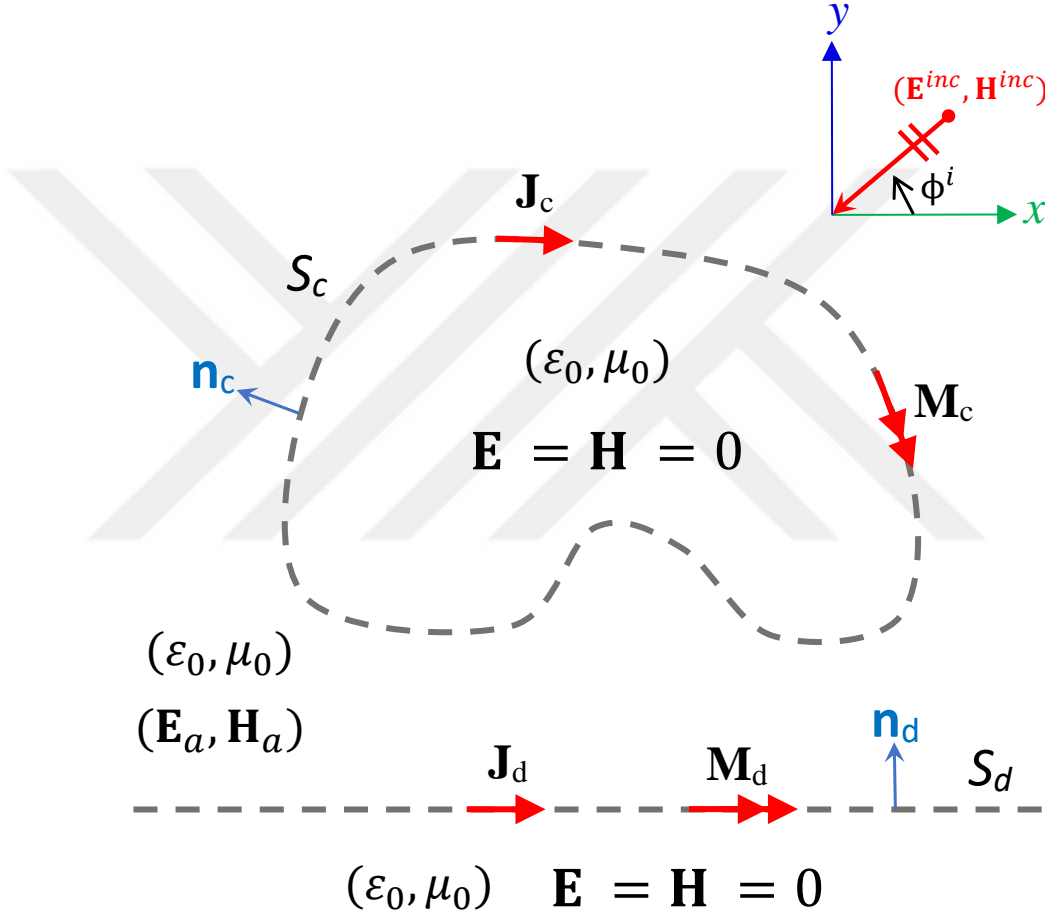


Figure 3.5: External equivalence for the the original problem of Fig. 3.4

These currents reside on  $S_c$  and  $S_d$ , and radiate into the unbounded external medium  $(\epsilon_0, \mu_0)$ . This field plus the incident field is equal to the total field  $(\mathbf{E}_a, \mathbf{H}_a)$  at any point above  $S_d$  and outside  $S_c$  of Fig. 3.5 and Fig. 3.4. That is,

$$\mathbf{E}_a = \mathbf{E}^{inc} + \mathbf{E}^a(\mathbf{J}_c, \mathbf{M}_c) + \mathbf{E}^a(\mathbf{J}_d, \mathbf{M}_d) \quad (3.5)$$

where superscript 'a' is used to remind us that the four equivalent surface currents are radiating in air  $(\epsilon_0, \mu_0)$ .

On the other hand, the incident field plus the field radiated by these four currents is equal to zero at any point inside  $S_c$  and  $S_d$  as shown in Fig. 3.5. This would be possible if,

$$[\mathbf{E}^{inc} + \mathbf{E}^a(\mathbf{J}_c, \mathbf{M}_c) + \mathbf{E}^a(\mathbf{J}_d, \mathbf{M}_d)]_{tan} = 0 \quad \text{on } S_c^- \quad (3.6)$$

$$[\mathbf{E}^{inc} + \mathbf{E}^a(\mathbf{J}_c, \mathbf{M}_c) + \mathbf{E}^a(\mathbf{J}_d, \mathbf{M}_d)]_{tan} = 0 \quad \text{on } S_d^- \quad (3.7)$$

where the subscript *tan* denotes the tangential component,  $S_c^-$  is the surface just inside  $S_c$ , and  $S_d^-$  is the surface just below  $S_d$ . Obviously similar equations apply for the magnetic field. In other words, one can replace  $\mathbf{E}$  with  $\mathbf{H}$  in the above three equations.

Figure 3.6 shows an equivalent problem for the dielectric half-space of Fig. 3.4. The incident field is not present here and the whole space is characterized by

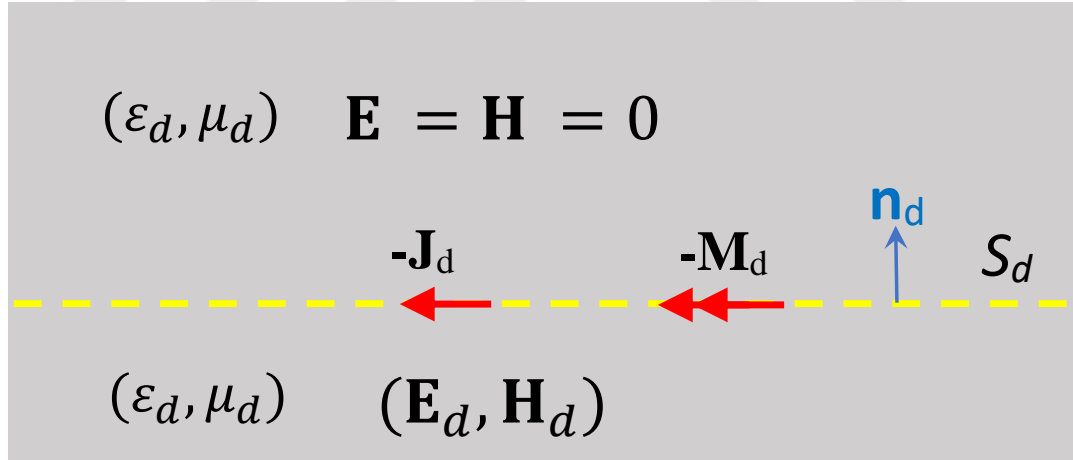


Figure 3.6: Internal equivalence for the dielectric half-space of the original problem in Fig. 3.4.

$(\epsilon_d, \mu_d)$ . In Fig. 3.6, the total field  $(\mathbf{E}_d, \mathbf{H}_d)$  at any point below the surface  $S_d$ , is assumed to be the same as the field at the same point of Fig. 3.4. This field is produced by the surface currents  $-\mathbf{J}_d$  and  $-\mathbf{M}_d$  residing on the surface  $S_d$  and radiating in the unbounded medium  $(\epsilon_d, \mu_d)$ . That is, at any point below the surface  $S_d$  in Fig. 3.6 and Fig. 3.4,

$$\mathbf{E}_d = \mathbf{E}^d(-\mathbf{J}_d, -\mathbf{M}_d) \quad (3.8)$$

where the superscript ‘d’ is used to remind us that the sources  $-\mathbf{J}_d$  and  $-\mathbf{M}_d$  radiate in the unbounded dielectric medium  $(\epsilon_d, \mu_d)$ .

In Fig. 3.6, the total field is zero at any point above the surface  $S_d$ . This would be possible if,

$$[\mathbf{E}^d(-\mathbf{J}_d, -\mathbf{M}_d)]_{tan} = 0 \quad \text{on } S_d^+ \quad (3.9)$$

where  $S_d^+$  represent the surface just above  $S_d$ . Obviously, similar equations apply for the magnetic field.

Finally to find the field  $(\mathbf{E}_c, \mathbf{H}_c)$  inside  $S_c$  of Fig. 3.4, we consider the equivalent problem shown in Fig. 3.7. Here, the surface currents  $-\mathbf{J}_c$  and  $-\mathbf{M}_c$  are placed on the fictitious surface  $S_c$  and are radiating in the unbounded chiral medium  $(\epsilon_c, \mu_c, \xi)$ . At any point inside  $S_c$  the field radiated by  $-\mathbf{J}_c$  and  $-\mathbf{M}_c$  is the same as the field  $\mathbf{E}_c$  and  $\mathbf{H}_c$  in Fig. 3.4. At such a point,

$$\mathbf{E}_c = \mathbf{E}^c(-\mathbf{J}_c, -\mathbf{M}_c) \quad (3.10)$$

where the superscript ‘c’ is used to remind us that the sources  $-\mathbf{J}_c$  and  $-\mathbf{M}_c$  radiate in the unbounded chiral medium  $(\epsilon_c, \mu_c, \xi)$ . At any point outside  $S_c$  the field radiated by these two currents is zero as shown in Fig. 3.7. This would be possible if,

$$[\mathbf{E}^c(-\mathbf{J}_c, -\mathbf{M}_c)]_{tan} = 0 \quad \text{on } S_c^+ \quad (3.11)$$

Obviously, similar equations apply for the magnetic field.

Equations (3.6), (3.7), (3.9), and (3.11) represent four coupled integral equations for the four unknown surface currents. These equations are in terms of the electric field, therefore they are known as the Electric Field Integral Equations (EFIE) for the problem at hand. Obviously, if  $\mathbf{E}$  is replaced by  $\mathbf{H}$  in these four equations, one would get the Magnetic Field Integral Equations (HFIE).

In this work, we will use EFIE, which is an exact and accurate representation of our problem. However, we cannot solve these equations by conventional MoM because the domain of (3.7) and (3.9) is infinite. Therefore, perturbation method will be used to replace some of the above equations with approximate ones. This is explained in the next section.



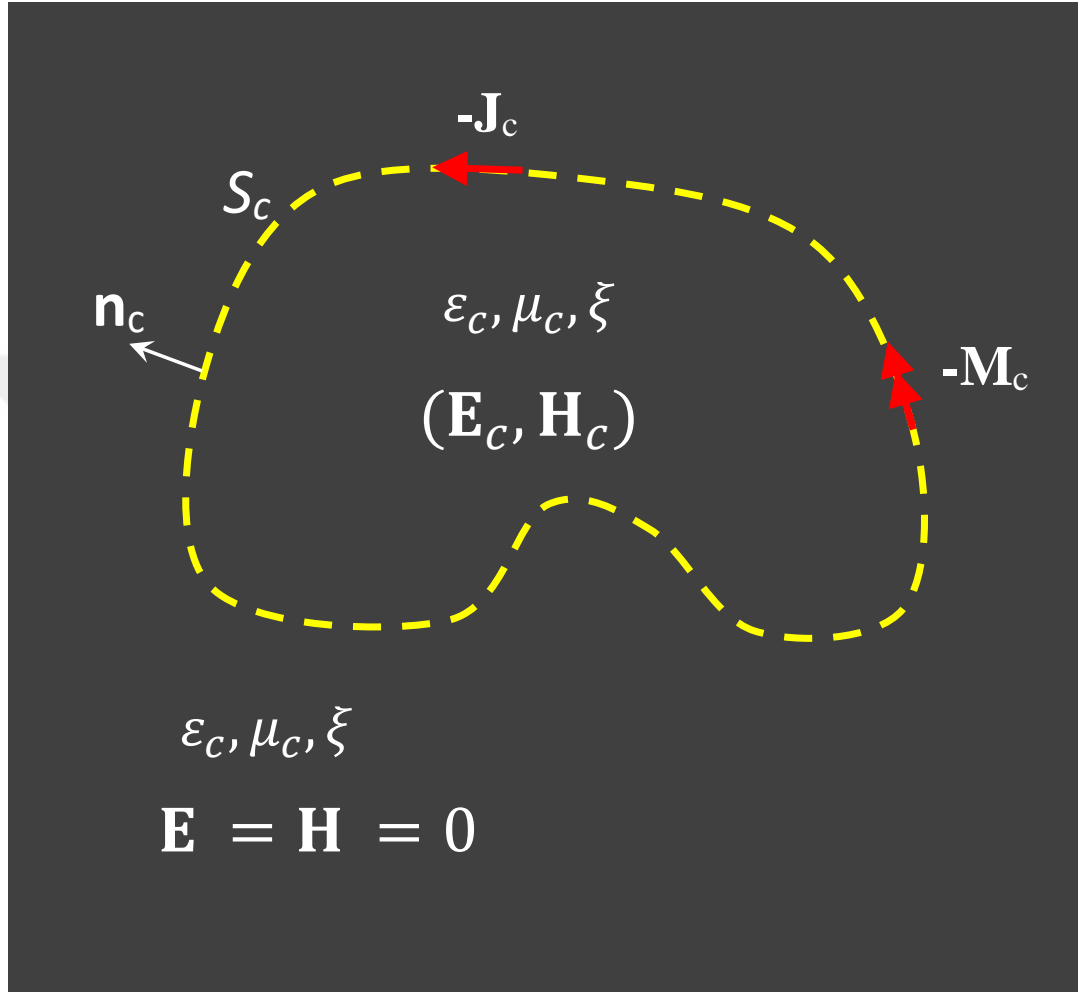


Figure 3.7: Internal equivalence for the chiral cylinder of the original problem in Fig. 3.4.

### 3.3 Application of The Perturbation Method

Consider the problem shown in Fig. 3.8. This is the same problem as the original problem of Fig. 1, except that the chiral cylinder is removed and the same half-space  $(\epsilon_d, \mu_d)$  is illuminated by the same plane wave  $(\mathbf{E}^{inc}, \mathbf{H}^{inc})$ .

The total field above  $S_d$  in Fig. 3.8 is represented by  $(\mathbf{E}_1, \mathbf{H}_1)$ . This field is the sum of the incident and the reflected field. Similarly, the total field below  $S_d$  in Fig. 3.8 is represented by  $(\mathbf{E}_2, \mathbf{H}_2)$ . This is the field transmitted into the dielectric region.

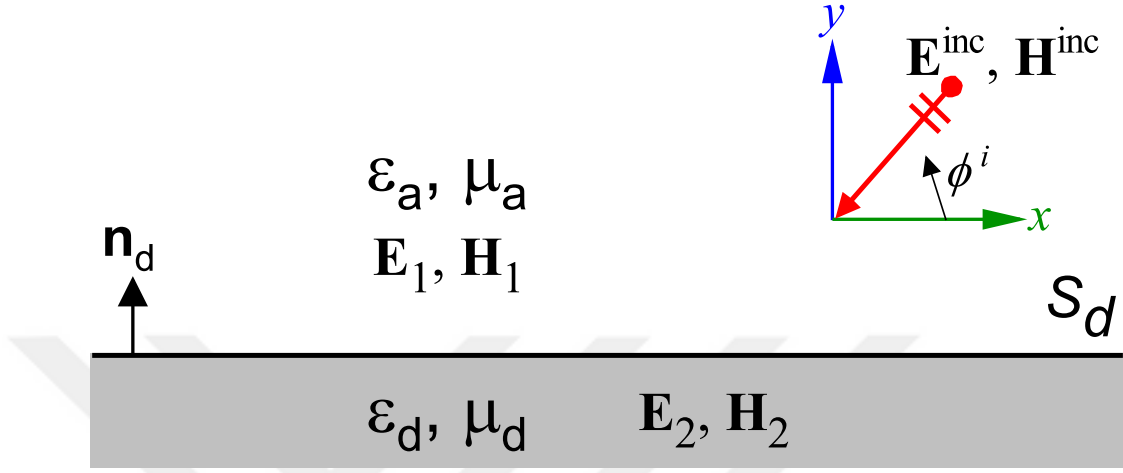


Figure 3.8: An auxiliary problem for the original problem of Fig. 3.4.

Figure 3.9 shows an equivalent problem for Fig. 3.8 for the region above  $S_d$ . At any point above  $S_d$  in Fig. 3.9 (or Fig. 3.8) the total field is given by,

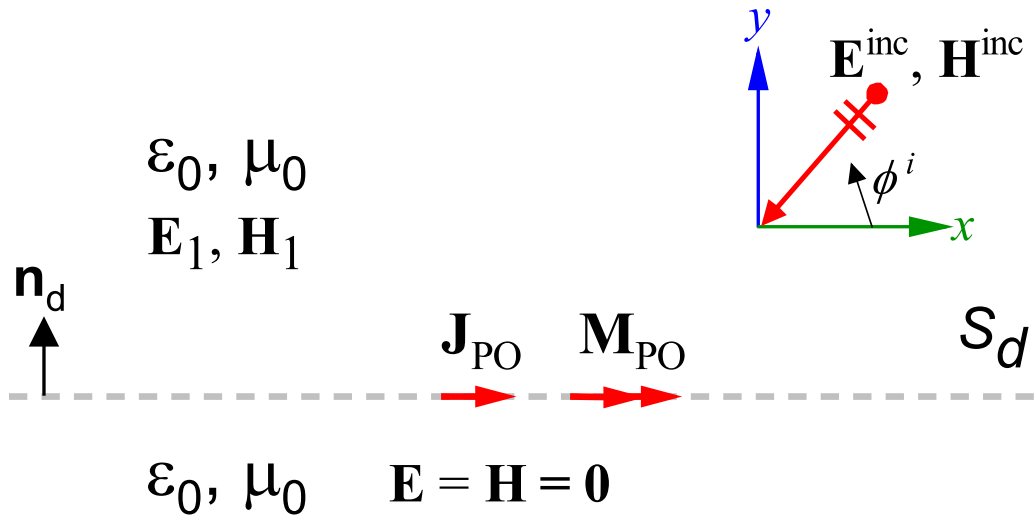


Figure 3.9: External equivalence for the auxiliary problem of Fig. 3.8.

$$\mathbf{E}_1 = \mathbf{E}^{inc} + \mathbf{E}^a(\mathbf{J}_{PO}, \mathbf{M}_{PO}) \quad (3.12)$$

where  $(\mathbf{J}_{PO}, \mathbf{M}_{PO})$  are the physical optic currents and are defined by,

$$\mathbf{J}_{PO} = \mathbf{n}_d \times \mathbf{H}_1^+ \quad (3.13)$$

$$\mathbf{M}_{PO} = \mathbf{E}_1^+ \times \mathbf{n}_d \quad (3.14)$$

Here,  $\mathbf{n}_d$  is the unit normal vector pointing upwards from  $S_d$ , and  $(\mathbf{E}_1^+, \mathbf{H}_1^+)$  denote the total field just above the interface in Fig. 3.8 (or Fig. 3.9). The superscript ‘a’ is used on the last term of (3.12) to remind us that the physical optic currents are radiating in the unbounded medium characterized by  $(\epsilon_a, \mu_a)$  which are taken to be  $(\epsilon_0, \mu_0)$ . The second term in (3.12) is equal to the reflected field in Fig. 3.8. From Fig. 3.9 we see that we must have,

$$\mathbf{E}_{tan}^{inc} + \mathbf{E}_{tan}^a(\mathbf{J}_{PO}, \mathbf{M}_{PO}) = 0 \quad \text{on } S_d^- \quad (3.15)$$

where,  $S_d^-$  is the surface just below  $S_d$ .

Figure 3.10 shows an equivalent problem for Fig. 3.8 for the region below  $S_d$ . At any point below  $S_d$  in Fig. 3.10 (or Fig. 3.8) the total field is given by,

$$\mathbf{E}_2 = -\mathbf{E}^d(\mathbf{J}_{PO}, \mathbf{M}_{PO}) \quad (3.16)$$

The superscript ‘d’ is used here to remind us that the physical optic currents are radiating in the unbounded medium characterized by  $(\epsilon_d, \mu_d)$ . The field in (3.16 )

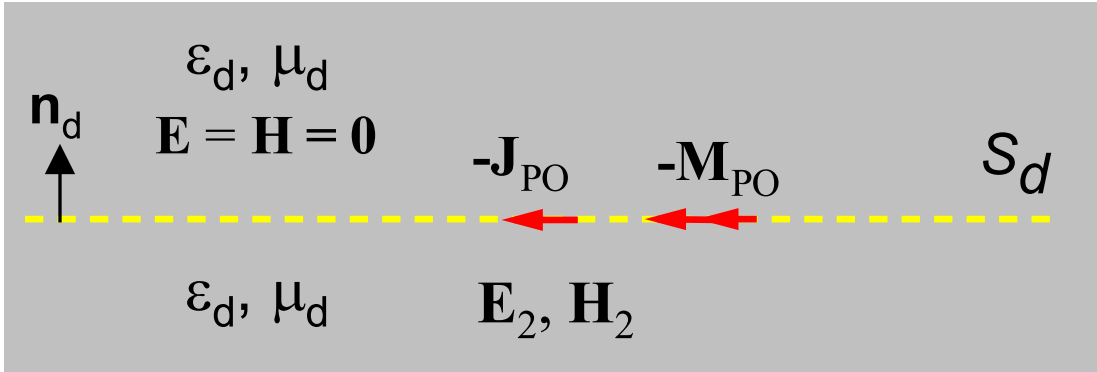


Figure 3.10: Internal equivalence for the auxiliary problem of Fig. 3.8.

is the transmitted field into the dielectric region of Fig. 3.8. From Fig. 3.10 we conclude that we must have,

$$\mathbf{E}_{tan}^d(\mathbf{J}_{PO}, \mathbf{M}_{PO}) = 0 \quad \text{on } S_d^+ \quad (3.17)$$

where,  $S_d^+$  is the surface just above  $S_d$ . Note that the reflected field denoted by  $\mathbf{E}^a(\mathbf{J}_{PO}, \mathbf{M}_{PO})$  and the transmitted field denoted by  $-\mathbf{E}^d(\mathbf{J}_{PO}, \mathbf{M}_{PO})$  can be found exactly.

Now let us go back to our original problem of Fig. 3.4, and divide the surface  $S_d$  into two parts as shown in Fig. 3.11.  $S_{dn}$  is that part of  $S_d$  which is close to the chiral surface  $S_c$ . The subscript ‘n’ here is used for ‘near’. As shown in Fig. 3.11, the rest of the surface  $S_d$  is denoted by  $S_{df}$ . The subscript ‘f’ here is used for ‘far’. The equivalent surface currents  $(\mathbf{J}_d, \mathbf{M}_d)$  of Fig. 3.5 are now divided into two parts  $(\mathbf{J}_d^n, \mathbf{M}_d^n)$  and  $(\mathbf{J}_d^f, \mathbf{M}_d^f)$  as shown in Fig. 3.12. In other words,  $(\mathbf{J}_d, \mathbf{M}_d)$  is denoted by  $(\mathbf{J}_d^n, \mathbf{M}_d^n)$  on  $S_{dn}$  and by  $(\mathbf{J}_d^f, \mathbf{M}_d^f)$  on  $S_{df}$ . Then, (3.5) can be rewritten as follows.

$$\mathbf{E}_a = \mathbf{E}^{inc} + \mathbf{E}^a(\mathbf{J}_c, \mathbf{M}_c) + \mathbf{E}^a(\mathbf{J}_d^n, \mathbf{M}_d^n) + \mathbf{E}^a(\mathbf{J}_d^f, \mathbf{M}_d^f) \quad (3.18)$$

It is reasonable to assume that the total field at any point just above the surface  $S_{df}$  in Fig. 3.11 would be approximately equal to the total field at the same point of Fig. 3.8 (and Fig. 3.9). Then using the definitions in (3.1)-(3.4), (3.13), and (3.14) one can write,

$$\mathbf{J}_d^f \cong \mathbf{J}_{PO}^f \quad (3.19)$$

$$\mathbf{M}_d^f \cong \mathbf{M}_{PO}^f \quad (3.20)$$

where  $(\mathbf{J}_{PO}^f, \mathbf{M}_{PO}^f)$  are known physical optic currents on  $S_{df}$ .

The total field at a point on  $S_{dn}$  of Fig. 3.11 (and Fig. 3.12) will be different than the total field at the same point of Fig. 3.8 (and Fig. 3.9). The difference will be denoted as the perturbation field. Then, one can write  $\mathbf{J}_d^n$  and  $\mathbf{M}_d^n$  on  $S_{dn}$  as follows.

$$\mathbf{J}_d^n = \mathbf{J}_{PO}^n + \mathbf{J}_p \quad (3.21)$$

$$\mathbf{M}_d^n = \mathbf{M}_{PO}^n + \mathbf{M}_p \quad (3.22)$$

Here,  $(\mathbf{J}_{PO}^n, \mathbf{M}_{PO}^n)$  represent the known physical optic currents on  $S_{dn}$  and  $(\mathbf{J}_p, \mathbf{M}_p)$  are unknown perturbation currents on  $S_{dn}$ . Then, (3.5) can be approximately written as,

$$\mathbf{E}_a = \mathbf{E}^{inc} + \mathbf{E}^a(\mathbf{J}_c, \mathbf{M}_c) + \mathbf{E}^a(\mathbf{J}_p, \mathbf{M}_p) + \mathbf{E}^a(\mathbf{J}_{PO}^n, \mathbf{M}_{PO}^n) + \mathbf{E}^a(\mathbf{J}_{PO}^f, \mathbf{M}_{PO}^f) \quad (3.23)$$

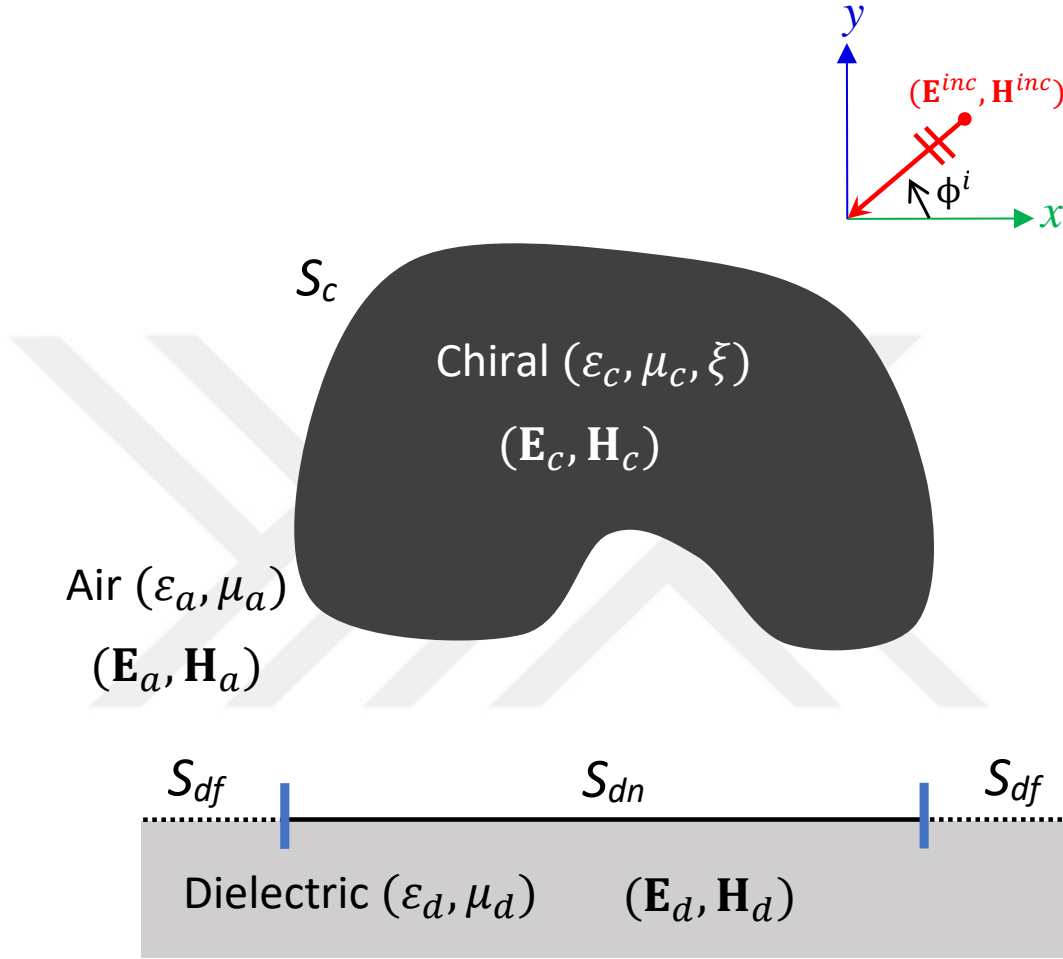


Figure 3.11: A different way of representing the original problem. The surface of the dielectric half-space is divided into near ( $S_{dn}$ ) and far ( $S_{df}$ ) regions.

Combining the last two terms, (3.23) can be rewritten as,

$$\mathbf{E}_a = \mathbf{E}^{inc} + \mathbf{E}^a(\mathbf{J}_c, \mathbf{M}_c) + \mathbf{E}^a(\mathbf{J}_p, \mathbf{M}_p) + \mathbf{E}^a(\mathbf{J}_{PO}, \mathbf{M}_{PO}) \quad (3.24)$$

Equation (3.6) requires that the tangential component of  $\mathbf{E}_a$  must be zero on  $S_c^-$ . Then, using (3.24), (3.6) can be approximately written as,

$$\mathbf{E}_{tan}^a(\mathbf{J}_c, \mathbf{M}_c) + \mathbf{E}_{tan}^a(\mathbf{J}_p, \mathbf{M}_p) = -\mathbf{E}_{tan}^{inc} - \mathbf{E}_{tan}^a(\mathbf{J}_{PO}, \mathbf{M}_{PO}) \quad \text{on } S_c^- \quad (3.25)$$

Note that the right hand side of (3.25) is the negative of the total field that would exist on  $S_c$  if the chiral cylinder were removed. That is, if chiral material inside  $S_c$  was replaced by air. This field is known and it is equal to the negative of the total field  $\mathbf{E}_1$  above  $S_d$  in Fig. 3.8 (or Fig. 3.9).

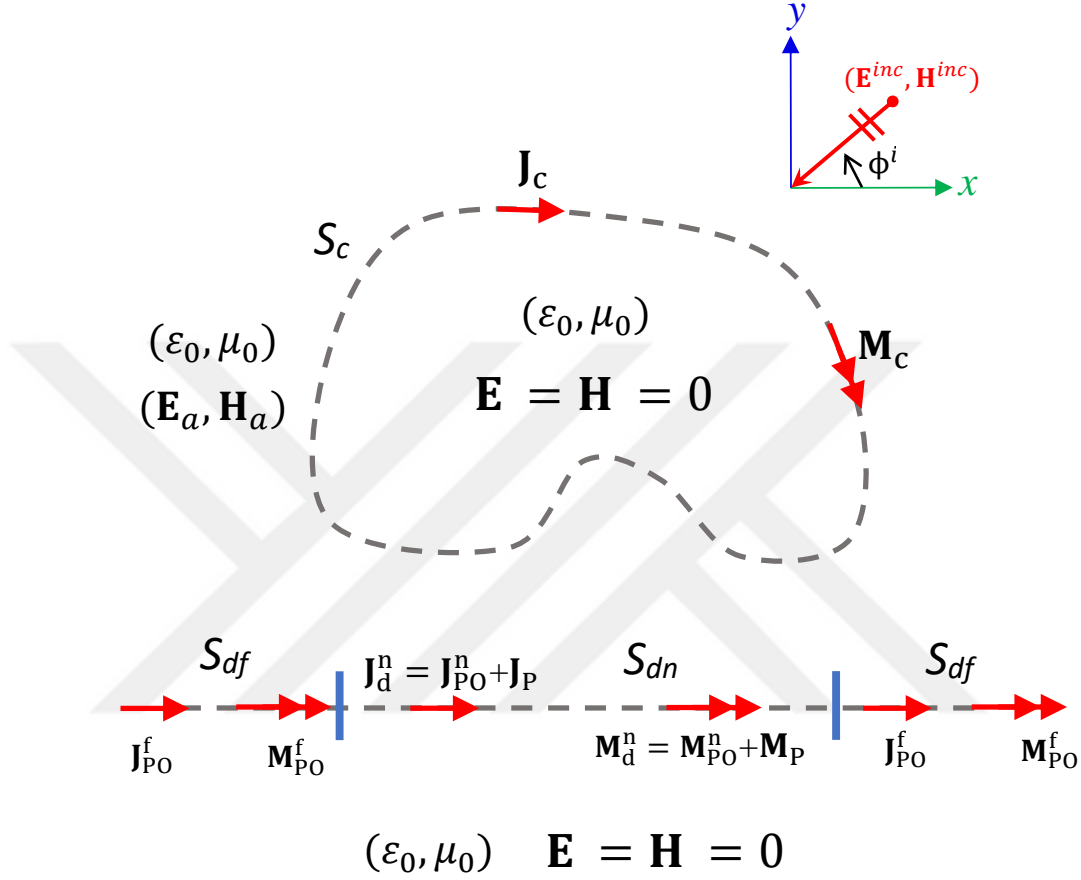


Figure 3.12: External equivalent problem, showing the excitation and the impressed currents.

Equation (3.7) requires that the tangential component of  $\mathbf{E}_a$  should be zero all over  $S_d^-$ . Since we assume that this field is known on  $S_{df}$ , we should enforce (3.7) on  $S_{dn}$  only. Then, (3.7) can be approximately written as,

$$\mathbf{E}_{tan}^a(\mathbf{J}_c, \mathbf{M}_c) + \mathbf{E}_{tan}^a(\mathbf{J}_p, \mathbf{M}_p) = -\mathbf{E}_{tan}^{inc} - \mathbf{E}_{tan}^a(\mathbf{J}_{PO}, \mathbf{M}_{PO}) \quad \text{on } S_{dn}^- \quad (3.26)$$

Using (3.15) we can see that the right hand side of (3.26) must be zero. Hence, (3.7) is approximately rewritten as follows.

$$\mathbf{E}_{tan}^a(\mathbf{J}_c, \mathbf{M}_c) + \mathbf{E}_{tan}^a(\mathbf{J}_p, \mathbf{M}_p) = 0 \quad \text{on } S_{dn}^- \quad (3.27)$$

Using similar reasoning, (3.8) can be written as,

$$\mathbf{E}_d = \mathbf{E}^d(-\mathbf{J}_p, -\mathbf{M}_p) + \mathbf{E}^d(-\mathbf{J}_{PO}, -\mathbf{M}_{PO}) \quad (3.28)$$

Then (3.9) can be approximated as follows,

$$\mathbf{E}_{tan}^d(-\mathbf{J}_p, -\mathbf{M}_p) = -\mathbf{E}_{tan}^d(\mathbf{J}_{PO}, \mathbf{M}_{PO}) \quad \text{on } S_{dn}^+ \quad (3.29)$$

Using (3.17) we see that the right hand side of (3.29) is zero. Then, (3.29) is approximately rewritten as follows.

$$\mathbf{E}_{tan}^d(-\mathbf{J}_p, -\mathbf{M}_p) = 0 \quad \text{on } S_{dn}^+ \quad (3.30)$$

In summary, the perturbation technique was used to approximate three of the original integral equations (3.6), (3.7), and (3.9) by (3.25), (3.27), and (3.30). We kept the original equation (3.11) as it is. In the next section, we will show how to use MoM to solve this new set of integral equations consisting of (3.11), (3.25), (3.27), and (3.30).

### 3.4 Application of Moments Method

Making use of the perturbation method, the unknown currents on the interface have been localized to a finite region ( $S_{dn}$ ) as opposed to infinite region  $S_d$  in the original problem of Fig. 3.4. Now, the final four equations (3.11), (3.25), (3.27), and (3.30) are solved numerically by MoM. In order to apply MoM, the two surfaces  $S_c$  and  $S_{dn}$  are discretized into  $N_1$  and  $N_2$  segments, respectively, as shown in Fig. 3.13. The unknown currents are approximated by pulse expansion functions as given below,

$$\mathbf{J}_c(r') = \hat{z} \sum_{n=1}^{N_1} a_n P_n^c + \sum_{n=1}^{N_1} c_n \hat{l}_n^c P_n^c \quad (3.31)$$

$$\mathbf{M}_c(r') = \hat{z} \sum_{n=1}^{N_1} e_n P_n^c + \sum_{n=1}^{N_1} g_n \hat{l}_n^c P_n^c \quad (3.32)$$

$$\mathbf{J}_p(r') = \hat{z} \sum_{n=N_1+1}^{N_1+N_2} b_n P_n^d + \sum_{n=N_1+1}^{N_1+N_2} d_n \hat{l}_n^d P_n^d \quad (3.33)$$

$$\mathbf{M}_p(r') = \hat{z} \sum_{n=N_1+1}^{N_1+N_2} f_n P_n^d + \sum_{n=N_1+1}^{N_1+N_2} h_n \hat{l}_n^d P_n^d \quad (3.34)$$

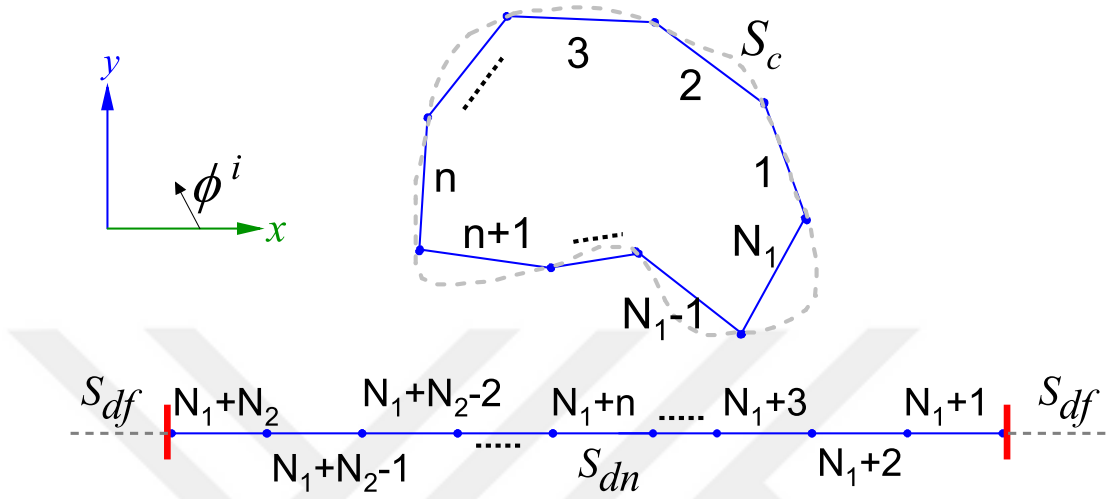


Figure 3.13: Discretization of the  $S_c$  and  $S_{dn}$  into  $N_1$  and  $N_2$  segments, respectively.

Here,  $a_n$  to  $h_n$  are the eight unknown expansion coefficients,  $\hat{z}$  denotes the unit vector in the longitudinal direction,  $\hat{l}_n^c$  represents the unit vector tangential to the  $n^{\text{th}}$  segment on the chiral cylinder ( $S_c$ ), and  $\hat{l}_n^d$  denotes the unit vector tangential to the  $n^{\text{th}}$  segment on the dielectric strip ( $S_{dn}$ ). The pulse function  $P_n^c$  is unity if it is on the  $n^{\text{th}}$  segment of  $S_c$ , otherwise zero. Similarly, the pulse function  $P_n^d$  is unity on the  $n^{\text{th}}$  segment of  $S_{dn}$  and zero otherwise. The unknowns can be computed by testing the final four integral equations using the approximate Galerkin's method as in [5]. Then the testing could be considered as a weighted point matching technique.

The result can be written in matrix form as shown in (3.35). The square matrix on the left is called the moment matrix. It consists of 64 sub-matrices. The size of the square moment matrix is  $4N \times 4N$ , where  $N = N_1 + N_2$ . The  $4N \times 1$  column matrix on the left contains the unknown expansion coefficients, and the  $4N \times 1$  column matrix on the right is called the excitation vector.



$$\begin{pmatrix}
Z_c J_Z^c \text{ext} & Z_c J_Z^d \text{ext} & Z_c J_L^c \text{ext} & Z_c J_L^d \text{ext} & Z_c M_Z^c \text{ext} & Z_c M_Z^d \text{ext} & Z_c M_L^c \text{ext} & Z_c M_L^d \text{ext} \\
Z_d J_Z^c \text{ext} & Z_d J_Z^d \text{ext} & Z_d J_L^c \text{ext} & Z_d J_L^d \text{ext} & Z_d M_Z^c \text{ext} & Z_d M_Z^d \text{ext} & Z_d M_L^c \text{ext} & Z_d M_L^d \text{ext} \\
L_c J_Z^c \text{ext} & L_c J_Z^d \text{ext} & L_c J_L^c \text{ext} & L_c J_L^d \text{ext} & L_c M_Z^c \text{ext} & L_c M_Z^d \text{ext} & L_c M_L^c \text{ext} & L_c M_L^d \text{ext} \\
L_d J_Z^c \text{ext} & L_d J_Z^d \text{ext} & L_d J_L^c \text{ext} & L_d J_L^d \text{ext} & L_d M_Z^c \text{ext} & L_d M_Z^d \text{ext} & L_d M_L^c \text{ext} & L_d M_L^d \text{ext} \\
Z_c J_Z^c \text{in1} & 0 & Z_c J_L^c \text{in1} & 0 & Z_c M_Z^c \text{in1} & 0 & Z_c M_L^c \text{in1} & 0 \\
L_c J_Z^c \text{in1} & 0 & L_c J_L^c \text{in1} & 0 & L_c M_Z^c \text{in1} & 0 & L_c M_L^c \text{in1} & 0 \\
0 & Z_d J_Z^d \text{in2} & 0 & Z_d J_L^d \text{in2} & 0 & Z_d M_Z^d \text{in2} & 0 & Z_d M_L^d \text{in2} \\
0 & L_d J_Z^d \text{in2} & 0 & L_d J_L^d \text{in2} & 0 & L_d M_Z^d \text{in2} & 0 & L_d M_L^d \text{in2}
\end{pmatrix}
\begin{pmatrix}
a_n \\
b_n \\
c_n \\
d_n \\
e_n \\
f_n \\
g_n \\
h_n
\end{pmatrix}
=
\begin{pmatrix}
-Z_{\text{Total}} \text{ on } S_c^- \\
0 \text{ on } S_d^- \\
-L_{\text{Total}} \text{ on } S_c^- \\
0 \text{ on } S_d^- \\
0 \text{ on } S_c^+ \\
0 \text{ on } S_c^+ \\
0 \text{ on } S_d^+ \\
0 \text{ on } S_d^+
\end{pmatrix}
\tag{3.35}$$

The notation used for the sub-matrices is as follows. Consider the block matrix  $Z_c J_Z^c \text{ext}$ , then the notation used is:

- **The first capital letter**, represents the computed electric field component: ‘Z’ for  $z$ -component and ‘L’ for the lateral component.
- **The first subscript**, represents the surface on which the electric field is computed: ‘c’ for the chiral surface  $S_c$  and ‘d’ for the dielectric strip  $S_{dn}$ .
- The second capital letter, shows the source of the computed field: ‘J’ for the electric current and ‘M’ for the magnetic current.
- **The second subscript**, shows the direction of the current source:  $z$ -directed ‘Z’ and lateral direction ‘L’
- **The Superscript**, represents the surface on which the current source is residing: ‘c’ for the chiral surface  $S_c$  and ‘d’ for the dielectric strip  $S_{dn}$ .
- **The last three lowercase letters**, represent the unbounded region in which the source current is radiating: ‘ext’ for external region  $(\epsilon_0, \mu_0)$ , ‘in1’ for the chiral region  $(\epsilon_c, \mu_c, \xi)$ , and ‘in2’ for the dielectric region  $(\epsilon_d, \mu_d)$ .

For example, the  $(m, n)^{th}$  element of the  $N_1 \times N_1$  sub-matrix  $Z_c J_Z^c \text{ext}(m, n)$  is the  $z$ -component (Z) of the electric field produced on the  $m^{th}$  segment of the chiral surface  $S_c$  (c) due to a  $z$ -directed (z) electric current (J) residing on the  $n^{th}$  segment of the chiral surface (c) when this current radiates in the external (ext) medium  $(\epsilon_a = \epsilon_0, \mu_a = \mu_0)$ .

Similarly, the element in the  $m^{th}$  row and  $n^{th}$  column of the  $N_2 \times N_1$  sub-matrix  $L_d M_L^c \text{ext}$  is the lateral (L) component of electric field produced on the  $m^{th}$  segment of the dielectric half-space  $S_{dn}$  (d) due to a lateral (L) magnetic current (M) located on the  $n^{th}$  segment of the chiral surface  $S_c$  (c) when this current radiates in the unbounded external (ext) medium  $(\epsilon_a = \epsilon_0, \mu_a = \mu_0)$ .

For the internal medium of the cylinder, the  $(m, n)^{th}$  element of the sub-matrix  $Z_c M_L^c \text{in1}$  is the  $z$ -component of electric field produced on the  $m^{th}$  segment of the

chiral surface  $S_c$  (c) due to a lateral (L) magnetic current (M) located on the  $n^{th}$  segment of the chiral surface (c) when this current radiates in the unbounded internal (in1) medium  $(\epsilon_c, \mu_c, \xi)$ .

Finally, for the internal medium of the dielectric half-space, the  $(m, n)^{th}$  element of the  $N_2 \times N_2$  sub-matrix  $L_d M_Z^d$  is the lateral (L) component of electric field produced on the  $m^{th}$  segment of the dielectric half-space  $S_{dn}$  (d) due to a  $z$ -directed (z) magnetic current (M) located on the  $n^{th}$  segment of the dielectric half-space (d) when this current radiates in the unbounded internal (in2) medium  $(\epsilon_d, \mu_d)$ .

The  $m^{th}$  element of the  $N \times 1$  sub-matrix  $-Z_{Total}$  on the right-hand side of (3.35) is equal to the negative of the  $z$ -component of the incident field plus the reflected field on the  $m^{th}$  segment of  $S_c$ . Similarly, the  $m^{th}$  element of the sub-matrix  $-L_{Total}$  represents negative of the lateral component of the total field on the  $m^{th}$  segment of  $S_c$ .

For computing these elements the method given in [49] is followed. For the sake of completeness one typical element is discussed here. Consider an element of  $Z_c J_Z^c \text{ext}(m, n)$ . This element is given by the following symmetric product,

$$Z_c J_Z^c \text{ext}(m, n) = \langle \mathbf{J}_Z^{mc}, \mathbf{E}_{ext}(\mathbf{J}_Z^{nc}) \rangle \quad (3.36)$$

The above equation gives the element in the  $m^{th}$  row and  $n^{th}$  column of the sub-matrix  $Z_c J_Z^c \text{ext}$ . It is the symmetric product between  $\mathbf{J}_Z^m$  with the electric field produced by  $\mathbf{J}_Z^n$  when it radiates in the unbounded external medium. The symmetric product is given by,

$$\langle \mathbf{J}_Z^{mc}, \mathbf{E}_{ext}(\mathbf{J}_Z^{nc}) \rangle = \int_{c^{mc}} \mathbf{J}_Z^{mc} \cdot \mathbf{E}_{ext}(\mathbf{J}_Z^{nc}) dl \quad (3.37)$$

Since the testing and the expansion functions are same, this looks like a Galerkin's method, however, we are using point matching so the above integrand is approximated by its value at the center of the  $m^{th}$  segment  $c^{mc}$  of the chiral surface as follows,

$$\langle \mathbf{J}_Z^{mc}, \mathbf{E}_{ext}(\mathbf{J}_Z^{nc}) \rangle \equiv \mathbf{E}_{ext}^m(\mathbf{J}_Z^{nc}) \cdot \hat{z} l_{mc} \quad (3.38)$$

$\mathbf{E}_{ext}^m(\mathbf{J}_Z^{nc})$  is the electric field at the center of  $c^{mc}$  segment on  $S_c$  produced by  $\mathbf{J}_Z^{nc}$  electric current residing on the chiral surface  $S_c$  when this current radiates in the

free-space ( $\epsilon_a = \epsilon_0$ ,  $\mu_a = \mu_0$ ),  $l_{mc}$  is the length of the  $m^{\text{th}}$  segment of the chiral surface  $S_c$ . Hence,  $Z_c J_Z^{\text{cext}}$  is given by,

$$Z_c J_Z^{\text{cext}}(m, n) = -\frac{\eta_a k_a l_{mc}}{4} \int_{c^{nc}} H_0^{(2)}(k_a |\boldsymbol{\rho}^{mc} - \boldsymbol{\rho}'|) dl' \quad (3.39)$$

where  $\boldsymbol{\rho}^{mc}$  is the position vector to the center of the  $m^{\text{th}}$  segment,  $H_0^{(2)}$  is the zeroth order Hankel function of the second kind and  $c^{nc}$  is the  $n^{\text{th}}$  segment of the cross-section of surface  $S_c$  in the  $xy$ -plane. Computation of the matrix elements is given in Appendix B.

The constitutive relations used in this work are as follows [4], [49],

$$\mathbf{D} = \epsilon_c \mathbf{E} - j\xi \mathbf{B} \quad (3.40)$$

$$\mathbf{H} = \frac{1}{\mu_c} \mathbf{B} - j\xi \mathbf{E} \quad (3.41)$$

where,  $\epsilon_c$ ,  $\mu_c$ , and  $\xi$  denote the permittivity, permeability, and chirality admittance of the chiral medium.

The electric field due to electric and magnetic surface currents ( $\mathbf{J}$ ,  $\mathbf{M}$ ) residing on a surface  $S$  and radiating into an unbounded chiral medium is given by [49].

$$\begin{aligned} \mathbf{E}(\mathbf{J}, \mathbf{M}) = & -\frac{\eta_c}{8} \int_C [h_1 H_0^{(2)}(h_1 R) + h_2 H_0^{(2)}(h_2 R) + \\ & \nabla \times H_0^{(2)}(h_1 R) - \nabla \times H_0^{(2)}(h_2 R)] \mathbf{J}(r') dl' \\ & - \frac{\eta_c}{8} \int_C [h_1^{-1} H_0^{(2)}(h_1 R) + h_2^{-1} H_0^{(2)}(h_2 R)] \nabla' \cdot \mathbf{J}(r') dl' \\ & + \frac{j}{8} \int_C [h_1 H_0^{(2)}(h_1 R) - h_2 H_0^{(2)}(h_2 R) + \nabla \times H_0^{(2)}(h_1 R) \\ & + \nabla \times H_0^{(2)}(h_2 R)] \mathbf{M}(r') dl' + \frac{j}{8} \int_C [h_1^{-1} H_0^{(2)}(h_1 R) \\ & - h_2^{-1} H_0^{(2)}(h_2 R)] \nabla' \cdot \mathbf{M}(r') dl' \quad (3.42) \end{aligned}$$

where,  $C$  denotes the contour of the surface in the  $xy$ -plane and  $R$  is the distance between the field and source point  $|\mathbf{r} - \mathbf{r}'|$ ,  $H_0^{(2)}$  is the Hankel function of zeroth

order and second kind,  $h_1$  and  $h_2$  represent the wave numbers given by,

$$h_1 = \omega\mu_c\xi + \sqrt{k^2 + (\omega\mu_c\xi)^2} \quad (3.43)$$

$$h_2 = -\omega\mu_c\xi + \sqrt{k^2 + (\omega\mu_c\xi)^2} \quad (3.44)$$

here,

$$k = \omega\sqrt{\mu_c\epsilon_c} \quad (3.45)$$

and the chiral wave impedance is given by,

$$\eta_c = \frac{\eta}{\sqrt{1 + (\eta\xi)^2}} \quad (3.46)$$

with

$$\eta = \sqrt{\mu_c/\epsilon_c} \quad (3.47)$$

If the unbounded medium in which the currents ( $\mathbf{J}$ ,  $\mathbf{M}$ ) are radiating is a regular dielectric ( $\epsilon$ ,  $\mu$ ), then (3.42) is valid with  $h_1 = h_2 = k = \omega\sqrt{\mu\epsilon}$  and  $\eta_c = \eta = \sqrt{\mu/\epsilon}$ .

Once, the unknown expansion coefficients  $a_n - h_n$  in (3.35) are computed, the co- and cross-polarized scattered fields in the  $\phi$ -direction can be easily computed as follows [49, 71],

$$\begin{aligned} \sigma_z(\phi) = \frac{k_a}{4} \left| \sum_{n=1}^{N_1} l_{nc} \left( a_n - \frac{g_n}{\eta_a} \hat{l}_n^c \cdot \hat{a}_\phi \right) e^{jk_a \rho^{nc} \cos(\phi - \phi^{nc})} \right. \\ \left. + \sum_{n=N_1+1}^{N_1+N_2} l_{nd} \left( b_n - \frac{h_n}{\eta_a} \hat{l}_n^d \cdot \hat{a}_\phi \right) e^{jk_a \rho^{nd} \cos(\phi - \phi^{nd})} \right|^2 \quad (3.48) \end{aligned}$$

$$\begin{aligned} \sigma_\phi(\phi) = \frac{k_a}{4} \left| \sum_{n=1}^{N_1} l_{nc} \left( \frac{e_n}{\eta_a} + c_n \hat{l}_n^c \cdot \hat{a}_\phi \right) e^{jk_a \rho^{nc} \cos(\phi - \phi^{nc})} \right. \\ \left. + \sum_{n=N_1+1}^{N_1+N_2} l_{nd} \left( \frac{f_n}{\eta_a} + d_n \hat{l}_n^d \cdot \hat{a}_\phi \right) e^{jk_a \rho^{nd} \cos(\phi - \phi^{nd})} \right|^2 \quad (3.49) \end{aligned}$$

where,  $\sigma$  denotes the bistatic radar scattering width,  $l_{nc}$  ( $l_{nd}$ ) is the length of the  $n^{\text{th}}$  segment on  $S_c$  ( $S_{dn}$ ),  $\hat{a}_\phi$  is the unit vector in the  $\phi$ -direction at the field point,

$\rho^{nc}$  ( $\rho^{nd}$ ) and  $\phi^{nc}$  ( $\phi^{nd}$ ) are the cylindrical coordinates of the center of the  $n^{th}$  segment on  $S_c$  ( $S_{dn}$ ),  $\eta_a$  is the free-space wave impedance, and  $k_a$  is the free-space wavenumber.

The next section presents numerical results and validation of the proposed method.



### 3.5 Numerical Results: Validation

Here, numerical results are presented for cylinder of arbitrary cross-section placed above a dielectric half-space. As mentioned in Sec. 3.2, MoM cannot be applied directly to the infinite interface. To overcome the problem, a region  $S_{dn}$  was assumed in the vicinity of the chiral cylinder which localized the unknowns to a finite region. For these numerical simulations, the perturbed region is assumed by a finite dielectric strip of width ‘w’. The perturbed currents on the dielectric strip are denoted by  $(\mathbf{J}_p, \mathbf{M}_p)$  and the currents on the chiral body above the strip (half-space) are represented by  $(\mathbf{J}_c, \mathbf{M}_c)$ . Each of the currents have a longitudinal ( $Z$ ) and a lateral ( $L$ ) component. The media for the selected problems is characterized by  $\mu_a = \mu_c = \mu_d = \mu_0$  and  $\epsilon_a = \epsilon_0$ , unless otherwise specified. Both, TM and TE excitations are treated here. In both cases, the setup is illuminated by a plane wave with an incident angle  $\phi^i$  given in degrees.

Scattered fields for the problem of a 2-D chiral cylinder above a dielectric half-space are unavailable in the literature, therefore, the results in this work are validated by solving some special cases and comparing with available results in the literature when possible. Two-dimensional cylinders of different cross-sections, namely, circular, rectangular, square, elliptical, and triangular shapes are analyzed in this dissertation. The basic problem setup is shown in Fig. 3.14. Radius of the circular cylinder is denoted by ‘r’, distance from the dielectric interface (strip) to the cylinder is given by ‘d’, width of the finite strip that approximates the dielectric half-space interface is given by ‘w’,  $L_1$  and  $L_2$  represent the two sides of the rectangular cylinder, and for a square cylinder  $L_2 = L_1$ . The setup for each problem maybe excited by a TM or TE plane wave with an incident angle  $\phi^i$ . The following sections present the numerical results.

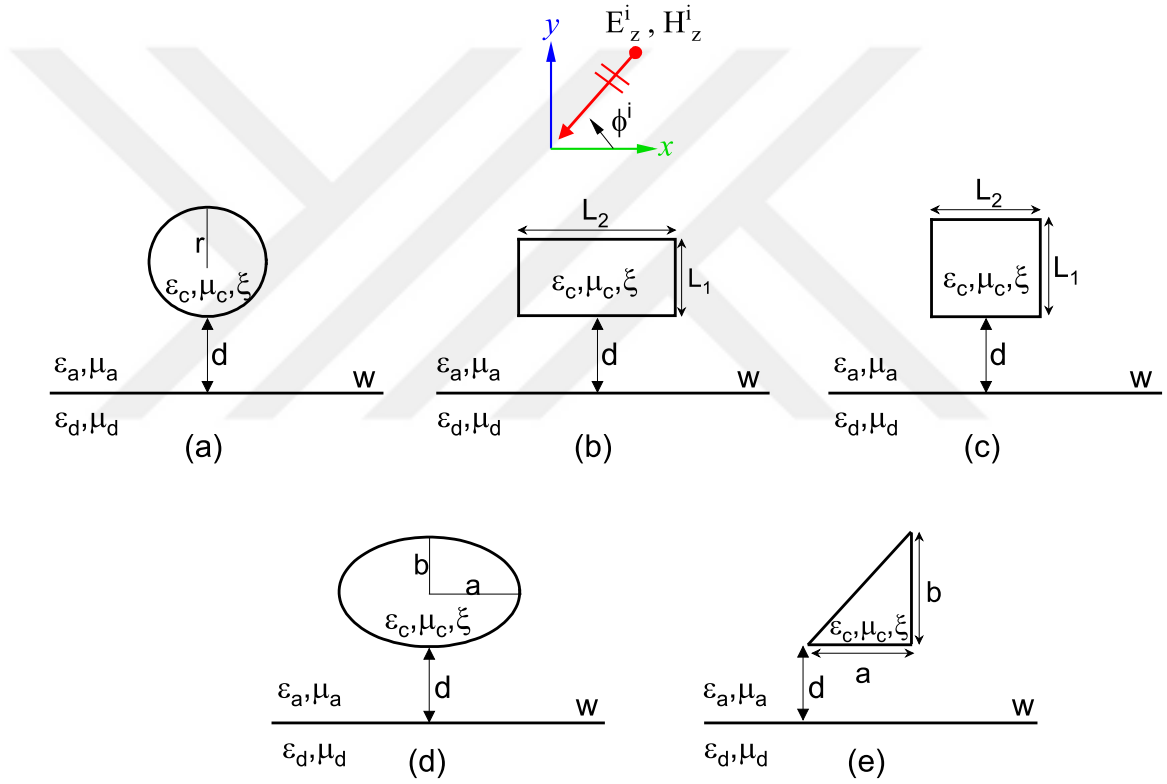


Figure 3.14: Different cross-sections of cylinders analyzed in this work. Subscripts  $a$ ,  $c$  and  $d$  represent the free-space, chiral cylinder, and dielectric half-space, respectively. The materials are characterized by  $\epsilon$ ,  $\mu$ , and  $\xi$  which, respectively, denotes the permittivity, permeability, and chiral admittance of the media. The scatterer can be a PEC, dielectric or chiral. In case of lossy scatterers the electric and magnetic loss is given by  $\tan\delta_e$  and  $\tan\delta_m$ , respectively.



### 3.5.1 Convergence Study for Strip Width

In this section, the problem for a chiral cylinder above a dielectric half-space is being solved. The half-space is replaced by a strip, wide enough so that it behaves similar to a half-space at the frequency of interest. Therefore, it is important to analyze the effect of the strip width ( $w$ ), especially, on the currents induced on the strip and the scattered fields. The convergence study for the strip width is presented below.

To gain some confidence in our method, instead of a chiral cylinder, we first consider a circular PEC cylinder of radius  $r = 0.5\lambda_0$  placed a distance  $d = 0.5\lambda_0$  above a dielectric half-space as shown in the inset of Fig. 3.15. The free-space wavelength  $\lambda_0$  is assumed to be 1 meter. Permittivity of the free-space is denoted by  $\epsilon_a = \epsilon_0$ , and that of the dielectric half-space is given by  $\epsilon_d = 4\epsilon_0$ . Permeability for both media is  $\mu_0$ . The setup is excited by a TM plane wave incident from  $\phi^i = 90^\circ$ . The currents induced on the dielectric strip, known as the *perturbed currents*, are shown in Figs. 3.15 to 3.20. In Fig. 3.15, the width ‘ $w$ ’ is assumed to be 10 wavelengths and it is seen that the perturbed electric currents at the edges of the strip are not small enough. Similarly, the results in Fig. 3.16 where ‘ $w$ ’ is assumed to be 30 wavelengths the result is not satisfactory. However, when ‘ $w$ ’ is assumed to be 60 wavelengths, the currents at the edges are practically equal to zero as shown in Fig. 3.17. Similar observations can be made for the equivalent magnetic currents on  $S_{dn}$  as presented in Fig. 3.18 to 3.20. From these figures we can conclude that the perturbation currents do in fact diminish as one goes away from the cylinder. On the other hand, for these value of  $r$ ,  $d$ , and  $\phi^i$  the electric current on the PEC cylinder is not too sensitive to the strip width as shown in Figure 3.21.

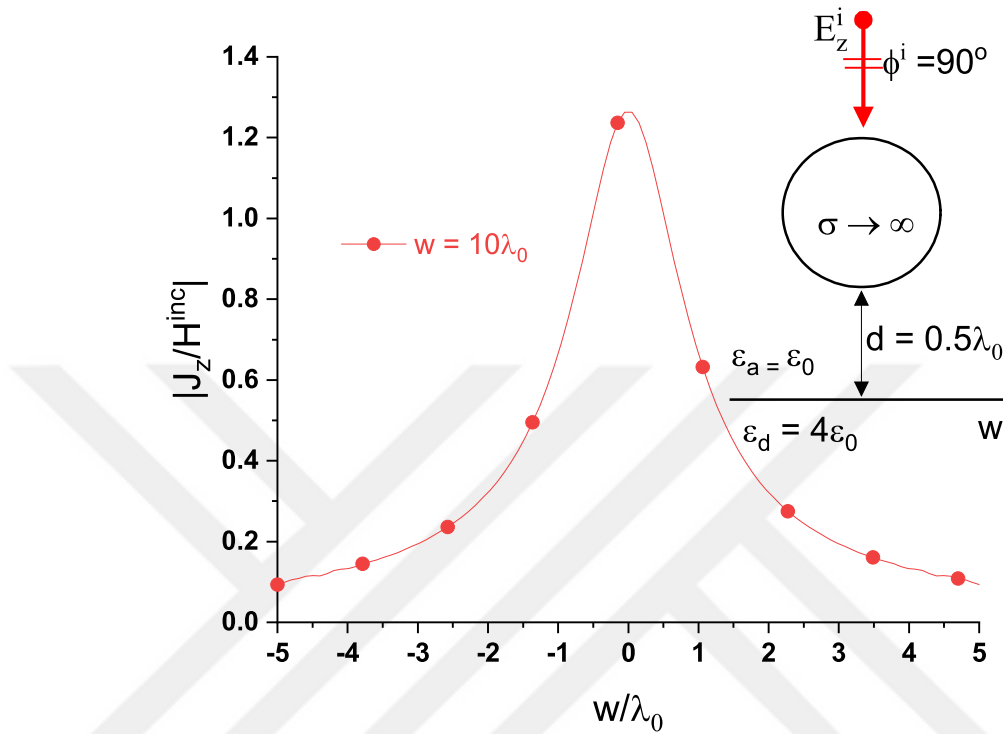


Figure 3.15: Equivalent perturbed electric surface current on a  $w = 10\lambda_0$  dielectric strip. PEC cylinder radius =  $0.5\lambda_0$ .

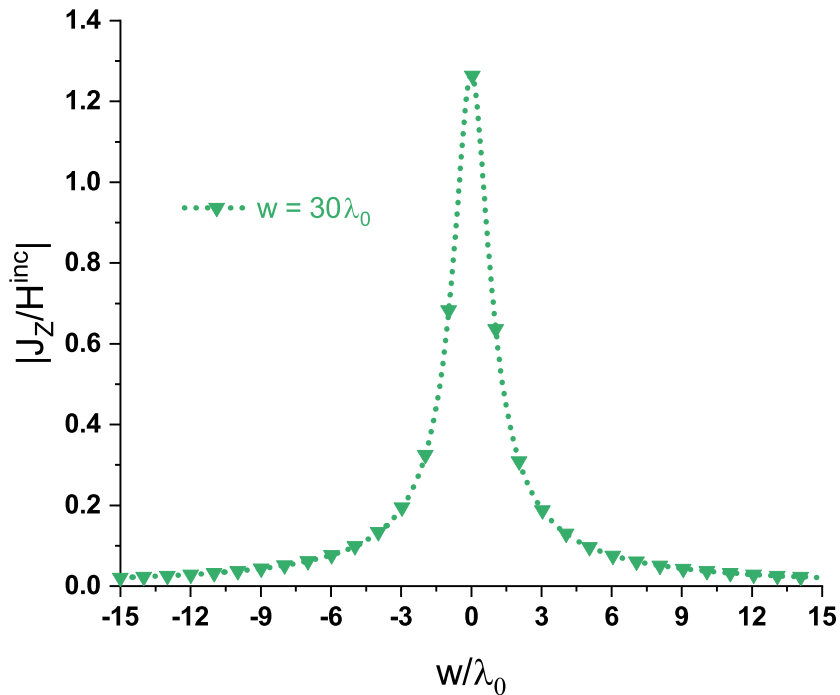


Figure 3.16: Equivalent perturbed electric surface current on a  $30\lambda_0$  dielectric strip for the setup in Fig. 3.15.

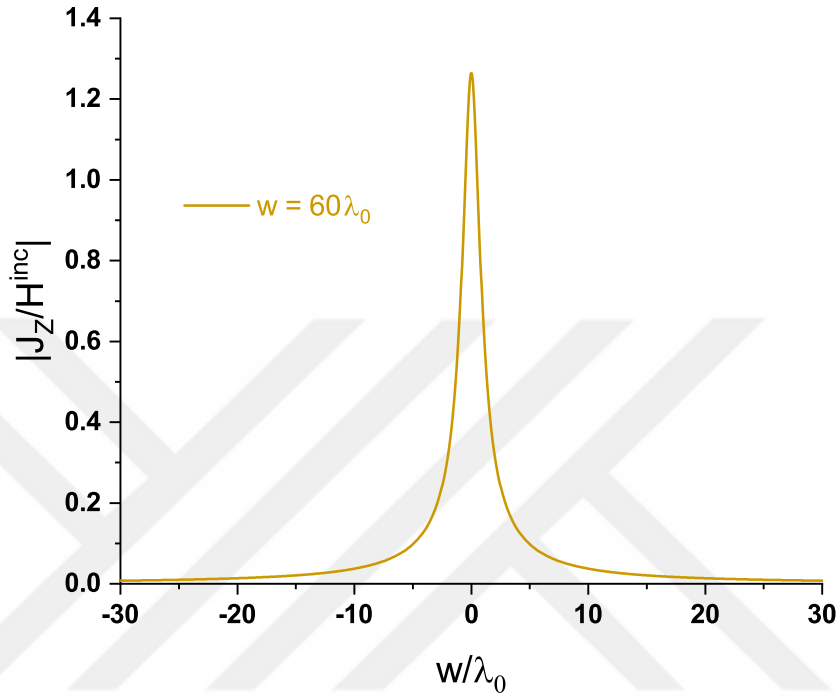


Figure 3.17: Equivalent perturbed electric surface current on a  $60\lambda_0$  dielectric strip for the setup in Fig. 3.15.

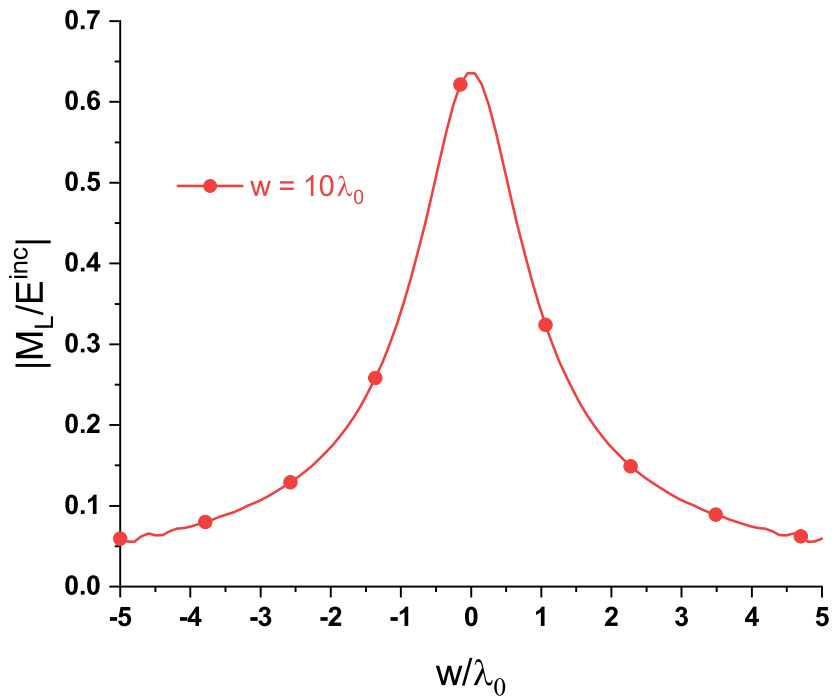


Figure 3.18: Equivalent perturbed magnetic surface current on a  $10\lambda_0$  dielectric strip for the setup in Fig. 3.15.

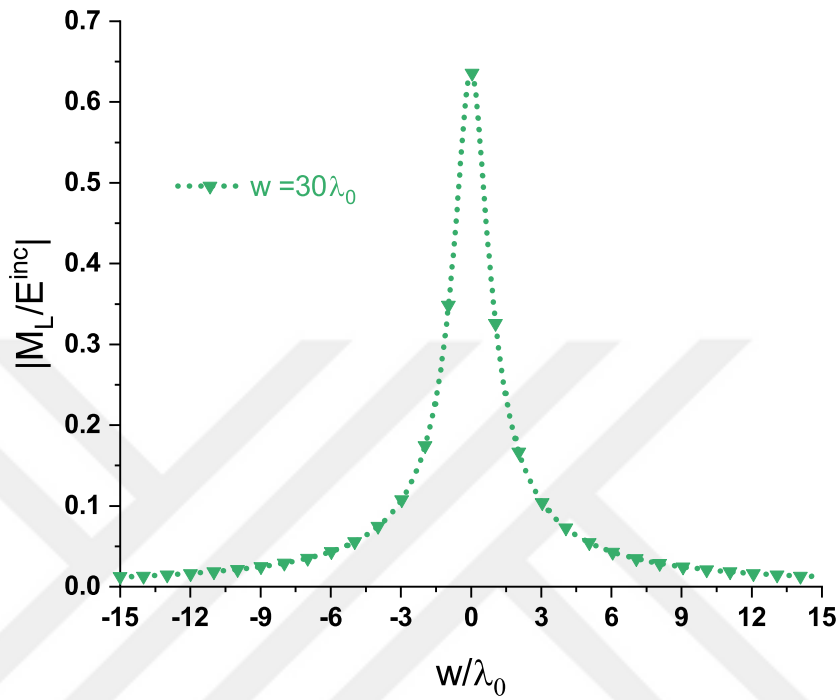


Figure 3.19: Equivalent perturbed magnetic surface current on a  $30\lambda_0$  dielectric strip for the setup in Fig. 3.15.

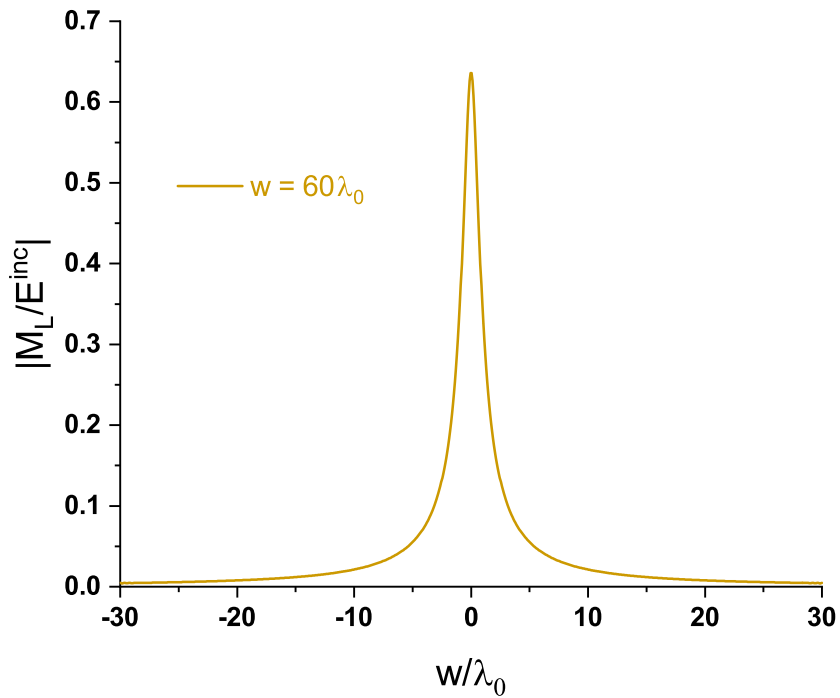


Figure 3.20: Equivalent perturbed magnetic surface current on a  $60\lambda_0$  dielectric strip for the setup in Fig. 3.15.

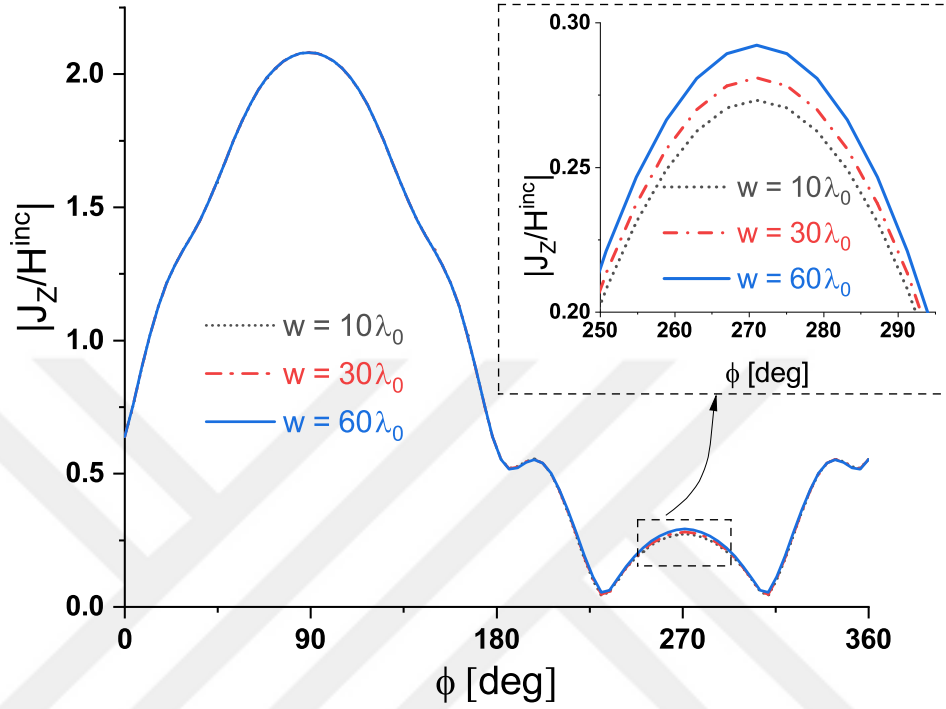


Figure 3.21: Equivalent surface electric current on the PEC cylinder for various strip widths for the setup shown in Fig. 3.15. TM excitation,  $\phi^i = 90^\circ$ ,  $r = 0.5\lambda_0$ ,  $d = 0.5\lambda_0$ ,  $\epsilon_b = \epsilon_c = 4\epsilon_0$ ,  $\mu_b = \mu_c = \mu_0$ .

It is expected that the perturbed surface currents on the dielectric interface must approach zero, as the distance from the cylinder increases. This can be seen, when the strip width is at least  $40\lambda_0$  or  $60\lambda_0$ . If the perturbed currents have not decayed considerably, the effect will be observable in the scattered far-field pattern. In order to obtain viable results, the strip width must be chosen carefully.

Figure 3.22 shows the bistatic scattering width for the problem considered above. The difference in results is more clearly visible for angles closer to horizon. This is because of the shadowing effect due to which the perturbed currents take longer to converge. The non-convergence of the currents reflect in the scattered fields for smaller strip widths. It is seen that, for all practical purposes the results have converged when the width  $w$  is 60 wavelengths.

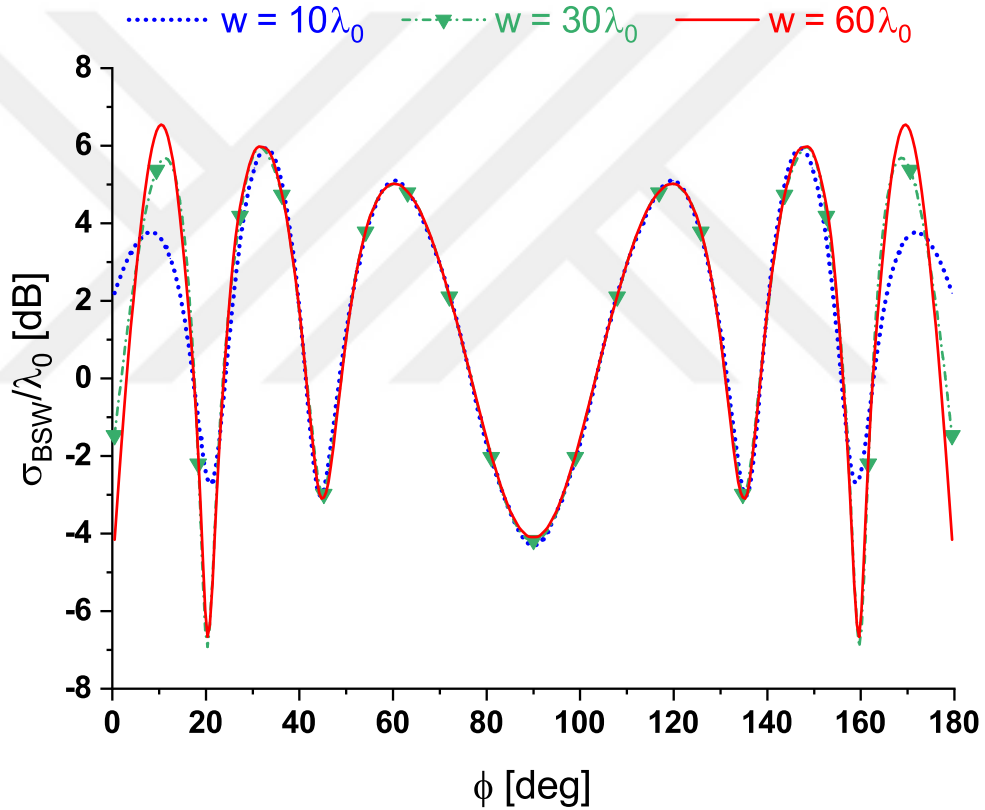


Figure 3.22: Bistatic scattering width for various dielectric strip widths for the setup shown in Fig. 3.15. TM excitation,  $\phi^i = 90^\circ$ ,  $r = 0.5\lambda_0$ ,  $d = 0.5\lambda_0$ ,  $\epsilon_b = \epsilon_c = 4\epsilon_0$ ,  $\mu_b = \mu_c = \mu_0$ .

Now that we have an idea of how to decide on the strip width we are ready to compare our results with the literature for some special cases.

## 3.5.2 Limiting Cases: Comparison with Literature

Published results for the problem under consideration are not available. Therefore, to validate the algorithm and our approach some limiting cases will be compared with the literature.

### 3.5.2.1 A Chiral/Dielectric Circular Cylinder Above a Dielectric Half-Space

In this case, two checks are applied using the same geometry. The results for a dielectric cylinder are compared with [62]. At the same time, the chirality of the scatterer is varied.

The cylinder has a radius  $r = 0.5531\lambda_0$  and is placed a distance  $d = 0.05\lambda_0$  away from the dielectric interface. The interface is represented by a strip of width  $w = 40\lambda_0$  and characterized by  $\epsilon_d = 14.44\epsilon_0$ ,  $\mu_d = \mu_0$ . The circular cylinder is characterized by  $\epsilon_c = 2.1316\epsilon_0$ ,  $\mu_c = \mu_0$ . The chirality admittance ( $\xi$ ) of the cylinder is decreased in steps, from 0.0004 to zero. When  $\xi$  is zero, the chiral cylinder becomes a regular dielectric. This problem has been solved in [62]. Figure 3.23 shows the co-polarized (co-pol) and the cross-polarized (x-pol) far-field amplitude for a chiral cylinder placed above a dielectric interface. The cross-polarized term is due to the polarization rotation in the chiral medium. The effect of chirality admittance on the scattering can be observed. As expected, when  $\xi = 0$ , the co-polar component of the far-field approaches that of a regular dielectric and the cross-polar term becomes zero. The results are in very good agreement with [62] for a dielectric cylinder placed above a dielectric half-space. Furthermore, two interesting observations can be made here,

1. The specular angle for the cross-polar component is in a different direction relative to the co-polar term.
2. The scattered field for the highest chirality is the lowest.

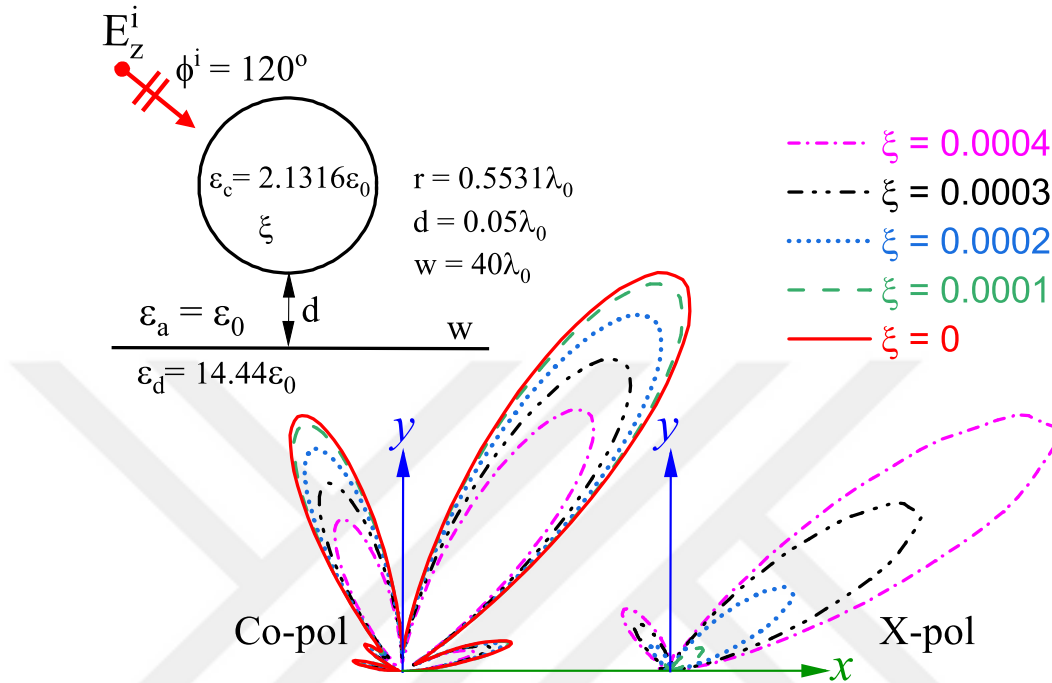


Figure 3.23: Verification I: The scattered far-field amplitude of a chiral cylinder for different chiral admittance ( $\xi$ ) above the interface. TM excitation (left) co-pol (right) x-pol. For  $\xi = 0$  results agree with [62].

Similar observations for the difference between the specular directions of the co-polar and cross-polar components were made in [38], where an axisymmetric chiral radome was analyzed using the moments method.



As a second verification, consider a circular chiral cylinder of radius  $0.5\lambda_0$  placed above a DHS as shown in Fig. 3.24. This figure also shows the bistatic scattered fields for TM plane wave incidence for  $\phi^i = 90^\circ$ . When  $\mu_c = \mu_0$ ,  $\xi = 0$ , and  $\epsilon_c$  is increased, it is noticed that the scattered field approaches that of a PEC cylinder above a DHS, as expected. For  $\epsilon_c = 2600\epsilon_0$ , the cylinder behaves as a PEC. These results are compared with published results in the next two figures.

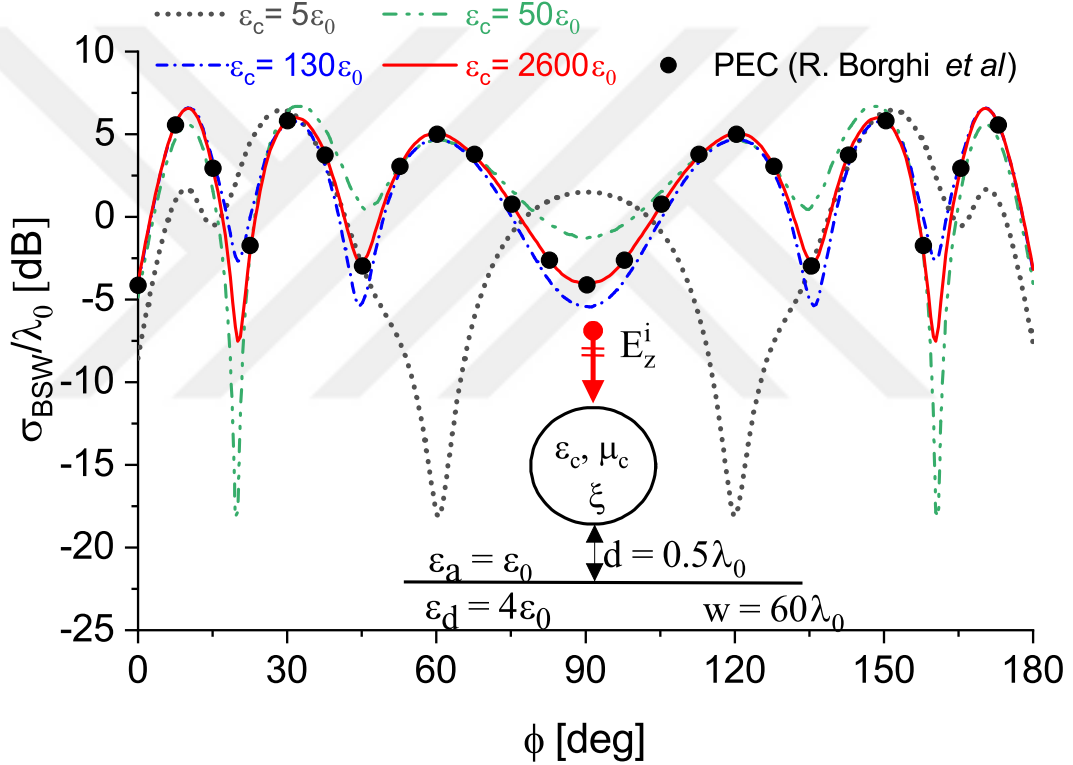


Figure 3.24: Verification II: Comparison of the bistatic scattering width (BSW) for different dielectric constants of the cylinder.

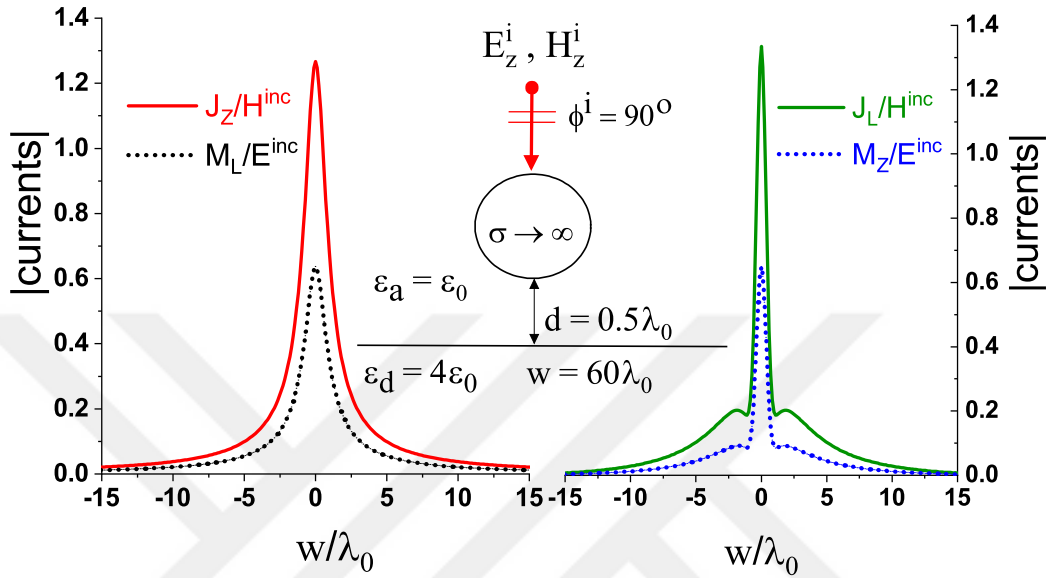
### 3.5.2.2 A Circular PEC Cylinder Above a Dielectric Half-Space

Two cases of a circular conducting cylinder placed above a dielectric half-space are compared with R. Borghi [58]. For the first check, the problem setup is shown in the inset of Fig. 3.25a. A circular conducting cylinder of radius  $r = 0.5\lambda_0$  is placed a distance  $d = 0.5\lambda_0$  above the dielectric half-space with permittivity  $\epsilon_b = 4\epsilon_0$ . A strip of width  $w = 60\lambda_0$  is used to approximate the half-space interface.

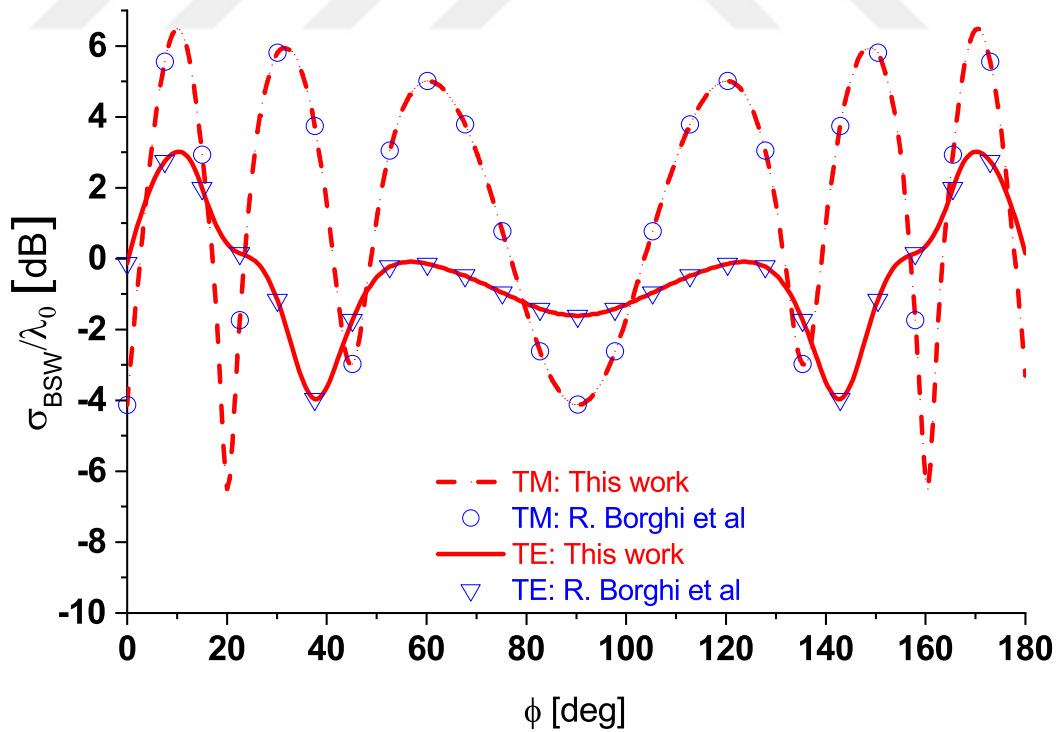
This value is chosen based on initial simulations which showed the perturbed currents approaching to zero. A strip width of  $40\lambda_0$  or above is required for a good convergence, with at least 12 segments per wavelength.  $\lambda_0$  is the free-space wavelength and is assumed to be 1 meter. The setup is excited by a plane wave with an incident angle  $\phi^i=90^\circ$ . TM and TE cases are compared in Fig. 3.25. The corresponding perturbed currents for the above problem are shown in Fig. 3.25a. The subplot on the left shows the currents on the interface for TM excitation and the plot on the right is for TE excitation. Note that the currents are only plotted for a strip width of  $30\lambda_0$  instead of  $60\lambda_0$  because they are converging to zero, as the distance from the cylinder increases. In [58], a different method was used, hence perturbed currents are not compared. The bistatic cross-section is shown in Fig. 3.25b. The results are in excellent agreement with published results as well as with the experiment shown in Fig. 3.24.

The excitation vector  $[V]$  is sensitive to the incident angle, therefore, a different excitation ( $\phi^i = 120^\circ$ ), for the same setup was compared with [58]. Figures 3.26a and 3.26b, respectively, shows the perturbed currents and the bistatic scattering width. A good agreement for the scattering width is achieved. The effect of the asymmetric excitation can be observed in the perturbed currents and the scattering width, as expected.

After validating the proposed method we are confident about the computed results. Further studies are performed in the following sub-sections.

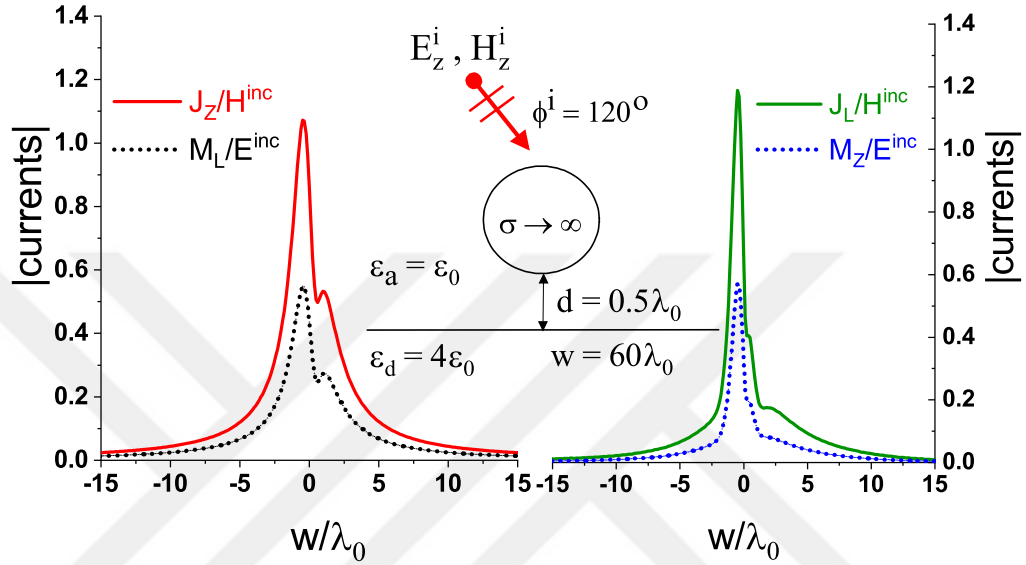


(a) (Left) TM and (right) TE excitation.

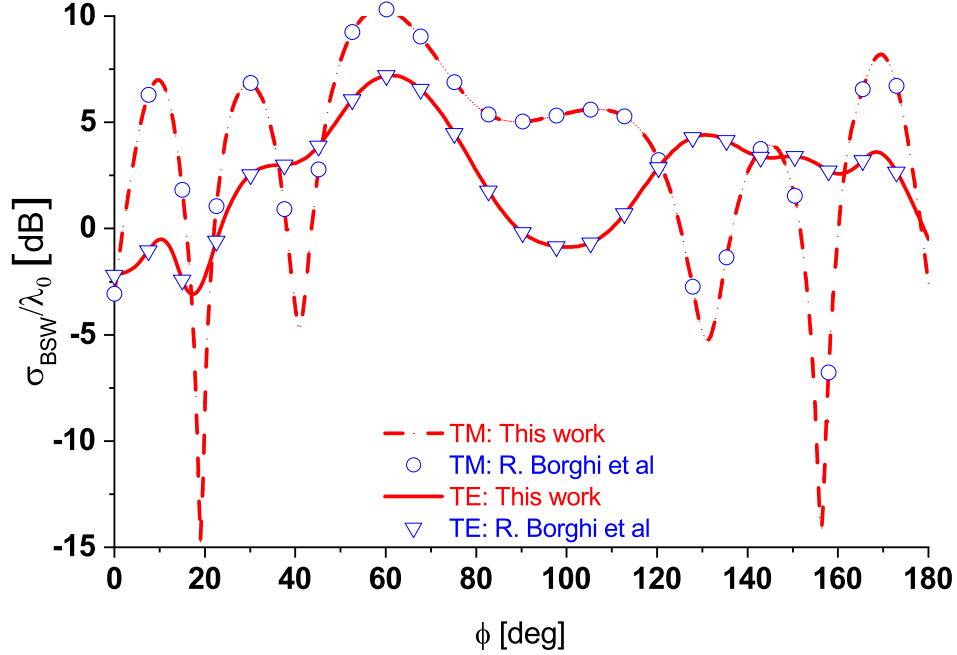


(b)

Figure 3.25: A circular conducting cylinder ( $r = 0.5\lambda_0$ ), placed symmetrically above a dielectric half-space. (a) Magnitude of the perturbed currents on the interface (b) Bistatic scattering width.  $\phi^i = 90^\circ$ , compared with [58].



(a) (Left) TM and (right) TE excitation



(b)

Figure 3.26: A circular conducting cylinder, of radius  $r = 0.5\lambda_0$ , placed symmetrically above a dielectric half-space. (a) Magnitude of the perturbed currents on the interface (b) Bistatic scattering width.  $\phi^i = 120^\circ$ , compared with [58].

### 3.5.3 Effect of Chirality on Scattering width

Previous research has shown that the chirality parameter effects the bistatic scattering width in an unpredictable manner. This effect can not be explained or predicted by simple theory. This phenomenon is shown in the following example. Consider a circular chiral cylinder of radius  $0.2\lambda_0$  immersed in free-space ( $\epsilon_a = \epsilon_0, \mu_a = \mu_0$ ) and placed a distance  $d = 0.5\lambda_0$  above a dielectric half-space approximated by a strip of width  $w = 40\lambda_0$ . The cylinder is characterized by ( $\epsilon_c = 4\epsilon_0, \mu_c = \mu_0, \xi$ ) and the half-space is characterized by ( $\epsilon_d = 4\epsilon_0, \mu_d = \mu_0$ ). Two different incident angles are observed, (i)  $\phi^i = \phi^s = 90^\circ$ , (ii)  $\phi^i = \phi^s = 45^\circ$ , where  $\phi^i$  and  $\phi^s$ , respectively, represent the incident angle and the angle at which the scattered field is computed. The incident field is a TM plane wave. The computed results are shown in Fig. 3.27. It can be observed that the fields vary in an unpredictable manner with chirality parameter ( $\xi$ ). Therefore, it is very important to study this problem for various parameters and other geometries. The following sections show such a detailed study.

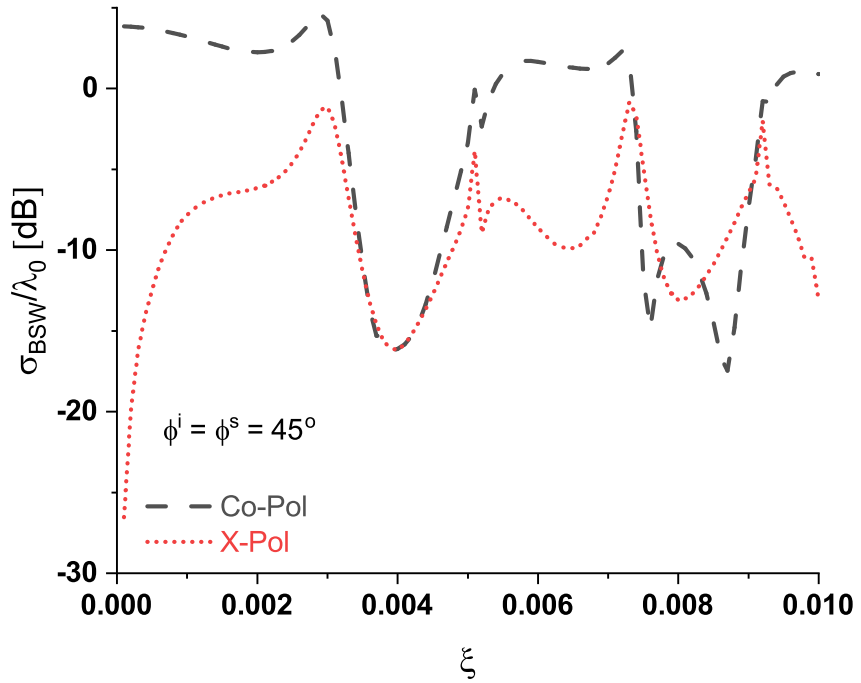
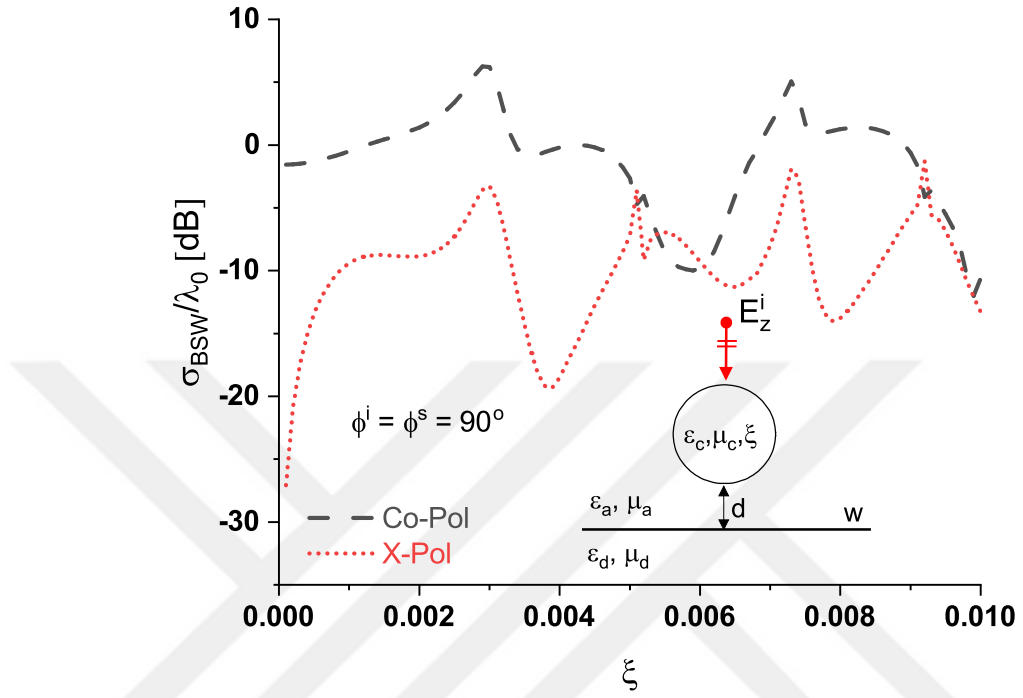


Figure 3.27: BSW variation of a circular chiral cylinder above a dielectric half-space when the chirality admittance of the cylinder is varied. Excitation: TM plane wave  $\phi^i = 45^\circ$ ,  $r = 0.2\lambda_0$ ,  $d = 0.5\lambda_0$ ,  $w = 40\lambda_0$ ,  $\epsilon_c = \epsilon_d = 4\epsilon_0$ ,  $\mu_c = \mu_d = \mu_0$  (a)  $\phi^i = \phi^s = 90^\circ$ , (b)  $\phi^i = \phi^s = 45^\circ$ .

### 3.5.4 Parametric Analysis: A Circular Dielectric Cylinder Above a Dielectric Half-Space

In this subsection, a parametric study of the circular dielectric cylinder placed above a dielectric interface is performed. This analysis will help in determining the approximate parameters to be used in further studies. If there are any convergence issues or spurious results they can be observed here. Three main parameters are studied (i) radius of the cylinder (ii) height of cylinder above the interface (iii) incident angle of the plane wave. The initial study is performed on the perturbed currents only to analyze its behaviour. Scattering fields are not presented for this analysis.

#### 3.5.4.1 Effect of Cylinder ‘Radius’ on Perturbed Current

The position of the scatterer relative to the interface and size of the scatterer affects the perturbed currents. Here, the radius ‘r’ of the circular dielectric cylinder is varied and its effect on the perturbation current is observed. The cylinder is placed a distance  $d=0.3\lambda_0$  above the strip of width  $40\lambda_0$ . The body and the dielectric interface, both, have a dielectric constant of  $\epsilon_c = \epsilon_d = 4\epsilon_0$ . The permeability ( $\mu_c = \mu_d = \mu_0$ ) of both mediums is set to unity. The setup is excited by a plane wave incident from  $\phi^i = 90^\circ$ . Figures 3.28 and 3.29, respectively, show the magnitude of the longitudinal and lateral, electric and magnetic surface currents for TM excitation. A zoomed in version of the same currents can be seen in the inset of each figure. Since the currents are symmetric, only one side is shown in the inset.

The effect of the bigger cylinder is obvious on the perturbation current. Bigger cylinder leads to more disturbance and it decays slower relative to the smaller cylinders. This shows again that if the scatterer is big, a relatively wider strip is required to approximate the half-space.

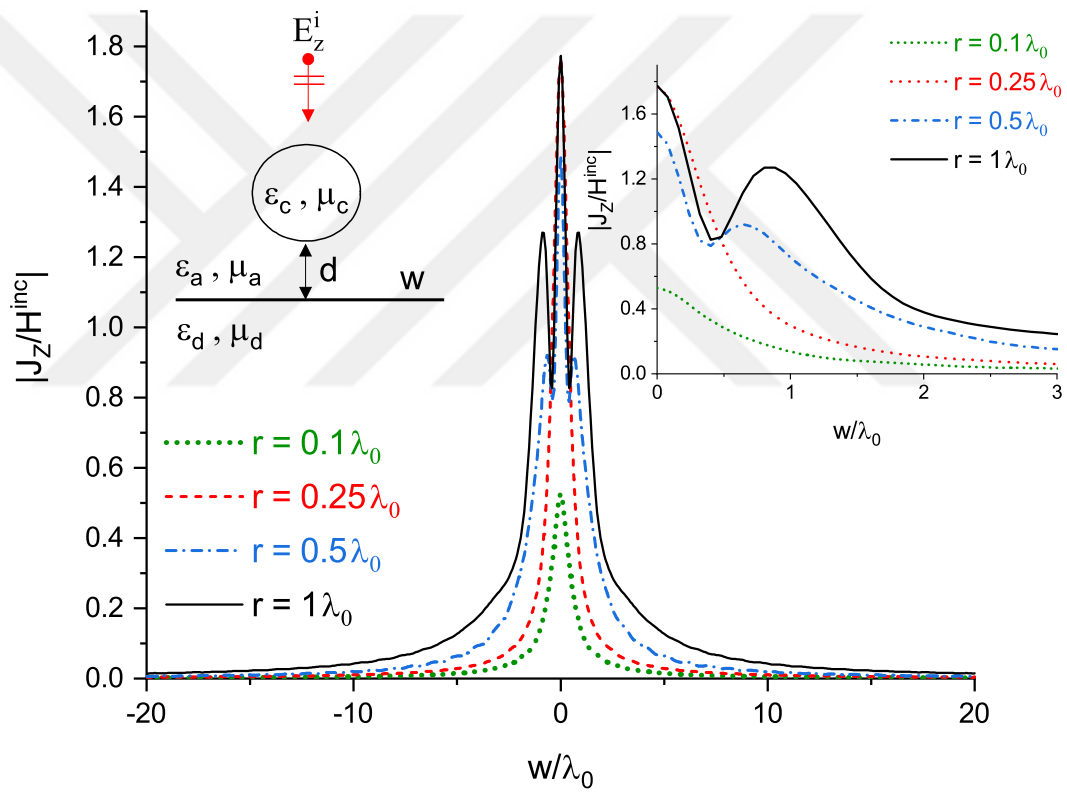


Figure 3.28: Magnitude of the perturbed electric currents due to a circular dielectric cylinder on a dielectric interface for TM excitation,  $\phi^i = 90^\circ$ ,  $d = 0.3\lambda_0$ ,  $w = 40\lambda_0$ ,  $\epsilon_c = \epsilon_d = 4\epsilon_0$ ,  $\mu_c = \mu_d = \mu_0$ . Inset figure shows zoomed in view for three wavelengths on the strip, starting from center of the strip.



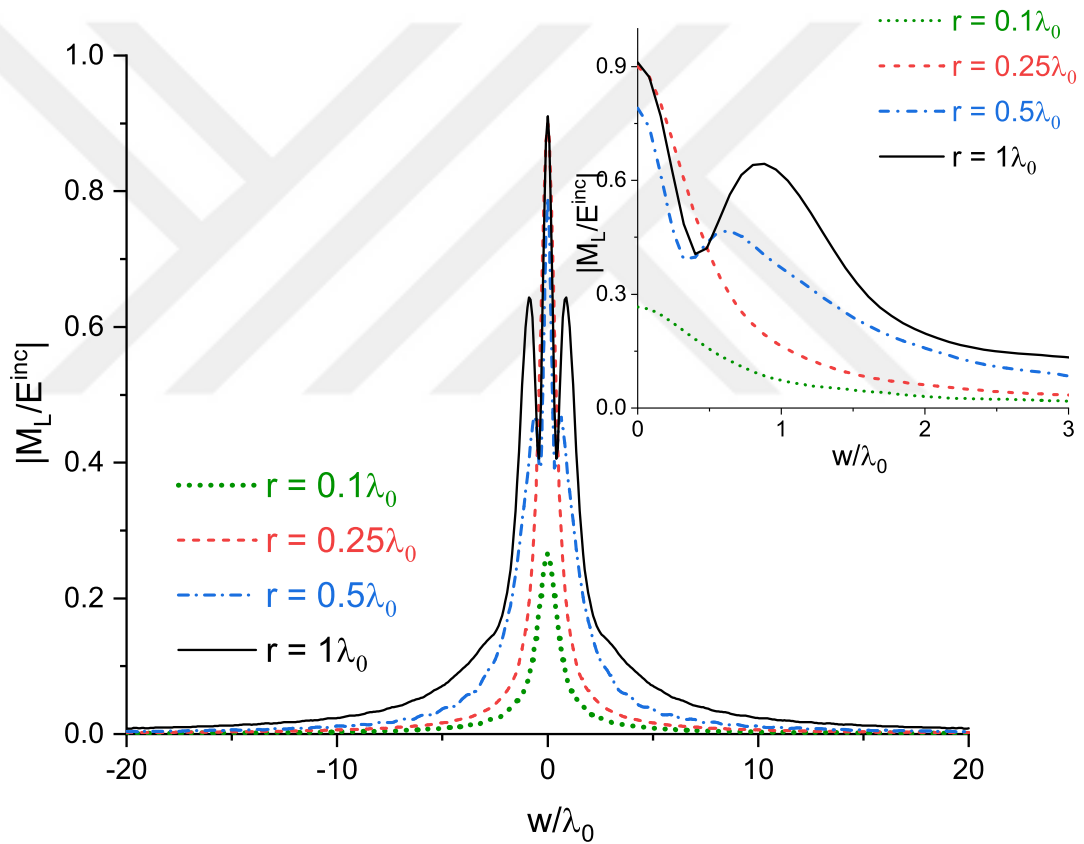


Figure 3.29: Corresponding perturbed magnetic current for TM excitation,  $\phi^i = 90^\circ$ ,  $d = 0.3\lambda_0$ ,  $w = 40\lambda_0$ ,  $\epsilon_c = \epsilon_d = 4\epsilon_0$ ,  $\mu_c = \mu_d = \mu_0$ . Inset figure shows zoomed in view for three wavelengths on the strip, starting from center of the strip.

For comparison purposes, the TE case was also simulated. The results for the lateral electric and longitudinal magnetic currents are shown in Figs. 3.30 and 3.31. A similar behaviour to the TM case was observed.

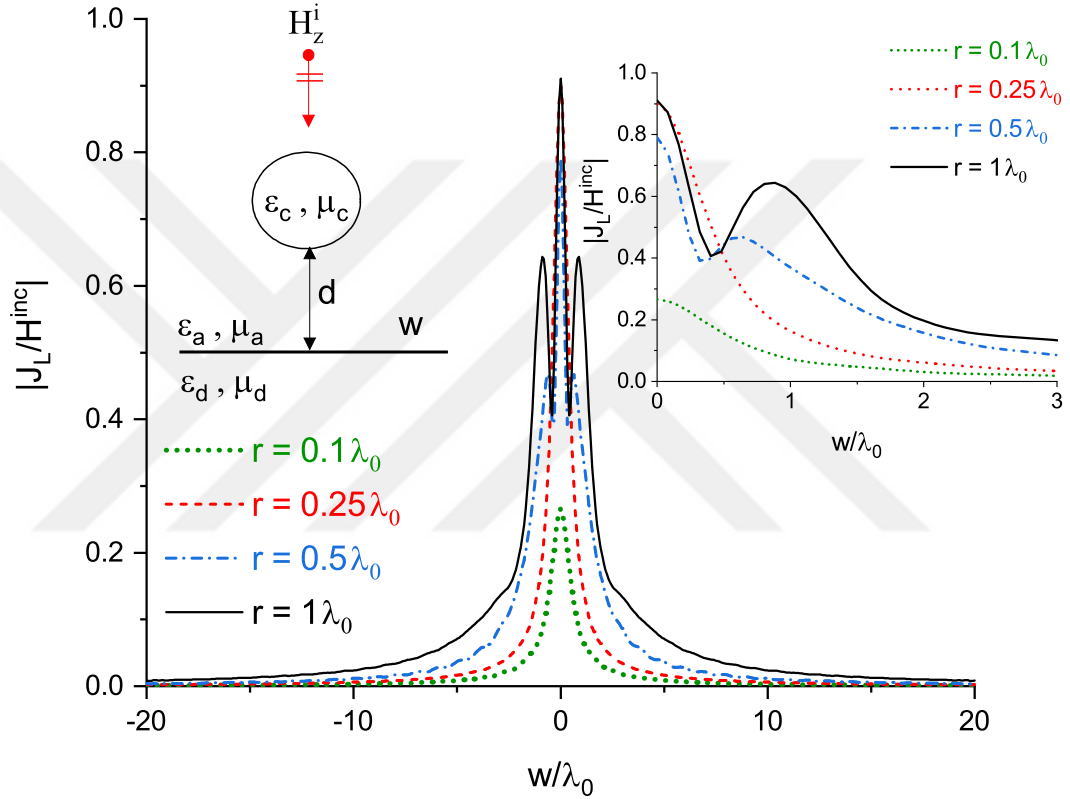


Figure 3.30: Magnitude of the perturbed electric current due to a circular dielectric cylinder on a dielectric interface for TE excitation,  $\phi^i = 90^\circ$ ,  $d = 0.3\lambda_0$ ,  $w = 40\lambda_0$ ,  $\epsilon_c = \epsilon_d = 4\epsilon_0$ ,  $\mu_c = \mu_d = \mu_0$ . Inset figure shows zoomed in view for three wavelengths on the strip, starting from center of the strip.

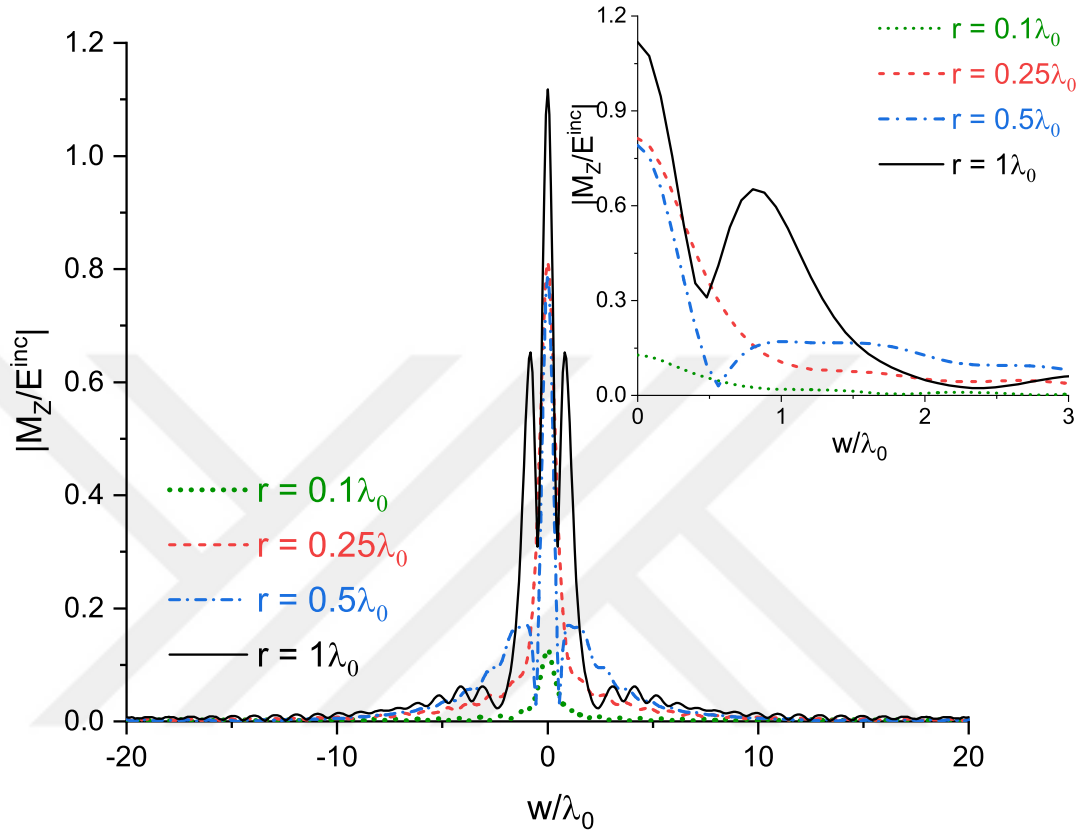


Figure 3.31: Magnitude of the perturbed magnetic current due to a circular dielectric cylinder on a dielectric interface for TE excitation,  $\phi^i = 90^\circ$ ,  $d = 0.3\lambda_0$ ,  $w = 40\lambda_0$ ,  $\epsilon_c = \epsilon_d = 4\epsilon_0$ ,  $\mu_c = \mu_d = \mu_0$ . Inset figure shows zoomed in view for three wavelengths on the strip, starting from center of the strip.

### 3.5.4.2 Effect of Cylinder ‘Height’ on Perturbed Current

Height of the scatterer is another important parameter which effects the perturbed currents. Three different heights for the circular dielectric cylinder are analyzed here. A dielectric cylinder of radius  $r = 0.5\lambda_0$  is placed at distances  $d = 0.1\lambda_0, 0.5\lambda_0, 1.5\lambda_0$  above a dielectric strip of width  $w = 40\lambda_0$ . The setup is excited by a TM plane wave with  $\phi^i = 90^\circ$ . The results for the magnitude of the surface electric and magnetic currents on the interface are shown in Figs. 3.32 and 3.33.

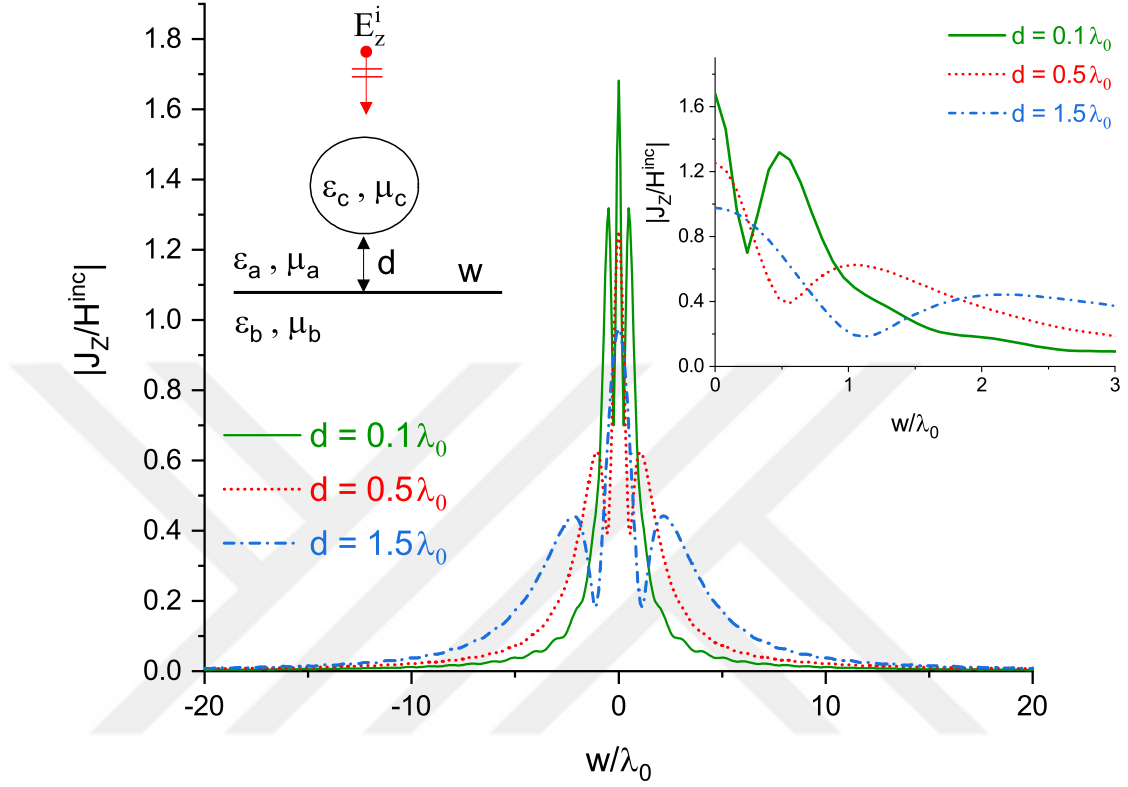


Figure 3.32: Effect of cylinder height on the magnitude of the perturbed electric currents for TM excitation,  $\phi^i = 90^\circ$ , radius  $r = 0.5\lambda_0$ ,  $w = 40\lambda_0$ ,  $\epsilon_c = \epsilon_d = 4\epsilon_0$ ,  $\mu_c = \mu_d = \mu_0$ . Inset figure shows zoomed in view for three wavelengths on the strip, starting from center of the strip.

Radius of the cylinder and other parameters are kept constant, only the distance from the interface is varied. It was observed that, the perturbed current due to the farthest cylinder took longer to converge. This is because it casts a bigger shadow on the interface. This can be explained by a light source and an object placed close to or far away from it. Consider, the light source and the object are close to each other. In this case, the object will block most of the light from the source and cast a bigger shadow, as opposed to when the object is far from the light source. The same phenomenon can be observed in Figs. 3.32 and 3.33. Note that the amplitude of the current decreases as the scatterer moves farther away from the interface.

TE plane wave excitation had a similar response in terms of the current decay, so it is not shown here. In that case too, current due to the farthest cylinder took

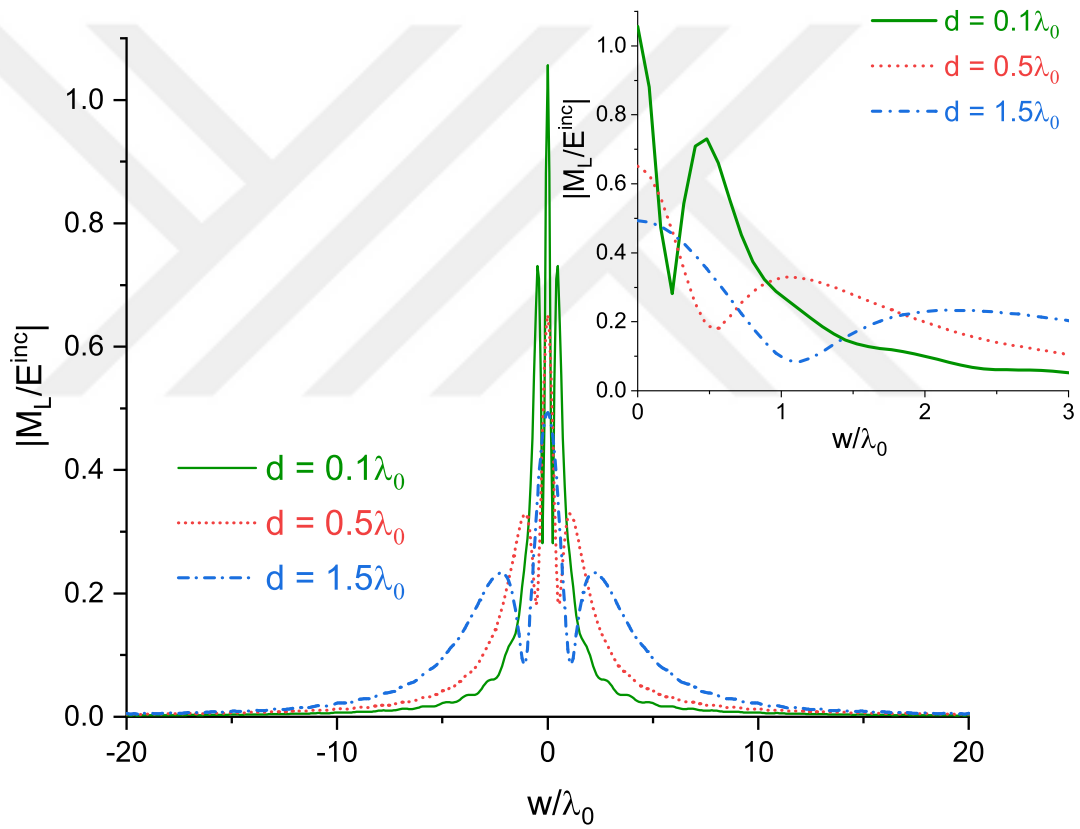


Figure 3.33: Effect of cylinder height on the magnitude of the perturbed magnetic current for TM excitation,  $\phi^i = 90^\circ$ , radius  $r = 0.5\lambda_0$ ,  $w = 40\lambda_0$ ,  $\epsilon_c = \epsilon_d = 4\epsilon_0$ ,  $\mu_c = \mu_d = \mu_0$ . Inset figure shows zoomed in view for three wavelengths on the strip, starting from center of the strip.

longer to converge for the same setup.

The same observations are true for a chiral body above a dielectric half-space as well. In case of a chiral cylinder, four currents are induced on the interface  $J_Z$ ,  $J_L$ ,  $M_Z$ , and  $M_L$ . A dielectric cylinder is chosen in this study to decrease the number of graphs. To show the fact that the observations are true in general, the currents induced on the interface due to a chiral cylinder are shown in Fig. 3.34. The strip is divided into 499 segments. Each 499 segments show a single current for three different heights. Starting from left to right,  $J_Z$ ,  $J_L$ ,  $M_Z$ , and  $M_L$ . As stated previously, the farthest cylinder has a bigger shadow, hence it takes longer to converge.

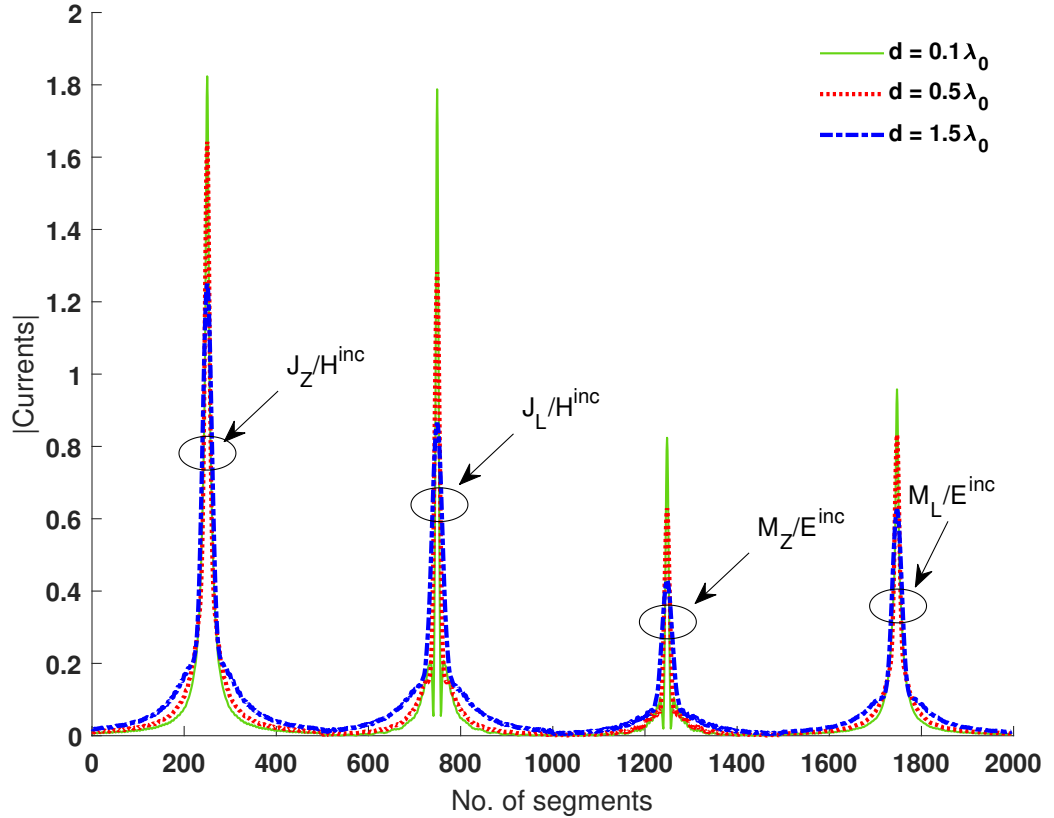
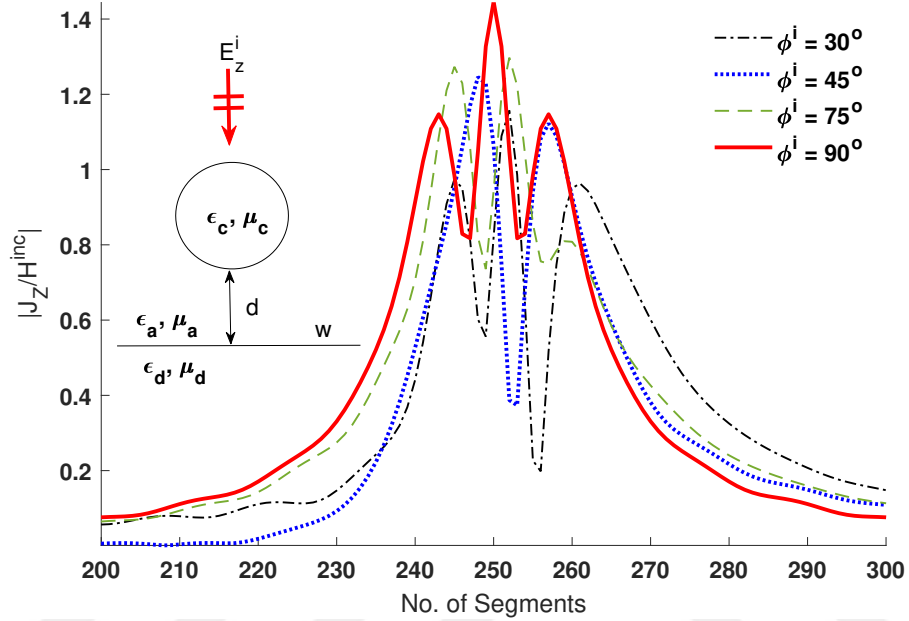


Figure 3.34: Circular chiral cylinder placed above a dielectric half-space. Its effect on the magnitude of the perturbed current for TM excitation,  $\phi^i = 90^\circ$ , radius  $r = 0.5\lambda_0$ ,  $w = 40\lambda_0$ ,  $\epsilon_c = \epsilon_d = 4\epsilon_0$ ,  $\mu_c = \mu_d = \mu_0$ ,  $\xi = 0.002$ .

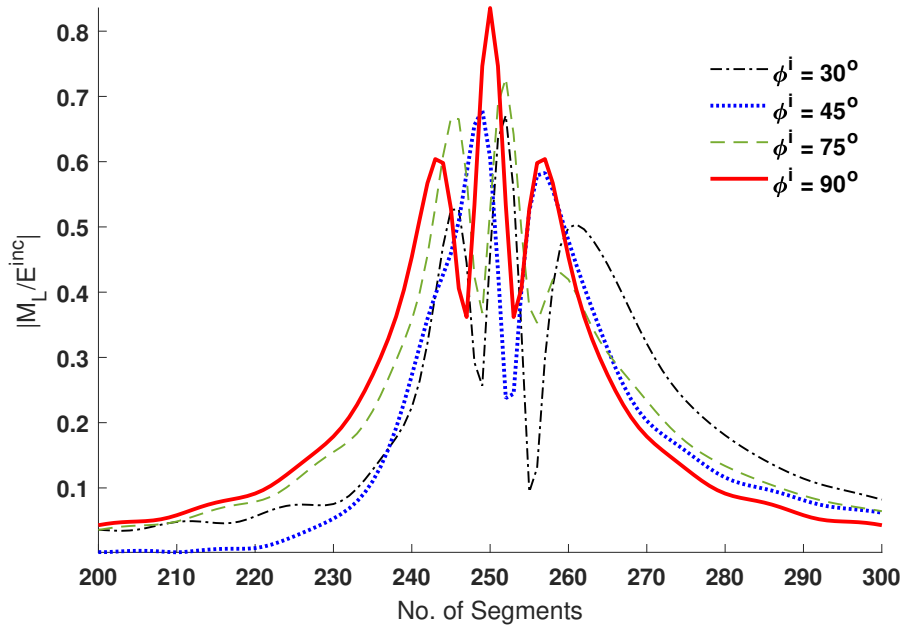
### 3.5.4.3 Effect of ‘Incident’ Angle on Perturbed Current

The effect of incident angle of the plane wave is an essential study. Till this point, most of the cases discussed were for normal incidence. The current distribution on the interface was symmetric. It decayed to zero, symmetrically on both sides of the strip, starting from a peak at the center. In this section, a plane wave is incident on a dielectric cylinder of radius  $r = 0.5\lambda_0$  which is placed a distance  $d = 0.2\lambda_0$  above a dielectric interface, represented by a strip of width  $w = 40\lambda_0$ . The setup is illuminated by different incident angles,  $\phi^i = 30^\circ, 45^\circ, 75^\circ,$  and  $90^\circ$ . The results for the TM and TE cases are presented in Figs. 3.35 and 3.36, respectively.

The strip is divided into 499 segments. However, on the  $x$ -axis only 100 segments are shown. This allows for a clear view of the currents. It is observed that, for angles close to horizon, the current converges slower than the normal incidence or for angles away from the horizon. This is because of the shadow of the scatterer and more surface waves on the interface. This is true for both TM and TE cases. For instance, currents due to  $30^\circ$  incidence converges relatively slower than other incident angles. Therefore, for incident angles close to the horizon, a wider strip should be used for better approximation of the half-space.



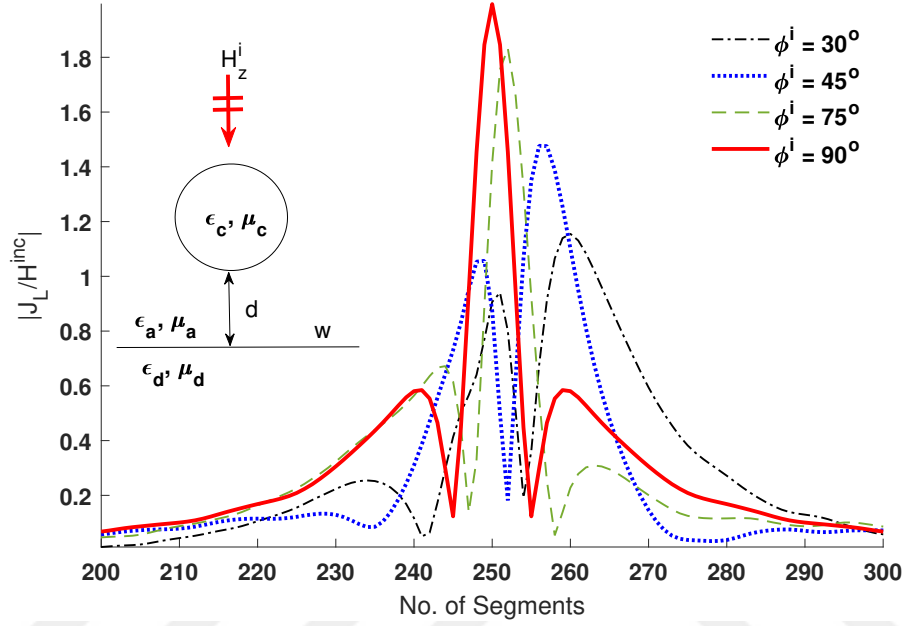
(a) Longitudinal surface electric current.



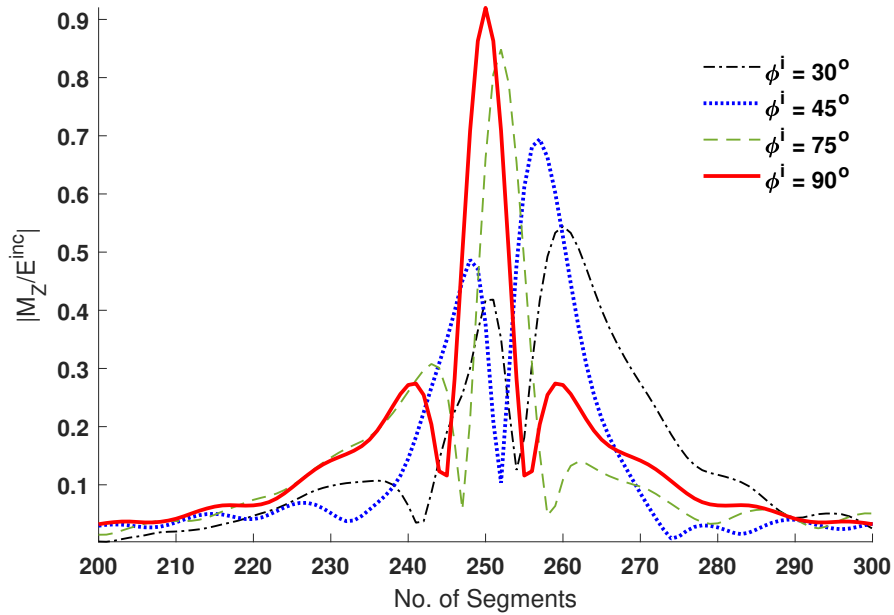
(b) Lateral surface magnetic current

Figure 3.35: Currents on the interface due to a circular dielectric cylinder of radius  $r = 0.5\lambda_0$  placed distance  $d = 0.2\lambda_0$  above dielectric interface of width  $w = 40\lambda_0$ . TM illumination with different incident angles. Dielectric constants of the body and the half-space are  $\epsilon_c = \epsilon_d = 4\epsilon_0$ ,  $\epsilon_a = \epsilon_0$ ,  $\mu_a = \mu_c = \mu_d = \mu_0$ .





(a) Lateral surface electric current.



(b) Longitudinal surface magnetic current

Figure 3.36: Currents on the interface due to a circular dielectric cylinder of radius  $r = 0.5\lambda_0$  placed distance  $d = 0.2\lambda_0$  above dielectric interface of width  $w = 40\lambda_0$ . TE illumination with different incident angles. Dielectric constants of the body and the half-space are  $\epsilon_c = \epsilon_d = 4\epsilon_0$ ,  $\epsilon_a = \epsilon_0$ ,  $\mu_a = \mu_c = \mu_d = \mu_0$ .

#### 3.5.4.4 Summary

For all the cases presented here and studied otherwise, no spurious results were observed. The main conclusions obtained from this study, which apply to the perturbed currents on the interface are:

- Current due to a far away scatterer, takes longer to converge.
- Current due to a big scatterer, takes longer to converge.
- The amplitude of the current is larger if the body is close to the interface.
- For incident angles close to the horizon, currents on the shadowed side of the scatterer takes longer to converge.
- The strip width chosen should be wide enough to allow for the current on the interface to approach to zero, as the distance from the scatterer increases.
- The results obtained for induced current due to dielectric scatterer applies to chiral scatterers too, however in the later case, the electric and magnetic currents have both longitudinal and lateral components.

The parameters used in the following sections are selected based on the above analysis.

## 3.6 Scattering from Circular Chiral Cylinders

In this section, circular homogeneous chiral cylinders of different parameters are studied. The currents on the interface are presented along with the bistatic scattering width (upper half-space only). Far-field amplitudes for various cases are also presented to observe the fields transmitted into the lower half-space. In some cases, scattering width for the chiral cylinder is compared with dielectric and conducting cylinders. This helps in identifying the effect of the chirality admittance. The section is divided into lossy and lossless cylinders.

### 3.6.1 Lossless Scatterers

After validating the algorithm and our approach, some results are presented for lossless chiral cylinders of circular cross-sections above a dielectric half-space. Consider a circular cylinder of radius  $r = 0.5\lambda_0$  placed at a height  $d = \lambda_0$  above a dielectric half-space ( $\epsilon_d = 4\epsilon_0$ ,  $\mu_d = \mu_0$ ). Perturbed currents are computed on a strip of width  $w = 40\lambda_0$ . The system, shown in the inset of Fig. 3.37a, is excited by a TM or TE plane wave incident from  $\phi^i = 90^\circ$ . The circular cylinder is either PEC, regular dielectric ( $\epsilon_c = 4\epsilon_0$ ,  $\mu_c = \mu_0$ ), or chiral ( $\epsilon_c = 4\epsilon_0$ ,  $\mu_c = \mu_0$ ,  $\xi = 0.002$ ).

When the circular cylinder is chiral then the perturbed currents for TM and TE excitations are shown in Fig. 3.37a. Although the width  $w$  of the dielectric strip was assumed to be  $40\lambda_0$  the results are shown only for a domain of  $20\lambda_0$  because the perturbed currents are minimal towards the edges. The perturbed currents for the TE case follow the same trend as the TM case, shown on the right in Fig. 3.37a. Note that for the TE case,  $J_L$  and  $M_Z$  have higher amplitudes than  $J_Z$  and  $M_L$ , which is expected.

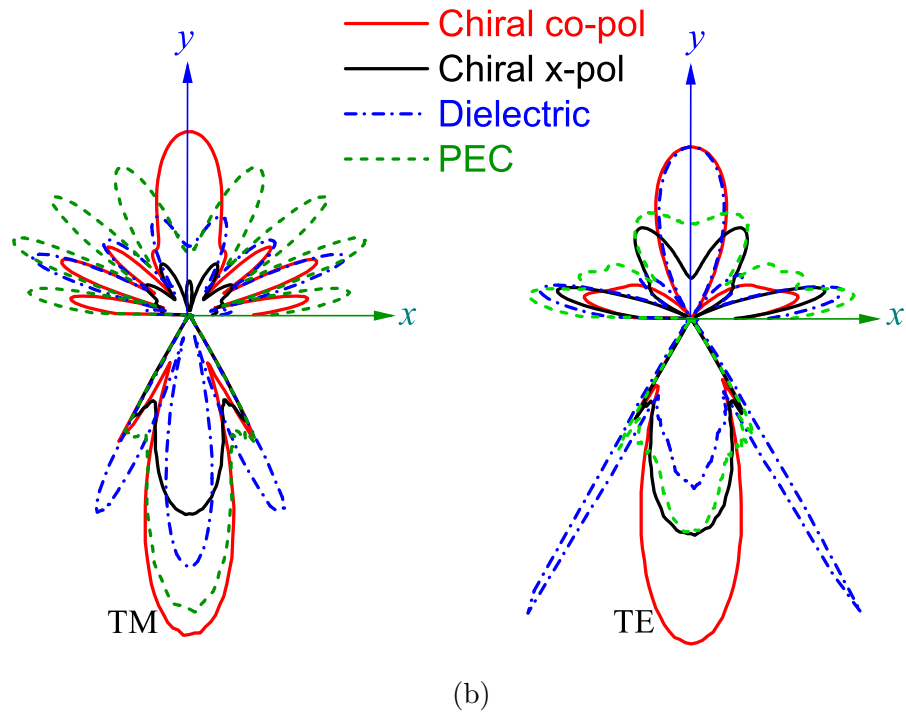
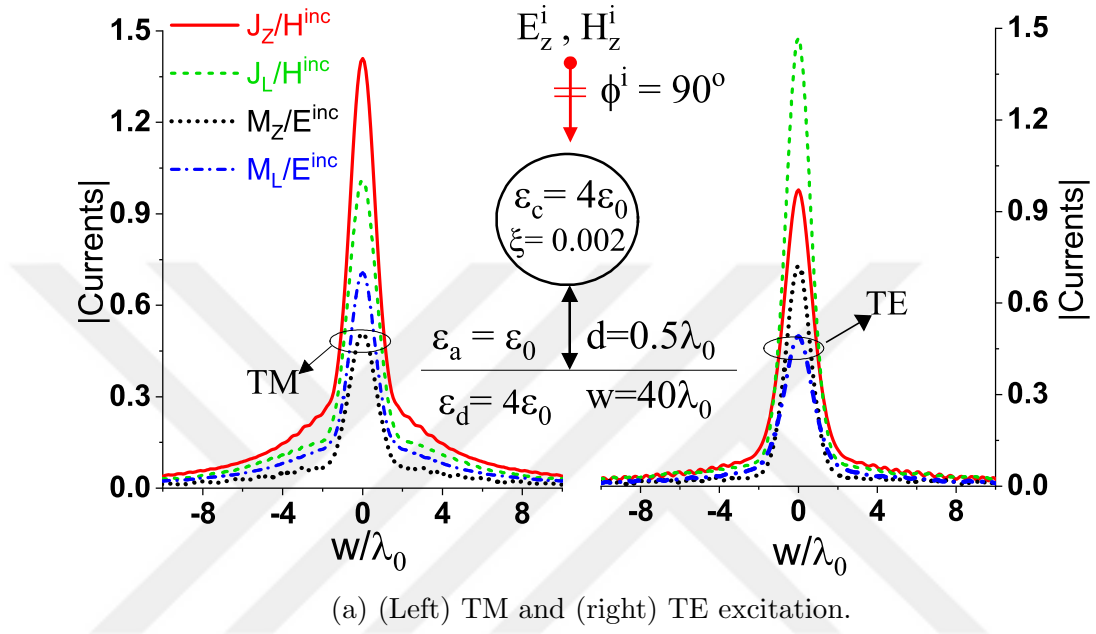


Figure 3.37: A circular chiral cylinder, of radius  $r = 0.5\lambda_0$ , placed symmetrically above a dielectric half-space. (a) Magnitude of the perturbed currents on the interface (b) Far-field amplitude.

Figure 3.37b compares the scattered far-field pattern of this cylinder when it is PEC, dielectric, or chiral. For the TM case, all of them have their main lobe in the forward scattering direction ( $\phi=270^\circ$ ) into the dielectric half-space. On the other hand, the scattered field pattern in the air is quite different for each cylinder. A clear back lobe ( $\phi=90^\circ$ ) exists for the co-polar component when the cylinder is chiral. The PEC or dielectric cylinder do not have their back lobe in the  $\phi=90^\circ$  direction. The patterns are quite interesting for the TE case as well. It is again concluded that this behavior is not predictable from a simple theory.

Figure 3.38 shows the BSW for a circular chiral cylinder ( $\epsilon_c=4\epsilon_0$ ,  $\mu_c=\mu_0$ ,  $\xi=0.002$ ) of radius  $0.5\lambda_0$  placed a distance  $d=\lambda_0$  above a DHS ( $\epsilon_d=2\epsilon_0$ ,  $\mu_d=\mu_0$ ). The excitation is a TE plane wave incident from  $\phi^i=90^\circ$  direction. Also included in this figure are the results for a PEC or a dielectric cylinder of ( $\epsilon_c=4\epsilon_0$ ,  $\mu_c=\mu_0$ ) of the same size. The three cylinders behave entirely different from each other. The back-scattered field ( $\phi=90^\circ$ ) is highest for the dielectric cylinder. It is also noted that the cross-polar component for the chiral cylinder is comparable with the scattering width of PEC or dielectric at certain angles. The cross-polar component is for the chiral cylinder, shown here for completeness.

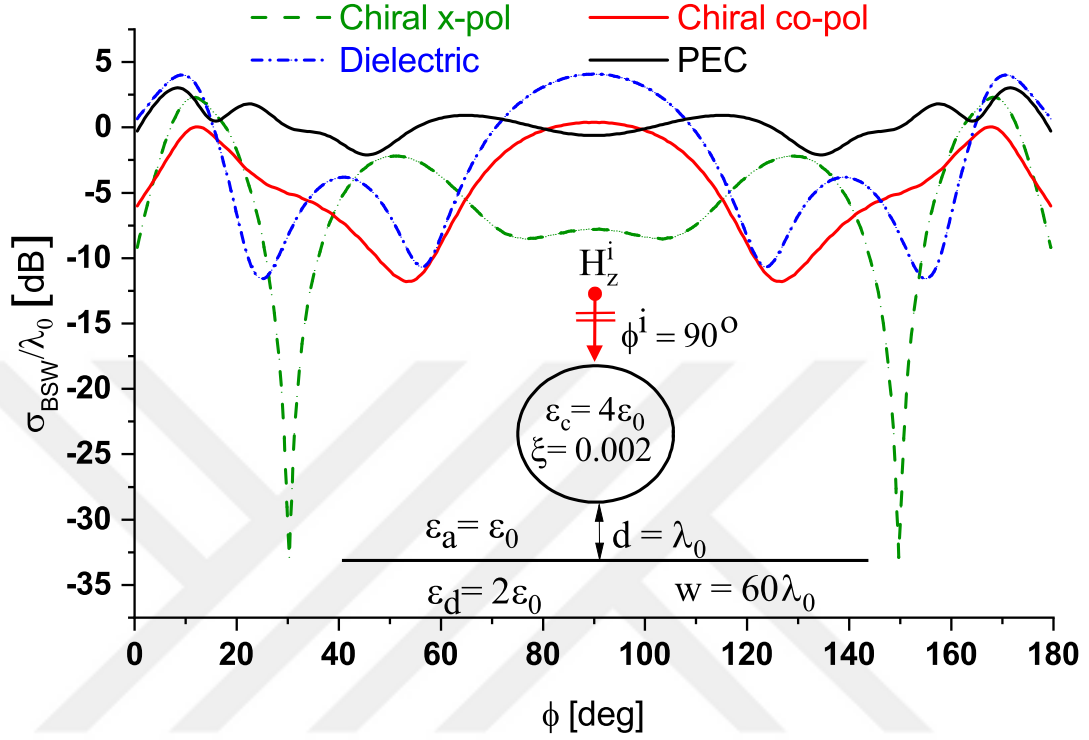


Figure 3.38: Bistatic scattering for a circular ( $r = 0.5\lambda_0$ ) chiral, dielectric, and a PEC cylinder placed above a DHS. TE excitation.

The effect of incident angle on the bistatic scattering width of a circular chiral cylinder placed above a dielectric interface is investigated. The incident plane wave is TM. The co-polarized components are presented in Fig. 3.39. Since we are interested in the scattering in the upper half-space, the scattering width is presented for the upper half-space only. It was observed that for excitation angles close to horizon, the perturbed currents on the shadowed side of the interface took longer to converge. This effect is shown in Sec. 3.5.4.3. Depending on the cylinder size and the incident angle, the strip width must be chosen properly for acceptable results.

Figure 3.40 shows the corresponding cross-polar component for the bistatic scattering width of the same circular cylinder for different incident angles.

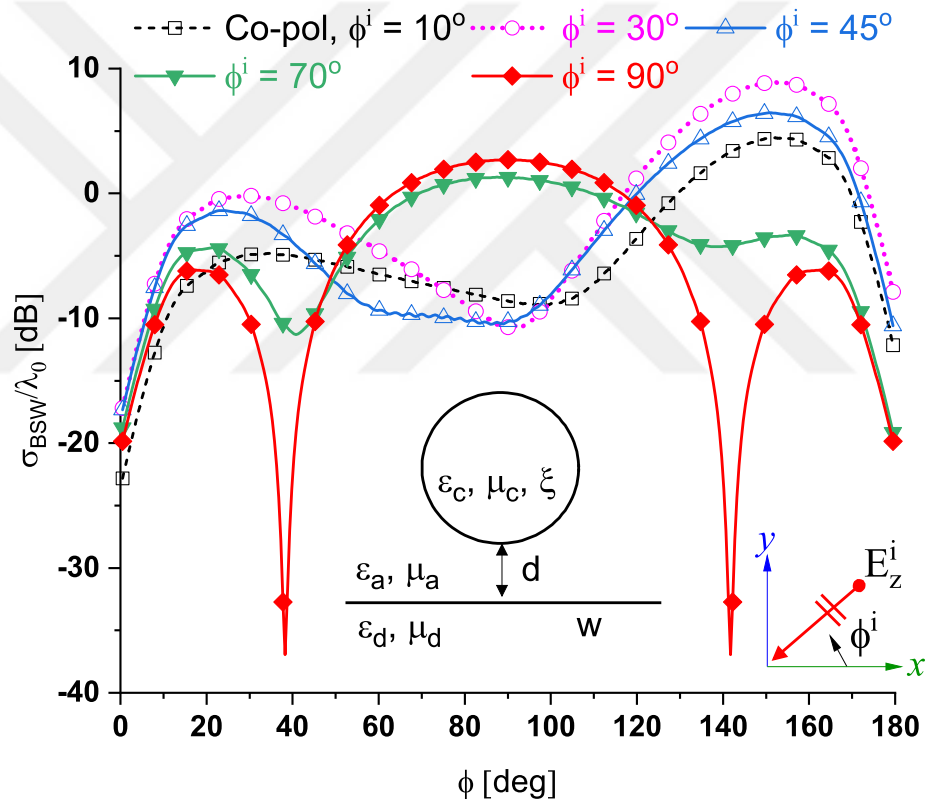


Figure 3.39: Co-polarized bistatic scattering width of a circular chiral cylinder above a dielectric half-space for TM excitation with different incident angles. Radius  $r = 0.15\lambda_0$ ,  $d = 0.25\lambda_0$ ,  $w = 40\lambda_0$ ,  $\epsilon_c = 4\epsilon_0$ ,  $\mu_c = 3.2\mu_0$ ,  $\xi = 0.002$ ,  $\epsilon_d = 10\epsilon_0$ ,  $\mu_d = 2.5\mu_0$ .

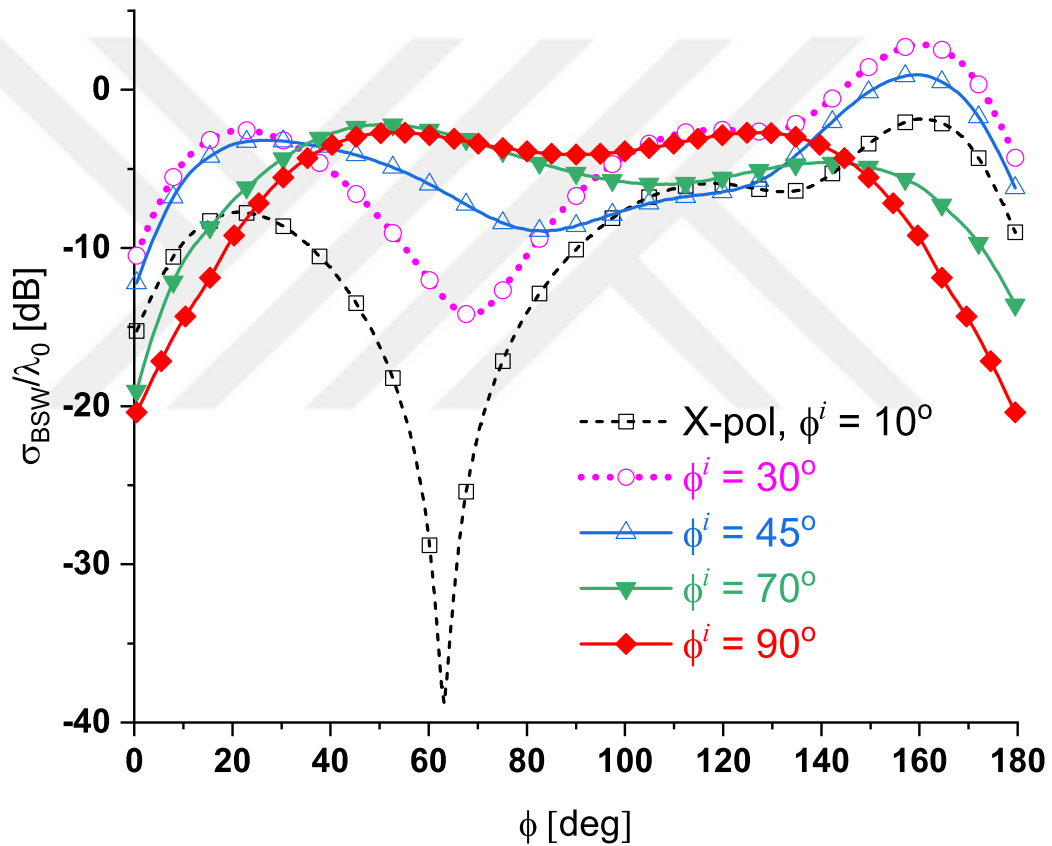


Figure 3.40: Cross-polarized bistatic scattering width of a circular chiral cylinder above a dielectric half-space for TM excitation with different incident angles. Radius  $r = 0.15\lambda_0$ ,  $d = 0.25\lambda_0$ ,  $w = 40\lambda_0$ ,  $\epsilon_c = 4\epsilon_0$ ,  $\mu_c = 3.2\mu_0$ ,  $\xi = 0.002$ ,  $\epsilon_d = 10\epsilon_0$ ,  $\mu_d = 2.5\mu_0$ .



### 3.6.2 Lossy Scatterers

Here, the effect of electric ( $\tan\delta_e$ ) and magnetic ( $\tan\delta_m$ ) losses is investigated. The bistatic scattering width for lossy and lossless cases is compared. It would be interesting to observe the difference of scattering with respect to dielectric and PEC cylinders as well. A circular cylinder of radius  $r = 0.3\lambda_0$  is placed distance  $d = 0.3\lambda_0$  above a strip of width  $w = 40\lambda_0$ . The scatterer is characterized by  $\epsilon_c = 4\epsilon_0$ ,  $\mu_c = 2.8\mu_0$ ,  $\xi = 0.002$ ,  $\tan\delta_e = \tan\delta_m = 0.05$ . The half-space is lossless and non-magnetic with a relative permittivity of  $\epsilon_d = 2\epsilon_0$ . The setup is illuminated by a TM plane wave from  $90^\circ$  off the  $x$ -axis.

The bistatic scattering width for the lossless and lossy chiral cylinder is compared with dielectric and PEC cylinder. The co-polarized components for chiral, dielectric, and PEC cylinders are shown in Fig. 3.41 followed by the cross-polar component for the chiral cylinder in Fig. 3.42. For the co-polar components, the scattering width of the chiral cylinder is lower than the PEC and dielectric cylinders on the lit side, for both lossless and lossy cases. In case of the chiral cylinder, the back-scattered field is greater for the lossy cylinder but in other directions field of lossless cylinder increases. Also, it can be seen that the cross-polar component, for the lossless case, on the lit side ( $90^\circ$ ) is greater than the co-polar component by 2.8 dB. However, the fields decay sharply to give a null in the cross-polar scattering width, for this case, at  $50^\circ$  and  $130^\circ$ . Notice also, there is 9 dB difference between the chiral (lossless) and the PEC and dielectric (lossless) cylinders at  $90^\circ$ . As mentioned in the literature review, chiral material can be used as EM absorbers, if the properties are chosen appropriately. The observations made here could not have been made with simple theory alone.

Figures 3.43a and 3.43b show the amplitude of the scattered far-field in the upper half-space and transmitted through the dielectric interface to the lower half-space. It can be seen that the cross-polar component has a similar pattern to the co-polar field but magnitude of the former is smaller.

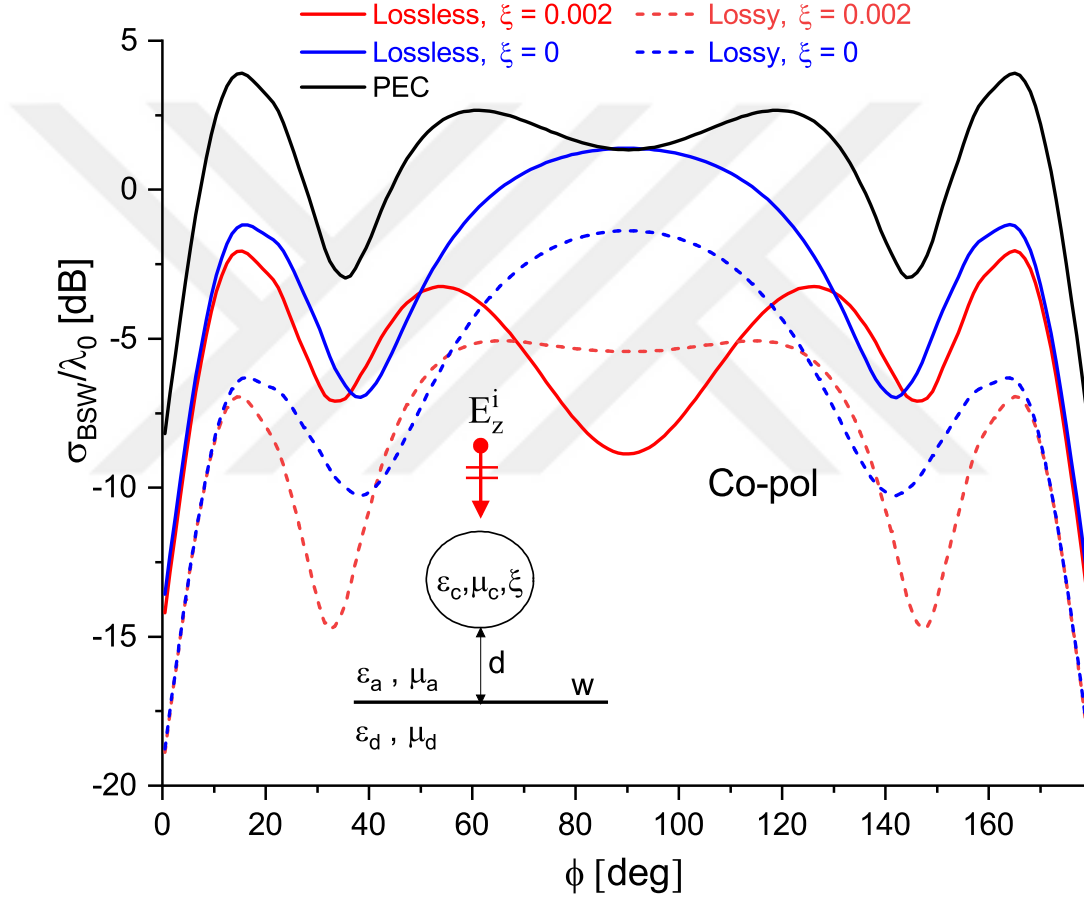


Figure 3.41: Comparison of co-polarized bistatic scattering width of a circular cylinder above a dielectric half-space for lossy and lossless cases. TM excitation at  $\phi^i = 90^\circ$ . Chiral, dielectric, and PEC cylinders are compared. Radius,  $r = 0.3\lambda_0$ ,  $d = 0.3\lambda_0$ ,  $w = 40\lambda_0$ ,  $\epsilon_d = 2\epsilon_0$ ,  $\mu_d = \mu_0$ ,  $\epsilon_c = 4\epsilon_0$ ,  $\mu_c = 2.8\mu_0$ ,  $\xi = 0.002$ ,  $\tan\delta_e = \tan\delta_m = 0.05$ . Solid and dashed lines, respectively, show the lossless and lossy cases.

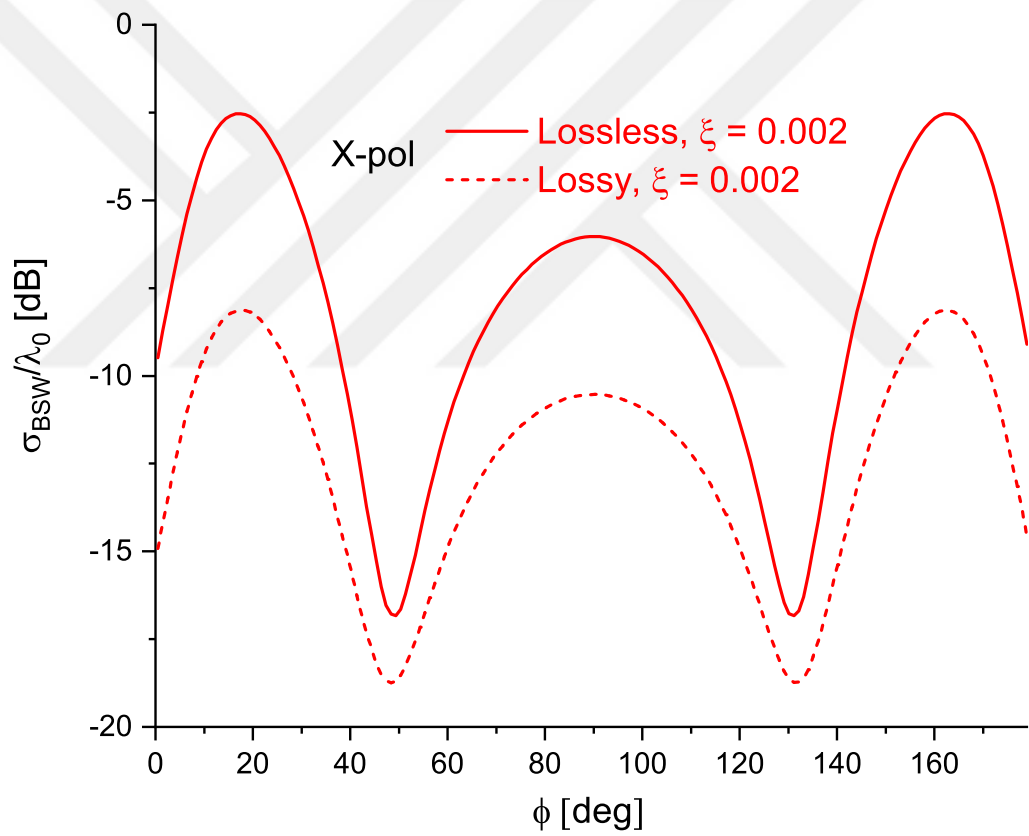


Figure 3.42: Corresponding cross-polarized component for the chiral lossy and lossless circular cylinder for the setup in Fig. 3.41.

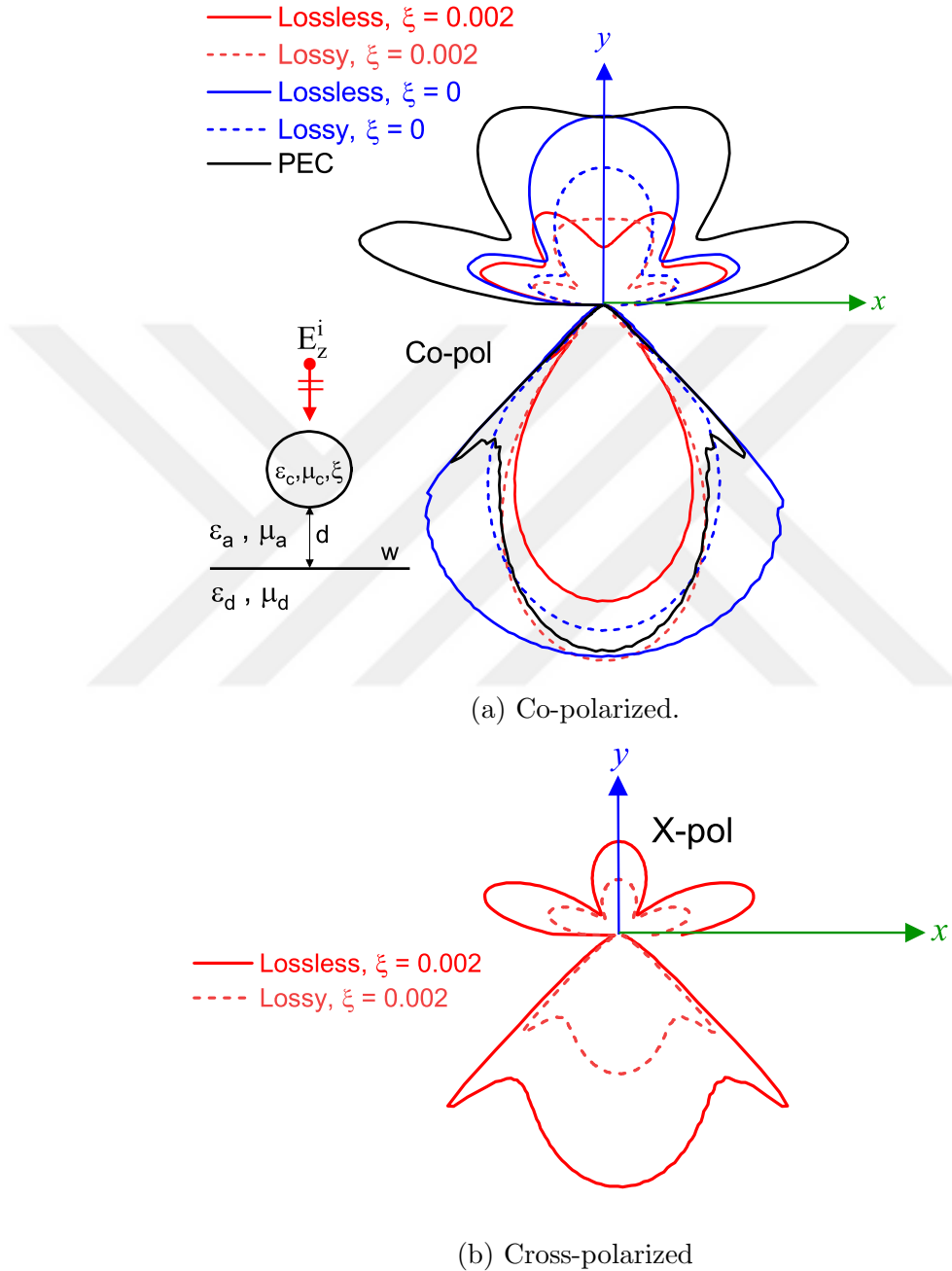


Figure 3.43: Amplitude of the scattered far-field. Co-polarized component for a circular cylinder above a dielectric half-space for lossy and lossless cases. TM excitation at  $\phi^i = 90^\circ$ . Chiral, dielectric, and PEC cylinders are compared. Radius,  $r = 0.3\lambda_0$ ,  $d = 0.3\lambda_0$ ,  $w = 40\lambda_0$ ,  $\epsilon_d = 2\epsilon_0$ ,  $\mu_d = \mu_0$ ,  $\epsilon_c = 4\epsilon_0$ ,  $\mu_c = 2.8\mu_0$ ,  $\xi = 0.002$ ,  $\tan\delta_e = \tan\delta_m = 0.05$ . Solid and dashed lines, respectively, show the lossless and lossy cases. Same setup as in Fig. 3.41. The scattered field in the upper half-space and the transmitted fields to the lower half-space are shown.  $y < 0$  is the dielectric half-space.

### 3.6.2.1 Effect of Chirality on Scattering

A lossy circular chiral cylinder is investigated in this section. The chirality admittance of the scatterer is changed to observe its effect on the scattering properties. The bistatic scattering width and the far-field amplitude are shown in Figs. 3.44 to 3.47. The results show an unpredictable behaviour due to variation in  $\xi$ . Finer steps must be taken in order to observe the effect more vividly as shown in Fig. 3.23. The idea here is to see the effect of abrupt change. For  $\xi = 0.001$  the cross-polar fields are greater than the co-polar components on the lit side. This is a different, but not surprising, behaviour of the chiral materials. Such observations were made in [5] as well.

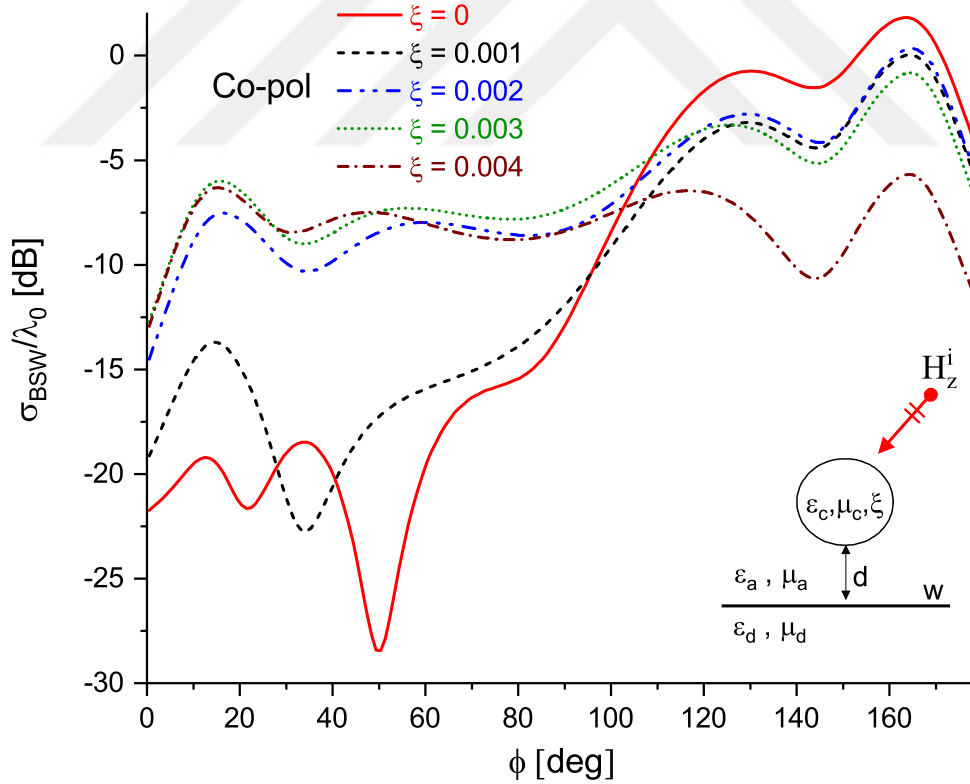


Figure 3.44: Co-polarized bistatic scattering width of a chiral circular cylinder above a dielectric half-space for various chirality admittance values. TE excitation at  $\phi^i = 45^\circ$ . Radius,  $r = 0.2\lambda_0$ ,  $d = 0.5\lambda_0$ ,  $w = 40\lambda_0$ ,  $\epsilon_d = 3\epsilon_0$ ,  $\mu_d = \mu_0$ ,  $\epsilon_c = 6\epsilon_0$ ,  $\mu_c = 1.5\mu_0$ ,  $\tan\delta_e = 0.1$ ,  $\tan\delta_m = 0$ .

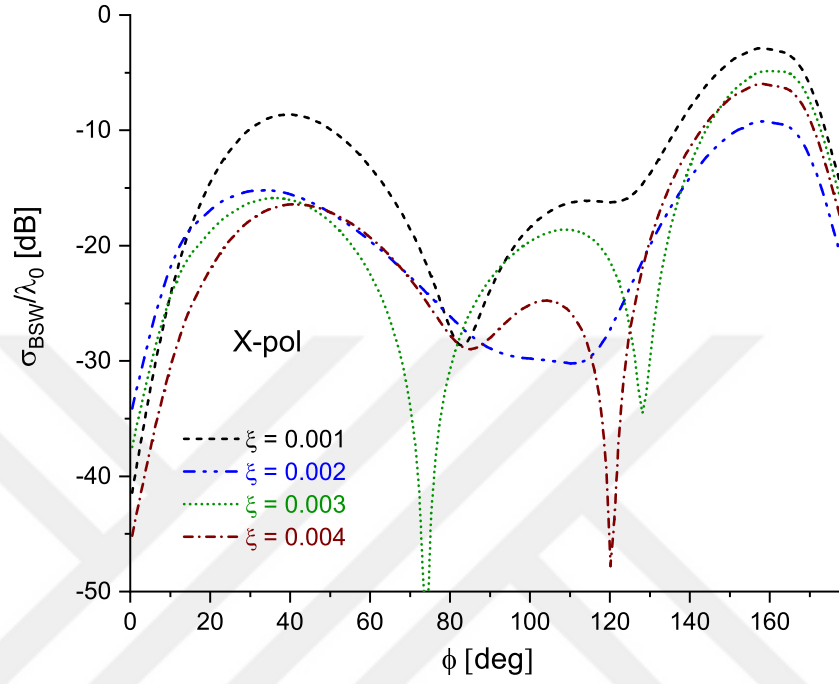


Figure 3.45: Corresponding cross-polarized component for the setup in Fig. 3.44.

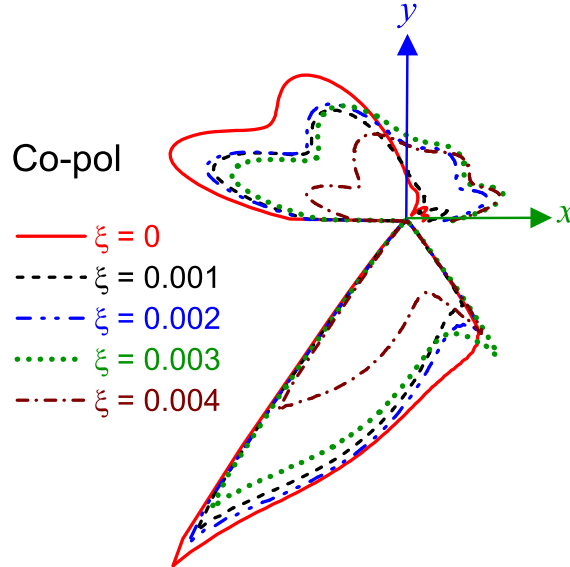


Figure 3.46: Amplitude of the co-polarized scattered far-field due to a chiral circular cylinder placed above a dielectric half-space for various chirality admittance values. TE excitation at  $\phi^i = 45^\circ$ . Radius,  $r = 0.2\lambda_0$ ,  $d = 0.5\lambda_0$ ,  $w = 40\lambda_0$ ,  $\epsilon_b = 3\epsilon_0$ ,  $\mu_b = \mu_0$ ,  $\epsilon_c = 6\epsilon_0$ ,  $\mu_c = 1.5\mu_0$ ,  $\tan\delta_e = 0.1$ , and  $\tan\delta_m = 0$ . Same setup as Fig. Fig. 3.44.

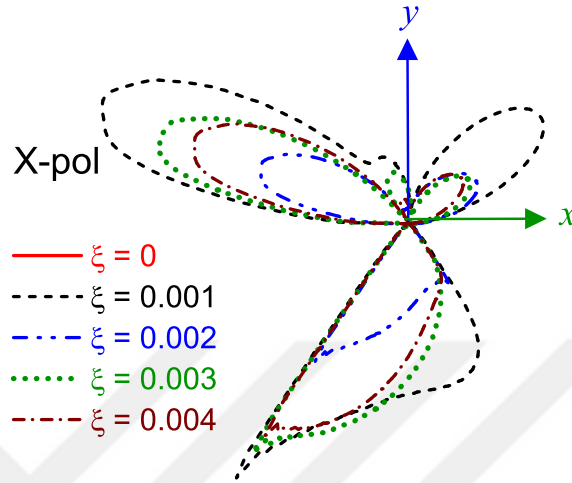


Figure 3.47: Corresponding cross-polarized component of the far-field for Fig. 3.46. We can see, there is no cross-polar component when  $\xi = 0$ , because the chiral becomes a regular dielectric.

### 3.6.2.2 Conclusion

The results computed in this section showed excellent agreement with published literature for limiting cases. Various circular cylinders; PEC, dielectric and chiral, were simulated with different parameters to gauge the accuracy and robustness of the solution method proposed here. Effect of lossy and lossless scatterer on the scattered fields was also studied. No spurious results were encountered in the above study. To test the method further, some arbitrary cross-sections are studied in the following sections.

### 3.7 Scattering from Rectangular Chiral Cylinder

To show the flexibility of the approach, a chiral cylinder of rectangular cross-section ( $0.25\lambda_0 \times 0.15\lambda_0$ ) is considered next. The problem setup is shown in the inset of Fig. 3.48. The system is excited by a TM plane wave incident from  $\phi^i = 30^\circ$ . The cylinder is placed a height  $d = 0.1\lambda_0$  above a dielectric half-space represented by a strip of width  $w = 40\lambda_0$  and characterized by  $\epsilon_d = 4\epsilon_0$ ,  $\mu_d = \mu_0$ . The chiral cylinder is characterized by  $\epsilon_c = 6\epsilon_0$ ,  $\mu_c = 2\mu_0$ ,  $\xi = 0.0005$ .

Figure 3.48 shows the magnitude of the perturbed surface currents on the dielectric strip. Although the dielectric strip width assumed for this problem was  $40\lambda_0$ , it can be observed that the currents are negligible after about  $10\lambda_0$ . The asymmetric behavior of the perturbed currents on the strip can be observed due to the asymmetric excitation. Figure 3.49 shows the scattered far-field pattern for the same problem. Note that the cross-polar component of the far-field is significantly smaller than the co-polar component. Once again, it is observed that the scattered fields are unpredictable.



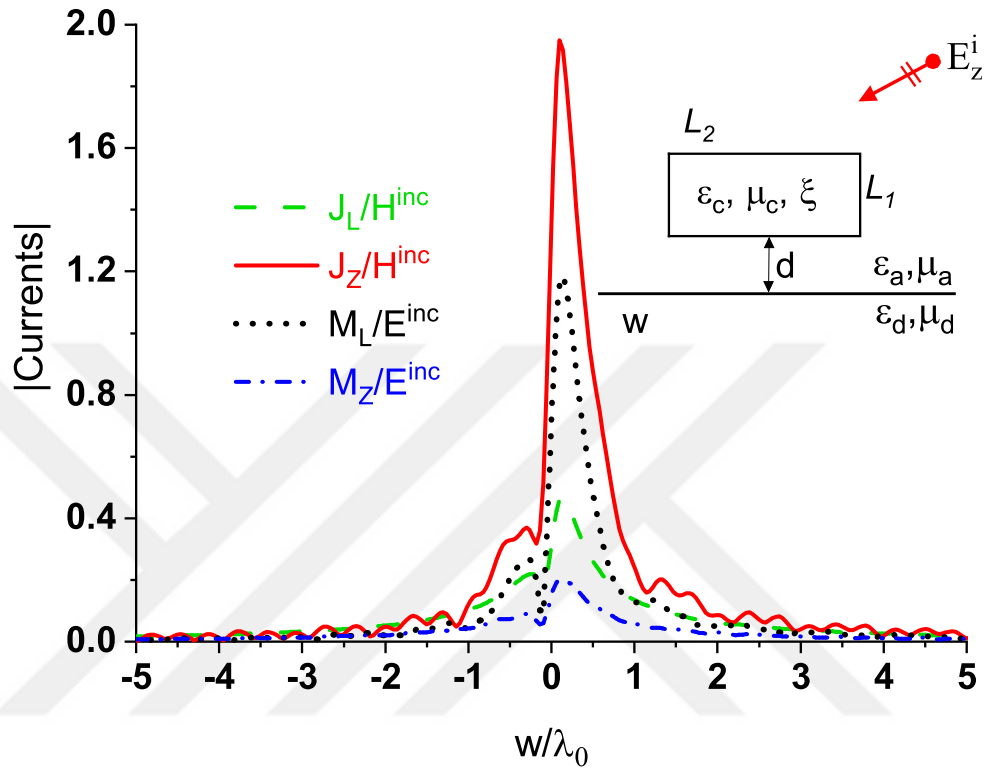


Figure 3.48: Magnitude of the perturbed currents induced on a dielectric half-space due to a rectangular chiral cylinder placed above it. TM excitation,  $L_1 = 0.15\lambda_0$ ,  $L_2 = 0.25\lambda_0$ ,  $d = 0.1\lambda_0$ ,  $w = 40\lambda_0$ ,  $\epsilon_d = 4\epsilon_0$ ,  $\epsilon_c = 6\epsilon_0$ ,  $\mu_c = 2\mu_0$ ,  $\xi = 0.0005$ ,  $\phi^i = 30^\circ$ .

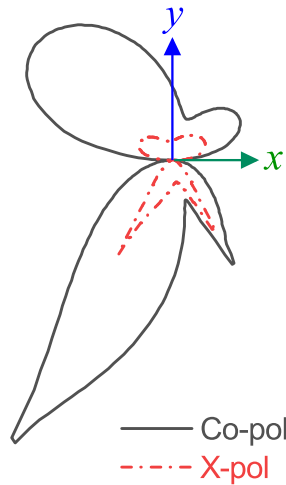


Figure 3.49: Scattered far-fields due to a rectangular chiral cylinder placed above a dielectric half-space. The setup is shown in inset of Fig. 3.48.

### 3.7.1 Effect of Chirality

The effect of chirality admittance on the scattering properties of a 2-D cylinder with rectangular cross-section is investigated. The problem setup and the bistatic scattering results are presented in Figs. 3.50 and 3.51. A cylinder with a rectangular cross-section of  $(0.2 \times 0.35)\lambda_0$ , is placed a distance  $d = 0.5\lambda_0$  above a dielectric half-space, represented by a strip of width  $w = 40\lambda_0$ . The half-space is characterized by  $\epsilon_d = 4\epsilon_0$ ,  $\mu_d = 1.5\mu_0$  and for the chiral cylinder  $\epsilon_c = 6\epsilon_0$ ,  $\mu_c = 2.5\mu_0$ . The setup is excited by a plane TM wave incident from  $\phi^i = 75^\circ$ . Electric and magnetic loss of the scatterer is given by  $\tan\delta_e = \tan\delta_m = 0.05$ , respectively.

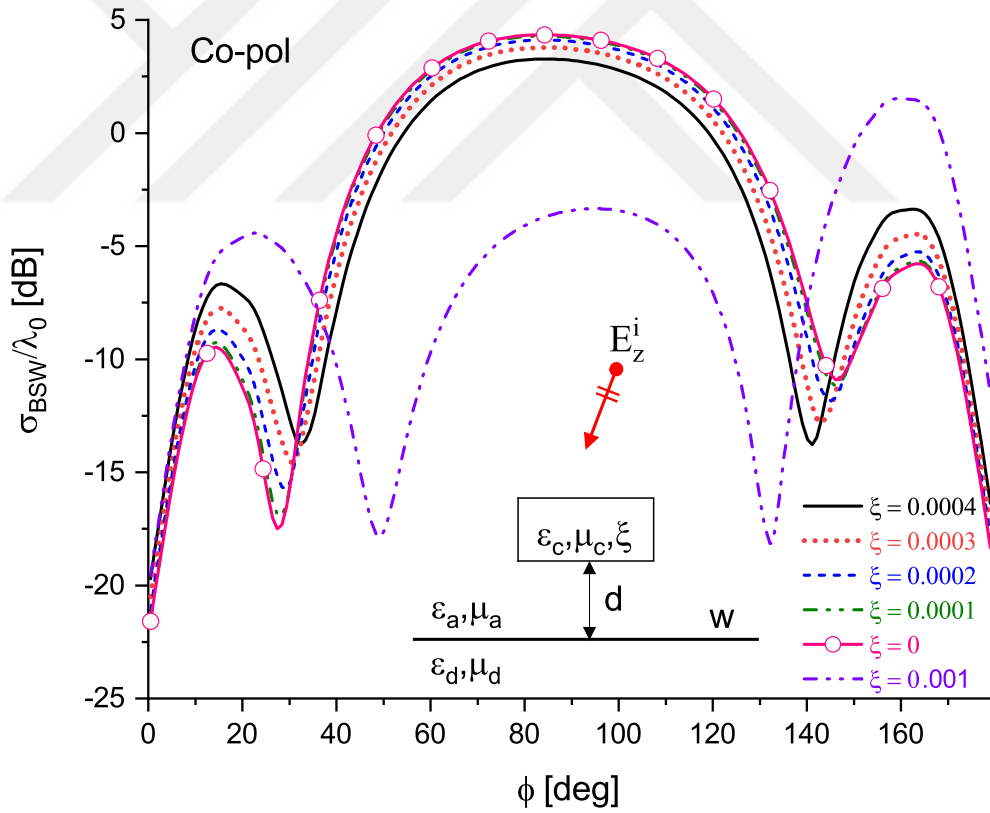


Figure 3.50: Co-polarized bistatic scattering width due to a rectangular chiral cylinder above a dielectric half-space. TM excitation,  $L_1 = 0.2\lambda_0$ ,  $L_2 = 0.35\lambda_0$ ,  $d = 0.5\lambda_0$ ,  $w = 40\lambda_0$ ,  $\epsilon_d = 4\epsilon_0$ ,  $\mu_d = 1.5\mu_0$ ,  $\epsilon_c = 6\epsilon_0$ ,  $\mu_c = 2.5\mu_0$ ,  $\phi^i = 75^\circ$ . Electric and magnetic losses for the scatterer are given by  $\tan\delta_e = \tan\delta_m = 0.05$ .

The currents on the interface smoothly decayed to zero and are not shown here. From the co-polar component of the scattering width, as the chirality changes

from zero to 0.0004, no surprising results are observed. The nulls become deeper and the side lobes increase in magnitude. Here, the chirality is changed in smaller steps. Finally, a random value of chirality admittance,  $\xi = 0.001$  is observed. This reduced the back-scattered fields and further enhanced the side lobes. The position of the nulls changed from approximately  $150^\circ$  for  $\xi = 0$  to  $137^\circ$  and the null depth increased by 6 dB. The cross-polarized component decreases as the chirality admittance decreases and finally disappears for  $\xi = 0$ .

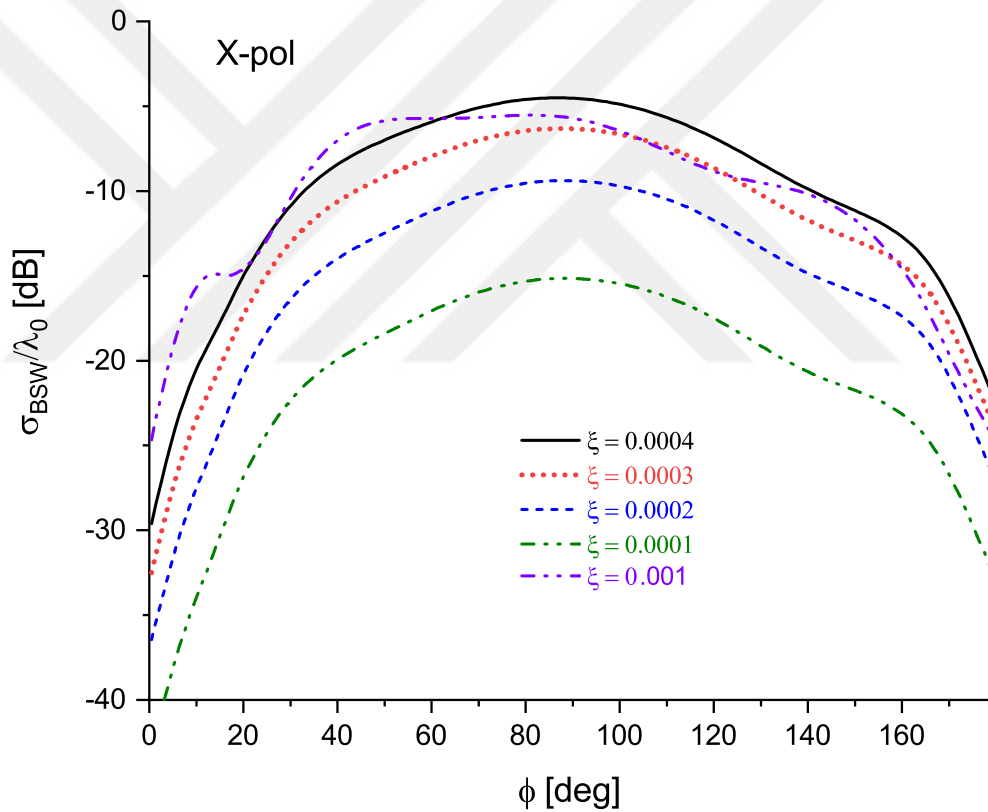


Figure 3.51: Corresponding cross-polarized component for the setup in Fig. 3.50. Note that there is no cross-polar component when  $\xi = 0$ , as expected.

### 3.7.2 Effect of Incident Angle

Incident angle plays an important role in the induction of currents on the scatterer. This section discusses the effect of incident angle on the scattering properties of a rectangular cylinder with different parameters than the case studied in the above section. The perturbed currents are shown in Fig. 3.52 and the problem setup is shown in Fig. 3.53 along with the amplitude of the scattered field in the upper half-space for the various angles. Figure 3.54 shows the corresponding cross-polarized component of the scattered field. The setup is illuminated by a TM plane wave from  $\phi^i = 20^\circ$ ,  $\phi^i = 60^\circ$ ,  $\phi^i = 90^\circ$ ,  $\phi^i = 120^\circ$ , and  $\phi^i = 160^\circ$ . The angles are symmetric about the normal direction.

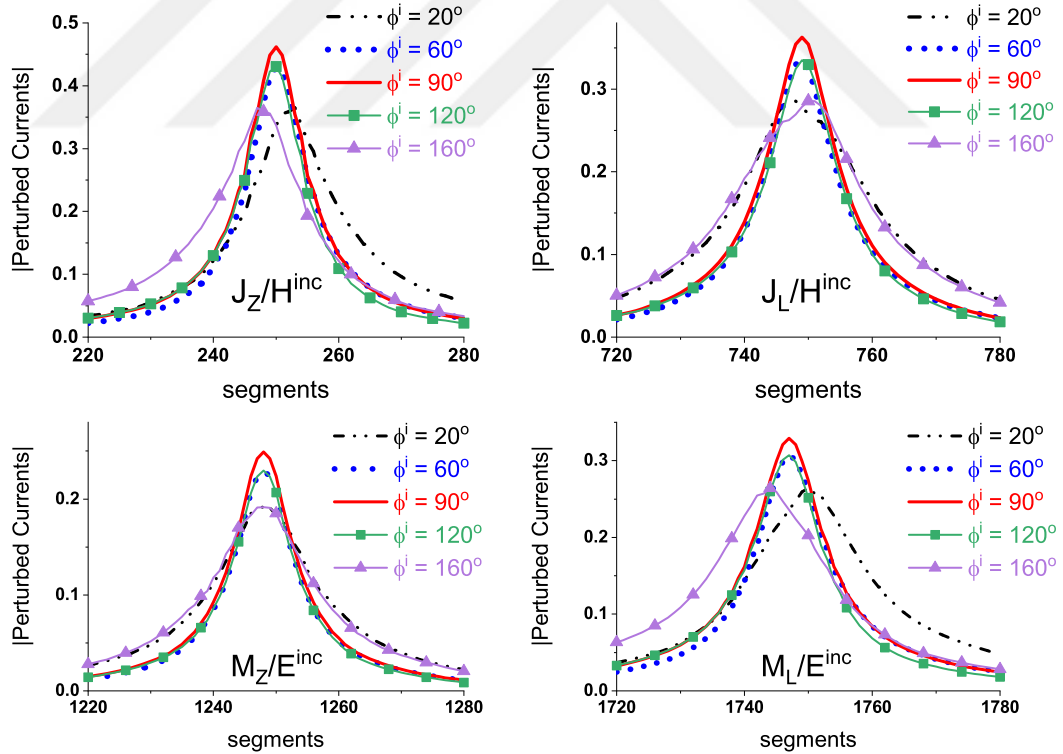


Figure 3.52: Perturbed currents due to a rectangular cylinder placed above a dielectric half-space, the setup is shown in Fig. 3.53. Currents plotted for  $3.5\lambda_0$  portion of the strip, starting from the center of the strip.  $L_1 = 0.25\lambda_0$ ,  $L_2 = 0.1\lambda_0$ ,  $d = 0.5\lambda_0$ ,  $w = 60\lambda_0$ ,  $\epsilon_d = 2\epsilon_0$ ,  $\mu_d = \mu_0$ ,  $\epsilon_c = 4.5\epsilon_0$ ,  $\mu_c = 2.5\mu_0$ ,  $\xi = 0.002$ ,  $\tan\delta_e = 0.1$ ,  $\tan\delta_m = 0.05$ .

The angles are chosen to observe the symmetry of the results, which is a good

indicator of the correct working of the algorithm. For instance, for the top left subplot in Fig. 3.52, the symmetry in  $|\mathbf{J}_z|$  can be observed. Its peak is centered at segment 251, which is the center of the strip. Angles  $20^\circ$  and  $160^\circ$  show the same off-set of peaks in opposite directions. Similarly, for angles  $60^\circ$  and  $120^\circ$ . Note that for angle of incidence close to the horizon, the perturbed currents take longer to converge, as expected. A similar symmetry is also observed in the far-fields for the co- and cross-polar components. Fields in the upper half-space are plotted only. The symmetry in the scattered fields due to the excitation and the shape of the scatterer can be observed.

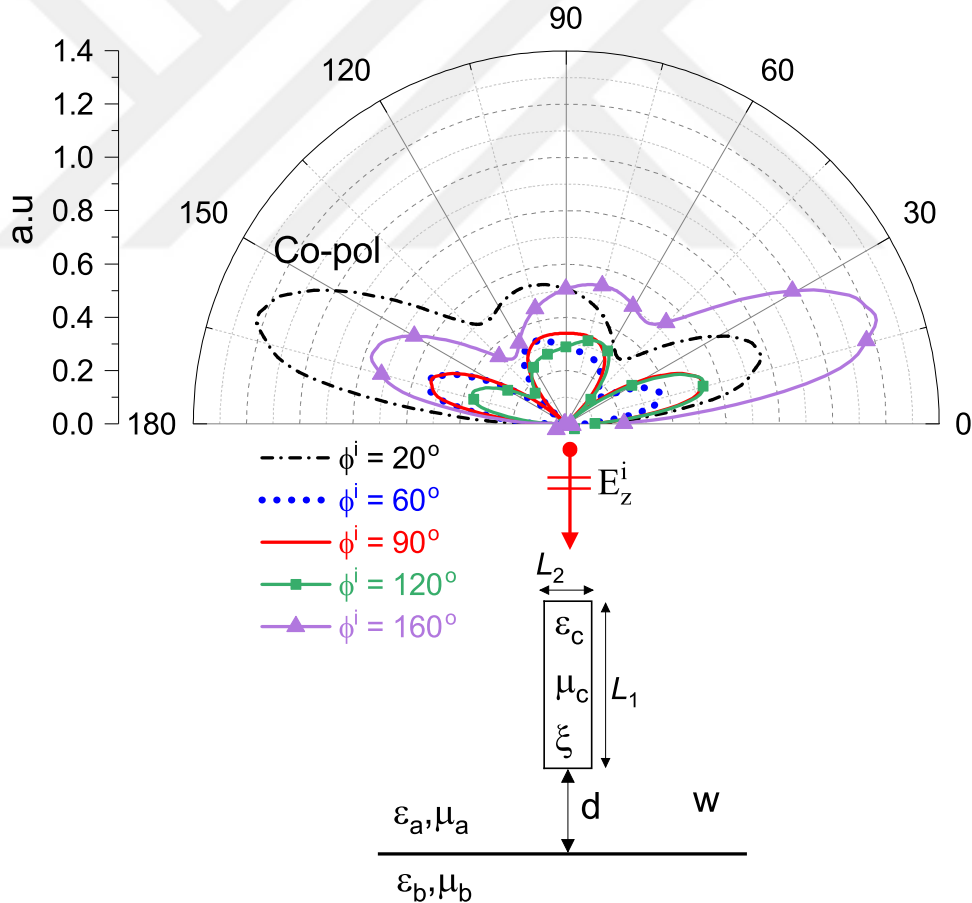


Figure 3.53: Co-polarized scattered far-field due to a rectangular chiral cylinder above a dielectric half-space. TM excitation,  $L_1 = 0.25\lambda_0$ ,  $L_2 = 0.1\lambda_0$ ,  $d = 0.5\lambda_0$ ,  $w = 60\lambda_0$ ,  $\epsilon_d = 2\epsilon_0$ ,  $\mu_d = \mu_0$ ,  $\epsilon_c = 4.5\epsilon_0$ ,  $\mu_c = 2.5\mu_0$ ,  $\xi = 0.002$ . Electric and magnetic losses for the scatterer are given by,  $\tan\delta_e = 0.1$  and  $\tan\delta_m = 0.05$ , respectively.

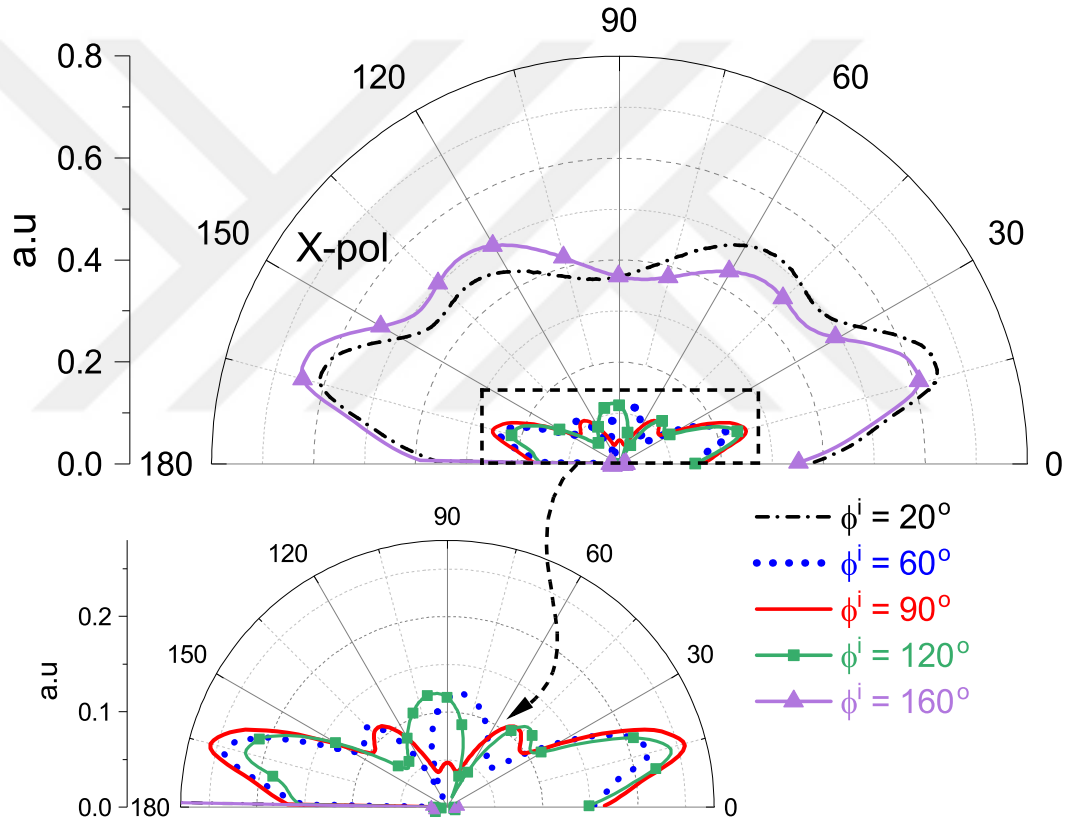


Figure 3.54: Corresponding cross-polarized component for the setup in Fig. 3.53. Zoomed in view for weaker fields is also shown. TM excitation,  $L_1 = 0.25\lambda_0$ ,  $L_2 = 0.1\lambda_0$ ,  $d = 0.5\lambda_0$ ,  $w = 60\lambda_0$ ,  $\epsilon_d = 2\epsilon_0$ ,  $\mu_d = \mu_0$ ,  $\epsilon_c = 4.5\epsilon_0$ ,  $\mu_c = 2.5\mu_0$ ,  $\xi = 0.002$ . Electric and magnetic losses for the scatterer are given by,  $\tan\delta_e = 0.1$  and  $\tan\delta_m = 0.05$ , respectively.

### 3.8 Scattering from Square Chiral Cylinder

Next, a chiral cylinder of square cross-section is analyzed. The setup is shown in the inset of Fig. 3.55, where a square cylinder of side length  $L_1 = 0.4\lambda_0$  is excited by a TM plane wave with  $\phi^i = 90^\circ$ . The lossless homogeneous square scatterer is characterized by  $\epsilon_c = 6\epsilon_0$ ,  $\mu_c = 2\mu_0$ ,  $\xi = 0.0005$ . The half-space is characterized by  $\epsilon_d = 4\epsilon_0$ ,  $\mu_d = \mu_0$  and is approximated by a finite width strip of  $40\lambda_0$ .

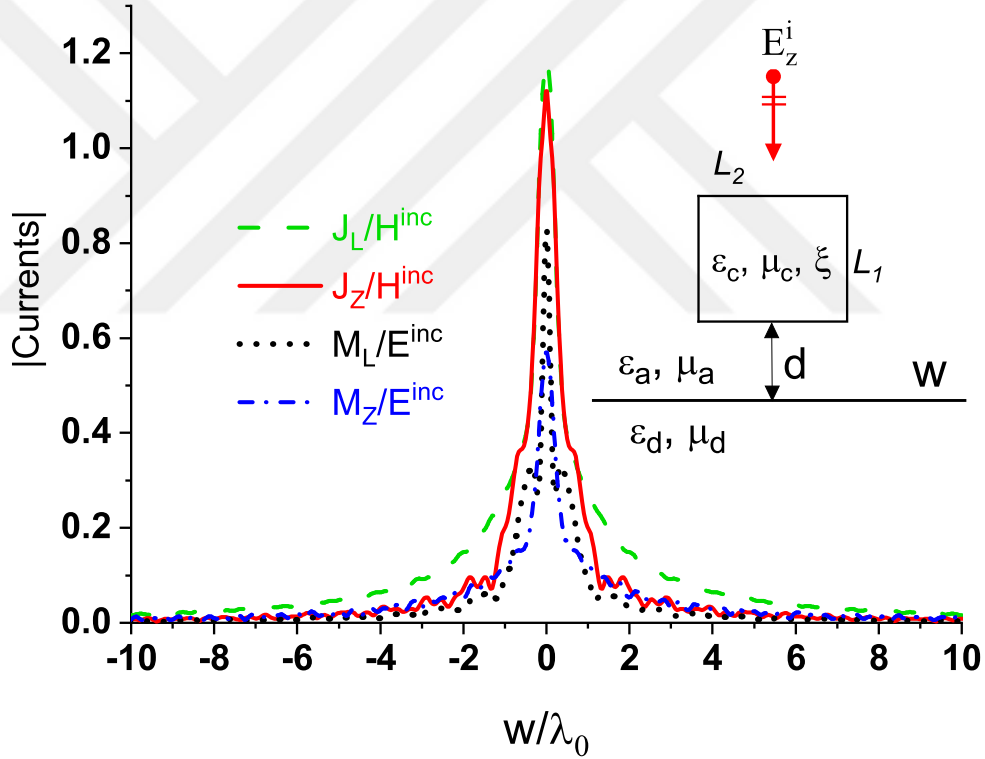


Figure 3.55: Magnitude of the perturbed currents induced on a dielectric interface due to a square chiral cylinder placed above it. TM excitation,  $L_1 = L_2 = 0.4\lambda_0$ ,  $d = 0.1\lambda_0$ ,  $w = 40\lambda_0$ ,  $\epsilon_d = 4\epsilon_0$ ,  $\epsilon_c = 6\epsilon_0$ ,  $\mu_c = 2\mu_0$ ,  $\xi = 0.0005$ ,  $\phi^i = 90^\circ$ .

The scatterer is placed close ( $d = 0.1\lambda_0$ ) to the interface, which causes more fluctuations in the induced currents, as shown in Fig. 3.55. Although the excitation is a TM wave, the lateral perturbed electric current is larger than the longitudinal one, and the cross-polar component of the back-scattered far-field is larger than the co-polar component, shown in Fig. 3.56.

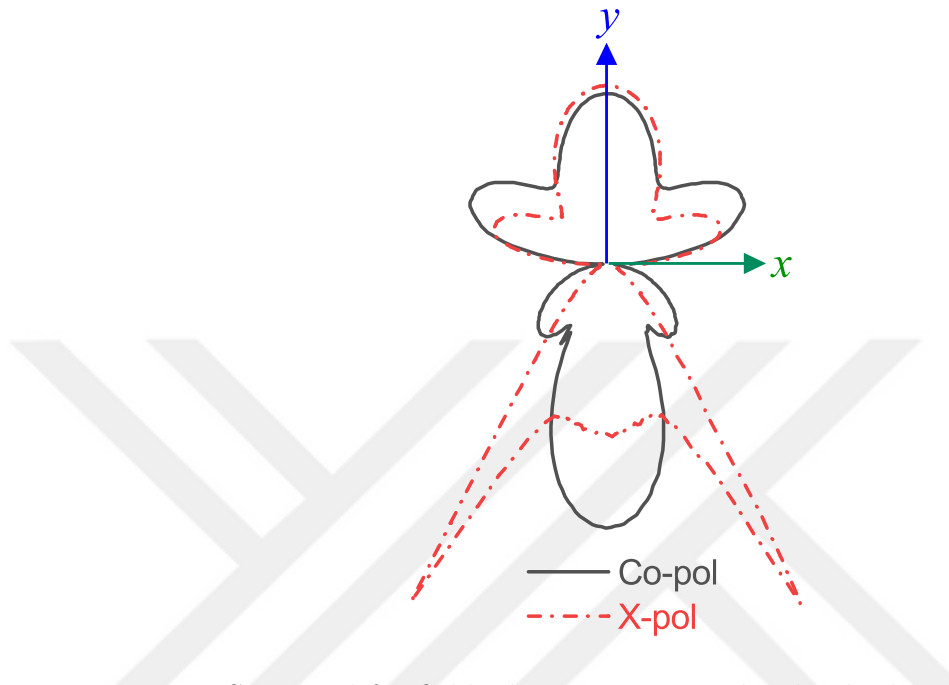


Figure 3.56: Scattered far-fields due to a square chiral cylinder placed above a dielectric half-space. The setup is shown in inset of Fig. 3.55.

To further investigate this, the chirality parameter ( $\xi$ ) was varied to observe its effect on the scattering. Results for the co- and cross-polarized bistatic scattering width for the same problem with different chirality admittance values are presented in Figs. 3.57 and 3.58, respectively. For the co-polar component it was observed that the side lobes became deeper and well defined. However, this behaviour is not predictable and will be completely different at some other admittance values.

Figure 3.58 shows how the cross-polar component dropped, from -8 dB (for  $\xi = 0.001$ ) to -15 dB (for  $\xi = 0.0015$ ) at  $90^\circ$ , by an increase of 0.0005 in the chirality admittance and then jumped to -4 dB (for  $\xi = 0.002$ ) with another increase of 0.0005. To verify this radical behavior, another study was performed where the chirality was changed from 0.0015 to 0.002 in smaller steps. It was seen (results not shown here) that the cross-polar component increased gradually and matched the value for  $\xi = 0.002$ . This phenomenon is unpredictable by simple theory. Such comparisons are not present in the literature even for chiral cylinders in free-space.



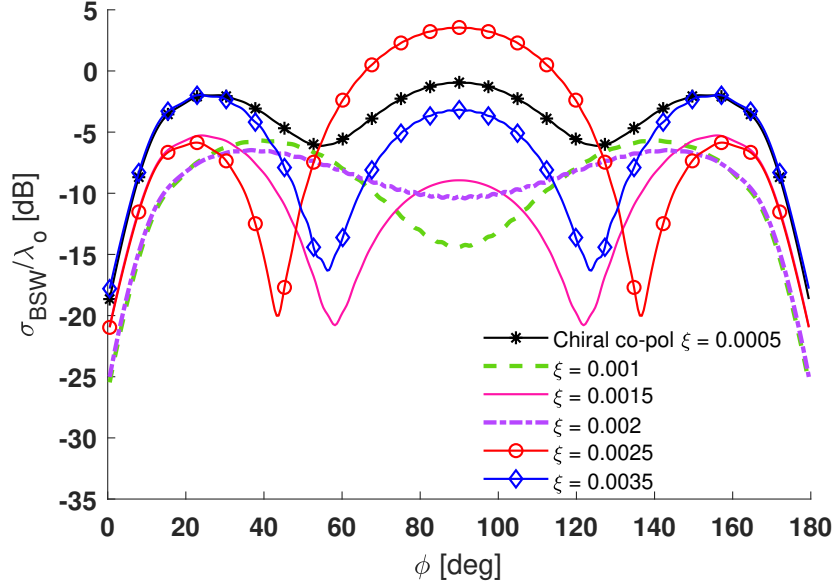


Figure 3.57: Effect of  $\xi$  variation on the bistatic scattering width (Co-polarized component) of a square chiral cylinder placed above a dielectric half-space. TM excitation,  $L_1 = L_2 = 0.4\lambda_0$ ,  $d = 0.1\lambda_0$ ,  $w = 40\lambda_0$ ,  $\epsilon_d = 4\epsilon_0$ ,  $\epsilon_c = 6\epsilon_0$ ,  $\mu_c = 2\mu_0$ ,  $\phi^i = 90^\circ$ . Same setup is used as in Fig. 3.55.

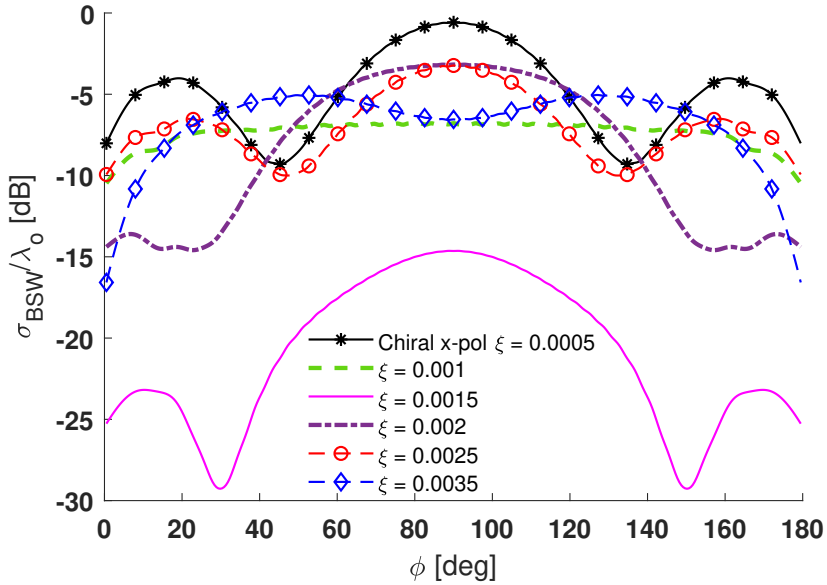


Figure 3.58: Effect of  $\xi$  on the cross-polar component of the scattering width of a square chiral cylinder placed above a dielectric half-space. Setup shown in Fig. 3.55

The study performed here shows that for the parameters used, the cross-polar component of the scattered field in the backward direction ( $\phi = 90^\circ$ ) is comparable to the co-polar component. This might not be the case for other geometries and parameters. For instance, in case of the rectangular chiral cylinder, the cross-polar component is much smaller than the co-polar component (see Sec. 3.7.1). It should also be noted that a variation in the chirality admittance can drastically change the scattering properties.

Figure 3.59 shows a comparison of the bistatic scattering width of a square chiral cylinder with a dielectric and a PEC cylinder of the same dimensions. While the back-scattered fields are similar for the dielectric and chiral cylinders, the side lobes of the chiral cylinder are at least 6 dB lower at  $30^\circ$  and  $160^\circ$  relative to those of the PEC and dielectric cylinders. Note that the cross-polar component of the chiral cylinder is comparable to the co-polar component of the back-scattered field. It is also interesting to see that the back-scattered field of the PEC is about 10 dB less than the field of the chiral and dielectric cylinders.

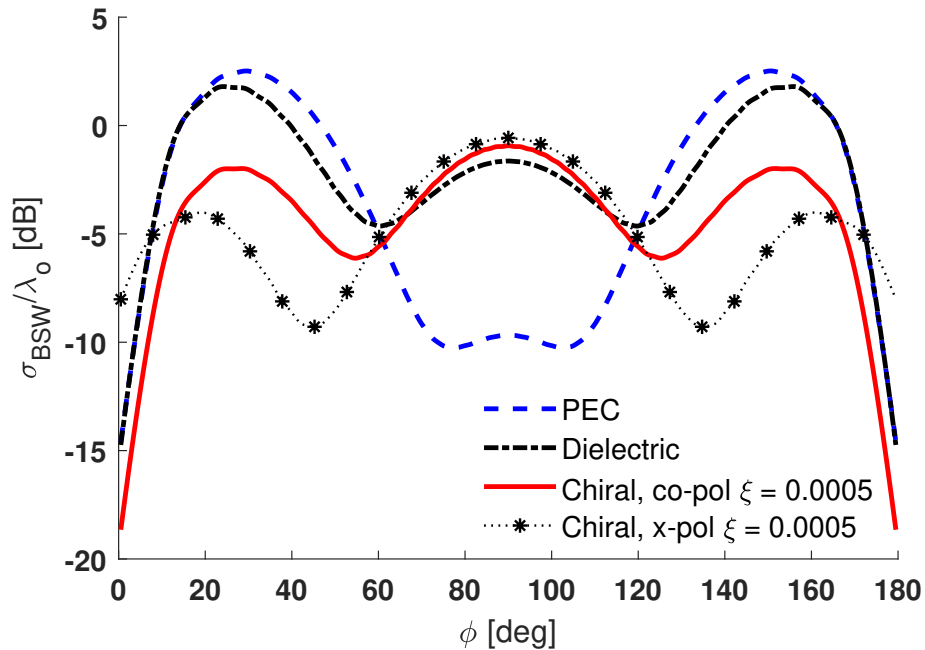


Figure 3.59: Bistatic scattering width comparison for PEC, dielectric, and chiral square cylinders. Setup shown in the inset of Fig. 3.55.

### 3.9 Scattering From Elliptical Cylinders

In this section, scattering properties for a homogeneous chiral elliptical cylinder is investigated for TM and TE plane wave excitations. The system setup is shown in Fig. 3.60. An elliptical chiral cylinder ( $\epsilon_c = 3\epsilon_0$ ,  $\mu_c = \mu_0$ ,  $\xi = 0.001$ ) of major axis  $a = 0.2\lambda_0$  and minor axis  $b = 0.1\lambda_0$  is placed at a height  $d = 0.5\lambda_0$  above a dielectric half-space ( $\epsilon_d = 2\epsilon_0$ ,  $\mu_d = \mu_0$ ). The dielectric half-space is represented by a finite dielectric strip of width  $w = 40\lambda_0$ . This strip was chosen based on numerical experimentation and observing the perturbed currents. It was made sure that the currents on the strip decayed to zero as the distance from the cylinder increased. The currents are not shown here.

Fig. 3.60 shows the bistatic scattering width in the upper half-space only ( $0^\circ < \phi < 180^\circ$ ). It can be seen that the co-polar components of the TM and TE excitations are comparable in the backward direction ( $\phi = 90^\circ$ ) but they are completely different in other directions. The cross-polar components are exactly the same in the backward direction and they follow an almost similar trend in other directions.

Figure 3.61 shows the amplitude of the scattered far-field in the two half-spaces, i.e., free-space ( $0^\circ < \phi < 180^\circ$ ) and the dielectric half-space ( $180^\circ < \phi < 360^\circ$ ). Figures 3.61a and 3.61b, respectively, show the co-polar and cross-polar components for the TM and TE excitations. It can be observed that the co- and cross-polar terms behave differently, except at  $\phi = 90^\circ$  in which case they are comparable.

Next, the effect of chirality admittance is studied on the scattering width of a lossy elliptical cylinder placed above a dielectric half-space. The setup is excited by a TE plane wave as shown in the inset of Fig. 3.62a. Other parameters of the setup are given in the figure caption. The co-polarized component of the scattering width shows that, as the chirality increases the side lobes increase and the back-scattered field decreases. The co- and cross-polar components of the bistatic scattering width in the upper half-space are given in Fig. 3.62.

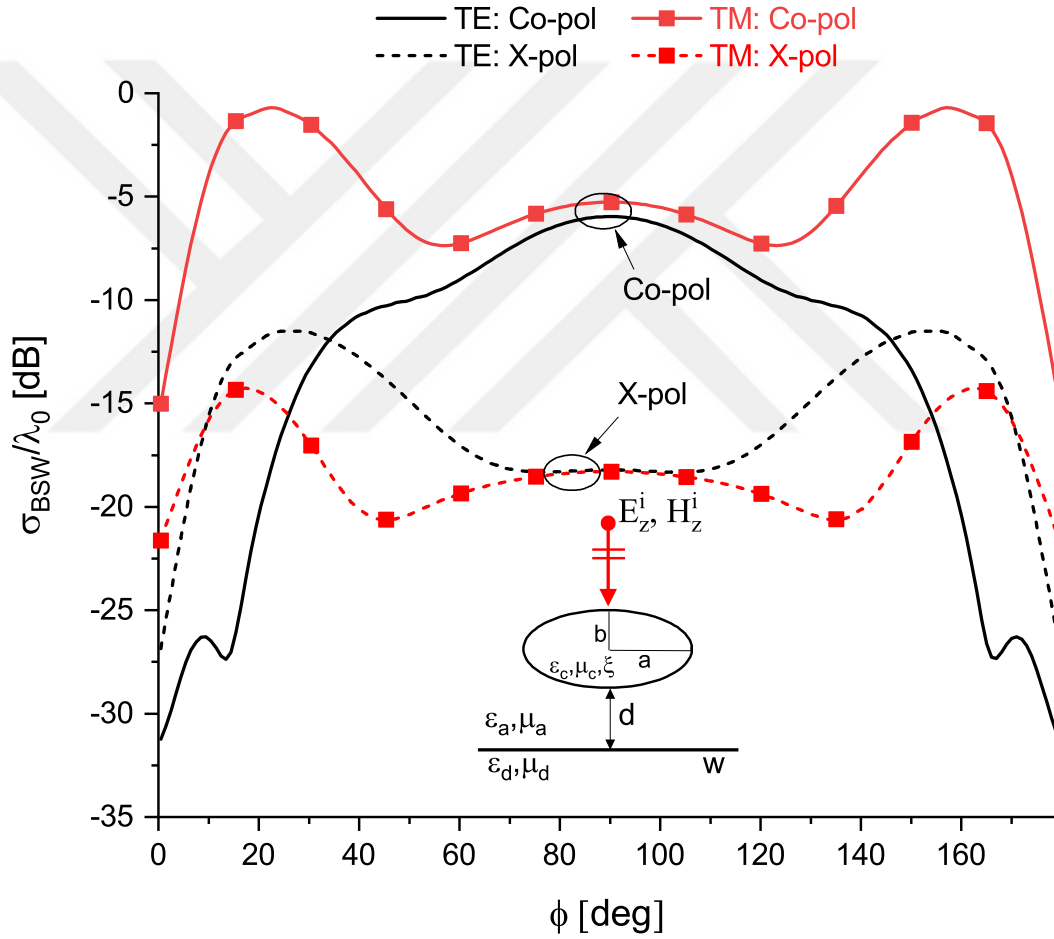
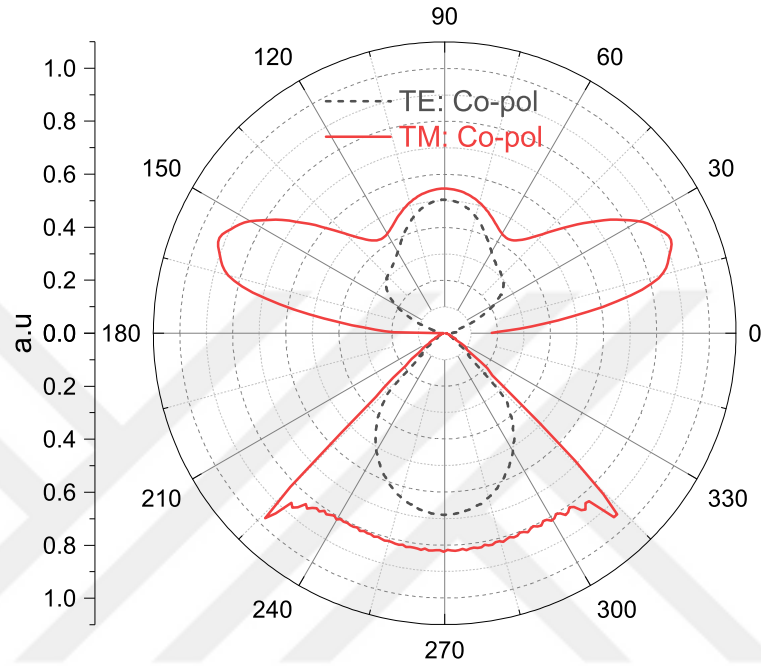
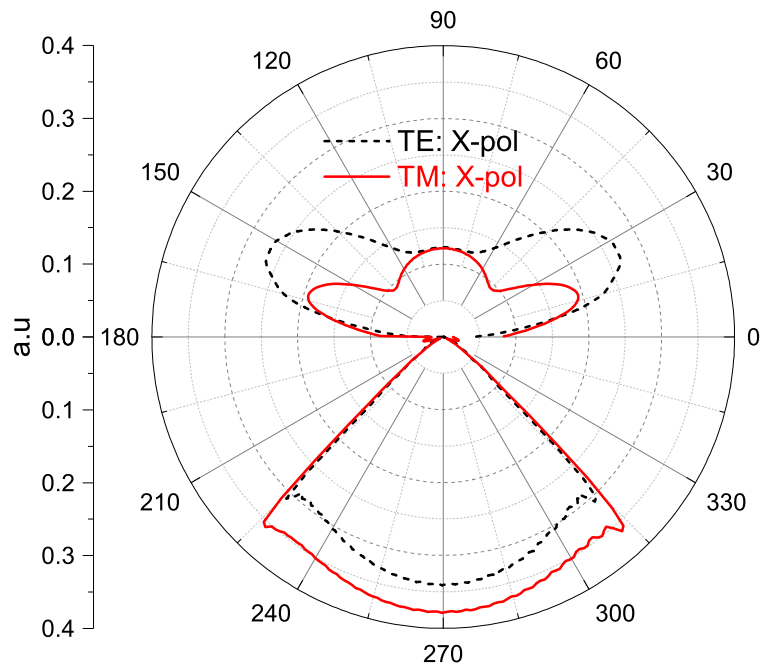


Figure 3.60: Bistatic scattering width of a chiral elliptical cylinder placed above a dielectric half-space. TM and TE excitation,  $a = 0.2\lambda_0$ ,  $b = 0.1\lambda_0$ ,  $d = 0.5\lambda_0$ ,  $w = 40\lambda_0$ ,  $\epsilon_d = 2\epsilon_0$ ,  $\epsilon_c = 3\epsilon_0$ ,  $\xi = 0.001$ ,  $\mu_d = \mu_c = \mu_0$ ,  $\phi^i = 90^\circ$ .



(a) co-polar component



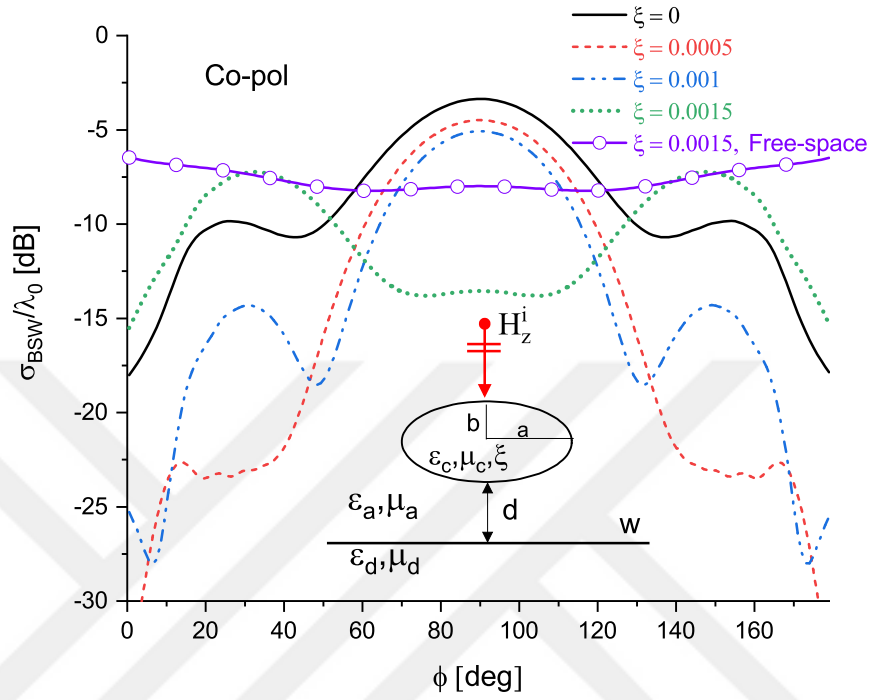
(b) cross-polar component

Figure 3.61: Amplitude of the scattered far-field for a chiral elliptical cylinder placed above a dielectric half-space. Same setup as in Fig. 3.60.

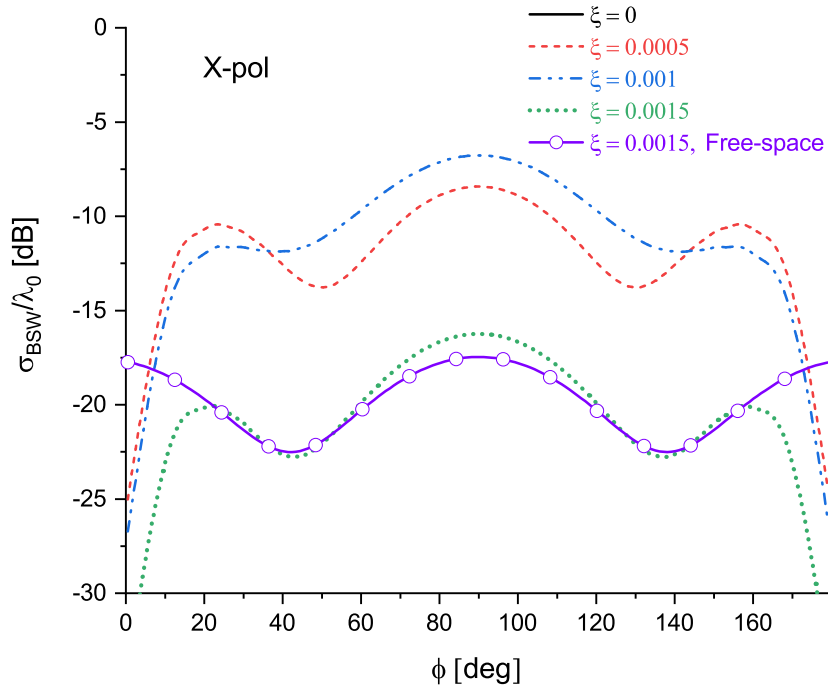
Figure 3.62a also shows the scattering width of the same elliptical cylinder with  $\xi = 0.0015$  when it is placed in free-space. The effect of the half-space on the scattering pattern is clearly visible. It can be seen that for this particular case, the back-scattered field ( $\phi = 90^\circ$ ) has increased by about 7 dB. In free-space, the scattered field is almost constant in all directions.

Figure 3.62b shows the corresponding cross-polar component for the same problem. It was observed that the cross-polar components decrease with an increase in the chirality admittance of the scatterer. Note also that the elliptical cylinder in free-space, behaves almost similar (in the upper half-space) to the case when it is placed above a dielectric half-space.

To observe the scattering properties of the same setup (inset of Fig. 3.62a) in the upper and lower half-spaces, the scattered far-field is presented in Fig. 3.63. It is clear from the scattering pattern of the co-polar component (Fig. 3.63a) that with an increase in the chirality of the scatterer, the back-scattered field ( $\phi = 90^\circ$ ) decreases and the transmitted field increases. However, for the cross-polar term of the scattered field shown in Fig. 3.63b, the field in the free-space decreases with an increase in chirality but the transmitted field is completely different for the three chirality admittance values considered here. Note that for  $\xi = 0$  there is no cross-polar field in both Figs. 3.62 and 3.63 .

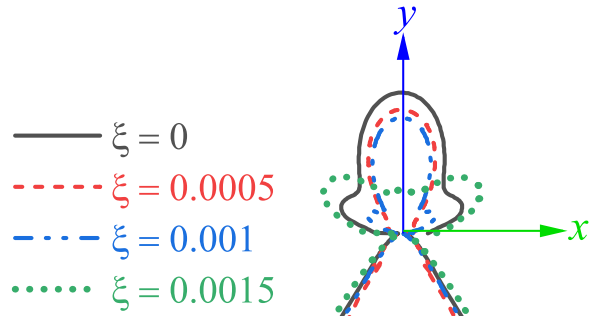


(a) co-polar component

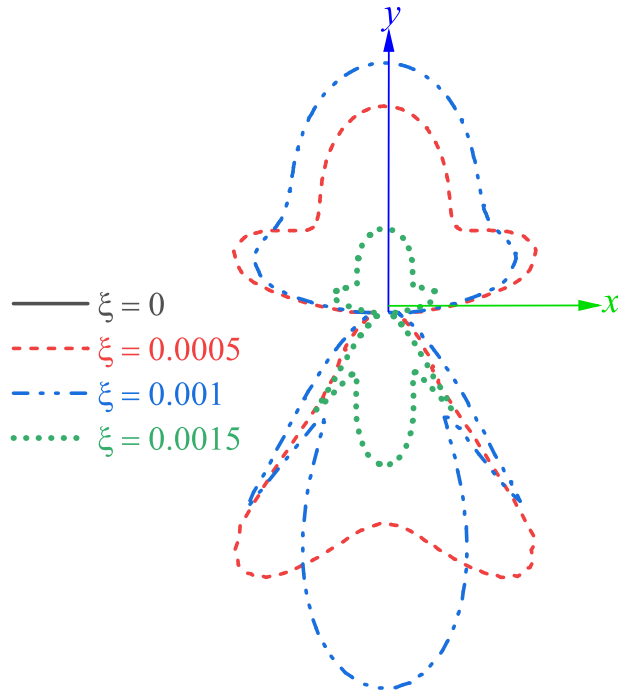


(b) cross-polar component

Figure 3.62: Bistatic scattering width of an elliptical cylinder, for different chirality admittance values, placed above a dielectric half-space. TE excitation,  $\phi^i = 90^\circ$ ,  $a = 0.3\lambda_0$ ,  $b = 0.15\lambda_0$ ,  $d = 0.3\lambda_0$ ,  $w = 40\lambda_0$ ,  $\epsilon_d = 3\epsilon_0$ ,  $\mu_d = 1.8\mu_0$ ,  $\epsilon_c = 5\epsilon_0$ ,  $\mu_c = 3\mu_0$ ,  $\tan\delta_e = 0.08$ ,  $\tan\delta_m = 0.05$ .



(a) co-polar component



(b) cross-polar component

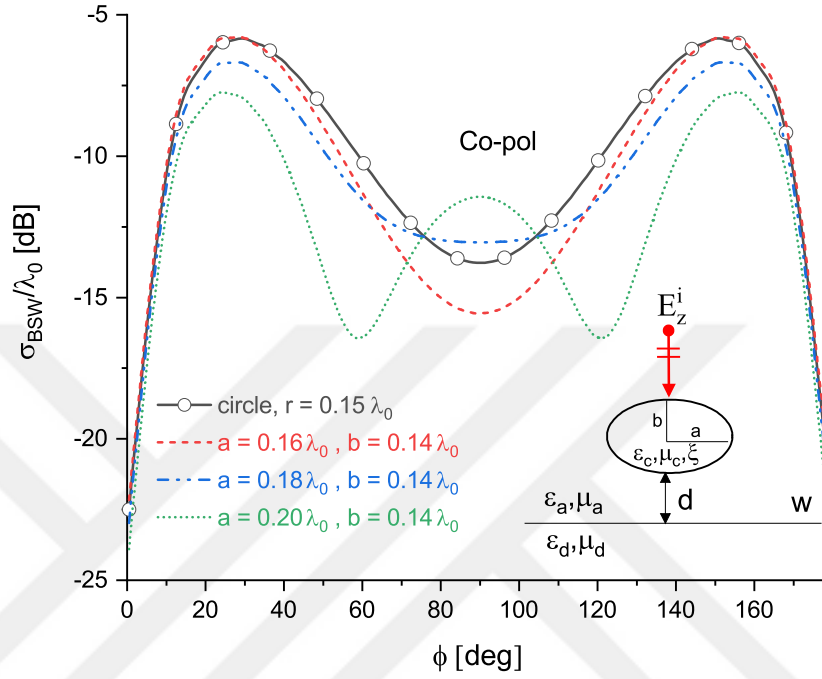
Figure 3.63: Scattered far-field amplitude of an elliptical cylinder, for different chirality admittance values, placed above a dielectric half-space. TE excitation,  $\phi^i = 90^\circ$ ,  $a = 0.3\lambda_0$ ,  $b = 0.15\lambda_0$ ,  $d = 0.3\lambda_0$ ,  $w = 40\lambda_0$ ,  $\epsilon_d = 3\epsilon_0$ ,  $\mu_d = 1.8\mu_0$ ,  $\epsilon_c = 5\epsilon_0$ ,  $\mu_c = 3\mu_0$ ,  $\tan\delta_e = 0.08$ ,  $\tan\delta_m = 0.05$ .



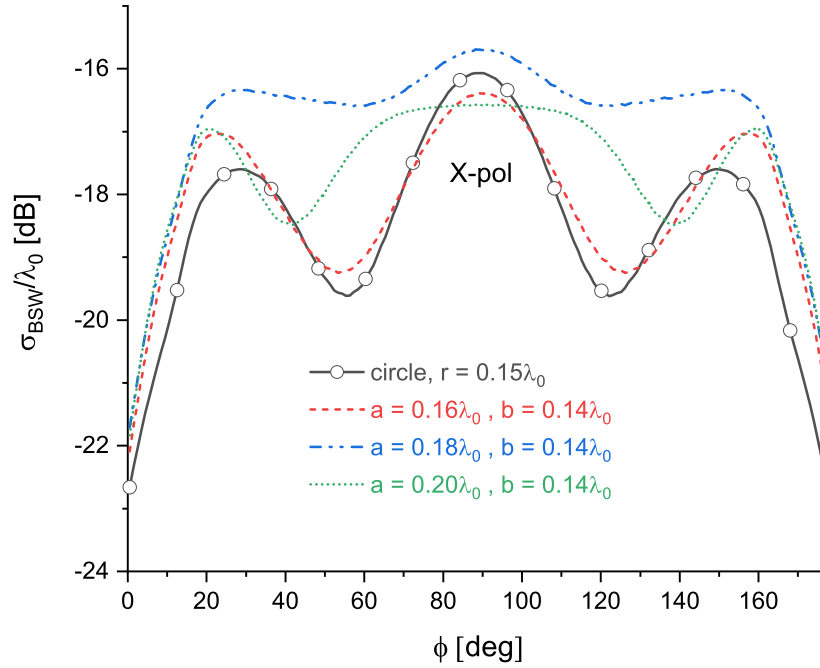
### 3.9.1 Different Eccentric Elliptical Cylinders

In this section a comparison of the bistatic scattering width of a circular chiral cylinder and an elliptical cylinder of three different major axes ( $a = 0.16\lambda_0$ ,  $0.18\lambda_0$ , and  $0.2\lambda_0$ ) is presented. The minor axis remains fixed at  $b = 0.14\lambda_0$ . In case of the circular scatterer the radius is  $0.15\lambda_0$ . The setup with an elliptical cylinder placed above the half-space is shown in the inset of Fig. 3.64a. This figure also shows the co-polar bistatic scattering width in the upper half-space. The system is illuminated by a plane TM wave incident from  $\phi^i = 90^\circ$ . For all cases, the chiral scatterer and the dielectric half-space have the material properties shown in the figure caption. The scatterers are considered to be lossy with  $\tan\delta_e = \tan\delta_m = 0.05$ . It is observed from Fig. 3.64 that, for low eccentricities (small  $a/b$  values) of the elliptical cylinder, the co- and cross-polarized components of the scattering width behaves similar to the fields of a circular chiral cylinder, as expected. This study also serves as a validity check for the scattering from elliptical cylinders, as the shape changes gradually from the elliptical cylinder to a circular one. Furthermore, it is seen that the co-polar component of the back-scattered field increase as the elliptical cylinder becomes narrower, i.e., the ratio of  $a$  to  $b$  increases. For  $a = 0.20\lambda_0$  and  $b = 0.14\lambda_0$ , the co-polar component of the back-scattered field ( $\phi = 90^\circ$ ) has increased and nulls are introduced at around  $60^\circ$  and  $120^\circ$ . The behavior of the cross-polar component is completely different for the three eccentricities as shown in Fig. 3.64b.

From these examples and the ones simulated in other sections, it is observed that the chirality admittance, when added to a regular dielectric, changes the scattering behavior in an unpredictable manner. In some cases the specular direction of the co- and cross-polar fields are different as well. The reflected fields might become stronger or might be absorbed, depending on the properties of the scatterer. The scattering properties are completely unpredictable by a simple theory.



(a)



(b)

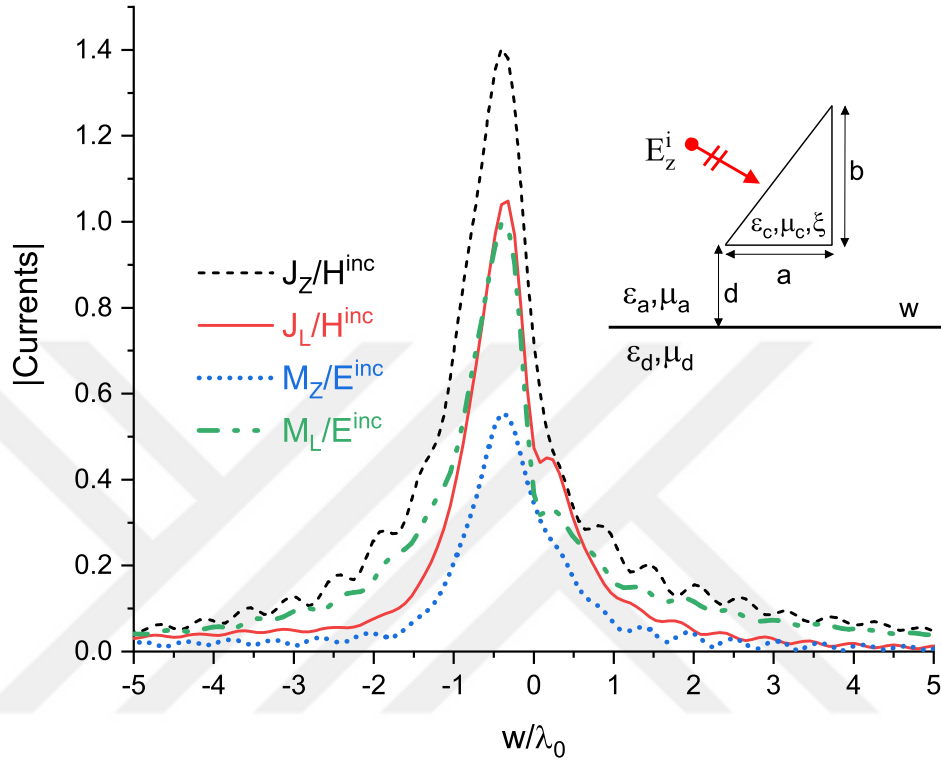
Figure 3.64: Comparing bistatic scattering width of circular and elliptical cylinders of different sizes placed above a dielectric half-space. TM excitation,  $\phi^i = 90^\circ$ ,  $d = 0.3\lambda_0$ ,  $w = 40\lambda_0$ ,  $\epsilon_d = 3\epsilon_0$ ,  $\mu_d = \mu_0$ ,  $\epsilon_c = 3\epsilon_0$ ,  $\mu_c = 2\mu_0$ ,  $\tan\delta_e = \tan\delta_m = 0.05$ .

### 3.10 Scattering From Triangular Cylinders

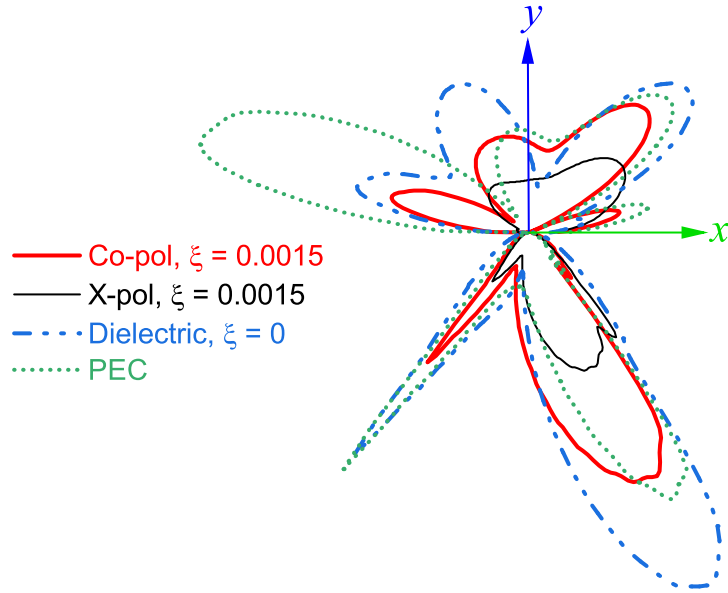
As a final arbitrary shape, presented in this dissertation, a triangular (wedge) cylinder is placed above a dielectric half-space. The setup is shown in Fig. 3.65. A TM plane wave is incident on the setup from  $\phi = 135^\circ$ . The scatterer is assumed to be lossless and homogeneous. It is characterized by  $\epsilon_c = 5\epsilon_0$ ,  $\mu_c = \mu_0$ , and  $\xi = 0.0015$ . Distance between the scatterer and the interface is  $d = 0.2\lambda_0$ . The dielectric half-space is represented by a finite strip of width  $w = 40\lambda_0$  which is characterized by  $\epsilon_d = 2.56\epsilon_0$ ,  $\mu_d = \mu_0$ . The perturbed currents on the interface are shown in Fig. 3.65a and the scattered far-field is shown in Fig. 3.65b. The currents on the interface are asymmetric due to the excitation and the shape of the triangle. It is seen that they take longer to converge on shadowed side of the strip relative to the lit side.

From the scattered fields in Fig. 3.65b, it is visible that the chiral wedge scatters less fields, in all directions, than the PEC and dielectric wedge of the same dimensions. The fields, in case of the dielectric wedge, penetrate the deepest into the dielectric half-space ( $180^\circ < \phi < 360^\circ$ ). The strongest scattered fields are produced by the PEC wedge in the upper half-space ( $0^\circ < \phi < 180^\circ$ ) on the lit side (around  $167^\circ$  off of  $x$ -axis). The specular direction of the cross-polar component is different from the co-polar component of the fields. This phenomenon was observed in Fig. 3.23 as well.

Figure 3.66 shows the bistatic scattering width for a chiral, dielectric, and a PEC wedge. It can be seen that the null in the co-polar component, at around  $25^\circ$ , are the same when the wedge is PEC or chiral. In case of the dielectric wedge, no such null is observed. The scattered fields for the three cylinders are different from each other in other directions. These results are completely random and unpredictable by simple theory. Therefore, solutions by numerical methods such as this work are vital to computing scattering from chiral objects of arbitrary cross-sections.



(a) Perturbed currents



(b) Scattered far-field amplitude

Figure 3.65: Perturbed currents and scattering due to a chiral wedge placed above a dielectric half-space. TM excitation,  $a = 0.5\lambda_0$ ,  $b = 1\lambda_0$ ,  $d = 0.2\lambda_0$ ,  $w = 40\lambda_0$ ,  $\epsilon_d = 2.56\epsilon_0$ ,  $\epsilon_c = 5\epsilon_0$ ,  $\xi = 0.0015$ ,  $\mu_d = \mu_c = \mu_0$ ,  $\phi^i = 135^\circ$ .

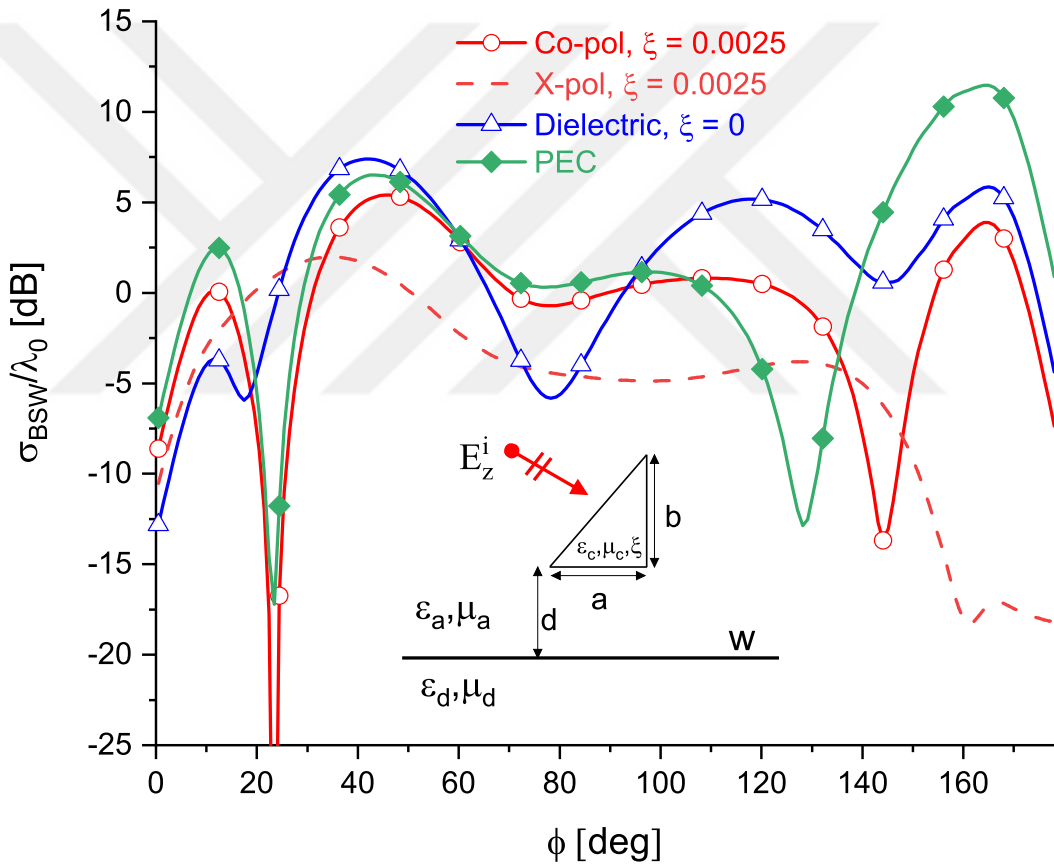


Figure 3.66: Bistatic scattering width of a chiral wedge placed above a dielectric half-space. TM excitation,  $a = 0.5\lambda_0$ ,  $b = 1\lambda_0$ ,  $d = 0.2\lambda_0$ ,  $w = 40\lambda_0$ ,  $\epsilon_d = 2.56\epsilon_0$ ,  $\epsilon_c = 5\epsilon_0$ ,  $\xi = 0.0015$ ,  $\mu_d = \mu_c = \mu_0$ ,  $\phi^i = 135^\circ$ .

### 3.11 Advantages and Disadvantages of Surface Formulation

The main problem discussed here can also be solved using volume equivalence principle. In case of surface formulation (used in this work) the surface of the cylinder is approximated by linear segments. For each segment, electric and magnetic currents are assumed. Both these currents have longitudinal and lateral components. Scattering from a chiral cylinder in free-space is solved using the volume formulation in [28], where the cross-section of the cylinder is divided into trapezoidal cells. Using pulses as expansion functions and point matching for testing in the MoM solution (same as in this work), the cell size is less than  $1/10^{th}$  of the wavelength in the chiral medium. For each electric and magnetic volume current on the cell, there are six components.

If  $N_{seg}$  denotes the number of total segments which divide the circumference of the cylinder in the surface formulation, there are a total of  $4N_{seg}$  unknowns. Whereas for the same problem,  $6M_{seg}$  unknowns are to be solved when using the volume formulation. Here,  $M_{seg}$  denotes the number of cells used to split the cross-section of the cylinder. The relation between  $N_{seg}$  and  $M_{seg}$  depends on the scatterer's size and shape. This relation is given by  $M_{seg} = kN_{seg}^2$ ,  $k$  depends on the shape of the scatterer. For instance, it is equal to  $1/16$  for square cylinders and  $1/4\pi$  for circular cylinders [49]. As an example, assume a square cylinder with side length  $\lambda$ . Dividing it into 12 segments per wavelength (as used in this dissertation for majority of the simulations), results in 192 unknowns in the surface formulation. The same problem, if solved by volume formulation, leads to 864 unknowns. This difference increases if high accuracy is required, which depends on the number of segments per wavelength. If larger bodies are considered, the surface formulation will lead to a much smaller moment matrix relative to the volume formulation. Therefore, to reduce the demand for huge storage memory and the need for extensive computation power, surface formulation is definitely preferable over the volume formulation. However, the volume formulation can solve for inhomogeneous chiral cylinders which the surface formulation fails to do.

It is important to mention here that the EFIE formulation used in this dissertation has some limitations. However, these limitation occur in a very narrow band and most of the time at discrete frequencies. For instance, frequencies that correspond to the cutoff frequencies of perfectly conducting waveguides [49]. At these frequencies the EFIEs do not have a unique solution because the moment matrix is singular and the method fails to provide a solution [72–74]. Therefore, to be sure about our computed results, we had to monitor the behavior of the condition number of the moment matrix. One such example of an ill-conditioned moment matrix due to spurious resonances is shown in Fig. 3.67. Consider a rectangular chiral cylinder characterized by  $\epsilon_c = 4\epsilon_0$ ,  $\mu_c = \mu_0$  and  $\xi = 0.0005$  placed above a dielectric half-space. The dielectric half-space is characterized by  $\epsilon_d = 3\epsilon_0$ , and  $\mu_d = \mu_0$ . Cross-section of the rectangular cylinder is  $(x_L \times 0.5x_L)\lambda_0$  and it is placed at a height  $d = \lambda_0$  above the half-space. Note that when  $k_0x_L = 6.302$ , the moment matrix becomes ill-conditioned (shown by the high condition number) and the computed results cannot be trusted. For all the results presented here, the moment matrix was well-conditioned.

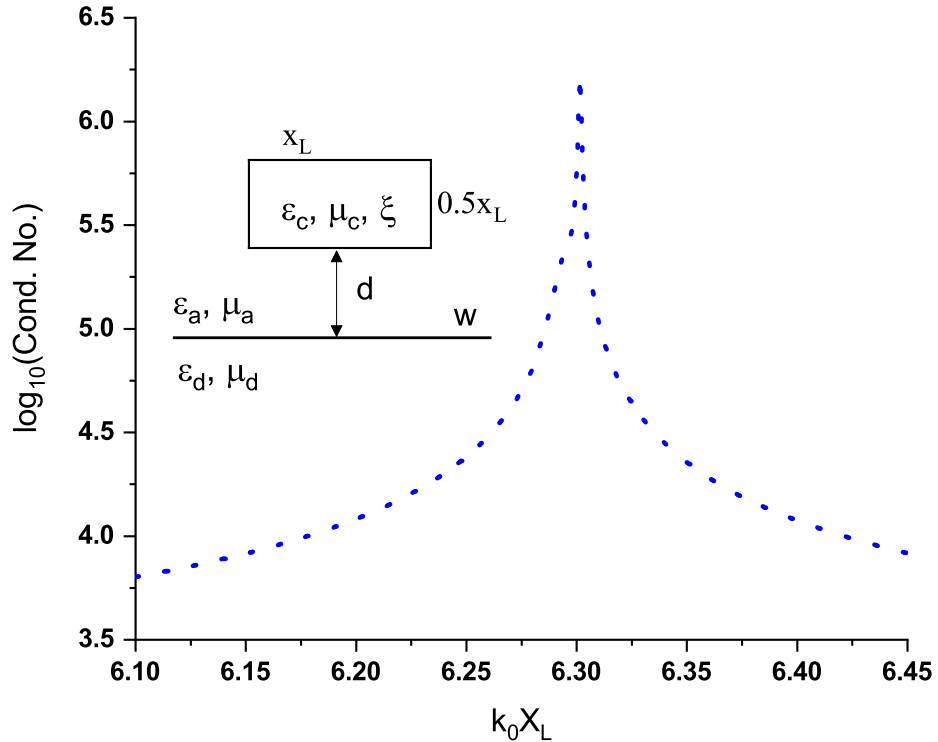


Figure 3.67: Condition number variation of the moment matrix with  $k_0x_L$  for a rectangular chiral cylinder placed above a dielectric half-space.

In addition to the above limitations the perturbation method, like any other approximate method, has its own limitations. For example, when the scatterer is assigned free-space properties (essentially removed from the problem space) then the proposed method breaks down because the perturbed current is exactly equal to zero. However, the algorithm still searches for a current, so whatever perturbed current that is computed 'numerically' contributes to the solution which ultimately results in incorrect fields. Furthermore, the perturbation method results may not be reliable, especially for angles close to the horizon, when the scatterer is less dense (i.e.,  $\epsilon_c$ ,  $\mu_c$ , and  $\xi$  are close to the free-space case). In this case, the perturbed currents are not exactly zero but close to zero. Again, a small error in perturbed current computations may result in a big error (percentage wise). Experiments showed that  $\epsilon_c < 1.1\epsilon_0$  caused ripples in the scattered field hence this threshold should not be ignored.

It should also be noted that for grazing incident angles (close to  $0^\circ$  or  $180^\circ$ ) a very wide strip is required for the perturbed currents to decay properly. However, making the strip too wide beats the purpose of the proposed method, hence the method breaks down if a narrow strip is used. To obtain reliable results from the proposed method, the above mentioned limitations must be taken into consideration.



# Chapter 4

## Conclusion

The problem of electromagnetic scattering from an isotropic homogeneous 2-D chiral cylinder of arbitrary cross-section placed above a dielectric half-space is solved using the method of moments and the perturbation method. The surface equivalence principle was applied to divide the original problem into three simpler problems. A set of vector coupled electric field integral equations was obtained. Due to infinite nature of the problem at hand, the conventional MoM could not be applied directly to the problem. The perturbation method was used to reduce the original problem to an approximate one. This resulted in another set of vector coupled electric field integral equations. These equations were solved, numerically, using MoM. Pulse expansion functions and point matching method is used. First, numerical results for a group of multi-body problems are solved to validate the multi-body chiral algorithm. Followed by numerical results for scatterers of arbitrary cross-sections, including circular, rectangular, square, elliptical, and triangular chiral cylinders. Bistatic scattering width (in the upper half-space) and the amplitude of the far-fields (in upper and lower half-spaces) are presented. The currents on the cylinders and the perturbed currents on the interface are also analyzed. The results are in excellent agreement with available numerical results for limiting cases.

It was observed that the chirality admittance has a huge effect on the scattering

properties of the scatterer. The results are not predictable by simple theory alone. Parametric studies on the incident angle, chiral admittance, dimensions of the scatterer, and the dielectric strip width are presented. Results for lossy and lossless scatterers are compared. It was observed that the bistatic RCS reduces in case of the lossy scatterers. Scatterers of various shapes were analyzed e.g., circular, rectangular, square, elliptical, and triangular.

Finally, the merits and demerits of the method used in this dissertation are discussed. Surface formulation out performs the volume formulation when analyzing fat (large) cylinders.

# Bibliography

- [1] P. Y. Ufimtsev, “Comments on diffraction principles and limitations of rcs reduction techniques,” *Proceedings of the IEEE*, vol. 84, pp. 1830–1851, Dec 1996.
- [2] N. Engheta and D. L. Jaggard, “Electromagnetic chirality and its applications,” *IEEE Antennas and Propagation Society Newsletter*, vol. 30, pp. 6–12, Oct 1988.
- [3] V. K. Varadan, V. V. Varadan, and A. Lakhtakia, “On the possibility of designing anti-reflection coatings using chiral materials,” *Journal of Wave Material Interaction*, vol. 2, no. 1, pp. 71–81, 1987.
- [4] D. L. Jaggard, A. R. Mickelson, and C. H. Papas, “On electromagnetic waves in chiral media,” *Applied physics*, vol. 18, pp. 211–216, Feb 1979.
- [5] M. A. Al-Kanhal and E. Arvas, “Electromagnetic scattering from a chiral cylinder of arbitrary cross section,” *IEEE Transactions on Antennas and Propagation*, vol. 44, no. 7, pp. 1041–1048, 1996.
- [6] R. F. Harrington, *Field Computation by Moment Methods*. New York: Macmillan, 1968.
- [7] R. F. Harrington, *Field Computation by Moment Methods*. New York: McGraw-Hill, 1961.
- [8] C. Caloz and A. Sihvola, “Electromagnetic chirality, part 1: The microscopic perspective [electromagnetic perspectives],” *IEEE Antennas and Propagation Magazine*, vol. 62, no. 1, pp. 58–71, 2020.

- [9] D. F. J. Arago, “Mémoire sur une modification remarquable qu’éprouvent les rayons lumineux dans leur passage á travers certains corps diaphanes et sur quelques autres nouveaux phénomènes d’optique,” *Mémoires de la Classe des Sciences, Mathématiques et Physiques de l’Institut Impérial de France Part 1*, pp. 93–134, 1811.
- [10] J. B. Biot, “Mémoires sur un nouveau genre d’oscillation que les molécules de la lumière éprouvent en traversant certains cristaux,” *Mémoires de la Classe des Sciences, Mathématiques et Physiques de l’Institut Impérial de France Part 1*, pp. 1–372, 1812.
- [11] L. Pasteur, “Sur les relations qui peuvent exister entre la forme cristalline, la composition chimique et le sens de la polarisation rotatoire,” *Ann. Chim. Phys.*, vol. 24, pp. 442–459, 1848.
- [12] J. C. Bose, “On the rotation of plane of polarization of electric waves by twisted structure,” *Proc. Royal Soc.*, vol. 63, pp. 146–152, 1898.
- [13] D. L. Jaggard, A. R. Mickelson, and C. H. Papas, “On electromagnetic waves in chiral media,” *Applied physics*, vol. 18, pp. 211–216, Feb 1979.
- [14] N. Engheta and A. Mickelson, “Transition radiation caused by a chiral plate,” *IEEE Transactions on Antennas and Propagation*, vol. 30, pp. 1213–1216, Nov 1982.
- [15] M. P. Silverman, “Reflection and refraction at the surface of a chiral medium: comparison of gyrotropic constitutive relations invariant or noninvariant under a duality transformation,” *Journal of the Optical Society of America A*, vol. 3, pp. 830–837, June 1986.
- [16] A. Lakhtakia, V. V. Varadan, and V. K. Varadan, “A parametric study of microwave reflection characteristics of a planar achiral-chiral interface,” *IEEE Transactions on Electromagnetic Compatibility*, vol. 28, pp. 90–95, May 1986.
- [17] A. Lakhtakia, V. K. Varadan, and V. V. Varadan, “Reflection of elastic plane waves at a planar achiral–chiral interface,” *The Journal of the Acoustical Society of America*, vol. 87, no. 6, pp. 2314–2318, 1990.

- [18] A. Lakhtakia, V. V. Varadan, and V. K. Varadan, "Reflection of plane waves at planar achiral–chiral interfaces: independence of the reflected polarization state from the incident polarization state," *J. Opt. Soc. Am. A*, vol. 7, pp. 1654–1656, Sep 1990.
- [19] A. Lakhtakia, V. V. Varadan, and V. K. Varadan, "What happens to plane waves at the planar interfaces of mirror-conjugated chiral media," *J. Opt. Soc. Am. A*, vol. 6, pp. 23–26, Jan 1989.
- [20] A. Lakhtakia, V. V. Varadan, and V. K. Varadan, "Scattering by periodic achiral–chiral interfaces," *J. Opt. Soc. Am. A*, vol. 6, pp. 1675–1681, Nov 1989.
- [21] T. Guire, V. V. Varadan, and V. K. Varadan, "Influence of chirality on the reflection of em waves by planar dielectric slabs," *IEEE Transactions on Electromagnetic Compatibility*, vol. 32, pp. 300–303, Nov 1990.
- [22] V. K. Varadan, V. K. Varadan, and A. Lakhtakia, "On the possibility of designing anti-reflection coating using chiral composites," *J. Wave-Mater. Interact.*, vol. 2, pp. 71–81, Jan 1987.
- [23] D. L. Jaggard and N. Engheta, "Chirosorb<sup>TM</sup> as an invisible medium," *Electron. Letters*, vol. 25, pp. 173–174, Feb 1989.
- [24] C. F. Bohren, "Light scattering by an optically active sphere," *Chemical Physics Letters*, vol. 29, no. 3, pp. 458 – 462, 1974.
- [25] C. F. Bohren, "Scattering of electromagnetic waves by an optically active spherical shell," *The Journal of Chemical Physics*, vol. 62, no. 4, pp. 1566–1571, 1975.
- [26] C. F. Bohren, "Scattering of electromagnetic waves by an optically active cylinder," *Journal of Colloid and Interface Science*, vol. 66, no. 1, pp. 105 – 109, 1978.
- [27] A. Lakhtakia, V. K. Varadan, and V. V. Varadan, "Eigenmodes of a chiral sphere with a perfectly conducting coating," *Journal of Physics D: Applied Physics*, vol. 22, no. 6, p. 825, 1989.

- [28] M. S. Kluskens and E. H. Newman, "Scattering by a chiral cylinder of arbitrary cross section," *IEEE Transactions on Antennas and Propagation*, vol. 38, pp. 1448–1455, Sep 1990.
- [29] N. Engheta and D. L. Jaggard, "Electromagnetic chirality and its applications," *IEEE Antennas and Propagation Society Newsletter*, vol. 30, pp. 6–12, October 1988.
- [30] A. Lakhtakia, V. V. Varadan, and V. K. Varadan, "Radiation by a straight thin-wire antenna embedded in an isotropic chiral medium," *IEEE Transactions on Electromagnetic Compatibility*, vol. 30, pp. 84–87, Feb 1988.
- [31] A. Lakhtakia, V. K. Varadan, and V. V. Varadan, "Radiation by a point electric dipole embedded in a chiral sphere," *Journal of Physics D: Applied Physics*, vol. 23, no. 5, p. 481, 1990.
- [32] A. Lakhtakia, V. K. Varadan, and V. V. Varadan, "Surface integral equations for scattering by pec scatterers in isotropic chiral media," *International Journal of Engineering Science*, vol. 29, no. 2, pp. 179 – 185, 1991.
- [33] T. Buber, E. Arvas, and M. Al-Kanhal, "Scattering from a chiral-coated metal cylinder of arbitrary cross section," *Electromagnetics*, vol. 19, no. 4, pp. 363–371, 1999.
- [34] A. M. M. Allam, "Chiral absorbing material," in *Radio Science Conference, 2000. 17th NRSC '2000. Seventeenth National*, pp. B3/1–B3/8, 2000.
- [35] M. Tanaka and A. Kusunoki, "Depolarization properties of a chiral coated dielectric cylinder with application to rcs reduction," in *Microwave Conference Proceedings, 1993. APMC '93., 1993 Asia-Pacific*, vol. 2, pp. 10–5–10–8 vol.2, 1993.
- [36] D. X. Wang, E. K. N. Yung, and R. S. Chen, "A coupled integral equation solution of chirally coated conducting bodies," in *2006 IEEE Antennas and Propagation Society International Symposium*, pp. 2843–2846, July 2006.
- [37] H. Li, W. Ye, and Z. Wu, "Plane wave scattering by a chiral-coating dielectric sphere," in *ISAPE2012*, pp. 791–794, Oct 2012.

- [38] H. Mustacoglu, J. R. Mautz, and E. Arvas, “Method of moments analysis of an axisymmetric chiral radome,” in *2011 XXXth URSI General Assembly and Scientific Symposium*, pp. 1–4, Aug 2011.
- [39] M. Afzaal, A. Syed, A. Imran, Q. Naqvi, and K. Hongo, “Scattering of electromagnetic plane wave by a pec strip in homogeneous isotropic chiral medium,” *Journal of Electromagnetic Waves and Applications*, vol. 28, no. 8, pp. 999–1010, 2014.
- [40] N. Iqbal and P. Choudhury, “Scattering due to twisted pec cylinder coated with chiral/chiroferrite mediums,” *Optik - International Journal for Light and Electron Optics*, vol. 127, no. 17, pp. 7030 – 7039, 2016.
- [41] F. I. Fedorov, “On the theory of optical activity of crystals. I. Energy conservation law and optical activity tensors,” *Optics and Spectroscopy*, vol. 6, no. 1, pp. 85–93, 1959.
- [42] P. Drude, *Lehrbuch der Optik*. Leipzig: S. Hirzel, 1990.
- [43] M. Born, *Optik*. Heidelberg: Springer-Verlag, 1972.
- [44] E. J. Post, *Formal Structure of Electromagnetics*. Amsterdam: North-Holland, 1962.
- [45] I. V. Lindell, A. H. Sihvola, S. A. Tretyakov, and A. J. Viitanen, *Electromagnetic Waves in Chiral and Bi-Isotropic Media*. Boston: Artech House, 1994.
- [46] E. Arvas, S. M. Rao, and T. K. Sarkar, “E-field solution of TM-scattering from multiple perfectly conducting and lossy dielectric cylinders of arbitrary cross-section,” *IEE Proceedings H-Microwaves, Antennas and Propagation*, vol. 133, pp. 115–121, April 1986.
- [47] C. A. Balanis, *Advanced Engineering Electromagnetics*. John Wiley & sons Inc., 2nd ed., 2012.
- [48] Z. Masouri and S. Hatamzadeh-Varmazyar, “An analysis of electromagnetic scattering from finite-width strips,” *Int. J. Industrial Mathematics*, vol. 5, pp. 199–204, April 2013.

- [49] M. Alkanhal, *Electromagnetic scattering from chiral cylinders of arbitrary cross section*. PhD thesis, Syracuse University, NY, USA, 1994.
- [50] I. V. Lindell, A. H. Sihvola, S. A. Tretyakov, and A. J. Viitanen, *Electromagnetic Waves in Chiral and Bi-isotropic Media*. Artech House, 1994.
- [51] V. K. Varadan, A. Lakhtakia, and V. V. Varadan, “Scattering by beaded helices: Anisotropy and chirality,” *J. Wave-Mater. Interact.*, vol. 15, p. 153–160, April 1987.
- [52] V. K. Varadan, V. V. Varadan, and A. Lakhtakia, “On the possibility of designing anti-reflection coatings using chiral materials,” *J. Wave-Mater. Interact.*, vol. 15, no. 2, p. 71–81, 1987.
- [53] A. Lakhtakia, V. K. Varadan, and V. V. Varadan, “Scattering and absorption characteristics of lossy dielectric, chiral, nonspherical objects,” *Appl. Opt.*, vol. 24, p. 4146–4154, 1985.
- [54] M. S. Kluskens and E. H. Newman, “Scattering by a chiral cylinder of arbitrary cross section,” *IEEE Trans. Antennas Propag.*, vol. 38, no. 9, p. 1448–1455, 1990.
- [55] C. F. Bohren and F. Craig, “Light scattering by an optically active sphere,” *Chem. Phys. Lett.*, vol. 29, p. 458–462, Dec. 1974.
- [56] V. Demir, A. Z. Elsherbeni, and E. Arvas, “FDTD formulation for dispersive chiral media using the transform method,” *IEEE Trans. Antennas Propag.*, vol. 53, p. 3374–3384, Oct. 2005.
- [57] D. Worasawate, J. R. Mautz, and E. Arvas, “Electromagnetic scattering from an arbitrarily shaped three-dimensional homogeneous chiral body,” *IEEE Trans. Antennas Propag.*, vol. 51, no. 5, p. 1077–1084, 2003.
- [58] R. Borghi, F. Gori, M. Santarsiero, F. Frezza, and G. Schettini, “Plane-wave scattering by a perfectly conducting circular cylinder near a plane surface: cylindrical-wave approach,” *J. Opt. Soc. Am. A*, vol. 13, pp. 483–493, Mar 1996.



- [59] P. G. Cottis and P. G. Kanellopoulos, "Scattering from a conducting cylinder above a lossy medium," *Int. J. Electron.*, vol. 65, p. 1031–1038, 1988.
- [60] B. P. D'Yakonov, "The diffraction of electromagnetic waves by a circular cylinder in a homogeneous half-space," *Bull. Acad. Sci. USSR, Geophys.*, vol. 9, p. 950–955, 1959.
- [61] C. Ozzaim, "Plane wave scattering by a conducting cylinder located near an interface between two dielectric half-spaces: a perturbation method," *IEEE Trans. Antennas Propag.*, vol. 65, p. 2754–2758, May 2017.
- [62] C. Ozzaim, "A mom solution for tm scattering by dielectric cylinders above an infinite flat surface," *Journal of Modern Optics*, vol. 66, no. 15, pp. 1550–1557, 2019.
- [63] C. M. Butler, X.-B. Xu, and A. W. Glisson, "Current induced on a conducting cylinder located near the planar interface between two semiinfinite half-spaces," *IEEE Trans. Antennas Propag.*, vol. 33, no. 6, p. 616–624, 1985.
- [64] D. Michalski, K. A. and Zheng, "Electromagnetic scattering and radiation by surface of arbitrary shape in layered media, part 1: theory," *IEEE Trans. Antennas Propag.*, vol. 38, no. 3, pp. 335–344, 1990.
- [65] B. Wang, J. Zhou, T. Koschny, M. Kafesaki, and C. M. Soukoulis, "Chiral metamaterials: simulations and experiments," *J. Opt. A: Pure Appl. Opt.*, vol. 11, pp. 1–10, 2009.
- [66] X. Wang, D. H. Werner, L. Li, and Y. Gan, "Interaction of electromagnetic waves with 3-d arbitrarily shaped homogeneous chiral targets in the presence of a lossy half space," *IEEE Trans. Antennas Propag.*, vol. 40, pp. 3647–3655, Dec. 2007.
- [67] D. Z. Ding and R. S. Chen, "Electromagnetic scattering by conducting bor coated with chiral media above a lossy half-space," *Prog. in Electromagnetics Research, PIER*, vol. 104, pp. 385–401, 2010.
- [68] R. S. Chen, Y. Q. Hu, Z. H. Fan, D. Z. Ding, D. X. Wang, and E. K. N. Yung, "An efficient surface integral equation solution to em scattering by chiral

- objects above a lossy half-space,” *IEEE Trans. Antennas Propag.*, vol. 57, no. 11, pp. 3586–3593, 2009.
- [69] Y. Hu, J. Zhu, Q. Wang, and T. Wan, “Electromagnetic modeling for chiral material coated conducting object above a lossy half space,” *Asia-Pacific Microwave Conference (APMC)*, pp. 1–3, 2015.
- [70] J. Zhu, M. M. Li, Z. H. Fan, and R. S. Chen, “Analysis of em scattering from 3d bi-anisotropic objects above a lossy half space using fe-bi with uv method,” *ACES Journal*, vol. 28, no. 10, pp. 917–923, 2013.
- [71] E. Arvas and T. K. Sarkar, “RCS of two-dimensional structures consisting of both dielectrics and conductors of arbitrary cross section,” *IEEE Transactions on Antennas and Propagation*, vol. 37, no. 5, pp. 546–554, 1989.
- [72] J. R. Mautz and R. F. Harrington, “Radiation and scattering from bodies of revolution,” *Applied Scientific Research*, vol. 20, pp. 405–435, Jan 1969.
- [73] E. Arvas and J. R. Mautz, “On the non-uniqueness of the surface EFIE applied to multiple conducting and/or dielectric bodies,” *AEU*, vol. 42, pp. 364–369, Nov/Dec 1988.
- [74] R. F. Harrington, “Boundary integral formulations of homogeneous material bodies,” *J. Electromagn. Waves Appl.*, vol. 3, pp. 1–15, 1989.
- [75] C. T. Tai, *Dyadic Green’s Functions in Electromagnetics Theory*. Scranton, PA: Intext, 1971.
- [76] J. A. Stratton, *Electromagnetic Theory*. New York: McGraw-Hill, 1941.
- [77] M. S. Kluskens and E. H. Newman, “Scattering by a multilayer chiral cylinder,” *IEEE Transactions on Antennas and Propagation*, vol. 39, no. 1, pp. 91–96, 1991.
- [78] S. Arvas, *A Method of Moment Analysis of Microstructured Optical Fibers*. PhD thesis, Syracuse University, NY, USA, 2009.
- [79] D. Worasawate, *Electromagnetic Scattering from an Arbitrarily Shaped Three Dimensional Chiral Body*. PhD thesis, Syracuse University, NY, USA, 2002.

# Appendix A

## Scattering By A Circular Chiral Cylinder: An Exact Solution

In order to verify our numerical solution for scattering by a chiral cylinder in free space an eigenfunction solution is presented for the same problem. The chiral cylinder is assumed to be homogeneous and infinitely long with its axis along the  $z$ -direction. A normal plane TM/TE plane wave propagating in the  $x$ -direction illuminates the cylinder. The problem setup is shown in Fig. A.1. The cylinder is of radius  $a$ , characterized by  $(\epsilon, \mu, \xi)$ , and denoted as medium 1. Equations (A.1) and (A.2), respectively, gives the right hand and left hand wave numbers of the decomposed waves in the chiral medium whereas the intrinsic impedance of the medium is given by (A.3). The external free-space is characterized by  $(\epsilon_0, \mu_0)$ , wave number  $k_0 = \omega\sqrt{\epsilon_0\mu_0}$ , intrinsic impedance  $\eta_0 = \sqrt{\mu_0/\epsilon_0}$ , and denoted as medium 2. TM and TE cases are presented separately in the following sections.

$$h_1 = \omega\mu\xi + \sqrt{k^2 + (\omega\mu\xi)^2} \quad (\text{A.1})$$

$$h_2 = -\omega\mu\xi + \sqrt{k^2 + (\omega\mu\xi)^2} \quad (\text{A.2})$$

$$\eta_c = \eta \left[ \frac{1}{\sqrt{1 + (\eta\xi)^2}} \right] \quad (\text{A.3})$$

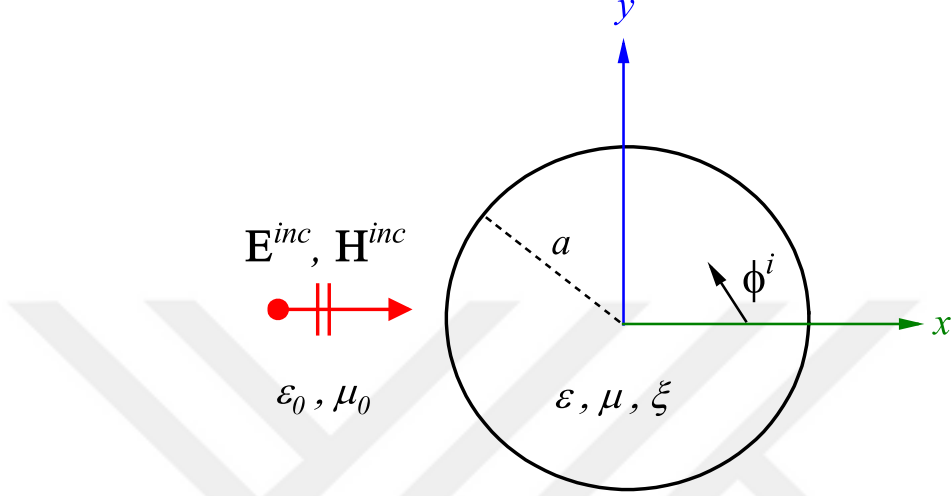


Figure A.1: A circular chiral cylinder illuminated by TM/TE plane wave.

## A.1 TM Incidence

First, TM wave incidence is presented. The wave is incident from  $\phi^i = 180^\circ$ . The incident electric field ( $\mathbf{E}^{\text{inc}}$ ) and magnetic field ( $\mathbf{H}^{\text{inc}}$ ) are given by the following expressions,

$$\mathbf{E}^{\text{inc}} = \hat{z}e^{-jk_0x} = \sum_{n=-\infty}^{\infty} j^{-n}\mathbf{N}_{\mathbf{n}}^{(1)}(k_0) \quad (\text{A.4})$$

$$\mathbf{H}^{\text{inc}} = -\hat{y}\frac{1}{\eta_0}je^{-jk_0x} = \frac{j}{\eta_0}\sum_{n=-\infty}^{\infty} j^{-n}\mathbf{M}_{\mathbf{n}}^{(1)}(k_0) \quad (\text{A.5})$$

where,  $\mathbf{M}_{\mathbf{n}}$  and  $\mathbf{N}_{\mathbf{n}}$  vector wave functions are solutions of the vector field equations given in [75, 76],

$$\mathbf{N}_{\mathbf{n}}^{\text{p}}(k) = \hat{z}e^{jn\phi}Z_n^{(p)}(k\rho) \quad (\text{A.6})$$

$$\mathbf{M}_{\mathbf{n}}^{\text{p}}(k) = \hat{\rho}\frac{jn}{k\rho}e^{jn\phi}Z_n^{(p)}(k\rho) - \hat{\phi}e^{jn\phi}Z_n^{(p)'}(k\rho) \quad (\text{A.7})$$

here,  $\hat{\rho}$  and  $\hat{\phi}$  represent the unit vectors in the  $\rho$  and  $\phi$  directions, respectively, whereas the prime denotes the derivative with respect to the argument.  $Z_n^{(p)}$  is a Bessel function of type  $p$ , e.g.,  $Z_n^{(1)} = J_n$ ,  $Z_n^{(2)} = Y_n$ ,  $Z_n^{(3)} = H_n^{(1)}$ ,  $Z_n^{(4)} = H_n^{(2)}$ .

Then (A.4) and (A.5) becomes,

$$\mathbf{E}^{\text{inc}} = \hat{z} \sum_{n=-\infty}^{\infty} j^{-n} e^{jn\phi} \mathbf{J}_{\mathbf{n}}(k_0\rho) \quad (\text{A.8})$$

$$\mathbf{H}^{\text{inc}} = \frac{j}{\eta_0} \sum_{n=-\infty}^{\infty} j^{-n} e^{jn\phi} \left[ \hat{\rho} \frac{jn}{k_0\rho} J_n(k_0) - \hat{\phi} J_n'(k_0\rho) \right] \quad (\text{A.9})$$

Since the medium is chiral the scattered fields will have both TM and TE components which are expressed as

$$\mathbf{E}^{\text{s}} = \sum_{n=-\infty}^{\infty} j^{-n} (a_n \mathbf{N}_{\mathbf{n}}^{(4)}(k_0) + b_n \mathbf{M}_{\mathbf{n}}^{(4)}(k_0)) \quad (\text{A.10a})$$

$$\mathbf{E}^{\text{s}} = \sum_{n=-\infty}^{\infty} j^{-n} e^{jn\phi} \left[ \hat{z} a_n H_n^{(2)}(k_0\rho) + b_n \left( \hat{\rho} \frac{jn}{k_0\rho} H_n^{(2)}(k_0\rho) - \hat{\phi} H_n^{(2)'}(k_0\rho) \right) \right] \quad (\text{A.10b})$$

$$\mathbf{H}^{\text{s}} = \frac{j}{\eta_0} \sum_{n=-\infty}^{\infty} j^{-n} (a_n \mathbf{M}_{\mathbf{n}}^{(4)}(k_0) + b_n \mathbf{N}_{\mathbf{n}}^{(4)}(k_0)) \quad (\text{A.11a})$$

$$\mathbf{H}^{\text{s}} = \frac{j}{\eta_0} \sum_{n=-\infty}^{\infty} j^{-n} e^{jn\phi} \left[ a_n \left( \hat{\rho} \frac{jn}{k_0\rho} H_n^{(2)}(k_0\rho) - \hat{\phi} H_n^{(2)'}(k_0\rho) \right) + \hat{z} b_n H_n^{(2)}(k_0\rho) \right] \quad (\text{A.11b})$$

where,  $a_n$  and  $b_n$  are the unknown expansion coefficients of the scattered fields. Similarly, following Bohren's decomposition [26], the internal fields in the chiral medium can be written as a combination of the right hand ( $\mathbf{Q}_1$ ) and left hand ( $\mathbf{Q}_2$ ) circularly polarized fields when the chirality is positive.

$$\mathbf{E}^1 = \mathbf{Q}_1 + \mathbf{Q}_2 \quad (\text{A.12})$$

$$\mathbf{H}^1 = \frac{j}{\eta_c} (\mathbf{Q}_1 + \mathbf{Q}_2) \quad (\text{A.13})$$

When expanded in terms of the vector functions, they can be written as

$$\mathbf{Q}_1 = \sum_{n=-\infty}^{\infty} j^{-n} c_n (\mathbf{N}_{\mathbf{n}}^{(1)}(h_1) + \mathbf{M}_{\mathbf{n}}^{(1)}(h_1)) \quad (\text{A.14})$$

$$\mathbf{Q}_2 = - \sum_{n=-\infty}^{\infty} j^{-n} d_n (\mathbf{N}_{\mathbf{n}}^{(1)}(h_2) - \mathbf{M}_{\mathbf{n}}^{(1)}(h_2)) \quad (\text{A.15})$$

where,  $c_n$  and  $d_n$  are the unknown expansion coefficients of the internal fields, and  $h_1, h_2$  are the right handed and left handed wave numbers, respectively. Using (A.6), (A.7), (A.12), (A.13), (A.14), and (A.15) explicit field expressions for the internal fields can be obtained [77],

$$\mathbf{E}_z^1 = \sum_{n=-\infty}^{\infty} j^{-n} (c_n J_n(h_1 \rho) - d_n J_n(h_2 \rho)) e^{jn\phi} \quad (\text{A.16a})$$

$$\mathbf{E}_\phi^1 = - \sum_{n=-\infty}^{\infty} j^{-n} (c_n J'_n(h_1 \rho) + d_n J'_n(h_2 \rho)) e^{jn\phi} \quad (\text{A.16b})$$

$$\mathbf{E}_\rho^1 = \frac{j}{\rho} \sum_{n=-\infty}^{\infty} n j^{-n} \left( \frac{c_n}{h_1} J_n(h_1 \rho) + \frac{d_n}{h_2} J_n(h_2 \rho) \right) e^{jn\phi} \quad (\text{A.16c})$$

$$\mathbf{H}_z^1 = \frac{j}{\eta_c} \sum_{n=-\infty}^{\infty} j^{-n} (c_n J_n(h_1 \rho) + d_n J_n(h_2 \rho)) e^{jn\phi} \quad (\text{A.16d})$$

$$\mathbf{H}_\phi^1 = \frac{-j}{\eta_c} \sum_{n=-\infty}^{\infty} j^{-n} (c_n J'_n(h_1 \rho) - d_n J'_n(h_2 \rho)) e^{jn\phi} \quad (\text{A.16e})$$

$$\mathbf{H}_\rho^1 = \frac{-1}{\rho \eta_c} \sum_{n=-\infty}^{\infty} n j^{-n} \left( \frac{c_n}{h_1} J_n(h_1 \rho) - \frac{d_n}{h_2} J_n(h_2 \rho) \right) e^{jn\phi} \quad (\text{A.16f})$$

The fields internal and external to the chiral cylinder must satisfy the boundary conditions at  $\rho = a$ ,

$$(\mathbf{E}^2 - \mathbf{E}^1) \times \hat{\rho} = 0 \quad (\text{A.17a})$$

$$(\mathbf{H}^2 - \mathbf{H}^1) \times \hat{\rho} = 0 \quad (\text{A.17b})$$

here,  $\hat{\rho}$  is the unit normal vector point outwards from the cylindrical surface,  $\mathbf{E}^1$  and  $\mathbf{E}^2$  are the internal and external fields, respectively. We also know that,

$$\mathbf{E}^2 = \mathbf{E}^{\text{inc}} + \mathbf{E}^{\text{s}} \quad (\text{A.18a})$$

$$\mathbf{H}^2 = \mathbf{H}^{\text{inc}} + \mathbf{H}^{\text{s}} \quad (\text{A.18b})$$

Solving (A.17a) for the  $z$ -component, i.e.,  $E_z^{inc} + E_z^s = E_z^1$  we get the following equation

$$a_n H_n^{(2)}(k_0 a) - c_n J_n(h_1 a) + d_n J_n(h_2 a) = -J_n(k_0 a) \quad (\text{A.19})$$

similarly for the  $\phi$ -component, i.e.,  $E_\phi^{inc} + E_\phi^s = E_\phi^1$ , knowing that  $E_\phi^{inc} = 0$ , we get the following simplified form,

$$b_n H_n^{(2)'}(k_0 a) - c_n J_n'(h_1 a) - d_n J_n'(h_2 a) = 0 \quad (\text{A.20})$$

Following the same process we get two more equations from (A.17b) for the  $z$  and  $\phi$ -components of  $\mathbf{H}$ , as follows

$$\frac{b_n}{\eta_0} H_n^{(2)}(k_0 a) - \frac{c_n}{\eta_c} J_n(h_1 a) - \frac{d_n}{\eta_c} J_n(h_2 a) = 0 \quad (\text{A.21})$$

$$\frac{a_n}{\eta_0} H_n^{(2)'}(k_0 a) - \frac{c_n}{\eta_c} J_n'(h_1 a) + \frac{d_n}{\eta_c} J_n'(h_2 a) = \frac{-1}{\eta_0} J_n'(k_0 a) \quad (\text{A.22})$$

Equations (A.19) - (A.22) can be written in matrix form as,

$$\begin{bmatrix} H_n^{(2)}(k_0 a) & 0 & -J_n(h_1 a) & J_n(h_2 a) \\ 0 & H_n^{(2)'}(k_0 a) & -J_n'(h_1 a) & -J_n'(h_2 a) \\ 0 & \frac{1}{\eta_0} H_n^{(2)}(k_0 a) & \frac{-1}{\eta_c} J_n(h_1 a) & \frac{-1}{\eta_c} J_n(h_2 a) \\ \frac{1}{\eta_0} H_n^{(2)'}(k_0 a) & 0 & \frac{-1}{\eta_c} J_n'(h_1 a) & \frac{1}{\eta_c} J_n'(h_2 a) \end{bmatrix} \begin{bmatrix} a_n \\ b_n \\ c_n \\ d_n \end{bmatrix} = \begin{bmatrix} -J_n(k_0 a) \\ 0 \\ 0 \\ \frac{-1}{\eta_0} J_n'(k_0 a) \end{bmatrix}$$

Solving for  $Ax = b$  gives us the unknown expansion coefficients for the internal and external fields.

## A.2 TE Incidence

In case of the TE plane wave incidence the incident electric field can not have a  $z$ -component. The fields are expressed as

$$\mathbf{E}^{inc} = \hat{y} j e^{-jk_0 x} = \sum_{n=-\infty}^{\infty} j^{-n} \mathbf{M}_n^{(1)}(k_0) \quad (\text{A.23})$$

$$\mathbf{H}^{inc} = -\hat{z} \frac{j}{\eta_0} j e^{-jk_0 x} = \frac{j}{\eta_0} \sum_{n=-\infty}^{\infty} j^{-n} \mathbf{N}_n^{(1)}(k_0) \quad (\text{A.24})$$

Following the same procedure of TM four equations are obtained for the TE incidence. The matrix form is given below. Notice that only the right hand side changed which comes from the incident fields.

$$\begin{bmatrix} H_n^{(2)}(k_0 a) & 0 & -J_n(h_1 a) & J_n(h_2 a) \\ 0 & H_n^{(2)'}(k_0 a) & -J_n'(h_1 a) & -J_n'(h_2 a) \\ 0 & \frac{1}{\eta_0} H_n^{(2)}(k_0 a) & \frac{-1}{\eta_c} J_n(h_1 a) & \frac{-1}{\eta_c} J_n(h_2 a) \\ \frac{1}{\eta_0} H_n^{(2)'}(k_0 a) & 0 & \frac{-1}{\eta_c} J_n'(h_1 a) & \frac{1}{\eta_c} J_n'(h_2 a) \end{bmatrix} \begin{bmatrix} a_n \\ b_n \\ c_n \\ d_n \end{bmatrix} = \begin{bmatrix} 0 \\ -J_n'(k_0 a) \\ \frac{-1}{\eta_0} J_n(k_0 a) \\ 0 \end{bmatrix}$$

### A.3 Scattered Fields

Using the large argument approximation for the Hankel function, the far scattered fields can be written as [77]

$$E_z = \sqrt{\frac{2j}{\rho\pi k_0}} e^{-jk_0\rho} \sum_{n=-\infty}^{\infty} a_n e^{jn\phi} \quad (\text{A.25})$$

$$E_\phi = j \sqrt{\frac{2j}{\rho\pi k_0}} e^{-jk_0\rho} \sum_{n=-\infty}^{\infty} b_n e^{jn\phi} \quad (\text{A.26})$$

where  $a_n$  and  $b_n$  have already are calculated above using the matrix inversion. The scattered fields are given as follows [49],

$$\begin{aligned} \sigma(\phi) &= \lim_{\rho \rightarrow \infty} \left[ 2\pi\rho \frac{|\mathbf{E}^s|^2}{|\mathbf{E}^{\text{inc}}|^2} \right] \\ &= \lim_{\rho \rightarrow \infty} 2\pi\rho \left| \sqrt{\frac{2j}{\rho\pi k_0}} \sum_{n=-\infty}^{\infty} a_n \right|^2 \\ &= 2\pi\rho \frac{2j}{\rho\pi k_0} \left| \sum_{n=-\infty}^{\infty} a_n \right|^2 \end{aligned} \quad (\text{A.27})$$

$j = e^{j\pi/4}$  and  $|e^{j\pi/4}| = 1$ , so (A.27) can be written as follows,

$$\sigma(\phi) = \frac{4}{k_0} \left| \sum_{n=-\infty}^{\infty} a_n \right|^2 \quad (\text{A.28})$$



Equation (A.28) has been coded in Matlab to compute the co-polarized ( $E_z$ ) component of the scattered field. Similar equation is used for the cross-polarized ( $E_\phi$ ) component, where  $a_n$  is replaced by  $b_n$ .

Figure A.2 shows scattering from a homogeneous and lossless circular chiral cylinder when it is illuminated by a TM plane wave incident from  $180^\circ$ . The chiral medium is characterized by  $\epsilon = 1.5\epsilon_0$ ,  $\mu = 4\mu_0$ , and  $\xi = 0.0005$ .  $Tan\delta_e = 0$  and  $Tan\delta_m = 0$  are the electric and magnetic losses, respectively. The problem setup is shown in Fig. A.1. The exact solution is compared with the MoM code that was developed using the surface equivalence formulation. The results are in very good agreement.

Figure A.3 shows scattering from the same circular chiral cylinder when it is illuminated by a TE plane wave incident from  $180^\circ$ . The results are in good agreement with the MoM solution.

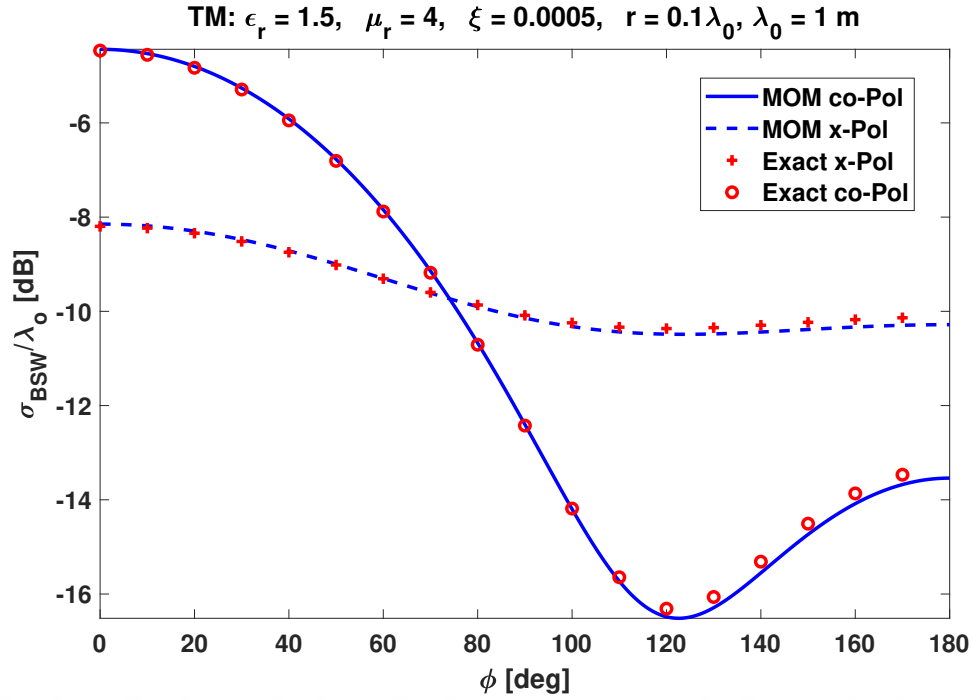


Figure A.2: TM case: Bistatic scattering width of a circular chiral cylinder excited from  $\phi^i = 180^\circ$ .

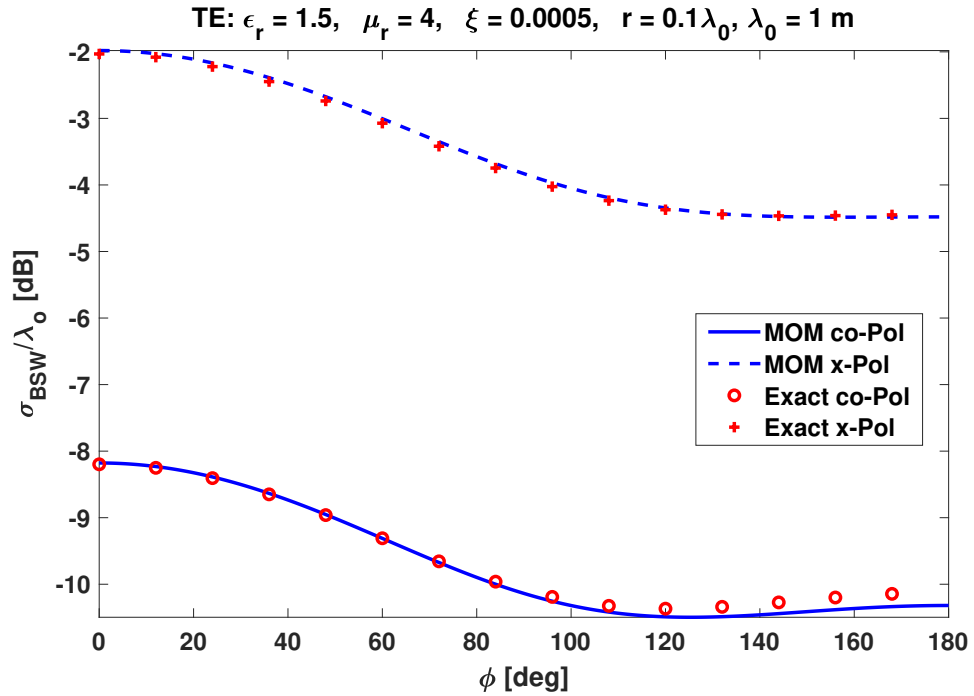


Figure A.3: TE case: Bistatic scattering width of a circular chiral cylinder excited from  $\phi^i = 180^\circ$ .

## Appendix B

# The Moment Matrix and Computation of Some Moment Matrix Elements

In this appendix, some typical elements of the sub-matrices of the moment matrix are discussed. In this dissertation we have followed the same procedure as in [49] where scattering from a single chiral cylinder is solved. Here, we have explained the matrix elements for multi-body problem and specifically when the chiral cylinder is above a dielectric half-space. Consider two surfaces  $S_c$  (chiral cylinder) and  $S_{dn}$  (dielectric half-space) in a two body problem.  $S_c$  and  $S_{dn}$  are shown with discretization in Fig. B.1. The two surfaces  $S_c$  and  $S_{dn}$  are divided into  $N_1$  and  $N_2$  segments, respectively. For the original problem (Fig. 3.4) and other explanations, refer to Chapter 3. Using the surface equivalence principle, unknown surface electric ( $\mathbf{J}$ ) and magnetic ( $\mathbf{M}$ ) currents are placed on these segments.

After applying the method of moments as discussed in Chapter 3, the following moment matrix, as shown in (B.1), is obtained. This is the same matrix from Chapter 3 presented here for easy reference.

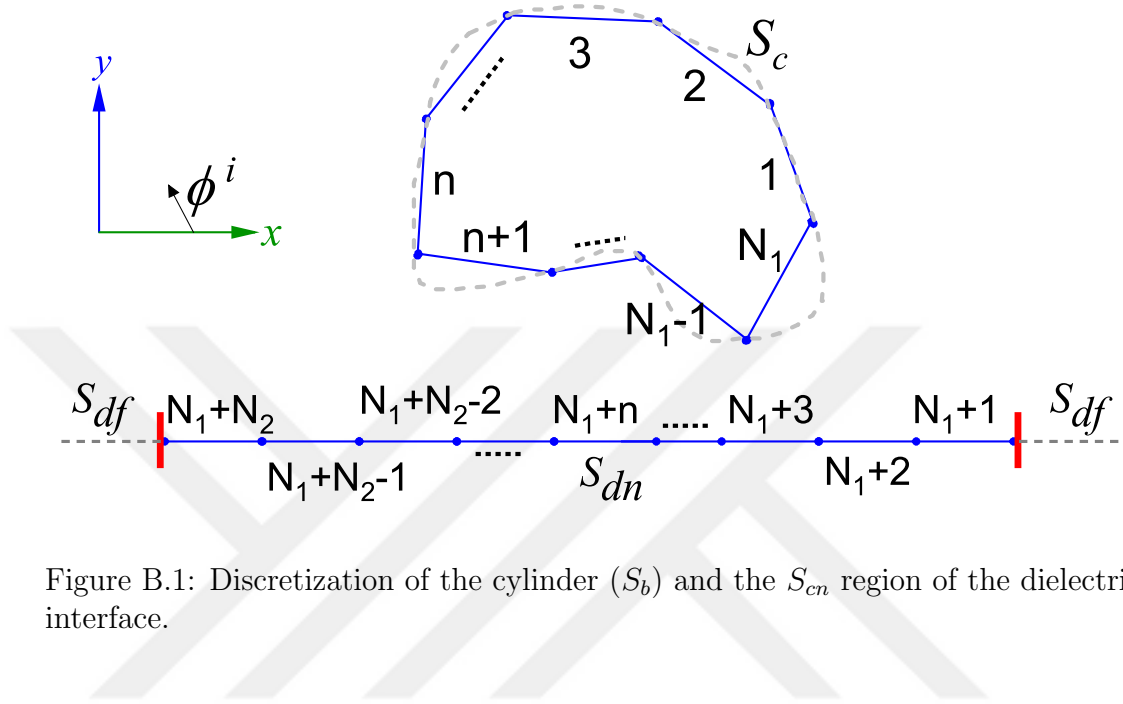


Figure B.1: Discretization of the cylinder ( $S_b$ ) and the  $S_{cn}$  region of the dielectric interface.

$$Z = \begin{bmatrix}
 Z_c J_z^c \text{ext} & Z_c J_z^d \text{ext} & Z_c J_L^c \text{ext} & Z_c J_L^d \text{ext} & Z_c M_z^c \text{ext} & Z_c M_z^d \text{ext} & Z_c M_L^c \text{ext} & Z_c M_L^d \text{ext} \\
 Z_d J_z^c \text{ext} & Z_d J_z^d \text{ext} & Z_d J_L^c \text{ext} & Z_d J_L^d \text{ext} & Z_d M_z^c \text{ext} & Z_d M_z^d \text{ext} & Z_d M_L^c \text{ext} & Z_d M_L^d \text{ext} \\
 L_c J_z^c \text{ext} & L_c J_z^d \text{ext} & L_c J_L^c \text{ext} & L_c J_L^d \text{ext} & L_c M_z^c \text{ext} & L_c M_z^d \text{ext} & L_c M_L^c \text{ext} & L_c M_L^d \text{ext} \\
 L_d J_z^c \text{ext} & L_d J_z^d \text{ext} & L_d J_L^c \text{ext} & L_d J_L^d \text{ext} & L_d M_z^c \text{ext} & L_d M_z^d \text{ext} & L_d M_L^c \text{ext} & L_d M_L^d \text{ext} \\
 Z_c J_z^c \text{in1} & 0 & Z_c J_L^c \text{in1} & 0 & Z_c M_z^c \text{in1} & 0 & Z_c M_L^c \text{in1} & 0 \\
 L_c J_z^c \text{in1} & 0 & L_c J_L^c \text{in1} & 0 & L_c M_z^c \text{in1} & 0 & L_c M_L^c \text{in1} & 0 \\
 0 & Z_d J_z^d \text{in2} & 0 & Z_d J_L^d \text{in2} & 0 & Z_d M_z^d \text{in2} & 0 & Z_d M_L^d \text{in2} \\
 0 & L_d J_z^d \text{in2} & 0 & L_d J_L^d \text{in2} & 0 & L_d M_z^d \text{in2} & 0 & L_d M_L^d \text{in2}
 \end{bmatrix} \tag{B.1}$$

The first capital letter shows the computed electric field component: ‘Z’ for the  $z$ -component and ‘L’ for the lateral component. The subscript of this capital letter shows the surface on which the field is computed: ‘c’ for the chiral surface  $S_c$  and ‘d’ for the dielectric strip  $S_{dn}$ . The second capital letter shows the source of the computed field: ‘J’ for the electric current and ‘M’ for the magnetic current. The subscript of this capital letter shows the component of the current source: ‘Z’ for  $z$ -direction and ‘L’ for lateral direction. The superscript of this letter shows where

this source current is residing: ‘c’ for chiral surface  $S_c$  and ‘d’ for the dielectric strip  $S_{dn}$ . The last three lowercase letters represent the unbounded region in which the source current is radiating: ‘ext’ for external region  $(\epsilon_0, \mu_0)$ , ‘in1’ for the chiral region  $(\epsilon_c, \mu_c, \xi)$ , and ‘in2’ for the dielectric region  $(\epsilon_d, \mu_d)$ .

### $Z_c J_Z^c \text{ext}$ :

The element in the  $m^{\text{th}}$  row and the  $n^{\text{th}}$  column of the sub-matrix  $Z_c J_Z^c \text{ext}$  is the  $z$ -component of the electric field on the  $m^{\text{th}}$  segment of  $S_c$ , produced by the  $z$ -directed electric current  $J_Z$  residing on the  $n^{\text{th}}$  segment of  $S_c$ , when this  $J_Z$  radiates in the unbounded external medium  $(\epsilon_a = \epsilon_0, \mu_a = \mu_0)$ . It is given by,

$$Z_c J_Z^c \text{ext}(m, n) = \frac{-\eta_a k_a l_{mc}}{4} \int_{C^{nc}} H_0^{(2)}(k_a |\boldsymbol{\rho}^{mc} - \boldsymbol{\rho}'|) dl' \quad (\text{B.2})$$

where,  $\eta_a$  is the intrinsic impedance of the external medium  $(\epsilon_0, \mu_0)$  and  $k_a$  denotes its wave number.  $C^{nc}$  represents the  $n^{\text{th}}$  segment on  $S_c$ ,  $\boldsymbol{\rho}^{mc}$  is position vector to the center of the  $m^{\text{th}}$  segment on  $S_c$ ,  $\boldsymbol{\rho}'$  is a position vector to the center of the  $n^{\text{th}}$  source segment (in this case on  $S_c$ ), and  $l_{mc}$  is the length of the  $m^{\text{th}}$  field segment on  $S_c$ .  $H_0^{(2)}(\cdot)$  is the zeroth order Hankel function of the second kind.

The same equation (B.2) can be used to compute the element in the  $m^{\text{th}}$  row and  $n^{\text{th}}$  column of the sub-matrix  $Z_c J_Z^d \text{ext}$  if we replace  $C^{nc}$  by  $C^{nd}$ . Similarly,  $Z_d J_Z^d \text{ext}$  can be computed, if we replace  $l_{mc}$ ,  $C^{nc}$ ,  $\rho_{mc}$  by  $l_{md}$ ,  $C^{nd}$ ,  $\rho_{md}$ . In this case, it is the  $z$ -component of the electric field produced on the  $m^{\text{th}}$  segment of  $S_{dn}$  (in Fig. B.1) when the  $z$ -directed electric current, residing on the  $n^{\text{th}}$  segment of  $S_{dn}$ , radiates into the external medium. Likewise, the elements of  $Z_d J_Z^c \text{ext}$  can also be computed using the above equation. This is the field produced on the dielectric interface by a source that resides on the surface of the chiral cylinder and radiates in the external medium  $(\epsilon_0, \mu_0)$ .

The sub-matrices  $Z_c J_L^c \text{ext}$ ,  $Z_c J_L^d \text{ext}$ ,  $Z_c M_Z^c \text{ext}$ ,  $Z_c M_Z^d \text{ext}$ ,  $Z_d J_L^c \text{ext}$ ,  $Z_d J_L^d \text{ext}$ ,  $Z_d M_Z^c \text{ext}$ , and  $Z_d M_Z^d \text{ext}$  are identically zero. This can be easily figured out by using the right hand rule for the magnetic field produced by an electric current, and

the left hand rule for the electric field produced by a magnetic current. Similarly, some of the sub-matrices containing the lateral component of the electric field are zero as well, for instance,  $L_c J_Z^c \text{ext}$ ,  $L_c J_Z^d \text{ext}$ ,  $L_d J_Z^c \text{ext}$ ,  $L_d J_Z^d \text{ext}$ ,  $L_c M_L^c \text{ext}$ ,  $L_c M_L^d \text{ext}$ ,  $L_d M_L^c \text{ext}$ , and  $L_d M_L^d \text{ext}$  are identically zero in the external medium  $(\epsilon_0, \mu_0)$ .

### $Z_c M_L^c \text{ext}$ :

The element in the  $m^{\text{th}}$  row and the  $n^{\text{th}}$  column of the block matrix  $Z_c M_L^c \text{ext}$  is  $z$ -component of the electric field produced on the  $m^{\text{th}}$  segment of  $S_c$  by the lateral magnetic current ( $M_L$ ) residing on the  $n^{\text{th}}$  segment of  $S_c$ . This current radiates in the unbounded external medium  $(\epsilon_a = \epsilon_0, \mu_a = \mu_0)$ . In other words,  $Z_c M_L^c \text{ext}$  is the electric field due to  $\mathbf{M}_L^n$  tested with  $\mathbf{J}_Z^m$  when the lateral magnetic current  $\mathbf{M}_L^n$  radiates into the external medium and is given by,

$$Z_c M_L^c \text{ext}(m, n) = \langle \mathbf{J}_Z^m, \mathbf{E}_{\text{ext}}(\mathbf{M}_L^n) \rangle \quad (\text{B.3})$$

$$= \int_{c^{mc}} \mathbf{E}_{\text{ext}}(\mathbf{M}_L^n) \cdot \mathbf{J}_Z^m dl \approx \mathbf{E}_{\text{ext}}^{mc}(\mathbf{M}_L^n) \cdot \hat{z} l_{mc} \quad (\text{B.4})$$

$\mathbf{E}_{\text{ext}}^{mc}(\mathbf{M}_L^n)$  represents the electric field produced at the center of the  $m^{\text{th}}$  segment of  $S_c$  by the tangential magnetic current, located on the  $n^{\text{th}}$  segment of  $S_c$ , when it radiates into the unbounded free-space. This can be written as,

$$Z_c M_L^c \text{ext}(m, n) = -j \frac{k_a l_{mc}}{4} \int_{c^{nc}} \hat{n}_c \cdot \frac{(\boldsymbol{\rho}^{mc} - \boldsymbol{\rho}')}{|\boldsymbol{\rho}^{mc} - \boldsymbol{\rho}'|} \times H_1^{(2)}(k_a |\boldsymbol{\rho}^{mc} - \boldsymbol{\rho}'|) dl' \quad (\text{B.5})$$

The unit normal vector to the  $n^{\text{th}}$  source segment  $c^{nc}$  on  $S_c$  is given by,

$$\hat{n}_c = \hat{l}_{nc} \times \hat{z}$$

where  $\hat{l}_{nc}$  is the unit vector tangential to the same  $n^{\text{th}}$  segment on  $S_c$ ,  $\boldsymbol{\rho}^{mc}$  and  $\boldsymbol{\rho}'$  are the position vectors to the field and source segments, respectively, and  $H_1^{(2)}(\cdot)$  is the Hankel function of order one and type two. The sub-matrix  $Z_c M_L^c \text{ext}$  can be computed by using (B.5) as well, however, now the source is residing on surface  $S_d$ . Likewise, typical elements of the sub-matrices  $Z_d M_L^c \text{ext}$ , and  $Z_d M_L^d \text{ext}$  have a similar form too.

## $\mathbf{L}_c \mathbf{J}_L^c \text{ext}$ :

The element  $(m, n)$  in the sub-matrix  $\mathbf{L}_c \mathbf{J}_L^c \text{ext}$  is the lateral component of the electric field produced on the  $m^{\text{th}}$  segment of the chiral cylinder  $S_c$  when a tangential electric current located on the  $n^{\text{th}}$  segment of the cylinder radiates in the unbounded external medium  $(\epsilon_0, \mu_0)$ . It is given by the following symmetric product,

$$\mathbf{L}_c \mathbf{J}_L^c \text{ext}(m, n) = \langle \mathbf{J}_L^{mc}, \mathbf{E}_{\text{ext}}(\mathbf{J}_L^{nc}) \rangle \quad (\text{B.6})$$

$$= \int_{c^{mc}} \mathbf{E}_{\text{ext}}(\mathbf{J}_L^{nc}) \cdot \mathbf{J}_L^{mc} dl \approx \mathbf{E}_{\text{ext}}^{mc}(\mathbf{J}_L^{nc}) \cdot \hat{l}_{mc} l_{mc} \quad (\text{B.7})$$

$\mathbf{E}_{\text{ext}}^{mc}(\mathbf{J}_L^{nc})$  is the electric field produced at the center of the  $m^{\text{th}}$  segment of  $S_c$  by the tangential electric current, residing on the  $n^{\text{th}}$  segment of  $S_c$  and radiating into the unbounded free-space. This can be written as,

$$\begin{aligned} \mathbf{L}_c \mathbf{J}_L^c \text{ext}(m, n) = & -\frac{k_a \eta_a}{4} (\hat{l}_{mc} \cdot \hat{l}_{nc}) l_{mc} \int_{c^{nc}} H_0^{(2)}(k_a |\boldsymbol{\rho}^{mc} - \boldsymbol{\rho}'|) dl' \\ & - \frac{\eta_a}{4k_a l_{nc}} \left[ \int_{(c^{nc-\frac{1}{2}} + c^{nc+\frac{1}{2}})} H_0^{(2)}(k_a |\boldsymbol{\rho}^{mc+} - \boldsymbol{\rho}'|) dl' \right. \\ & \left. - \int_{(c^{nc-\frac{1}{2}} + c^{nc+\frac{1}{2}})} H_0^{(2)}(k_a |\boldsymbol{\rho}^{mc-} - \boldsymbol{\rho}'|) dl' \right] \quad (\text{B.8}) \end{aligned}$$

The charge associated with the lateral current of the  $m^{\text{th}}$  segment is approximated by two displaced pulses as shown in Fig. B.2. Where,  $[c^{nc-\frac{1}{2}} + c^{nc+\frac{1}{2}}]$  shows the domain of the two charge pulses (dotted lines) as in Fig. B.2. In (B.8),  $\boldsymbol{\rho}^{mc-}$  and  $\boldsymbol{\rho}^{mc+}$  respectively denote the beginning and the end of  $m^{\text{th}}$  segment on  $S_c$  as shown in Fig. B.2. A similar equation to (B.8) can be used to compute the typical elements of the sub-matrices  $\mathbf{L}_c \mathbf{J}_L^d \text{ext}$ ,  $\mathbf{L}_d \mathbf{J}_L^c \text{ext}$ , and  $\mathbf{L}_d \mathbf{J}_L^d \text{ext}$ .

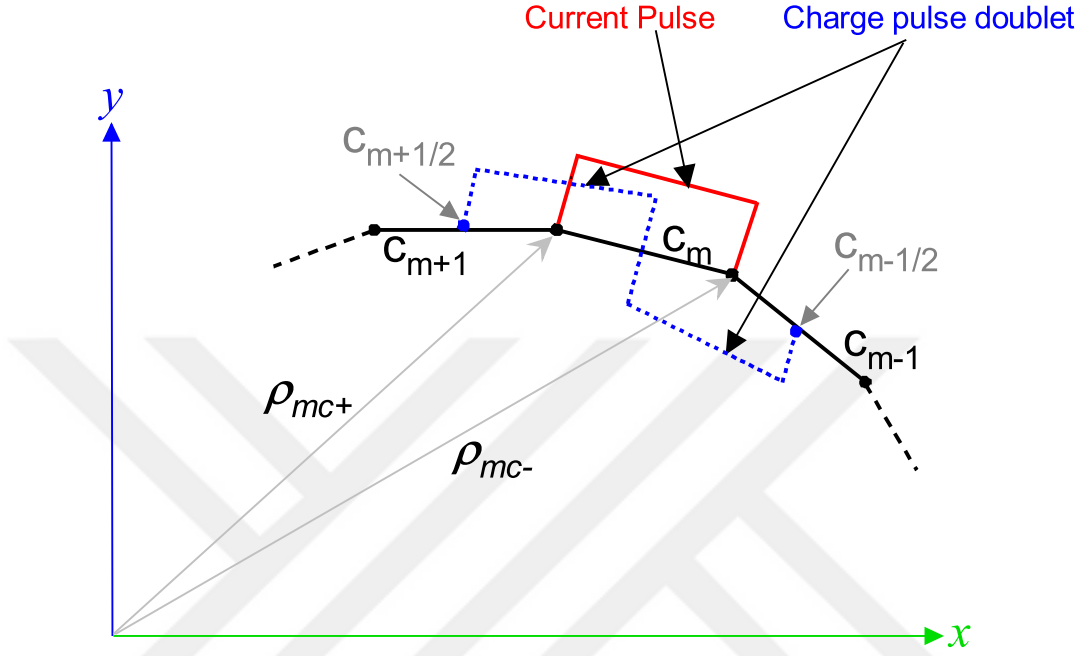


Figure B.2: The lateral current on the  $m^{\text{th}}$  segment of surface  $S_c$  and the charge associated with it.

### $L_c M_Z^c \text{ext}$ :

The element  $(m, n)$  in the sub-matrix  $L_c M_Z^c \text{ext}$  is the lateral component of the electric field produced on the  $m^{\text{th}}$  segment of the chiral cylinder  $S_c$  when a  $z$ -directed magnetic current ( $M_Z$ ), located on the  $n^{\text{th}}$  segment of the cylinder radiates in the unbounded external medium  $(\epsilon_0, \mu_0)$ . A typical element of the sub-matrix is given by,

$$L_c M_Z^c \text{ext}(m, n) = j \frac{k_a l_{mc}}{4} \int_{c^{nc}} \hat{n}_f \cdot \frac{(\boldsymbol{\rho}^{mc} - \boldsymbol{\rho}')}{|\boldsymbol{\rho}^{mc} - \boldsymbol{\rho}'|} \times H_1^{(2)}(k_a |\boldsymbol{\rho}^{mc} - \boldsymbol{\rho}'|) dl' \quad (\text{B.9})$$

Here,  $\hat{n}_f$  is the unit vector normal to the field segment. Elements of the sub-matrices  $L_c M_Z^d \text{ext}$ ,  $L_d M_Z^c \text{ext}$ , and  $L_d M_Z^d \text{ext}$  can be computed using an equation similar to (B.9). For instance, in case of the sub-matrix  $L_d M_Z^c \text{ext}$ , the electric field is produced on the  $m^{\text{th}}$  segment of the dielectric half-space when the current  $M_Z$  resides on the  $n^{\text{th}}$  segment of  $S_c$  and radiates into the unbounded external medium  $(\epsilon_0, \mu_0)$ .



The above equations are used to compute the fields when the sources on  $S_c$  and  $S_d$  radiate in the external medium ( $\epsilon_a = \epsilon_0$ ,  $\mu_a = \mu_0$ ). Now, the fields in the internal medium of the chiral cylinder, characterized by  $(\epsilon_c, \mu_c, \xi)$  will be presented.

Rows five and six of (B.1) show the fields produced in the internal medium (in1) of the chiral cylinder  $((\epsilon_c, \mu_c, \xi))$  and rows seven and eight represent the fields in the internal medium of the dielectric half-space  $(\epsilon_d, \mu_d)$ .

### $Z_c J_Z^c \text{in1}$ :

The element  $(m, n)$  in the sub-matrix  $Z_c J_Z^c \text{in1}$  is the  $z$ -component of the electric field produced on the  $m^{\text{th}}$  segment of the chiral cylinder  $S_c$  when a  $z$ -directed electric current ( $J_Z$ ), located on the  $n^{\text{th}}$  segment of the cylinder radiates into the unbounded internal medium characterized by  $(\epsilon_c, \mu_c, \xi)$ . A typical element is given by,

$$Z_c J_Z^c \text{in1}(m, n) = -\frac{\eta_c l_{mc}}{8} \left[ h_1 \int_{c^{nc}} H_0^{(2)}(h_1 |\boldsymbol{\rho}^{mc} - \boldsymbol{\rho}'|) dl' + h_2 \int_{c^{nc}} H_0^{(2)}(h_2 |\boldsymbol{\rho}^{mc} - \boldsymbol{\rho}'|) dl' \right] \quad (\text{B.10})$$

Here,  $\eta_c$  represents the intrinsic impedance of the chiral cylinder and is given by,

$$\eta_c = \frac{\eta}{\sqrt{1 + (\eta\xi)^2}}. \quad (\text{B.11})$$

where,  $\eta = \sqrt{\mu_c \epsilon_c}$ ,  $h_1$  and  $h_2$ , respectively, are the wave numbers of the right and left hand circularly polarized waves in the chiral medium, given by,

$$h_1 = \omega \mu_c \xi + \sqrt{(k_c)^2 + (\omega \mu_c \xi)^2} \quad (\text{B.12})$$

$$h_2 = -\omega \mu_c \xi + \sqrt{(k_c)^2 + (\omega \mu_c \xi)^2} \quad (\text{B.13})$$

and

$$k_c = \omega \sqrt{\mu_c \epsilon_c}. \quad (\text{B.14})$$

### $\mathbf{Z_c J_L^c in1}$ :

The element  $(m, n)$  in the sub-matrix  $Z_c J_L^c in1$  is the  $z$ -component of the electric field produced on the  $m^{th}$  segment of the chiral cylinder  $S_c$  when the lateral electric current ( $J_L$ ), located on the  $n^{th}$  segment of the cylinder radiates into the unbounded internal medium characterized by  $(\epsilon_c, \mu_c, \xi)$ . A typical element is given by,

$$\begin{aligned} Z_c J_L^c in1(m, n) = \frac{\eta_c l_{mc}}{8} & \left[ h_1 \int_{c^{nc}} \left( \hat{n}_c \cdot \frac{(\boldsymbol{\rho}^{mc} - \boldsymbol{\rho}')}{|\boldsymbol{\rho}^{mc} - \boldsymbol{\rho}'|} \right) H_1^{(2)}(h_1 |\boldsymbol{\rho}^{mc} - \boldsymbol{\rho}'|) dl' \right. \\ & \left. - h_2 \int_{c^{nc}} \left( \hat{n}_c \cdot \frac{(\boldsymbol{\rho}^{mc} - \boldsymbol{\rho}')}{|\boldsymbol{\rho}^{mc} - \boldsymbol{\rho}'|} \right) H_1^{(2)}(h_2 |\boldsymbol{\rho}^{mc} - \boldsymbol{\rho}'|) dl' \right] \quad (\text{B.15}) \end{aligned}$$

### $\mathbf{Z_c M_Z^c in1}$ :

The element  $(m, n)$  in the sub-matrix  $Z_c M_Z^c in1$  is the  $z$ -component of the electric field produced on the  $m^{th}$  segment of the chiral cylinder  $S_c$  when a  $z$ -directed magnetic current ( $M_Z$ ), located on the  $n^{th}$  segment of the cylinder radiates into the unbounded internal medium characterized by  $(\epsilon_c, \mu_c, \xi)$ . A typical element is given by,

$$\begin{aligned} Z_c M_Z^c in1(m, n) = \frac{j l_{mc}}{8} & \left[ h_1 \int_{c^{nc}} H_0^{(2)}(h_1 |\boldsymbol{\rho}^{mc} - \boldsymbol{\rho}'|) dl' \right. \\ & \left. - h_2 \int_{c^{nc}} H_0^{(2)}(h_2 |\boldsymbol{\rho}^{mc} - \boldsymbol{\rho}'|) dl' \right] \quad (\text{B.16}) \end{aligned}$$

### $\mathbf{Z_c M_L^c in1}$ :

The element  $(m, n)$  in the sub-matrix  $Z_c M_L^c in1$  is the  $z$ -component of the electric field produced on the  $m^{th}$  segment of the chiral cylinder  $S_c$  when the lateral

magnetic current ( $M_L$ ), located on the  $n^{th}$  segment of the cylinder radiates into the unbounded internal medium characterized by  $(\epsilon_c, \mu_c, \xi)$ . A typical element is given by,

$$\begin{aligned} Z_c M_L^c \text{in1}(m, n) = & -\frac{j l_{mc}}{8} \left[ h_1 \int_{c^{nc}} \left( \hat{n}_c \cdot \frac{(\boldsymbol{\rho}^{mc} - \boldsymbol{\rho}')}{|\boldsymbol{\rho}^{mc} - \boldsymbol{\rho}'|} \right) H_1^{(2)}(h_1 |\boldsymbol{\rho}^{mc} - \boldsymbol{\rho}'|) dl' \right. \\ & \left. + h_2 \int_{c^{nc}} \left( \hat{n}_c \cdot \frac{(\boldsymbol{\rho}^{mc} - \boldsymbol{\rho}')}{|\boldsymbol{\rho}^{mc} - \boldsymbol{\rho}'|} \right) H_1^{(2)}(h_2 |\boldsymbol{\rho}^{mc} - \boldsymbol{\rho}'|) dl' \right] \quad (\text{B.17}) \end{aligned}$$

### $L_c M_L^c \text{in1}$ :

The element  $(m, n)$  in the sub-matrix  $L_c M_L^c \text{in1}$  is the lateral component of the electric field produced on the  $m^{th}$  segment of the chiral cylinder  $S_c$  when the lateral magnetic current ( $M_L$ ), located on the  $n^{th}$  segment of the cylinder radiates into the unbounded internal medium characterized by  $(\epsilon_c, \mu_c, \xi)$ . A typical element is given by,

$$\begin{aligned} L_c M_L^c \text{in1}(m, n) = & -\frac{j l_{mc}}{8} (\hat{l}_{nc} \cdot \hat{l}_{mc}) \left[ h_1 \int_{c^{nc}} H_0^{(2)}(h_1 |\boldsymbol{\rho}^{mc} - \boldsymbol{\rho}'|) dl' \right. \\ & \left. - h_2 \int_{C_{n_1}} H_0^{(2)}(h_2 |\boldsymbol{\rho}^{mc} - \boldsymbol{\rho}'|) dl' \right] \\ & + \frac{j}{8 l_{nc}} \left[ h_1^{-1} \int_{(c^{nc-\frac{1}{2}} + c^{nc+\frac{1}{2}})} H_0^{(2)}(h_1 |\boldsymbol{\rho}^{mc+} - \boldsymbol{\rho}'|) dl' \right. \\ & \left. + h_2^{-1} \int_{(c^{nc-\frac{1}{2}} + c^{nc+\frac{1}{2}})} H_0^{(2)}(h_2 |\boldsymbol{\rho}^{mc+} - \boldsymbol{\rho}'|) dl' \right] \\ & - \frac{j}{8 l_{nc}} \left[ h_1^{-1} \int_{(c^{nc-\frac{1}{2}} + c^{nc+\frac{1}{2}})} H_0^{(2)}(h_1 |\boldsymbol{\rho}^{mc-} - \boldsymbol{\rho}'|) dl' \right. \\ & \left. + h_2^{-1} \int_{(c^{nc-\frac{1}{2}} + c^{nc+\frac{1}{2}})} H_0^{(2)}(h_2 |\boldsymbol{\rho}^{mc-} - \boldsymbol{\rho}'|) dl' \right] \quad (\text{B.18}) \end{aligned}$$

### $\mathbf{L}_c \mathbf{J}_Z^c \text{in1}$ :

The element  $(m, n)$  in the sub-matrix  $\mathbf{L}_c \mathbf{J}_Z^c \text{in1}$  is the lateral component of the electric field produced on the  $m^{\text{th}}$  segment of the chiral cylinder  $S_c$  when a  $z$ -directed electric current ( $\mathbf{J}_Z$ ), located on the  $n^{\text{th}}$  segment of the cylinder radiates into the unbounded internal medium characterized by  $(\epsilon_c, \mu_c, \xi)$ . A typical element of the sub-matrix is given by,

$$\begin{aligned} \mathbf{L}_c \mathbf{J}_Z^c \text{in1}(m, n) = & -\frac{\eta_c l_{mc}}{8} \left[ h_1 \int_{c^{nc}} \left( \hat{n}_f \cdot \frac{(\boldsymbol{\rho}^{mc} - \boldsymbol{\rho}')}{|\boldsymbol{\rho}^{mc} - \boldsymbol{\rho}'|} \right) H_1^{(2)}(h_1 |\boldsymbol{\rho}^{mc} - \boldsymbol{\rho}'|) dl' \right. \\ & \left. - h_2 \int_{c^{nc}} \left( \hat{n}_f \cdot \frac{(\boldsymbol{\rho}^{mc} - \boldsymbol{\rho}')}{|\boldsymbol{\rho}^{mc} - \boldsymbol{\rho}'|} \right) H_1^{(2)}(h_2 |\boldsymbol{\rho}^{mc} - \boldsymbol{\rho}'|) dl' \right] \quad (\text{B.19}) \end{aligned}$$

### $\mathbf{L}_c \mathbf{J}_L^c \text{in1}$ :

The element  $(m, n)$  in the sub-matrix  $\mathbf{L}_c \mathbf{J}_L^c \text{in1}$  is the lateral component of the electric field produced on the  $m^{\text{th}}$  segment of the chiral cylinder  $S_c$  when a lateral electric current ( $\mathbf{J}_L$ ), located on the  $n^{\text{th}}$  segment of the cylinder radiates into the unbounded internal medium characterized by  $(\epsilon_c, \mu_c, \xi)$ . A typical element of

the sub-matrix is given by,

$$\begin{aligned}
L_c J_L^c \text{in1}(m, n) = & -\frac{\eta_c l_{mc}}{8} (\hat{l}_{nc} \cdot \hat{l}_{mc}) \left[ h_1 \int_{c^{nc}} H_0^{(2)}(h_1 |\boldsymbol{\rho}^{mc} - \boldsymbol{\rho}'|) dl' \right. \\
& + h_2 \int_{c^{nc}} H_0^{(2)}(h_2 |\boldsymbol{\rho}^{mc} - \boldsymbol{\rho}'|) dl' \left. \right] \\
& - \frac{\eta_c}{8 l_{nc}} \left[ h_1^{-1} \int_{(c^{nc-\frac{1}{2}} + c^{nc+\frac{1}{2}})} H_0^{(2)}(h_1 |\boldsymbol{\rho}^{mc+} - \boldsymbol{\rho}'|) dl' \right. \\
& + h_2^{-1} \int_{(c^{nc-\frac{1}{2}} + c^{nc+\frac{1}{2}})} H_0^{(2)}(h_2 |\boldsymbol{\rho}^{mc+} - \boldsymbol{\rho}'|) dl' \left. \right] \\
& + \frac{\eta_c}{8 l_{nc}} \left[ h_1^{-1} \int_{(c^{nc-\frac{1}{2}} + c^{nc+\frac{1}{2}})} H_0^{(2)}(h_1 |\boldsymbol{\rho}^{mc-} - \boldsymbol{\rho}'|) dl' \right. \\
& + h_2^{-1} \int_{(c^{nc-\frac{1}{2}} + c^{nc+\frac{1}{2}})} H_0^{(2)}(h_2 |\boldsymbol{\rho}^{mc-} - \boldsymbol{\rho}'|) dl' \left. \right] \quad (\text{B.20})
\end{aligned}$$

## $L_c M_Z^c \text{in1}$ :

The element  $(m, n)$  in the sub-matrix  $L_c M_Z^c \text{in1}$  is the lateral component of the electric field produced on the  $m^{\text{th}}$  segment of the chiral cylinder  $S_c$  when a lateral electric current ( $J_L$ ), located on the  $n^{\text{th}}$  segment of the cylinder radiates into the unbounded internal medium characterized by  $(\epsilon_c, \mu_c, \xi)$ . A typical element of the sub-matrix is given by,

$$\begin{aligned}
L_c M_Z^c \text{in1}(m, n) = & \frac{j l_{mc}}{8} \left[ h_1 \int_{c^{nc}} \left( \hat{n}_f \cdot \frac{(\boldsymbol{\rho}^{mc} - \boldsymbol{\rho}')}{|\boldsymbol{\rho}^{mc} - \boldsymbol{\rho}'|} \right) H_1^{(2)}(h_1 |\boldsymbol{\rho}^{mc} - \boldsymbol{\rho}'|) dl' \right. \\
& + h_2 \int_{c^{nc}} \left( \hat{n}_f \cdot \frac{(\boldsymbol{\rho}^{mc} - \boldsymbol{\rho}')}{|\boldsymbol{\rho}^{mc} - \boldsymbol{\rho}'|} \right) H_1^{(2)}(h_2 |\boldsymbol{\rho}^{mc} - \boldsymbol{\rho}'|) dl' \left. \right] \quad (\text{B.21})
\end{aligned}$$

The last two rows of (B.1) denote the fields that are produced in the unbounded internal medium of the dielectric half-space  $(\epsilon_d, \mu_d)$ . These sub-matrices can be

computed by using similar expressions as in (B.2) - (B.9). Note that the currents radiate in the unbounded dielectric medium.

## $Z_d J_Z^d$ in 2 :

As an example, the element  $(m, n)$  in the sub-matrix  $Z_d J_Z^d$  in 2 is the  $z$ -component of the electric field produced on the  $m^{th}$  segment of the dielectric half-space  $S_{dn}$  when a  $z$ -directed electric current ( $J_Z$ ), located on the  $n^{th}$  segment of the dielectric half-space, radiates into the unbounded internal medium characterized by  $(\epsilon_d, \mu_d)$ . A typical element of the sub-matrix is given by,

$$Z_d J_Z^d \text{in2}(m, n) = -\frac{\eta_d k_d l_{md}}{4} \int_{c^{nd}} H_0^{(2)}(|\boldsymbol{\rho}^{md} - \boldsymbol{\rho}'|) dl' \quad (\text{B.22})$$

Where,  $\eta_d$  is the intrinsic impedance of the dielectric half-space  $(\epsilon_d, \mu_d)$  and is given by  $\eta_d = \sqrt{\mu_d/\epsilon_d}$  and  $k_d = \omega\sqrt{\mu_d\epsilon_d}$ .

# Appendix C

## Plane Waves in Chiral Media

General plane waves in chiral media are discussed in Sec. 2.3. Here, an example, plane waves due to an infinite current sheet in a chiral medium is presented. The source-free Maxwell's Equations are given below.

$$\nabla \times \mathbf{E} = -j\omega\mathbf{B} \quad (\text{C.1})$$

$$\nabla \times \mathbf{H} = j\omega\mathbf{D} \quad (\text{C.2})$$

Post's [44] constitutive parameters are:

$$\mathbf{D} = \epsilon\mathbf{E} - j\xi\mathbf{B} \quad (\text{C.3})$$

$$\mathbf{H} = \frac{1}{\mu}\mathbf{B} - j\xi\mathbf{E} \quad (\text{C.4})$$

Substituting (C.3) and (C.4) in (C.1) and (C.2) yields the following set of Maxwell's Equations for chiral media.

$$\nabla \times \mathbf{E} = \omega(\xi\mu\mathbf{E} - j\mu\mathbf{H}) \quad (\text{C.5})$$

$$\nabla \times \mathbf{H} = \omega[j(\epsilon + \mu\xi^2)\mathbf{E} + \mu\xi\mathbf{H}] \quad (\text{C.6})$$

Researchers use different constitutive parameters in the literature. Therefore, another way of writing the fields due to an infinite current sheet is presented in

Sec. C.2. A different set of constitutive parameters, proposed by Lindell [50], is used. It is shown that both the sets of constitutive parameters yields the same solution.

## C.1 Plane Waves Produced by an Electric Current Sheet in a Chiral Medium

Consider an infinite current sheet placed at  $z = -d$  plane in an unbounded chiral medium  $(\epsilon, \mu, \xi)$ , as shown in Fig. C.1. The current  $\mathbf{J}$  is assumed to be,

$$\mathbf{J} = -4J_0\hat{x} \quad (\text{C.7})$$

Where  $J_0$  is a constant.

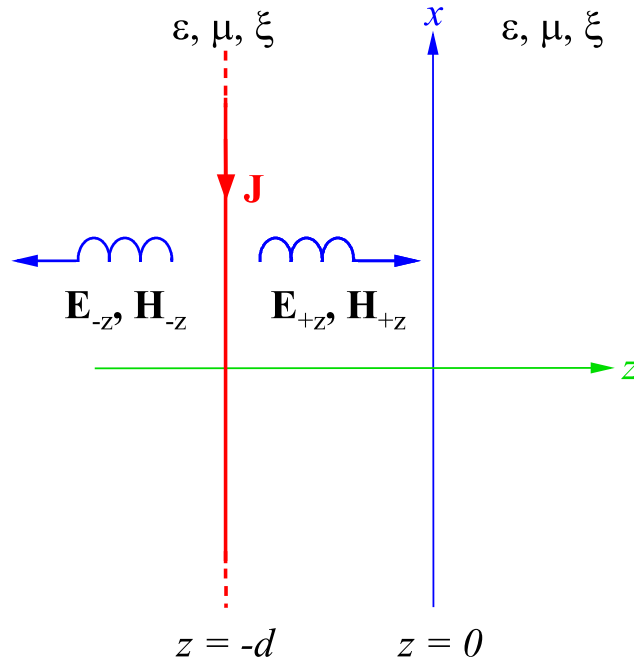


Figure C.1: An infinite current sheet in an unbounded chiral medium.



The field produced by this source, for  $z < -d$  is given by,

$$\mathbf{E}_{-z}(\mathbf{J}) = \eta_c J_0 \left\{ (\hat{x} + j\hat{y})e^{jh_1(z+d)} + (\hat{x} - j\hat{y})e^{jh_2(z+d)} \right\} \quad (\text{C.8})$$

$$\mathbf{H}_{-z}(\mathbf{J}) = J_0 \left\{ (-\hat{y} + j\hat{x})e^{jh_1(z+d)} + (-\hat{y} - j\hat{x})e^{jh_2(z+d)} \right\} \quad (\text{C.9})$$

The subscript  $-z$  represents the field traveling in  $-z$ -direction. The terms in (C.8) and (C.9) with wavenumber  $h_1$  denote the right hand circularly polarized (RHCP) waves and the terms with wavenumber  $h_2$  represent the left hand circular polarized (LHCP) waves. The two wavenumbers are given by,

$$h_1 = \omega\mu\xi + \sqrt{k^2 + (\omega\mu\xi)^2} \quad (\text{C.10})$$

$$h_2 = -\omega\mu\xi + \sqrt{k^2 + (\omega\mu\xi)^2} \quad (\text{C.11})$$

and

$$\eta_c = \frac{\eta}{\sqrt{1 + (\eta\xi)^2}} \quad (\text{C.12})$$

is the impedance of the chiral medium, where,  $k = \omega\sqrt{\mu\epsilon}$  and  $\eta = \sqrt{\mu/\epsilon}$  are the wave number and the wave impedance in a regular dielectric medium.

Similarly, the field for  $z > -d$  is given by,

$$\mathbf{E}_{+z}(\mathbf{J}) = \eta_c J_0 \left\{ (\hat{x} - j\hat{y})e^{-jh_1(z+d)} + (\hat{x} + j\hat{y})e^{-jh_2(z+d)} \right\} \quad (\text{C.13})$$

$$\mathbf{H}_{+z}(\mathbf{J}) = J_0 \left\{ (\hat{y} + j\hat{x})e^{-jh_1(z+d)} + (\hat{y} - j\hat{x})e^{-jh_2(z+d)} \right\} \quad (\text{C.14})$$

The subscript  $+z$  denotes the fields traveling in the  $+z$ -direction. Note that the pairs (C.8) and (C.9), and (C.13) and (C.14) satisfy (C.5) and (C.6). Furthermore,  $\mathbf{E}_{+z}(\mathbf{J}) = \mathbf{E}_{-z}(\mathbf{J})$  at  $z = -d$ , and  $\hat{z} \times [\mathbf{H}_{+z}(\mathbf{J}) - \mathbf{H}_{-z}(\mathbf{J})] = \mathbf{J}$  at  $z = -d$ .

## C.2 Another Way of Writing The Fields

It is very well established that the fields ( $\mathbf{E}, \mathbf{H}$ ) due to  $\mathbf{J}$  and  $\mathbf{M}$  currents in chiral media ( $\epsilon, \mu, \xi$ ) can be written as the sum of two fields ( $\mathbf{E}^+, \mathbf{H}^+$ ) and ( $\mathbf{E}^-, \mathbf{H}^-$ ). The former are called the *plus* fields and the latter are called the *minus* fields.

The plus fields ( $\mathbf{E}^+$ ,  $\mathbf{H}^+$ ) are produced when the plus sources ( $\mathbf{J}^+$ ,  $\mathbf{M}^+$ ) radiate in a regular dielectric medium characterized by  $(\epsilon^+, \mu^+)$ . Similarly, when the minus currents ( $\mathbf{J}^-$ ,  $\mathbf{M}^-$ ) radiate in the regular dielectric medium  $(\epsilon^-, \mu^-)$ , they produce the minus fields ( $\mathbf{E}^-$ ,  $\mathbf{H}^-$ ). For derivation of these quantities and the relative Maxwell's Equations based on the new parameters, refer to an elegant derivation in [78, 79]. Here, the constitutive parameters (Lindell, [45]) and the derived Maxwell's Equations are presented for completeness.

$$\mathbf{D} = \epsilon_L \mathbf{E} - j\xi_L \mathbf{H} \quad (\text{C.15})$$

$$\mathbf{B} = \mu_L \mathbf{H} + j\xi_L \mathbf{E} \quad (\text{C.16})$$

The subscript  $L$  reminds us that these are Lindell's constitutive parameters. Replacing (C.15) and (C.16) in the source free Maxwell's Equations result in the following equations for chiral media.

$$\nabla \times \mathbf{E} = \omega\xi_L \mathbf{E} - j\omega\mu_L \mathbf{H} \quad (\text{C.17})$$

$$\nabla \times \mathbf{H} = j\omega\epsilon_L \mathbf{E} + \omega\xi_L \mathbf{H} \quad (\text{C.18})$$

The  $\pm$  fields, currents, and media parameters are given below [78].

$$\mathbf{E}^+ = \frac{\mathbf{E} - j\eta\mathbf{H}}{2} \quad (\text{C.19})$$

$$\mathbf{E}^- = \frac{\mathbf{E} + j\eta\mathbf{H}}{2} \quad (\text{C.20})$$

$$\mathbf{E} = \mathbf{E}^+ + \mathbf{E}^- \quad (\text{C.21})$$

$$\mathbf{H}^+ = \frac{\mathbf{H} + j\mathbf{E}/\eta}{2} \quad (\text{C.22})$$

$$\mathbf{H}^- = \frac{\mathbf{H} - j\mathbf{E}/\eta}{2} \quad (\text{C.23})$$

$$\mathbf{H} = \mathbf{H}^+ + \mathbf{H}^- \quad (\text{C.24})$$

$$\mathbf{J}^+ = \frac{\mathbf{J} - j\mathbf{M}/\eta}{2} \quad (\text{C.25})$$

$$\mathbf{J}^- = \frac{\mathbf{J} + j\mathbf{M}/\eta}{2} \quad (\text{C.26})$$

$$\mathbf{J} = \mathbf{J}^+ + \mathbf{J}^- \quad (\text{C.27})$$

$$\mathbf{M}^+ = \frac{\mathbf{M} + j\mathbf{J}\eta}{2} \quad (\text{C.28})$$

$$\mathbf{M}^- = \frac{\mathbf{M} - j\mathbf{J}\eta}{2} \quad (\text{C.29})$$

$$\mathbf{M} = \mathbf{M}^+ + \mathbf{M}^- \quad (\text{C.30})$$

$$\epsilon^+ = \epsilon_L + \xi/\eta \quad (\text{C.31})$$

$$\epsilon^- = \epsilon_L - \xi/\eta \quad (\text{C.32})$$

$$\mu^+ = \mu_L + \xi\eta \quad (\text{C.33})$$

$$\mu^- = \mu_L - \xi\eta \quad (\text{C.34})$$

Then the Maxwell's Equations for the plus and minus regular dielectric medium can be rewritten as follows:

$$\nabla \times \mathbf{E}^+ = -j\omega\mu^+\mathbf{H}^+ \quad (\text{C.35})$$

$$\nabla \times \mathbf{H}^+ = j\omega\epsilon^+\mathbf{E}^+ \quad (\text{C.36})$$

$$\nabla \times \mathbf{E}^- = -j\omega\mu^-\mathbf{H}^- \quad (\text{C.37})$$

$$\nabla \times \mathbf{H}^- = j\omega\epsilon^-\mathbf{E}^- \quad (\text{C.38})$$

Using the above decomposition, the problem in Fig. C.1 can be divided into the following two problems shown in Fig. C.2.

It can be shown that the RHCP wave in the chiral medium, first part of (C.8) and (C.13), can be produced by a  $(\mathbf{J}^+, \mathbf{M}^+)$  radiating in a regular dielectric medium characterized by  $(\epsilon^+, \mu^+)$ , where,

$$\mathbf{J}^+ = -\hat{x}2J_0 \quad (\text{C.39})$$

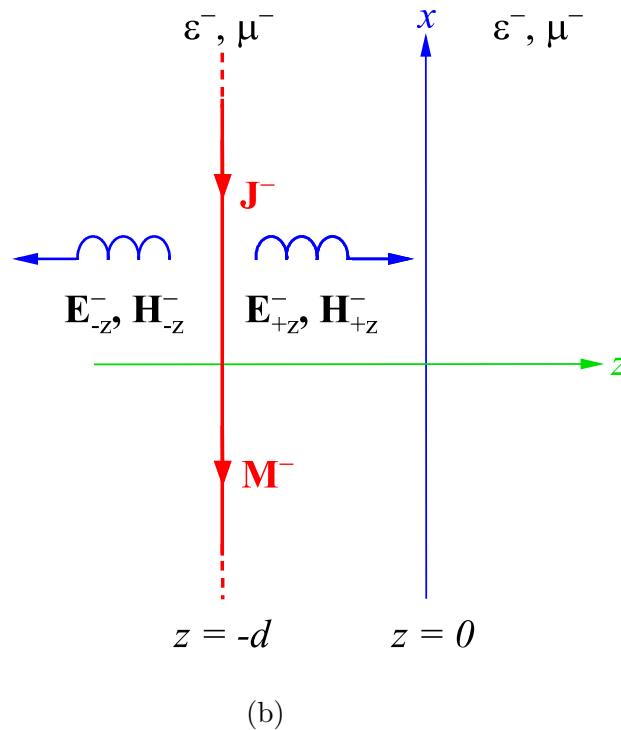
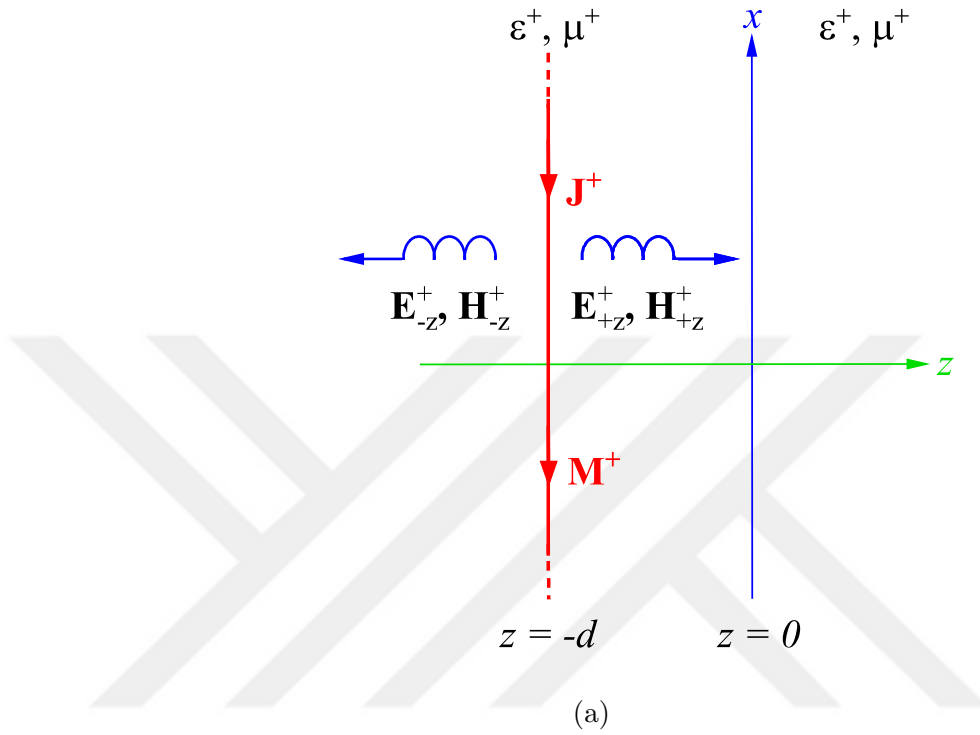


Figure C.2: Equivalent problem for Fig. C.1. (a) Setup for the *plus* medium and (b) Setup for the *minus* medium.

and

$$\mathbf{M}^+ = -\hat{x}j2\eta J_0 \quad (\text{C.40})$$

The fields produced due to  $\mathbf{M}^+$  for  $z < -d$  are

$$\mathbf{E}_{-z}^+(\mathbf{M}^+) = \hat{y}j\eta J_0 e^{jk^+(z+d)} \quad (\text{C.41})$$

$$\mathbf{H}_{-z}^+(\mathbf{M}^+) = \hat{x}jJ_0 e^{jk^+(z+d)} \quad (\text{C.42})$$

Here, the superscript ‘+’ shows that the fields are produced in the  $(\epsilon^+, \mu^+)$  regular dielectric, and the subscript  $-z$  shows that the fields are propagating to the left of the current sheet, i.e., in the  $-z$ -direction. The wavenumber in the plus medium is given by [79],

$$k^+ = \omega(\sqrt{\mu_L \epsilon_L + \xi_L}) = \omega\sqrt{\mu^+ \epsilon^+} \quad (\text{C.43})$$

Similarly, the fields produced due to  $\mathbf{J}^+$  for  $z < -d$  are

$$\mathbf{H}_{-z}^+(\mathbf{J}^+) = -\hat{y}J_0 e^{jk^+(z+d)} \quad (\text{C.44})$$

$$\mathbf{E}_{-z}^+(\mathbf{J}^+) = \eta[\mathbf{H}_{-z}^+(\mathbf{J}^+) \times (-\hat{z})] \quad (\text{C.45})$$

then

$$\mathbf{E}_{-z}^+(\mathbf{J}^+) = \hat{x}\eta J_0 e^{jk^+(z+d)} \quad (\text{C.46})$$

The total field for  $z < -d$  is,

$$\mathbf{E}_{-z}^+(\mathbf{J}^+, \mathbf{M}^+) = \eta J_0 (\hat{x} + j\hat{y}) e^{jk^+(z+d)} \quad (\text{C.47})$$

$$\mathbf{H}_{-z}^+(\mathbf{J}^+, \mathbf{M}^+) = J_0 (-\hat{y} + j\hat{x}) e^{jk^+(z+d)} \quad (\text{C.48})$$

Similarly, the total field for  $z > -d$  can be written as,

$$\mathbf{E}_{+z}^+(\mathbf{J}^+, \mathbf{M}^+) = \eta J_0 (\hat{x} - j\hat{y}) e^{-jk^+(z+d)} \quad (\text{C.49})$$

$$\mathbf{H}_{+z}^+(\mathbf{J}^+, \mathbf{M}^+) = J_0 (\hat{y} + j\hat{x}) e^{-jk^+(z+d)} \quad (\text{C.50})$$

The subscript  $+z$  shows that the fields are propagating to the right of the current sheet, i.e., in the  $+z$ -direction.

Equations (C.47) and (C.48) are the RHCP waves traveling in the  $-z$ -direction whereas (C.49) and (C.50) are the RHCP waves traveling in the  $+z$ -direction. Note that these fields are similar to RHCP waves in (C.8) and (C.13).

The transformation between  $(\epsilon, \mu, \xi)$  in Post's parameters and  $(\epsilon_L, \mu_L, \xi_L)$  in Lindell's parameters are as follows [79]:

$$\epsilon_L = \epsilon + \mu\xi^2 \quad (\text{C.51})$$

$$\mu_L = \mu \quad (\text{C.52})$$

$$\xi_L = \mu\xi \quad (\text{C.53})$$

This means,

$$\epsilon = \epsilon_L + \frac{\xi_L^2}{\mu_L} \quad (\text{C.54})$$

$$\mu = \mu_L \quad (\text{C.55})$$

$$\xi = \frac{\xi_L}{\mu_L} \quad (\text{C.56})$$

Substituting (C.54) - (C.56) in Post's constitutive parameters ((C.3) and (C.4)) one can easily get Lindell's constitutive relations ((C.15) and (C.16)). Furthermore, the wavenumbers for the RHCP/LHCP waves,  $h_{1,2}$  and  $k^{pm}$ , can be equated using the above transformations.

In a similar fashion, using Fig. C.2b, it can be shown that when the currents  $(\mathbf{J}^-, \mathbf{M}^-)$ ,

$$\mathbf{J}^- = -\hat{x}2J_0 \quad (\text{C.57})$$

$$\mathbf{M}^- = \hat{x}j2\eta J_0 \quad (\text{C.58})$$

radiate in the regular dielectric medium  $(\epsilon^-, \mu^-)$ , they produce the minus fields  $(\mathbf{E}^-, \mathbf{H}^-)$  given below.

$$\mathbf{E}_{-z}^-(\mathbf{J}^-, \mathbf{M}^-) = \eta J_0(\hat{x} - j\hat{y})e^{jk^-(z+d)} \quad (\text{C.59})$$

$$\mathbf{H}_{-z}^-(\mathbf{J}^-, \mathbf{M}^-) = J_0(-\hat{y} - j\hat{x})e^{jk^-(z+d)} \quad (\text{C.60})$$

$$\mathbf{E}_{+z}^-(\mathbf{J}^-, \mathbf{M}^-) = \eta J_0(\hat{x} + j\hat{y})e^{-jk^-(z+d)} \quad (\text{C.61})$$

$$\mathbf{H}_{+z}^-(\mathbf{J}^-, \mathbf{M}^-) = J_0(\hat{y} - j\hat{x})e^{-jk^-(z+d)} \quad (\text{C.62})$$

with

$$k^- = \omega(\sqrt{\mu_L \epsilon_L + \xi_L}) = \omega\sqrt{\mu^- \epsilon^-} \quad (\text{C.63})$$

Equations (C.59) and (C.60) are left hand circularly polarized (LHCP) waves traveling in the  $-z$ -direction (denoted by the subscript  $-z$ ). Similarly, (C.61) and (C.62) are LHCP waves traveling in the  $+z$ -direction (denoted by the subscript  $+z$ ). Note that  $\mathbf{E}^+ + \mathbf{E}^- = \mathbf{E}$  and  $\mathbf{H}^+ + \mathbf{H}^- = \mathbf{H}$  which are the same fields as in the original problem of Fig. C.1. The fields are written again for completeness.

The field produced by this source, for  $z < -d$  is given by,

$$\mathbf{E}_{-z}(\mathbf{J}) = \eta_c J_0 \left\{ (\hat{x} + j\hat{y})e^{jk^+(z+d)} + (\hat{x} - j\hat{y})e^{jk^-(z+d)} \right\} \quad (\text{C.64})$$

$$\mathbf{H}_{-z}(\mathbf{J}) = J_0 \left\{ (-\hat{y} + j\hat{x})e^{jk^+(z+d)} + (-\hat{y} - j\hat{x})e^{jk^-(z+d)} \right\} \quad (\text{C.65})$$

Similarly, the field for  $z > -d$  is given by,

$$\mathbf{E}_{+z}(\mathbf{J}) = \eta_c J_0 \left\{ (\hat{x} - j\hat{y})e^{-jk^+(z+d)} + (\hat{x} + j\hat{y})e^{-jk^-(z+d)} \right\} \quad (\text{C.66})$$

$$\mathbf{H}_{+z}(\mathbf{J}) = J_0 \left\{ (\hat{y} + j\hat{x})e^{-jk^+(z+d)} + (\hat{y} - j\hat{x})e^{-jk^-(z+d)} \right\} \quad (\text{C.67})$$

# SCATTERING FROM A CHIRAL CYLINDER OF ARBITRARY CROSS-SECTION ABOVE A DIELECTRIC HALF-SPACE

ORIJINALLIK RAPORU

% **14**

BENZERLIK ENDEKSI

% **8**

İNTERNET  
KAYNAKLARI

% **11**

YAYINLAR

% **1**

ÖĞRENCİ ÖDEVLERİ

Alıntıları çıkart

Kapat

Eşleşmeleri çıkar

Kapat

Bibliyografyayı Çıkart

Kapat